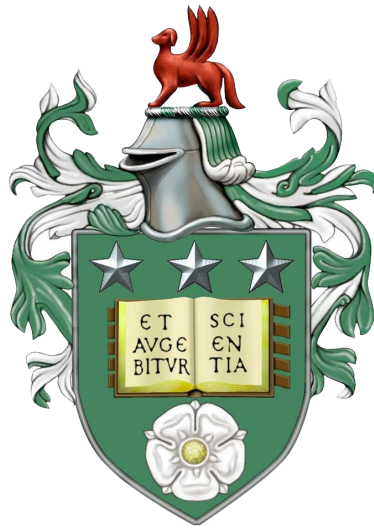


Investigating Pitting Corrosion on X65 Carbon Steel in Sweet Oil and Gas Environment



Sikiru Adepoju Mohammed

B Eng(Mech), MIASS, FSS, psc, MNACE, MICORR

Submitted in accordance with the requirements for the degree of
Doctor of Philosophy

The University of Leeds
School of Mechanical Engineering
Leeds, UK



July 2018

The candidate confirms that the work submitted is his own, except where work which has formed part of jointly authored publications has been included. The contribution of the candidate and other co-authors in published work from this thesis has been clearly indicated. The candidate confirms that appropriate credit has been given within the thesis where reference has been made to the work of others.

In the papers contributing to this thesis, the candidate (first author) carried out all the experiments, analysis and preparation of the manuscripts. All other authors contributed by proof reading and providing insight on the discussions.

This copy has been supplied on the understanding that it is copyright material and that no quotation from this thesis may be published without proper acknowledgement.

© 2018 The University of Leeds and Sikiru Adepoju Mohammed

Dedication

To all fallen heroes.

Publication and conferences

The following conference presentations and publications have been derived from this thesis:

1. Sikiru Mohammed, Yong Hua, Richard Barker, Anne Neville, Effect of calcium on X65 carbon steel pitting in saturated CO₂ environment: Presented at the Joint Electrochem 2017 & 58th Corrosion Corrosion Science Symposium held at the Great Hall, University of Birmingham from 10-12 September 2017.
2. Sikiru Adepoju Mohammed, Yong Hua, Richard Barker, Anne Neville: Investigating healing of reproducible shallow pits on X65 carbon steel in sweet oil and gas environment; Presented at the Joint European Corrosion Congress 2017, 20th International Corrosion Congress & Process Safety Congress 2017 held at Prague Convention Center, Prague, Czech Republic from 3-7 September 2017.
3. Sikiru Mohammed, Yong Hua, Richard Barker, Anne Neville: Investigating pitting in X65 carbon steel using potentiostatic polarisation, Applied Surface Science, Volume 423, 30 November 2017, Pages 25-32, ISSN 0169-4332, <https://doi.org/10.1016/j.apsusc.2017.06.015>.
4. Sikiru Mohammed, Yong Hua, Richard Barker, Anne Neville, Investigating pitting corrosion of X65 carbon steel in sweet environment using potentiostatic polarisation; Presented at the NACE Corrosion Conference 2017, Ernest N. Morial Convention Centre, New Orleans, Louisiana, LA USA from 26-30 March 2017.
5. Sikiru Mohammed, Yong Hua, Richard Barker, Anne Neville: An assessment of pitting corrosion of X65 carbon steel in sweet oil and gas environment; Presented at the 57th Corrosion Science Symposium 2016, Swansea UK from 5-6 September 2016.

The under-listed are jointly authored submission/publication that were conducted during this research but not featured in this thesis:

- a. Sikiru Mohammed, Yong Hua, Richard Barker, Anne Neville: The effect of steel Cr content on the formation of corrosion scales and their protective capability against general and localized corrosion in high pressure CO₂ saturated brine. submitted to the International Journal of Engineering Failure Analysis.
- b. Lawrence Onyeji, Sikiru Mohammed, Girish Kale: Electrochemical response of micro-alloyed steel under potentiostatic polarization in CO₂ saturated brine, Corrosion Science, Volume 138, 2018, Pages 146-153, ISSN 0010-938X, <https://doi.org/10.1016/j.corsci.2018.04.001>.

Awards received

The following awards were received during the conduct of this research work:

- a. First Place in the Department of Mechanical Engineering and the Faculty of Engineering for the Year 2017 University-wide Postgraduate Researcher of the Year competition.
- b. Joint Second Place: University of Leeds Postgraduate Researcher of the Year 2017.

Acknowledgements

Many people contributed to the success of this study. It would be difficult to thank them all enough but I think I owe them a lot of gratitude for their contributions. I am highly indebted to my primary supervisor, Professor Anne Neville for her painstaking effort at brewing ideas that diligently guided the conduct of this work. My sincere appreciation also goes to Dr Richard Barker for his professional innovation during the modeling and experimental phase of this work. Many thanks to Dr Yong Hua for his gentle but persuasive critique and support.

I am indebted to Michael Huggan for his dedication and professional input towards machining the artificial pit components. I must not forget to acknowledge the contributions of Andrew O'Brien, Jordan and Paul for their technical support. My thanks as well goes to Dr John Holt, Lorraine Moyles, Vicky Masters and Fiona Slade for their professional support.

I appreciate the support of my LabView comrades, Dr Earle Jamieson and Dr James Chandler as well as my brother in \LaTeX , Ali Hayajneh. I also enjoyed the kind support of my accommodation neighbor, Saad Luaib. Many thanks to Dr NA David and Engineer S Oyekunle of Nigerian Defence Academy for their recommendations. My acknowledgement cannot be complete without recognizing the effort of colleagues like Hussaini Majia, Lawrence Onyeji, Haithem, Bethan Warren, Mohammed Abdulmajeed, Dushyant Goordyal, Jun Wai Kow, Abdulkhateeb, Alex, Josh Owen, Roselina, Loubna and other lovely friends on Level-3 (Mechanical).

This research wouldn't have been possible without the sponsorship opportunity offered by the Petroleum Technology Development Fund, Nigeria. Special gratitude also goes to the Nigerian Army for granting study leave to enable me undertake this work. Finally, I thank Alimi Kamal, Atinuke, Bros Galo, Bilal, Caroline, Chiweumba, Dako, Ernest, Grace, Idayat, Iman, Mary, Medina, Mistura, Rekiya, Sharon, Shehu, Svetlana, Tawa, Vero and my parent, Engineer Adekunle Mohammed & Alhaja S Mohammed for standing by me always. I plead with those whose names could not be mentioned here to bear with me. They should note that this work would not have been possible without their support.

Abstract

Low carbon steel is widely applied for engineering purposes such as construction of pipelines, vessels, refinery components amongst others. The set-back in low carbon steel is in its corrosion performance which takes a toll on operations, economy as well as health and safety. Pitting corrosion ranks among the highest level of corrosion defects and it is inevitable due to the effect of nature, design and operation parameters. Pitting is hard to predict while pitting in sweet (CO_2) environments remains the most dangerous form of localised corrosion. Pitting in passive materials is generally well understood but pitting in actively corroding materials has received much less attention and remains poorly understood to date. Pitting can progress beneath films formed on metal surfaces while cations such as calcium are known to influence pitting kinetics and there are no well established models to describe such processes.

A comprehensive study of pitting in API-X65 carbon steel was conducted by examining how pits of predetermined depth behave in a calcium-free and calcium-rich environment. Reproducible stress-free pits with depths of approximately $70 \mu\text{m}$ were generated using a novel potentiostatic polarisation approach. The relationship between general and pitting corrosion was established using profilometry data and electrochemical results. Pit growth on steel samples was investigated in a calcium-rich environment to understand how Ca^{2+} influences pitting kinetics and how the different CaCO_3 polymorphs influence pitting in low carbon steel under conditions typical to crude oil storage and other oil & gas exploration settings. The investigation was extended to include the use of an artificial pit to understand how the galvanic trend influences pitting under mixed carbonate ($\text{Ca}_x\text{Fe}_{(1-x)}\text{CO}_3$) film conditions and also to reveal events within an actively corroding pit. Robust analytical tools such as XRD, SEM, Raman and white light interferometry were utilised to examine formed products and reveal details of pitting recorded beneath formed films.

It was observed that pseudo-passivation occurs in a calcium-rich environment and that the pitting trend relates to the nature of the CaCO_3 polymorph formed on the steel surface. It was also revealed that the presence of calcium increases galvanic

current between film-covered and compromised spots in low carbon steel and that the magnitude of galvanic current recorded in Ca^{2+} systems relates to pitting threshold recorded on the metal. Corrosion products that form on steel surfaces were also detected inside actively corroding pits.

Ideas don't come out fully formed. They only become clear as you work on them.

Mark Zuckerberg

Nomenclature

Terms	Units	Description
α_a		Anodic charge transfer coefficient
α_c		Cathodic charge transfer coefficient
B	mV/decade	Stern-Geary Constant ($\frac{1}{2.303}(\frac{\beta_a\beta_c}{\beta_a+\beta_c})$)
β_a	mV/decade	Anodic Tafel
β_c	mV/decade	Cathodic Tafel
E_{corr}	Volts	Corrosion potential
E_p	Volts	Pitting potential
E_{rev}	Volts	Reversible potential
E_{rev}°	Volts	Reversible potential under standard conditions
E_w	grams	Equivalent weight
F	$CMol^{-1}$	Faraday constant
ΔG	Joules	Free energy change
ΔG°	Joules	Free energy change under standard conditions
ΔG_a°	Joules	Energy barrier for anodic reaction
ΔG_c°	Joules	Energy barrier for cathodic reaction
i_a	mA/cm^2	Anodic current density
i_{corr}	mA/cm^2	Corrosion current density
i_c	mA/cm^2	Cathodic current density
i_o	mA/cm^2	Exchange current density
K_a		Activity constant
K_c		Molarity constant
$K_{sp(FeCO_3)}$	$gMol^{-1}$	$FeCO_3$ Solubility limit
m	grams	Mass
M	g/Mol	Molar mass
n		Number of electrons involved in reaction
R	$Jmol^{-1}K^{-1}$	Ideal Gas Constant
R_{FeCO_3}	mmS^{-1}	$FeCO_3$ Precipitation rate
R_p	$ohms\text{-}cm^2$	Corrosion (polarisation or transfer) resistance
R_v	μm	Pit depth from reference plane (2-Dimension)
SS_{FeCO_3}	Dimensionless	$FeCO_3$ Super saturation
S_v	μm	Pit depth from reference plane (3-Dimension)
t	Seconds	Time
T	Kelvin	Temperature
Z	gC^{-1}	Electrochemical equivalent
$E_{Fe^{2+}/Fe}^\circ$	Volts	Equilibrium potential of Iron
E_{H^+/H_2}°	Volts	Equilibrium potential of Hydrogen
η	Volts	Over-potential
η_a	Volts	Anodic over-potential
η_c	Volts	Cathodic over-potential
ρ	g/cm^3	Density

Abbreviations

Abbreviation	Definition
ACC	Amorphous calcium carbonate
AR	Area ratio of anode to cathode electrode in artificial pit
CaCO ₃	Calcium carbonate
$Ca_xFe_{(1-x)}CO_3$	Mixed calcium iron carbonate
CO ₂	Carbon-dioxide
Cl ⁻	Chloride ion
CRA	Corrosion Resistance Alloy
CSI	Coherence Scanning Interferometry
D	Average metal penetration
EDX	Energy Dispersive X-Ray Spectroscopy
Fe ₃ C	Iron carbide
FeCO ₃	Iron carbonate
H ₂ S	Hydrogen sulphide
IHP	Inner Helmholtz Plane
J	Joule
LPR	Linear Polarisation Resistance
OCP	Open Circuit Potential
OHP	Outer Helmholtz Plane
P	Deepest metal penetration
Pf	Pitting factor
pH	Acidity index
ppb	Part per billion
ppm	Part per million
SCC	Stress corrosion cracking
SEM	Scanning Electron Microscopy
SiC	Silicon carbide paper
XRD	X-Ray Diffraction

Contents

Publication and conferences	iii
Awards received	v
Acknowledgements	vi
Abstract	vii
Nomenclature	x
Abbreviations	x
1 Introduction	1
1.1 Overview	1
1.2 Statement of research problem	5
1.3 Objective and scope of research	6
1.4 Thesis outline	8
2 Corrosion Fundamentals	10
2.1 Introduction	10
2.2 Aqueous corrosion chemistry	11

2.2.1	Electrochemical cell chemistry	11
2.2.2	Electrical double layer	12
2.3	Corrosion kinetics	14
2.3.1	Open circuit potential, equilibrium potential and polarisation	15
2.3.2	Evans' diagram	17
2.3.3	Corrosion potential	19
2.4	Corrosion thermodynamics	20
2.4.1	Gibb's free energy, Vant Hoff's reaction isotherm and Nernst's equation	20
2.4.2	Pourbaix diagram for Fe-H ₂ O and Fe-CO ₂ -H ₂ O systems	22
2.5	Electrochemical corrosion testing	25
2.5.1	Galvanic coupling measurement	25
2.5.2	Open circuit potential	26
2.5.3	Butler Volmer equation	26
2.5.4	Tafel plots	27
2.5.5	Linear polarisation resistance and Stern-Geary's equation	28
3	Literature Review	31
3.1	Carbon steel corrosion	31
3.2	Effect of dissolved CO ₂ on carbon steel electrochemical reactions	34
3.3	Forms of CO ₂ induced corrosion	36
3.3.1	Mesa attack	36
3.3.2	Flow induced localised corrosion	36

3.3.3	Galvanic corrosion	37
3.4	Pitting corrosion	37
3.5	Carbon steel pitting in sweet environment	38
3.5.1	Carbon steel pitting initiation in sweet environments	40
3.5.2	Propagation of carbon steel pitting	42
3.5.3	Pit termination	43
3.5.4	Schematic representation of carbon steel pitting in a CO ₂ environment	43
3.6	Identification and characterisation of corrosion pits	45
3.6.1	Metal penetration and pitting factor	46
3.6.2	Characterisation of corrosion pits	47
3.7	Corrosion products formed on carbon steel in sweet environments	48
3.7.1	Grey zone conditions	50
3.7.2	Iron carbonate and localised corrosion	51
3.7.3	Magnetite (Fe ₃ O ₄)	54
3.7.4	Iron carbide (Fe ₃ C)	55
3.7.5	Mixed Ca _x Fe _(1-x) CO ₃ Films	57
3.7.6	Calcium carbonate and localised corrosion	58
3.8	Parameters governing pitting corrosion	59
3.8.1	Area ratio of anode to cathode	59
3.8.2	Salt concentration / Halides	59
3.8.3	Acetic Acid (HAc)	60
3.8.4	Temperature	61

3.8.5	pH and flow velocity	61
3.9	Techniques for investigating pitting corrosion	62
3.10	Simulating pitting corrosion in the laboratory for corrosion test	64
3.10.1	Newman artificial pit	64
3.10.2	Turnbull's pencil pit	64
3.10.3	Palmer's artificial pit	66
3.10.4	Han's artificial pit	66
3.10.5	Amri et al. pit	68
3.11	Application of artificial pits for pitting studies	71
3.12	General and pitting corrosion	72
3.13	Summary of literature review	73
3.14	Research questions and work approach	74
4	Materials and Experimental Procedures	76
4.1	Materials	76
4.2	Sample preparation and procedure for potentiostatic polarisation tests	77
4.2.1	Post experiment analysis	78
4.3	Test procedure for pit propagation tests	79
4.3.1	Post experiment analysis	81
4.4	Artificial pit and test procedure for artificial pit experiments	81
4.4.1	Artificial pit design	81
4.4.2	Samples preparation and experimental approach	83
4.5	Corrosion measurement set-up	86

4.6	Analysis tools	87
4.6.1	PHILIPS X-Pert X-Ray Diffraction analysis	88
4.6.2	Scanning Electron Microscope (SEM) analysis	88
4.6.3	Raman Analysis	90
4.6.4	Coherence Scanning Interferometry	91
4.6.5	Identification of pits and profiling technique	93
4.6.6	Profiling technique for pit analysis	96
4.6.7	Application of NPFLEX CSI for pitting corrosion measurement	97
4.7	Confirmation of electrochemical response	99
4.8	Tafel plot on test conditions	100
4.8.1	Tafel properties of X65 carbon after 24 h polarisation test . .	103
5	Effect of potentiostatic polarisation on carbon steel corrosion	105
5.1	Introduction	105
5.2	Effect of applied potential on pitting	106
5.2.1	Analysis of pitting trend	109
5.2.2	Application of Faraday's law of electrolysis to potentiostatic test result	112
5.2.3	Derivation of pitting factor	115
5.3	Pit growth under active conditions	117
5.3.1	Effect of potentiostatic duration on pitting trend	118
5.3.2	Polarisation curves under film-free and passive film conditions	118
5.3.3	Statistical trend of discrete pit profiles	124

5.4	Potential induced pitting under protective film conditions	125
5.4.1	Analysis of pitting under protective-film conditions	129
5.5	Conclusions	131
6	Effect of calcium on X65 carbon steel corrosion in saturated CO₂ environment	133
6.1	Introduction	133
6.2	Pitting in 0 ppm Ca ²⁺	134
6.3	Effect of pH on Calcium Pitting at 80 °C	135
6.3.1	Calcium pitting at low pH	139
6.3.2	Calcium pitting at high pH	146
6.4	Effect of pH on formed film	147
6.4.1	Metal thinning due to general corrosion	153
6.4.2	Determination of pitting factor	156
6.4.3	Absolute metal thinning and pitting	157
6.5	Comparison of Ca ²⁺ pitting under pH 3.8 and pH 6	157
6.6	Conclusions	158
7	Assessing the influence of calcium on X65 carbon steel pitting using an artificial pit	160
7.1	Introduction	160
7.2	Cathode disc passivation/results	161
7.2.1	Analysis of mixed carbonate formed in 682 ppm Ca ²⁺	165
7.2.2	Pitting trend in 682 ppm Ca ²⁺	169

7.2.3	Measured corrosion rate for anode and cathode electrodes	174
7.2.4	Derivation of charge associated with galvanic current in artificial pit	179
7.3	Conclusions	180
8	Discussion	182
8.1	Introduction	182
8.2	Rationale for considering the top-10 pits as a measure of pitting severity	183
8.3	Generating stress free stochastic pits	183
8.3.1	Effect of pH on carbon steel pitting	184
8.4	Comparison of Ca^{2+} pitting under pH 3.8 and pH 6	186
8.5	Calcium polymorphs and the pitting trend	187
8.6	The effect of chloride ion on carbon steel pitting in Ca^{2+} solution . .	193
8.7	Artificial pit concept in pitting investigation	194
8.7.1	Suggested sign convention in Artificial pit	195
8.8	Effect of calcium on carbon steel pitting	196
8.9	Pseudo-passivation and galvanic effects in calcium pitting	198
8.10	The effect of anode / cathode area ratio on carbon steel pitting in 682 ppm Ca^{2+} solution	199
8.11	The relationship between charge and carbon steel pitting in 682 ppm Ca^{2+} solution	200
8.12	Pitting and steel micro-structure	201

9	Conclusions, research relevance and future work	203
9.1	Conclusions	203
9.1.1	Generating stress free stochastic pits	204
9.1.2	Calcium polymorphs and pitting trend	205
9.1.3	Calcium influence on galvanic current and pitting	207
9.2	Relevance of research	208
9.3	Industrial application	209
9.4	Future Work	209
	Bibliography	210
	Appendices	241
A	Pit count technique	242
B	2D profilometry of corroded pit	258
C	Tafel plot for Calcium tests	260
D	EDX spectrum of corrosion product detected inside pit in 682 ppm Ca ²⁺ solution	261

List of Tables

1.1	Cost associated with Corrosion Prevention	4
2.1	Conditions for corrosion reaction	22
3.1	Corrosion caused failures in petroleum related industries	31
3.2	Possible electrochemical reactions during the anodic dissolution of iron in CO ₂ environment	33
3.3	Research question and work approach	74
4.1	Chemical composition (wt%) of X65 carbon steel	76
4.2	Test matrix	77
4.3	Test matrix	79
4.4	Matrix of Tafel constants obtained under experimental conditions	80
4.5	Some NPFlex terms used for pitting analysis	94
4.6	Derivations from Tafel Extrapolation	103
5.1	Parameters for determining pitting factor (Test 1)	116
5.2	Parameters for determining pitting factor (Test 2)	117
5.3	Applied potential and pit attributes	125
5.4	Exposure time and pit attributes	125

5.5	Test matrix for polarisation tests under protective film condition . . .	129
6.1	Average metal loss obtained from LPR measurement under different pH conditions.	154
6.2	General metal thinning and pitting of API-X65 carbon steel in Calcium-free and 5,000ppm Ca ²⁺ solutions	157
7.1	Artificial pit test matrix	163
7.2	Tafel constant	163
7.3	Corrosion data obtained using 1mm anode pit coupling	176
7.4	Charge recorded in artificial pit coupling in saturated CO ₂ , 3.3 wt.% NaCl, pH 7.5, 50 °C in 682ppm Ca ²⁺ and Ca ²⁺ -free solutions.	180
8.1	Advantages and disadvantages of artificial pi model in use	194

List of Figures

1.1	Pie chart displaying Global GDP cost of corrosion	2
1.2	Cleaning-up operations at Refugio Beach and underwater pipeline leakage in Taylor Creek (Bayelsa-Nigeria)	2
1.3	Images of Pitting Attack on Steel	3
1.4	Summary of Work Scope	7
2.1	Schematic representation of Evan’s Diagram for a metal corroding in an acid	12
2.2	Electrical Double Layer Schematics	13
2.3	Polarisation Diagram for Redox in Fe	17
2.4	Potential vs current curve for steel corrosion	17
2.5	Evan’s diagram of Iron corrosion in acidic medium	18
2.6	Illustration of Corrosion Potential due to Polarisation effect	19
2.7	Relationship between Gibb’s Free Energy, Cell Potential and Equilibrium Constant	21
2.8	Modified energy diagram (reaction barrier) for corrosion reactions in Fe	22
2.9	Potential-pH diagram for Fe-H ₂ O System	23

2.10	Generated Potential-pH diagrams at: (a) 25 °C (b) 80 °C (c) 120 °C (d) 150 °C (e) 200 °C and (f) 250 °C	25
2.11	Galvanic Model in Compromised Film	26
2.12	Typical Anodic and Cathodic Tafel Plot	28
2.13	Typical LPR Plot	29
3.1	Effect of CO ₂ on cathodic current	35
3.2	Typical picture of Mesa attack	36
3.3	Carbon steel under uniform attack	41
3.4	Localised attack in carbon steel	41
3.5	Galvanic model for CO ₂ induced pitting corrosion in mild Steel	42
3.6	Schematic diagram of corrosion process at film free surface (pit anode) on Carbon Steel	44
3.7	Schematic diagram of corrosion occurring on passive layer on protected surface (cathodic site) leading to formation of Fe ₃ O ₄	44
3.8	Galvanic cell schematic diagram featuring bare anode and protected cathode	45
3.9	William R. Thorpe Lever type Pit Gauge	45
3.10	Tri Gauge Pit Gauge	46
3.11	Schematics depicting pitting factor parameters	47
3.12	Cross section featuring corrosion pit shapes	48
3.13	ASTM Standard charts for rating corrosion pits	49
3.14	Steps involved in formation of FeCO ₃ film	52
3.15	SEM Image showing FeCO ₃ deposits on X65 carbon steel	52

3.16 Schematic of properties of FeCO ₃ morphology for low Cr-alloy steel	53
3.17 Image depicting boundary line between outer and inner FeCO ₃ layers	54
3.18 GIXRD and SEM indicating Fe ₃ O ₄ presence in FeCO ₃ Film	55
3.19 Element profile of EDX scan depicting likely Fe ₃ O ₄ beneath FeCO ₃ film	56
3.20 SEM Image of Fe ₃ C deposits	57
3.21 Image of Fe ₃ C anchoring FeCO ₃ deposits	57
3.22 Effect of NaCl at grey zone condition (80°C, 0.53bar CO ₂ , and pH 6.0)	60
3.23 3D morphology of a mechanical indented pit on X65 carbon steel featuring crack tips	63
3.24 Schematic of Newman’s artificial pit cell	65
3.25 Diagram of two compartment cell with pencil pit assembly	65
3.26 Schematic representation of Turnbull’s 2-compartment pit cell	66
3.27 Schematic representation of Palmer’s artificial pit assembly	67
3.28 Han’s artificial pit	68
3.29 Conditions favouring: (a) Passive Artificial Pit under high FeCO ₃ SS of 3-9, 80°C,0.53bar P _{CO₂} , pH5.5 and 1wt% NaCl (b) Passive Artificial Pit under low FeCO ₃ SS of 0.2-0.5, 80°C,0.53bar P _{CO₂} , pH5.8 and 1wt% NaCl (c) Active Artificial Pit under moderate FeCO ₃ SS of 0.4-4, 80°C,0.53bar P _{CO₂} , pH5.9 and 1wt% NaCl (d) Active Artificial Pit under low FeCO ₃ , SS of 0.3-0.8, 80°C,0.53bar P _{CO₂} , pH6.0 and 10wt% NaCl	69
3.30 Current density recorded from coupled Anode/Cathode pit area ratio 1:1000, pH5.85, SS _{FeCO₃} of 0.2-4 at 80°C and 1wt%NaCl	69
3.31 Amri et al. Artificial Pit	70

3.32	Pseudopassivation recorded at pH 6.6, 80 °C, 1 wt.% NaCl	72
4.1	Micrograph of X65 carbon steel.	77
4.2	Schematic representation depicting parameters for calculating pitting factor	80
4.3	Artificial pit showing materials components of artificial pit	82
4.4	Artificial pit for pitting corrosion test featuring (a) pit components and (b) pit assembly in test beaker.	84
4.5	Artificial Pit design showing: (a) Solidworks drawing of anode pin (b) Solidworks drawing of cathode disc and (c) coupled artificial pit	85
4.6	Schematic representation of the 3-electrode cell	87
4.7	Corrosion test using multi-channel Ivium Potentiostat	87
4.8	Schematic representation of the experimental set-up	88
4.9	PHILIPS XPert XRD machine	89
4.10	EVO MA15 Scanning Electron Microscope	90
4.11	RENISHAW Raman	91
4.12	Schematics of Coherence Scanning Interferometry Layout	92
4.13	Bruker NPFLEX used for pitting analysis	93
4.14	Schematic of amplitude parameters featuring Roughness Peak (R_p), Roughness Valley (R_v) and Roughness Peak to Valley (R_t) with reference from Mean Line	94
4.15	Depiction of Positive and Negative Skew	95
4.16	Interface showing data collection process	96
4.17	Description of Sample Scan area comprising 172 stitches in 10mm diameter	97

4.18	Spiral scan pattern adopted for CSI analysis	97
4.19	Computer interface featuring a multiple region analysis of corrosion pits formed on X65 carbon steel under 150mV potentiostatics in 3.5% NaCl solution, unbuffered, 30°C, P _{CO₂} of 1bar for 72 Hrs.	99
4.20	SEM image of corrosion product formed on X65 carbon steel under (a) 150mV potentiostatic and (b) free corrosion in sweet environment.	100
4.21	SEM Image after 150mV potentiostatic in 3.5% NaCl solution, pH of 6.6, 80°C for 24h.	100
4.22	Tafel curves after 7h tests on 4.9cm ² X65 carbon steel in 3.5%NaCl and atmospheric pressure under (a) 150mV potentiostatic (b) LPR and OCP measurement on cathode disc (c) LPR and OCP measurement on 3mm anode pit.	102
4.23	Tafel plots after 24h, 150mV potentiostatic test in (a) 3.5% NaCl solution, pH of 3.8, 30°C. (b) 3.5% NaCl solution, pH 6.6, 80°C. . . .	104
5.1	Current transient plot of 50mV, 100mV and 150mV potentiostatic polarisation on X65 carbon steel over a duration of 24h in a 3.5 wt.% NaCl solution saturated with CO ₂ at 30°C at pH3.8.	107
5.2	SEM image of pit formed through carbide films on X65 carbon steel under 150mV potentiostatics in 3.5% NaCl solution, pH of 3.8, 30°C for 24h after cleaning with Clarke's solution.	108
5.3	Cross section of pit formed through carbide films on X65 carbon steel under 150mV potentiostatics in 3.5% NaCl solution, pH of 3.8, 30°C for 24h.	108
5.4	XRD pattern showing Fe ₃ C deposit on X65 carbon steel after 50mV, 100mV and 150mV potentiostatic in 3.5% NaCl solution, pH of 3.8, 30°C for 24h	109

5.5	White light profilometry images showing maximum pit depth recorded on X65 carbon steel after 24h exposure in CO ₂ saturated, 3.5% NaCl solution, pH3.8, 30°C under (a&b) 50mV, (c&d) 100mV and (e&f) 150mV polarisation.	110
5.6	Pit depth chart depicting top-10 average and maximum depth recorded for samples subjected to 50mV, 100mV and 150mV potentiostatic polarisation at 30°C, pH3.8, 3.5wt% NaCl, CO ₂ saturated for 24h. (Note: Max depth (red bars) indicates deepest valley; average of top ten pits (black bars) is termed top-10 average; error bars are based on standard deviation of two set of tests).	111
5.7	Cross-section morphology of pit formed after 150mV at 3.5% NaCl, 30°C, pH3.8, 24h.	111
5.8	Plot depicting magnitude of charge expended for repeated test of 50mV, 100mV and 150mV potentiostatic at 30°C, pH3.8, 3.5%wt NaCl for 24h.	114
5.9	Plot of void volume depicting trend for general and pitting corrosion after 50mV, 100mV and 150mV potentiostatic at 30°C, pH3.8, 3.5%wt NaCl for 24h.	115
5.10	Plot depicting trend of pit from initial depth of 70µm exposed to saturated CO ₂ unbuffered solution at 80°C up to 48h.	117
5.11	Current transient plot of 150mV Potentiostatic on X65 Carbon steel over a duration of 24h, 48h and 72h in unbuffered 3.5 wt.% NaCl solution saturated with CO ₂ at 30°C.	119
5.12	Pit depth analysis depicting average depth and maximum depth of samples subjected to 150mV potentiostatic at 30°C, unbuffered, 3.5wt% NaCl, CO ₂ saturated for 24h, 48h and 72h.	119
5.13	Polarisation curve of X65 carbon steel under film-free condition (pH 3.8, 30°C, 3.5wt% NaCl, -15mV to 1,000mV, scan rate 0.25mV/S, 250RPM.	120

5.14	Polarisation curve of X65 carbon steel under protective film condition (pH6.6, 80°C, 3.5%NaCl, -15mV to 1,000mV, scan rate 0.25mV/S, 250RPM).	120
5.15	SEM images of corrosion pits formed on X65 carbon steel under (a) 50mV, (b) 100mV and (c) 150mV potentiostatics in 3.5% NaCl solution, pH 3.8, 30°C, P _{CO₂} of 1bar for 24h.	121
5.16	XRD pattern images of corrosion product formed on X65 carbon steel under 150mV potentiostatic in 3.5% NaCl solution, pH of 3.8, 30°C for 24 Hrs	121
5.17	SEM image of corrosion products formed on X65 carbon steel under 150mV potentiostatics in 3.5% NaCl solution, pH of 4.0, 30°C for 24h.	122
5.18	Raman image of corrosion products formed on X65 carbon steel under 150mV potentiostatics in 3.5% NaCl solution, pH of 4.0, 30°C for 24 Hrs.	122
5.19	SEM images of corrosion products formed on X65 carbon steel under 150mV potentiostatics in 3.5% NaCl solution, pH of 4.0, 30°C for 24 Hrs under SEM Magnification of X500.	123
5.20	SEM images showing cracks in Fe ₃ C film on X65 carbon steel under 150mV potentiostatics in 3.5% NaCl solution, pH 3.8, 30°C for 24 h. .	123
5.21	Statistical data showing discrete plots of (a) R _v versus Diameter, (b) R _v versus Volume and (c) R _a versus Diameter of corroded sample after 100mV polarisation in 3.5% NaCl solution, unbuffered, 30°C, P _{CO₂} of 1bar for 24h.	126
5.22	Statistical data showing discrete plots of (a) R _v versus Diameter, (b) R _v versus Volume and (c) R _a versus Diameter of corroded sample after 150mV polarisation in 3.5% NaCl solution, unbuffered, 30°C, P _{CO₂} of 1bar for 24h.	127

5.23	Statistical data showing discrete plots of (a) R_v versus Diameter, (b) R_v versus Volume and (c) R_a versus Diameter of corroded sample after 150mV polarisation in 3.5% NaCl solution, unbuffered, 30°C, P_{CO_2} of 1bar for 72h.	128
5.24	Current transient plot of 50mV, 100mV and 150mV Potentiostatic on X65 Carbon steel over a duration of 1h in 3.5 wt.% NaCl solution in saturated CO_2 at pH6.6, 80°C.	129
5.25	Current transient plot of 150mV potentiostatic on X65 Carbon steel over a duration of 24h in 3.5 wt.% NaCl in saturated CO_2	130
5.26	Chart depicting average pit depth and maximum depth of samples subjected to 50mV, 100mV and 150mV potentiostatic at 80°C, pH6.6, 3.5wt% NaCl, CO_2 condition for 24h.	131
6.1	LPR/OCP and top view SEM image featuring corrosion products formed on pitted X65 carbon steel in saturated CO_2 , 3.5 wt% NaCl, 0 ppm Ca^{2+} , 80 °C over a duration of 24 h for pH 3.8	135
6.2	Corrosion rate plot and top view SEM image featuring corrosion products formed on pitted X65 carbon steel in saturated CO_2 , 3.5 wt% NaCl, 0 ppm Ca^{2+} , 80 °C over a duration of 24 h for pH 6	136
6.3	Bar chart depicting pitting trend (top-10 average) of pits from initial 70 μm depth in saturated CO_2 , 3.5 wt% NaCl, 0 ppm Ca^{2+} , 80 °C over a duration of 4 days at pH 3.8 and pH 6	137
6.4	LPR/OCP plot of X65 carbon steel corroded in 2 wt% NaCl, 5000 ppm Ca^{2+} at 80 °C for 96 h in (a) pH 3.8 (b) pH 6.	138
6.5	Bar chart depicting pitting trend (top-10 average) of pits from initial 70 μm depth in saturated CO_2 , 5000 ppm Ca^{2+} , 80 °C over a duration of 4 days at pH 3.8 and pH 6	139

6.6	White light profilometry images showing maximum pit depth recorded after 70 μm pit was corroded in saturated CO_2 , 2 wt.% NaCl, 5000 ppm Ca^{2+} , pH 3.8, 80 °C for (a) 24 h, (b) 48 h and (c) 96 h exposure. Measurements relative to corroded surface.	140
6.7	XRD scan pattern of formed product on X65 carbon steel corroded in saturated CO_2 , 2 wt.% NaCl, 5,000 ppm Ca^{2+} , 80 °C, pH 3.8, for (a) 24 h, (b) 48 h, (c) 96 h.	141
6.8	Top view SEM image and cross section featuring corrosion products formed on X65 carbon steel in saturated CO_2 , 2 wt.% NaCl, 5000 ppm Ca^{2+} , 80 °C, pH 3.8 over a duration of (a) 24 h (b) 48 h and (c) 96 h	142
6.9	Raman image of corrosion product formed on X65 carbon steel corroded in saturated CO_2 , 2 wt.% NaCl, 5,000 ppm Ca^{2+} , 80 °C over a duration of 72 h at pH 3.8	143
6.10	Polymorphs of calcium carbonate showing (a) calcite in six coordinate and (b) aragonite in 9 coordinate environment. Images were generated using molview and CrystalMaker9	144
6.11	Cross section showing Ca^{2+} inside a pit on X65 carbon steel corroded at 2 wt.% NaCl, 5,000 ppm Ca^{2+} , 80 °C for 96 h at pH 3.8	145
6.12	EDX mapping showing Ca^{2+} inside a pit on X65 carbon steel corroded at 2 wt.% NaCl, 5,000 ppm Ca^{2+} , 80 °C for 96 h at pH 3.8	145
6.13	EDX line scan showing Ca^{2+} inside a pit on X65 carbon steel corroded at 2 wt.% NaCl, 5,000 ppm Ca^{2+} , 80 °C for 96 h at pH 3.8	146
6.14	White light profilometry images showing maximum pit depth recorded after 70 μm pit was corroded in saturated CO_2 , 2 wt.% NaCl, 5,000 ppm Ca^{2+} , pH 6, 80 °C for (a) 24 h, (b) 48 h and (c) 96 h exposure. Measurements relative to corroded surface.	148

6.15	Top view SEM image and cross section featuring corrosion products formed on X65 carbon steel in saturated CO ₂ , 2 wt.% NaCl, 5000 ppm Ca ²⁺ , 80 °C, pH 6 over a duration of (a) 24 h (b) 48 h and (c) 96 h	149
6.16	Plot depicting comparison of XRD ^o 2Theta position of FeCO ₃ and CaCO ₃ from literature to that of detected peaks for X65 carbon steel corroded in 2 wt% NaCl, 5,000 ppm Ca ²⁺ , 80 °C for 96 h at pH 6 . .	149
6.17	Top-view SEM of film formed on pits in X65 carbon steel corroded in 5,000 ppm Ca ²⁺ at 80 °C for 96 h in (a) 2 % NaCl, (b) 3.5 % NaCl, .	150
6.18	Top-view SEM of film formed on pits in X65 carbon steel corroded in 2 % NaCl, 5000 ppm Ca ²⁺ at 80 °C for 24 h in (a) pH 3.8 (b) pH 6. .	150
6.19	Cross-section view of film formed in 2 wt% NaCl, 5000 ppm Ca ²⁺ , 80°C for 96 h at (a) pH 3.8 and (b) pH6.	152
6.20	Top-view SEM depicting amorphous film transformation to aragonite in 2 wt% NaCl, 5000 ppm Ca ²⁺ , pH3.8, 80 °C under (a) X1.0 K and (b) X2.0 K magnification.	152
6.21	Top-view SEM depicting products formed under 2 wt% NaCl, 5000 ppm Ca ²⁺ , 80 °C for 96 h at (a) pH 3.8 and (b) pH6.	152
6.22	EDX showing composition of products formed at (a) pit mouth and (b) inside pit under pH6 in 2 wt% NaCl, 5000 ppm Ca ²⁺ , 80°C for 96 h	153
6.23	Bar chart depicting trend in relative and absolute pitting from initial 70µm depth in saturated CO ₂ , 2 wt% NaCl, 80°C over a duration of 4 days at pH 3.8	155
6.24	Plot showing trend in pitting factor <i>P_f</i> , derived for experiments conducted under (a) non-protective scale condition (b) Protective scale condition	156

7.1	Tafel plots showing i_{corr} , β_a and β_c derivatives for experiment conducted in saturated CO ₂ , 2 wt.% NaCl, 50 °C containing 682 ppm Ca ²⁺ , pH 7.5	162
7.2	Top-view SEM image of mixed Ca _x Fe _(1-x) CO ₃ formed on X65 carbon steel corroded for 96 h at pH 7.5, saturated CO ₂ in (a) 3.5 wt% NaCl, 0 ppm Ca ²⁺ (b) 3.3 wt% NaCl, 682 ppm Ca ²⁺ and (c) 3.1 wt% NaCl, 1364 ppm Ca ²⁺	162
7.3	Corrosion rate plot for X65 carbon steel corroded for 96 h at pH 7.5, saturated CO ₂ in (a) 3.5 wt% NaCl, 0 ppm Ca ²⁺ (b) 3.3 wt% NaCl, 682 ppm Ca ²⁺ , (c) 3.1 wt% NaCl, 1364 ppm Ca ²⁺	163
7.4	(a) Test 1 and (b) Test 2 result for LPR/OCP plot of X65 carbon steel corroded in 21,000 ppm Cl, at 50 °C, pH 7.5 for 96 h in 0 ppm Ca ²⁺	165
7.5	(a) Test 1 and (b) Test 2 result for LPR/OCP plot of X65 carbon steel corroded in 21,000 ppm Cl, at 50 °C, pH 7.5 for 96 h in 682 ppm Ca ²⁺	166
7.6	Top view SEM showing mixed FeCO ₃ and CaCO ₃ formed on X65 carbon steel corroded in 3.3 wt% NaCl, 682 ppm Ca ²⁺ , 50 °C for 96 h at pH 7.5 under (a) X1000 (b) X2000 (c) X5000 magnification and (d) calcite cluster zoom	167
7.7	EDX showing percentage composition of elements detected on X65 carbon steel corroded in 2 wt% NaCl, 682 ppm Ca ²⁺ , 50 °C for 96 h at pH 7.5	168
7.8	Plot depicting comparison of XRD °2Theta position of CaCO ₃ and FeCO ₃ from literature to that of detected peaks for X65 carbon steel corroded in 3.3 wt% NaCl, 682 ppm Ca ²⁺ , 50 °C for 96 h at pH 7.5	168
7.9	Schematic representation of a typical hexagonal lattice structure	170
7.10	Plot of parameter "c" versus molar fraction of Ca ²⁺	170

7.11	Plot of unit volume "v" versus molar fraction of Ca ²⁺	171
7.12	Repeated galvanic trend for freshly polished (a) 1mm anode (Test1) and (b) 1mm anode (Test-2) in 0.625mm pit for 24 h in 3.3 wt% NaCl, 682 ppm Ca ²⁺ at 50 °C, pH 7.5, saturated CO ₂	172
7.13	Repeated galvanic trend for freshly polished (a) 2mm anode (Test1) and (b) 2mm anode (Test-2) in 0.625mm pit for 24 h in 3.3 wt% NaCl, 682 ppm Ca ²⁺ at 50 °C, pH 7.5, saturated CO ₂	173
7.14	Repeated galvanic trend for freshly polished (a) 3mm anode (Test1) and (b) 3mm anode (Test-2) in 0.625mm pit for 24 h in 3.3 wt% NaCl, 682 ppm Ca ²⁺ at 50 °C, pH 7.5, saturated CO ₂	173
7.15	Galvanic trend for freshly polished (1) 1mm anode, (b) 2mm anode and (c) 3mm anode in passivated 4.9 cm ² cathode, 0.625mm pit for 24 h in 3.5 wt% NaCl, 0 ppm Ca ²⁺ at 50 °C, pH 7.5, saturated CO ₂	174
7.16	Morphology of maximum pit depth recorded on (a) 1 mm anode, (b) 2 mm anode and (c) 3 mm anode in artificial pit under saturated CO ₂ , 3.3 wt.% NaCl, 682 ppm Ca ²⁺ , pH 7.5, 50°C for 24 h.	175
7.17	Profilometry of 1mm anode (a) freshly polished before coupling into artificial pit assembly (b) after corrosion in an artificial pit	176
7.18	Chart depicting general corrosion rate (CR) for passivated cathode and freshly polished 1 mm anode electrode in coupled and uncoupled pit at experiment start, 12 h into test and towards test finishing under saturated CO ₂ , 3.3 wt.% NaCl, 682 ppm Ca ²⁺ , pH 7.5, 50 °C.	177
7.19	SEM results featuring (a) x1000 magnification (b) x5000 magnification and (c) atomic composition of mixed CaCO ₃ and FeCO ₃ formed on anode pin in 3.3 wt% NaCl, 682 ppm Ca ²⁺ , pH 7.5, 50 °C for 24 h	177

7.20	SEM results featuring (a) X1000 magnification (b) X5000 magnification and (c) atomic composition of FeCO ₃ formed on anode pin in 3.5 wt% NaCl, 0 ppm Ca ²⁺ , pH 7.5, 50 °C for 24 h	178
7.21	Bar chart depicting pitting trend (top-10 average) of pits formed on coupled anodes in saturated CO ₂ , 80°C over a duration of 1 h in (a) 682 ppm Ca ²⁺ , 3.3 wt% NaCl and (b) 0 ppm Ca ²⁺ , 3.5 wt% NaCl . .	178
7.22	Plot depicting charge recorded for 1mm, 2mm and 3mm anode diameter in artificial pit coupling in saturated CO ₂ , 3.3 wt.% NaCl, pH 7.5, 50 °C in 682ppm Ca ²⁺ and Ca ²⁺ -free solutions.	180
8.1	Pit depth profile of samples subjected to 150mV potentiostatic test at pH 3.8 and pH 6.6 for test conducted at 30°C, 3.5wt% NaCl, CO ₂ condition for 24Hrs.	185
8.2	Polarisation curve of X65 carbon steel under film-free condition (pH 4, 30°C, 3.5wt% NaCl, -15mV to 1,000mV, scan rate 0.25mV/s, 250RPM. 185	
8.3	Polarisation curve of X65 carbon steel under protective film conditions (pH6.6, 80°C, 3.5%NaCl, -15mV to 1,000mV, scan rate 0.25mV/s, 250RPM).	186
8.4	Plot showing (a) relative pit depth and (b) absolute pit depth recorded on X65 carbon steel corroded for 96 h	188
8.5	Plot showing maximum pit depth and top-10 average of pits from initial 70µm depth in solution containing 5,000ppm Ca ²⁺ , 2 wt% NaCl at 80 °C for 96 h	189
8.6	Cross section showing Ca ²⁺ inside a pit on X65 carbon steel corroded at 2 wt% NaCl, 5,000 ppm Ca ²⁺ , 80 °C for 96 h at pH 3.8	190
8.7	EDX mapping showing Ca ²⁺ inside a pit on X65 carbon steel corroded at 2 wt% NaCl, 5,000 ppm Ca ²⁺ , 80 °C for 96 h at pH 3.8	190
8.8	EDX line scan showing Ca ²⁺ inside a pit on X65 carbon steel corroded at 2 wt% NaCl, 5,000 ppm Ca ²⁺ , 80 °C for 96 h at pH 3.8	191

8.9	Top-view SEM of film formed on pits in X65 carbon steel corroded in 5,000 ppm Ca^{2+} at 80 °C for 96 h in (a) 2 % NaCl, (b) 3.5 % NaCl, .	192
8.10	Top-view SEM of film formed on pits in X65 carbon steel corroded in 2 % NaCl, 5,000 ppm Ca^{2+} at 80 °C for 24 h in (a) pH 3.8 (b) pH 6.	193
8.11	Artificial Pit in Flush Position	195
8.12	Schematic representation of the electrochemistry in an artificial Pit .	195
8.13	Bar chart depicting trend in relative and absolute pitting from initial 70 μm depth in saturated CO_2 , 2 wt% NaCl, 80°C over a duration of 4 days at pH 3.8	197
8.14	Galvanic trend for freshly polished (1) 1mm anode, (b) 2mm anode and (c) 3mm anode in passivated 4.9 cm^2 cathode, 0.625mm pit for 24 h in 3.5 wt% NaCl, 0 ppm Ca^{2+} at 50 °C, pH 7.5, saturated CO_2	200
8.15	Charge recorded for 1mm, 2mm and 3mm anode diameter in artificial pit coupling in saturated CO_2 , 3.3 wt.% NaCl, pH 7.5, 50 °C in 682ppm Ca^{2+} and Ca^{2+} -free solutions.	201
8.16	Micrograph of X65 carbon steel.	202
A.1	Interface showing data collection process	242
B.1	NPFlex images of corrosion pits formed on X65 carbon steel under (a) 50mV, (b) 100mV and (c) 150mV potentiostatics in 3.5% NaCl solution, unbuffered, 30°C, P_{CO_2} of 1bar for 24 Hrs.	259
C.1	Tafel plots featuring β_a , β_c and I_{corr} derivatives from anodic and cathodic linear extrapolations at OCP for experiments conducted in saturated CO_2 , 2 wt.% NaCl, 80 °C containing (a) 0ppm Ca^{2+} , pH3.8 (b) 0ppm Ca^{2+} , pH6 (c) 5,000ppm Ca^{2+} , pH 3.8 (d) 5,000ppm Ca^{2+} , pH 6	260

Chapter 1

Introduction

1.1 Overview

Most metals exist as stable ores but are often refined to obtain useful products by the application of energy. Corrosion is simply the natural reversal of metals from their refined state to a more stable (or natural) state. Corrosion will always tend to occur as metals are more stable in their ore states than in their refined states. Corrosion causes loss in thickness which can lead to structural failure and disruption in the supply of essential services. Deterioration due to corrosion reduces commodity value and poses a threat to the environment. Corrosion products can contaminate fluids in pipes, clog supply lines or even generate current that can trigger unforeseen processes. Corrosion poses significant challenge not only to the engineering industry but to the world at large. Corrosion accounts for losses equivalent to 3.4% of the entire world GDP annually, equivalence of 2.5 trillion US dollars annually as depicted in Figure 1.1 [1]. Corrosion cost continues to increase annually. For the United States, it was \$ 1.1 trillion in the Year 2016 (6.2% of the US GDP) [2, 3]. The cost of corrosion in the UK amounts to £46 billion annually, which could cater for 763,600 social homes annually in the UK [4]. Corrosion progresses in an array of metals such as low carbon steel and other alloys.

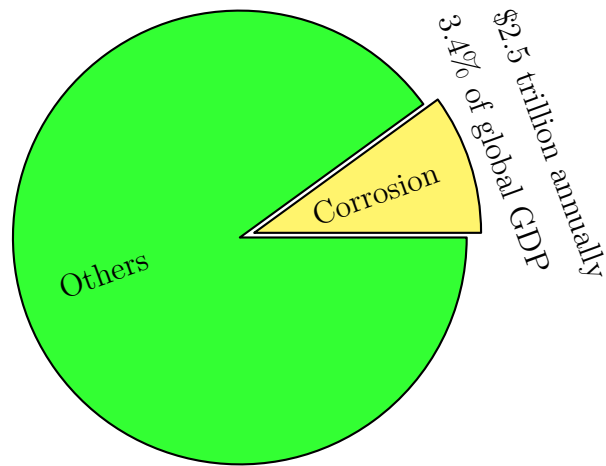


Figure 1.1: Pie chart displaying Global GDP cost of corrosion [1]

Carbon steel is a major component of engineering structures and are employed in the construction of pipelines, vessels and other refinery components [5, 6, 7]. Carbon steel is a preferred design option due to its availability, cost, strength, ease of fabrication as well as developed technology emanating from carbon steel research [8, 9]. The set-back in carbon steel application is in its corrosion performance [10, 11, 12, 13, 14, 15] in both aerobic and anaerobic environments [16]. Corrosion in oil pipelines take a toll on operations, the economy as well as Health and Safety concerns, typical of the California pipeline spill of 19 May 2015 shown in Figure 1.2(a) and the underwater gas leakage of Nigeria-Agip oilfield which occurred in Bayelsa, Nigeria on 22 February 2016, featured in Figure 1.2(b).



(a) Santa Barbara spill, California (USA)



(b) Taylor Creek, Bayelsa Nigeria

Figure 1.2: (a) Cleaning-up operations at Refugio Beach off the Santa Barbara County Coast, California [17]

(b) Bubbles on Taylor Creek (Bayelsa-Nigeria) caused by leakage from underwater pipeline on 22 February 2016 [18].

Despite corrosion challenges, low carbon steels continue to gain acceptance in the oil and gas industry [9, 19, 20, 21, 22]. In some instances, carbon steel possesses the ability to form protective films in a solution of dissolved carbon dioxide [23] while chemical inhibitors are sometimes applied to pipe flow constituents in non-film forming conditions [24, 25]. Iron carbonate (FeCO_3) is the main corrosion product formed on carbon steel in oil and gas conditions. The ability of carbon steels to form a protective layer of FeCO_3 makes it suitable for oil and gas applications [26]. Protective film breakdown causes localised corrosion which poses a significant threat to carbon steel structures [27]. Heterogeneity of metallic structures such as corrosion resistant alloys also accounts for localised attack such as pitting [28]. Figure 1.3 depicts images of pitting corrosion reported on some metallic structures.



Figure 1.3: Images of Pitting Attack on Steel [29]

Corrosion remains a common problem in the oil and gas industry as a result of intricate operating conditions like multiphase flow, high temperature, high pressure, ion concentrations and pH values [30]. Localised corrosion of carbon steel persists in most environments including regions of sand deposits in flow pipes [31]. Pitting corrosion may also manifest in regions of higher corrosion magnitudes in a metal surface undergoing general (uniform) corrosion [32]. Pitting occurs in an anaerobic environment (marine immersions) due to biological influence like activities of sulphate reducing bacteria (SRB) [33, 34] in which SRB utilise sulphate to consume electrons released during anodic dissolution [35]. Other factors such as alternating current interference could promote pitting corrosion in petroleum pipelines by inducing anodic polarisation and degrading protective films [36]. Corrosion takes

a toll on project capital expenditure, operational expenditure, health, safety and the environment [37]. Cost of mitigating pitting corrosion feasibly ranks highest among other corrosion-related expenditure [38]. The implication of corrosion and its mitigation is estimated to range from 2% and 4% GNP on a global scale [39]. Petroleum production accounts for 1% while refining plants represent 2.7% of the total estimated cost [39]. Bruker [40] reported that corrosion degradation accounts for losses of about \$8 billion annually in refinery and oil transport business. Corrosion-related failures therefore cost a significant amount of money annually with pitting corrosion ranking among the highest level of corrosion defects [41, 42, 43]. Lots of resources therefore go into efforts to control corrosion. Table 1.1 features a breakdown of funds associated with corrosion control.

Table 1.1: Cost associated with Corrosion Prevention [40]

Material and Services	Range	Average Cost	
	(\$ x billion)	(\$ x billion)	(%)
Organic Coatings	40.2-174.2	107.2	88.3
Metallic Coatings	1.4	1.4	1.2
Metals & Alloys	7.7	7.7	6.3
Corrosion Inhibitors	1.1	1.1	0.9
Polymers	1.8	1.8	1.5
Anodic & Cathodic Protection	0.73-1.22	0.98	0.8
Services	1.2	1.2	1.0
Research & Development	0.02	0.02	<0.1
Education & Training	0.01	0.01	<0.1
Total	\$54.16-\$188.65	\$121.41	100%

Corrosion sometimes remains unnoticed under physical inspection until catastrophic failure occurs [41]. Pitting corrosion could initiate and propagate unnoticed in the internal wall of steel pipes only to be revealed as a hole piercing through the pipe wall with its attendant consequence [44]. For instance, from 1970 to 2006, 68% of corrosion related problems in the European Union cross country pipelines were pitting related [6]. Pitting corrosion accounted for 79% of onshore transmission problems recorded by the United States pipeline safety unit from 2002 to 2008 [6]. From 1994 to 2004 in Mexico, pitting corrosion was responsible for 99% of external corrosion incidents [6]. The great danger of localised corrosion and how

to effectively contain it therefore becomes a great concern to corrosion engineers [14, 45, 46, 47, 48, 49].

1.2 Statement of research problem

Carbon dioxide exists naturally in the dissolved state as carbonic acid at pressures similar to that observed in petroleum reservoirs which generally comprise of carbon steel constituents [8]. Steels are normally confronted with CO₂ - related corrosion particularly in oil and gas flows with high CO₂ and H₂O level [20, 23, 27, 40, 49, 50, 51, 52, 53, 54]. Most pipeline failures in the oil industry are not due to general corrosion but localised corrosion [44, 52, 55, 56]. Oil and gas pipelines are mostly threatened by localised CO₂ attack on the inner wall of the pipes [26, 41, 57]. Localised corrosion is hard to predict [22, 49, 58] and remains the most dangerous form of CO₂ corrosion [49, 58, 59]. Most literature on localised corrosion focussed on passive steels which possess alloying elements and also have the ability to self-repair; much less is known about the origin and rates of low carbon steel pitting particularly in a CO₂ environment [19]. Some studies have been conducted on carbon steel corrosion in aqueous CO₂ environments probably due to its extensive application in the oil and gas industry but obscurity still trails its interpretation [37, 53, 60, 61]. A holistic picture of CO₂ corrosion is yet to be presented despite extensive research being conducted on the subject [23, 24, 50, 62]. Moreover, most pitting work on low carbon steel considered the FeCO₃ film environment whereas corrosion products are sometimes in the form of mixed carbonates due to presence of cations such as calcium in a typical oil & gas environment. In the same vein, available literature on localised corrosion of carbon steel in CO₂ environments is still debatable [51, 57, 63, 64]. The kinetics of pitting perforation in carbon steel is yet to be fully ascertained [22, 39]. Managing pitting corrosion in carbon steel is among the greatest challenges faced by corrosion engineers [5, 56, 65, 66]. The inability to accurately explain the chemistry vis-à-vis parameters governing localised corrosion

still exists [67]. This brings to the fore the need to investigate pitting corrosion of X65 carbon steel in sweet conditions.

1.3 Objective and scope of research

Pitting corrosion of carbon steel in a sweet environment progresses from pit initiation to pit propagation but a clear interpretation of these processes calls for further investigation [62]. This research was generally muted to improve understanding of localised corrosion in low carbon steel which is generally used in the oil and gas industry as well as other engineering applications. The scope of work was in 3 phases as depicted in Figure 1.4 with an overall aim of improving knowledge on X65 carbon steel pitting in sweet conditions.

This research work was specifically aimed at addressing the following gaps:

- **Need to generate stochastic pit profiles for laboratory studies:**

As considerably long periods of time are required to generate pits on steel naturally, this work presents a methodology for generating stress-free stochastic pits in a practical time-frame. This was achieved by subjecting X65 carbon steel to potentiostatic polarisation in order to induce stochastic pits of which top-10 average pit depth can be reliably reproduced.

- **Need to understand how mixed carbonates ($\text{Ca}_x\text{Fe}_{(1-x)}\text{CO}_3$)**

influence pitting in low carbon steel: This work assessed how pitting progresses under mixed carbonate film conditions and how some CaCO_3 polymorphs influence pitting. Growth of stochastic pits induced by potentiostatic polarisation was investigated in calcium-rich solutions. Result was compared with pitting under FeCO_3 film condition.

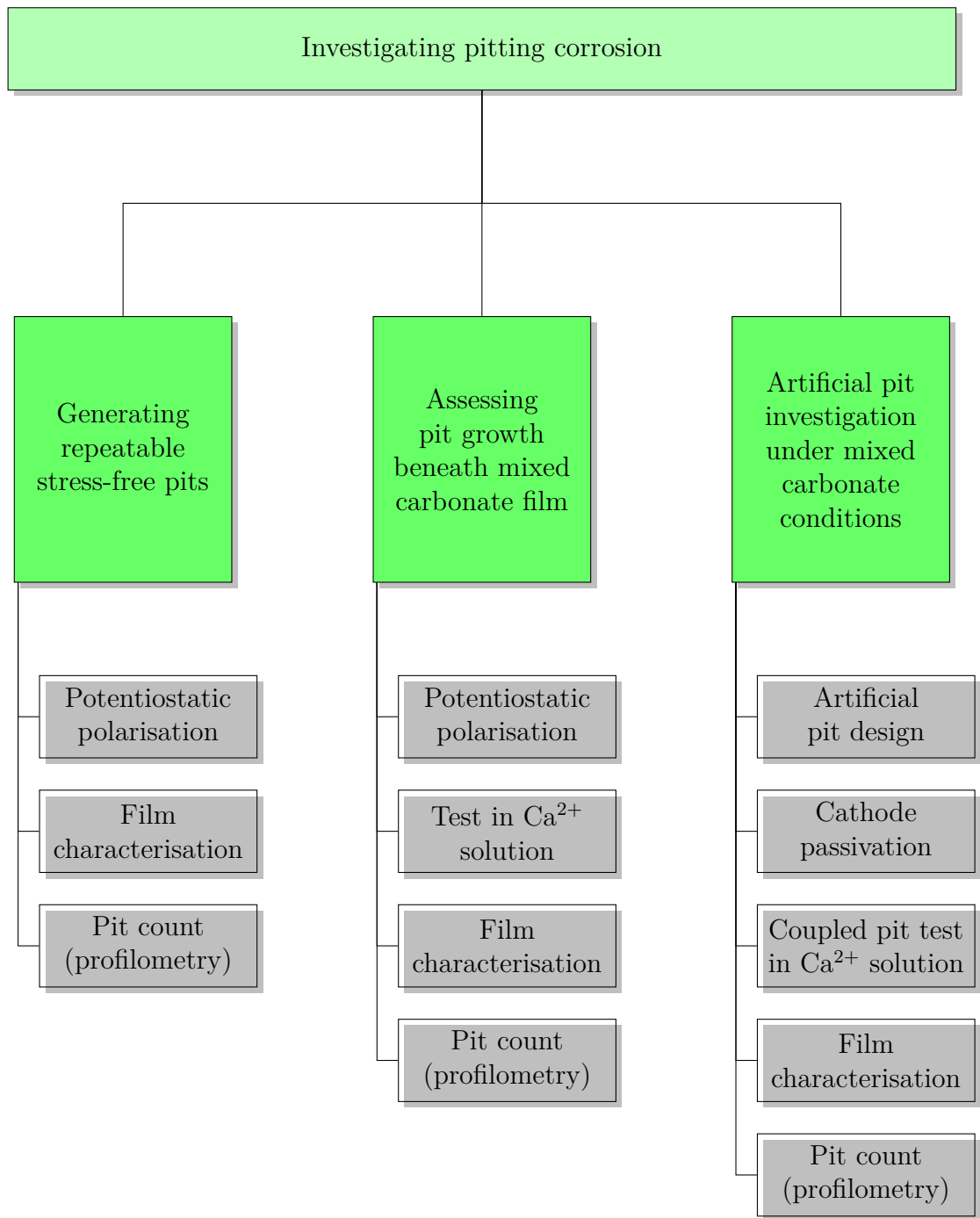


Figure 1.4: Summary of Work Scope

- **Need to understand the event(s) that occur in an actively corroding pit and how calcium influences galvanic currents in pitting:** An artificial pit was designed to reveal event(s) that occur on the film free anode beside the general corrosion reported in literature. A relationship between calcium, galvanic current and pitting tend was also revealed.

1.4 Thesis outline

This thesis covers pitting corrosion of API-X65 carbon steel in a carbon-dioxide environment with the aim of addressing observed gaps in the concept of localised corrosion in low carbon steel. This thesis is presented in 9 chapters covering the aspects highlighted below:

- **Chapter-1:** Provides the research rationale and work scope.
- **Chapter-2:** Presents the fundamentals of corrosion science.
- **Chapter-3:** A review of relevant literature is presented.
- **Chapter-4:** Materials and experimental procedures employed in this work are presented.
- **Chapter-5:** Novel techniques for generating stress-free repeatable pits on API-X65 carbon steel are presented and the results are shown.
- **Chapter-6:** The effect of calcium on growth of stochastic pits generated by methods featured in Chapter 5 of this thesis is presented. Initial test was conducted in calcium-free solution and later compared with tests in calcium-rich solution. In addition, an investigation was conducted on how polymorphs of calcium carbonate (calcite, aragonite and vaterite) influence general and pitting corrosion.
- **Chapter-7:** Presentation of artificial pit designed and utilised to investigate events that occur in actively corroding pits under mixed carbonate ($\text{Ca}_x\text{Fe}_{(1-x)}\text{CO}_3$) film conditions. The influence of galvanic current on pitting was examined.

- **Chapter-8:** Detailed discussion on experimental results obtained from Chapter-5 to Chapter-7.

- **Chapter-9:** Conclusions, industrial relevance and recommendations for future work.

Chapter 2

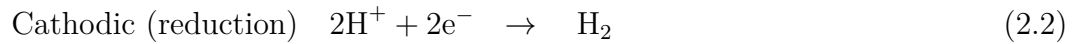
Corrosion Fundamentals

2.1 Introduction

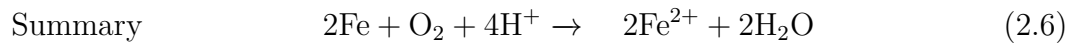
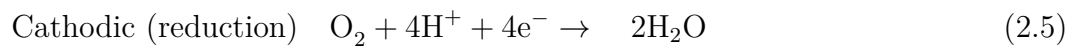
Corrosion can be defined as metallic degradation caused by electrochemical reactions of metal with the environment [41]. Corrosion can be classified as wet or dry corrosion based on the environment. Dry corrosion often occurs at relatively high temperature without liquid presence while wet corrosion is more common type that occurs in aqueous environment. Carbon dioxide and Hydrogen Sulphide presence in petroleum crude cause significant damage to oil production and transport lines [68]. Solution chemistry environment is classified as **sweet** system in CO₂ corrosion and **sour** system if H₂S gas is involved. Exposed metals often form protective films depending on the environment and such films could become defective under certain circumstances. Pitting corrosion is an accelerated form of localised attack in which compromised protective films promote galvanic effect that drives pits at discrete spots on a metal.

2.2 Aqueous corrosion chemistry

When a metal is immersed in a corrosive electrolyte, dissolution (oxidation) occurs at the anode while reduction takes place at the cathode. The anodic (metal dissolution) site of a corroding metal liberates electrons which are eventually consumed by cathodic reaction. The corrosion process entails energy dissipation which obeys extant energy and mass laws. Corrosion is generally expressed as electrochemical current since electrons liberated by anodic dissolution are consumed by cathodic reaction. For mass balance in the electrochemical system, total current flowing from the anodic site must be equal and opposite (in sign) to the total current entering the cathodic site [69, 70]. Anodic and cathodic reactions of corroding iron in acid solutions are expressed in equations 5.1, 2.2 and 2.3.



In aerated environments (out of scope of this study) where dissolved oxygen is present, the reaction proceeds as shown in equations 2.4, 2.5 and 2.6.



2.2.1 Electrochemical cell chemistry

Corrosion is termed as an electrochemical process as it entails simultaneous oxidation and reduction in which electrons generated at anodic sites flow through the corroding

metal to cathodic sites and get consumed by cathodic reactions [71]. The potential difference between the anodic and cathodic sites is the driving force for corrosion reaction (metal dissolution), current therefore flows through the cell as shown in Figure 2.1. Electrons flow from anode to cathode through metallic path while electrolyte conveys positive current from anode to the cathode [72]. Solution chemistry contains ions or molecules known as electrochemical active species (EAS) which can include dissolved carbon dioxide, dissolved oxygen, inorganic acids such as HCl, organic acids and H₂S amongst others, depending on the environment.

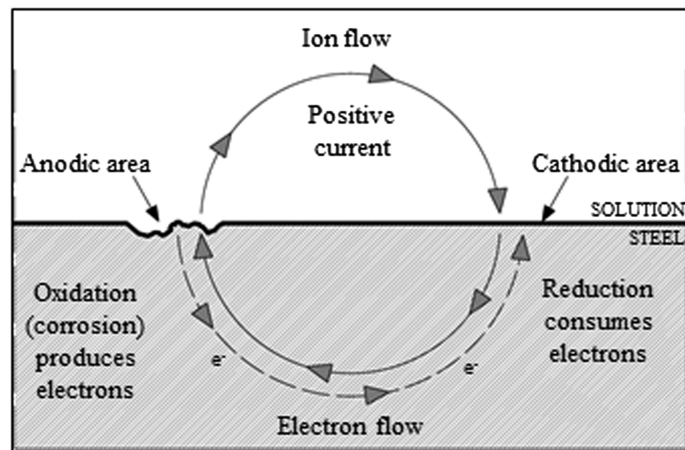


Figure 2.1: Schematic of Evan's Diagram for a metal corroding in an acid [71]

The EAS play a vital role in corrosion as they could influence the chemical reactions in several ways. For instance, charged Hydrogen could increase anodic dissolution of a corroding metal [73] by enhancing cathodic reactions.

2.2.2 Electrical double layer

As corrosion progresses in metal 'M' immersed in a corrosive electrolyte, the metal corrodes forming Mn^+ ions with the release of ne^- electrons as depicted in equation 2.7. The dissolved cations are hydrated and diffuse freely from the metal which becomes negatively charged due to excess electrons [74].



The negatively charged metal surface attracts the positively charged Mn^+ ions in solution thereby creating a potential difference as well as dynamic equilibrium between the bulk solution and the metal surface [75]. Substantial ratio of the cations line close to the metal surface but are unable to contact the excess electrons due to barrier of water layers. Contact with the surface electrons would lead to the cations being reduced to metal atoms. The electrolyte metal interphase therefore compose of bulk electrolyte, cations and water molecule [74]. This scenario results in the formation of a thin electric charged layer of about one nanometer thick at the metal electrolyte interphase [75]. The thin layer is known as Electrical Double Layer (EDL). Different EDL models have been revealed while Figure 2.2 is a simplified EDL model showing scenarios leading to charge build up.

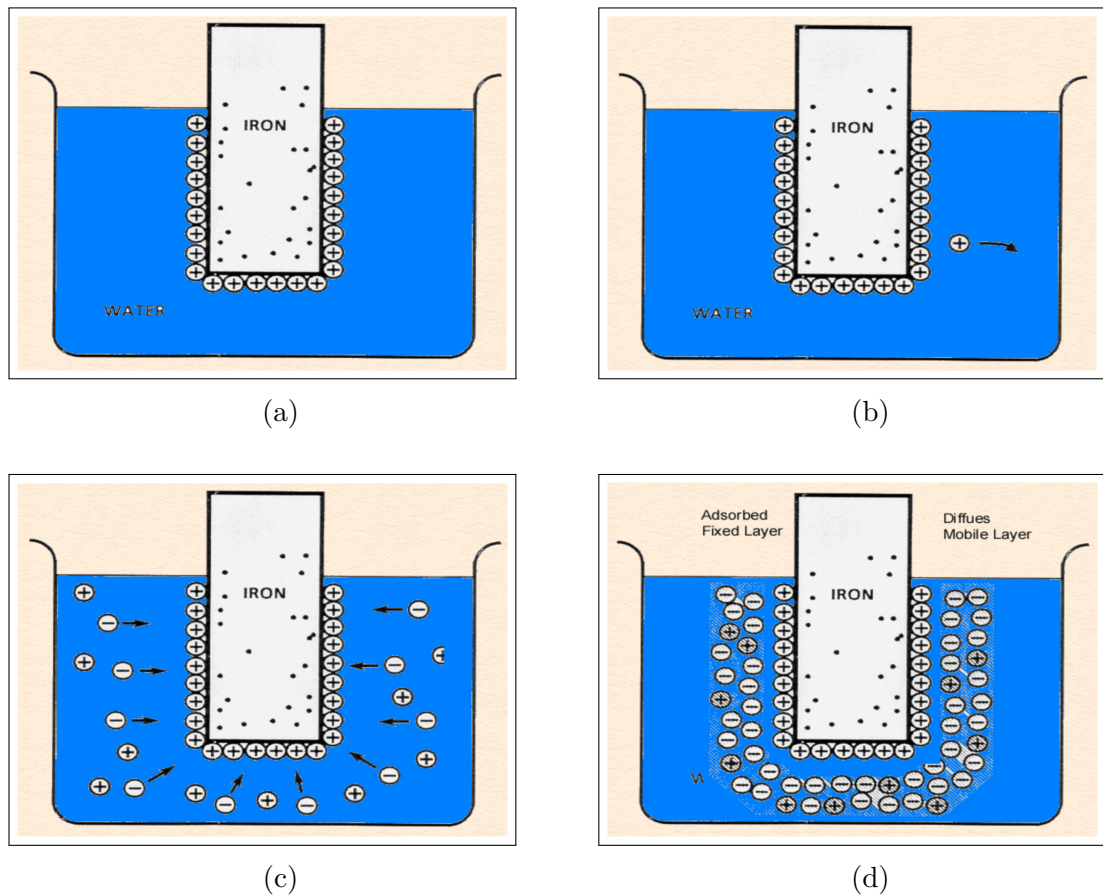


Figure 2.2: Typical Electrical Double Layer showing: (a) metal in corrosive electrolyte; (b) Fe^{2+} dissolution into solution; (c) charge build up following further dissolution; (d) Fully built EDL [76].

Considering the corrosion reaction described in equation 2.7 where electrons are

released following dissolution of Fe^{2+} ions. The Iron-water interphase is such that water layer separates aligned excess electrons from corresponding opposite charged cations. The attraction between the opposite charged ions (anions and cations) as well as repulsion of like charges forms an EDL at the metal-solution interphase. The charge interaction continues until dynamic equilibrium is reached. When EDL is at equilibrium, the rate of Fe^{2+} dissolution equals rate of Fe^{2+} precipitation (i.e. sum of forward reactions equal sum of backward reactions). A corroding metal is however not in equilibrium as cations continue to migrate from the EDL as the metal corrodes. This is due to presence of EAS such as the cathodic Hydrogen reduction described in equation 2.2. The EAS diffuse to steel surface and gets reduced by excess electrons in the EDL. This create imbalance in the EDL structure causing anodic dissolution to neutralise the effect [74]. Corrosion will therefore progress as long as EAS are available to consume the excess electrons released by anodic dissolution.

The EDL accounts for the potential difference recorded when metals are immersed in electrolytes [75]. The presence of such electrical potential vis-à-vis electron transfer concept in corrosion process led to the study of relationships between voltage, current and EDL composition [77]. Corrosion studies can be approached in two broad fronts; corrosion kinetics and corrosion thermodynamics. Corrosion thermodynamics is concerned with potentials, which is the driving force in electrochemical reactions while kinetics relates to current measurement which is linked to the rate of electrochemical reactions [71].

2.3 Corrosion kinetics

Faraday's laws of electrolysis are the fundamental theories employed in corrosion kinetics. Faraday's first law states that: 'the mass (m) of an element discharged during an electrolysis is directly proportional to the quantity of electricity (Q)

passing through it' i.e $m \propto Q \implies m = Z I t$. Where I = current (amperes), t = time (seconds), m = mass (grams), Z is the electrochemical equivalent (mass liberated by 1 ampere-second of current (coulomb)) [72, 78]. Faraday's second law of electrolysis states that when the same quantity of electricity is passed through different electrolytes, the relative number of moles of elements discharged are inversely proportional to the charges on the ions of the elements [78]. $m_1 \propto \frac{M_1}{n_1} \propto Z_1$ and $m_2 \propto \frac{M_2}{n_2} \propto Z_2$ Where m_1, m_2 = masses of products (grams), M_1, M_2 = respective molar masses (gmol^{-1}), n_1, n_2 = number of electrons, Z_1, Z_2 = Electrochemical equivalence [72, 78]. Electrochemical corrosion model assumes that rate of anodic and cathodic reactions are governed by kinetics of electron transfer which occurs at metal surface [79]. Tafel relationship featured in Equation 2.8 [79] represents kinetically controlled electrochemical process.

$$i = i_o \exp\left[\frac{2.303E - E^o}{\beta}\right] \quad (2.8)$$

Where i = current density generated from reaction, i_o = exchange current density, E = electrode potential, E^o = Equilibrium electrode potential for reaction and β = Tafel Constant (Volts/decade). The Tafel equation can be obtained for both anodic and cathodic reactions of a corroding metal to generate the Butler-Volmer equation stated in Equation 2.12 [79]. The Butler-Volmer equation is important in corrosion measurement due to the common practice of kinetically controlling electrochemical processes to measure corrosion response.

2.3.1 Open circuit potential, equilibrium potential and polarisation

When a metal is placed in a corrosive electrolyte, anodic (oxidation) and cathodic (reduction) reactions occur concurrently on the surface of the metal. The rate of anodic and cathodic reactions balances at an open circuit potential (OCP) [80]. The

OCP can be defined as an experimental potential recorded at zero external current flow and it changes when cell conditions are altered. OCP measurement is taken versus a reference electrode having high impedance voltmeter such that current flow is hindered between the test electrode and the reference. From thermodynamic concepts, the reaction of an electrode is reversible at point of equilibrium potential where net reaction sums to zero [75]. Equilibrium potential (E_{rev}) can therefore be defined as the potential measured at reversible oxidation state of same element at whatever condition (concentration, pressure, pH, or temperature) it occurs.

Equilibrium implies a state when reaction components are at par and there is no net formation of ions as the metal ions dissolution (anodic reaction) is balanced by metal deposition (cathodic reaction). It does not however imply that the system is in equilibrium with the standard Hydrogen electrode. It is worthy to note that exchange net current (I_{rev}) is zero at equilibrium but exchange net current density (i_o) needs not be zero as current density is a function of electrode surface area in contact with electrolyte [75].

Polarisation is the deviation from equilibrium potential because of current flow or net charge flow. Polarisation is quantified in the form of over-potential (η) = $E' - E_{\text{rev}}$ where E' and E_{rev} are final potential and equilibrium potential respectively. Positive overpotential (η_a) is termed **anodic polarisation** while negative overpotential (η_c) is known as **cathodic polarisation**. Figure 2.3 depicts schematics of polarisation diagram for RedOx in Fe. Polarisation is **activation controlled** when the metal supply rate at metal surface is greater than rate at which metal ion is getting deposited [81]. Polarisation is **diffusion (concentration) controlled** when metal deposition rate is greater than diffusion rate of metal ions through the bulk solution. Concentration polarisation is associated with availability of cations around the cathode. Polarisation tends to be mass transport (diffusion) controlled as ionic species around the cathode tends to zero [72]. Diffusion is not an issue during anodic polarisation due to; adequate metal ions available at the anode surface, negligible limiting current during oxidation (anodic process) and corrosion product formed at

the anode.

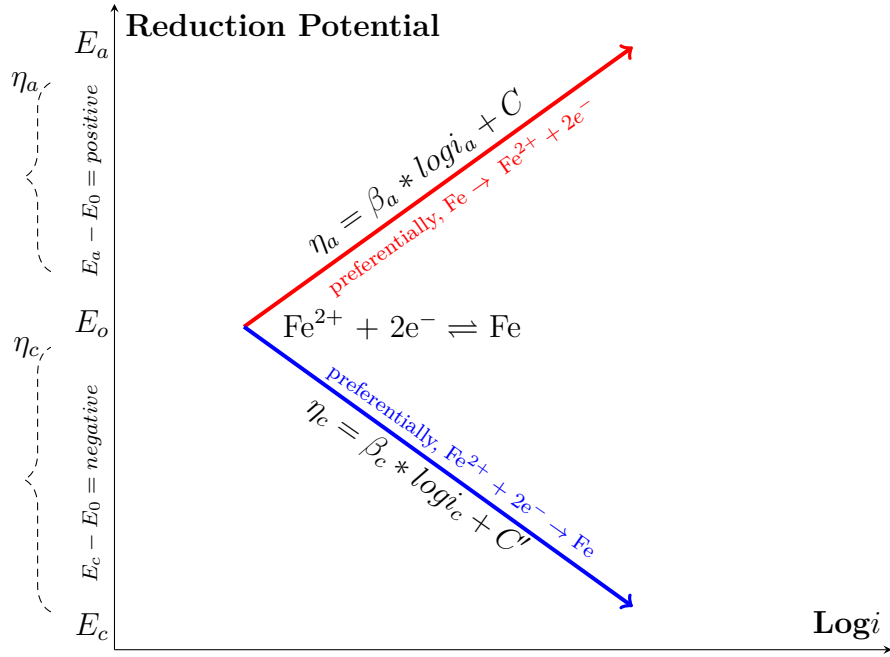


Figure 2.3: Polarisation Diagram for Redox in Fe

2.3.2 Evans' diagram

Corrosion kinetics can be described using polarisation curves obtained by plotting current/ potential relationship [75]. In this manner, potential is plotted against the logarithm of current as depicted in Figure 2.4.

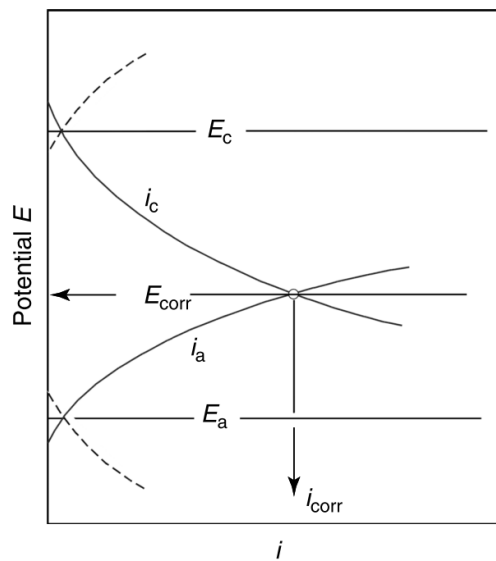


Figure 2.4: Potential vs current curve for steel corrosion [75]

Where i_a and i_c are respectively anodic and cathodic reaction currents, E_a and E_c are equilibrium potential of anodic and cathodic half reactions while E_{corr} and i_{corr} are the corrosion potential and corrosion current density respectively. Figure 2.4 shows that the corrosion state of a metal is determined by the intersection of the anodic and cathodic half reactions which implies that either of anodic and cathodic half reactions can control a corrosion process. Most metallic corrosion in acidic medium are controlled by Hydrogen ion reduction but oxygen preferentially controls corrosion of metals in neutral environment [75]. Hydrogen ion cathodic reduction of iron is represented in Figure 2.5 in which the polarisation curves are represented linearly for sake of clarity. Such simplified representation of the polarisation curve using absolute values of current is called the **Evan's diagram**.

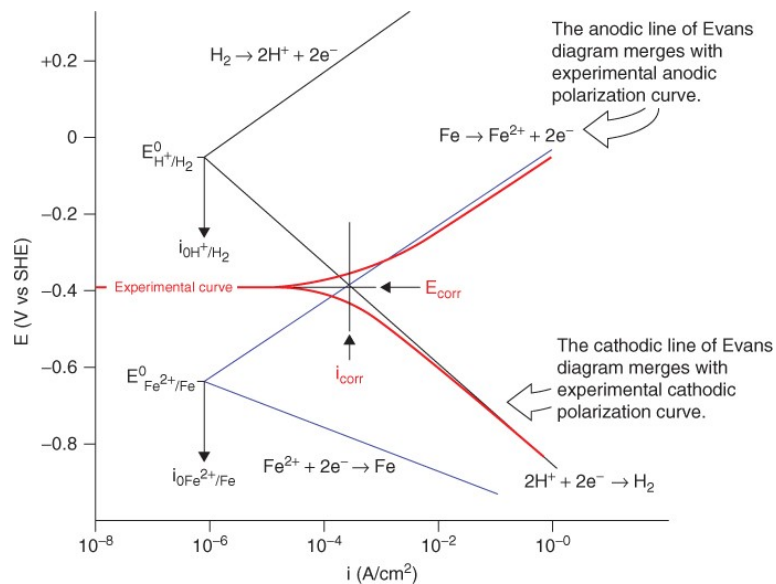


Figure 2.5: Evan's diagram of Iron corrosion in acidic medium [82]

Figure 2.5 shows that Hydrogen ion (H^+) diffuse towards the surface of the metal to get reduced since equilibrium potential of iron ($E_{Fe^{2+}/Fe}^0$) is more negative than equilibrium potential for Hydrogen (E_{H^+/H_2}^0).

2.3.3 Corrosion potential

When steel corrodes, the anode increases positively towards nobility while the cathode drops to more negative value as shown in Figure 2.6. Potential is related to corrosion rate in that anodic reactions generally increase with increase in applied potential while cathodic reactions increase with decrease in applied potential [80].

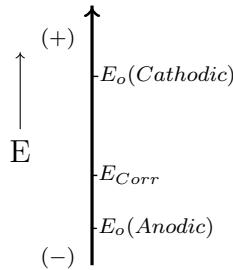


Figure 2.6: Illustration of Corrosion Potential due to Polarisation effect [71]

The anode and cathode potentials tends to polarise towards each other at point E_{corr} which lies between equilibrium potentials of the anodic and cathodic half reactions [71]. Cathodic curve of Evans diagram is the average of all cathodic reactions while Anodic curve is the average of all anodic processes since corrosion entails one or more anodic and cathodic reactions [72]. The anodic and cathodic polarisation curve intersects at the point E_{corr} called the mixed potential, free corrosion potential or simply, corrosion potential [72]. The E_{corr} value measured in a freely corroding metal is termed as open circuit potential (OCP) or mixed potential (being an average of anodic and cathodic reactions) [72].

2.4 Corrosion thermodynamics

2.4.1 Gibb's free energy, Vant Hoff's reaction isotherm and Nernst's equation

In an EDL system, there is the tendency of ions transfer within electrolyte as well as electron flow through metal electrolyte interface. The flow pattern depends on electrochemical energy termed as Gibb's free energy (per unit ion) or activation energy. Equilibrium state of EDL in terms of Gibb's free energy (ΔG°) and transfer charge magnitude ($-nFE_{\text{rev}}$) follows the first law of thermodynamics which states that;

At equilibrium, the Gibb's free energy or electrochemical free energy (ΔG°), which is the driving force for the transfer of electrons from the metal to the solution, is exactly balanced by the electrochemical potential difference ($-nFE_{\text{rev}}$) which is the driving force for attracting the ions back to the metal crystals [72, 83].

The reversible electrode potential is related to the free energy of anodic and cathodic reactions based on thermodynamics law for isothermal and isobaric system as shown in equation 2.9 [72, 83].

$$\Delta G = -nFE_{\text{rev}} \quad (2.9)$$

Where ΔG is the free energy change of the process and $-nFE_{\text{rev}}$ is the energy involved. E_{rev} is termed reversible potential indicating reversibility of the process, F is Faraday constant and n is the number of electrons involved in the reaction. Vant Hoff established a relationship between Gibb's free energy and concentration of electrochemical active species at constant temperature. The relationship termed

Vant Hoff's reaction isotherm is expressed in equation 2.10 [70, 84].

$$\Delta G = \Delta G^\circ + RT \ln k_a \quad \text{or} \quad \Delta G = \Delta G^\circ + RT \ln k_c \quad (2.10)$$

Where ΔG° = Free energy change at standard conditions, R = Ideal Gas constant, T represents Temperature in Kelvin, K_a = Constant (If expressed in terms of equation reaction activities), K_c = Constant (If expressed in terms of concentration molarity) = f_c (while $f=1$ for an ideal solution). Substituting equation 2.9 into equation 2.10 (expressing in terms of potential) as shown in equation 2.11 [85] gives the Nernst equation, applied in the study of electrochemical reactions.

$$E_{\text{rev}} = E_{\text{rev}}^\circ - \frac{RT}{nF} \ln K \quad (2.11)$$

Where E_{rev}° = reversible potential at standard conditions (at reference temp, pressure and unit concentration), E_{rev} = reversible potential, R = Ideal gas constant = 1.986 calories/moleK⁻¹, T = temperature (K), n = number of electrons in the anodic half reaction, $\frac{RT}{F}$ = 25.6mV equivalents at 298K (25°C). The relationship between Gibb's free energy, cell potential and equilibrium constant is summarised in Figure 2.7.

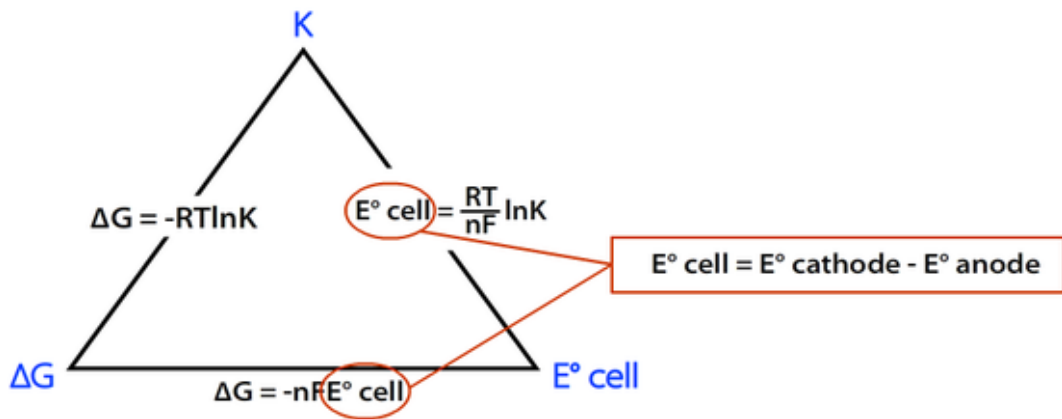


Figure 2.7: Relationship between Gibb's Free Energy, Cell Potential and Equilibrium Constant [86]

Where R = 8.314 JK⁻¹mol⁻¹, T = Temp in K, n = moles of e⁻ from balanced redox reaction, F = Faraday's constant = 96,485Cmol⁻¹ Thermodynamic conditions for corrosion reaction are presented in Table 2.1 and Figure 2.8. The Inner Helmholtz

Plane (IHP) and Outer Helmholtz Plane (OHP) are part of the EDL structure. OHP is the EDL layer where solvent particles surround ions. Adsorbed ions are however dominant at the IHP. Anodic over-potential η_a promotes metallic dissolution while cathodic over-potential η_c favours deposition of metal.

Table 2.1: Conditions for corrosion reaction [87]

ΔG°	E_{cell}°	K	Direction of Reaction
<0	>0	>1	Spontaneous in forward direction
>0	<0	<1	Spontaneous in reverse direction
0	0	1	No net reaction, system at equilibrium

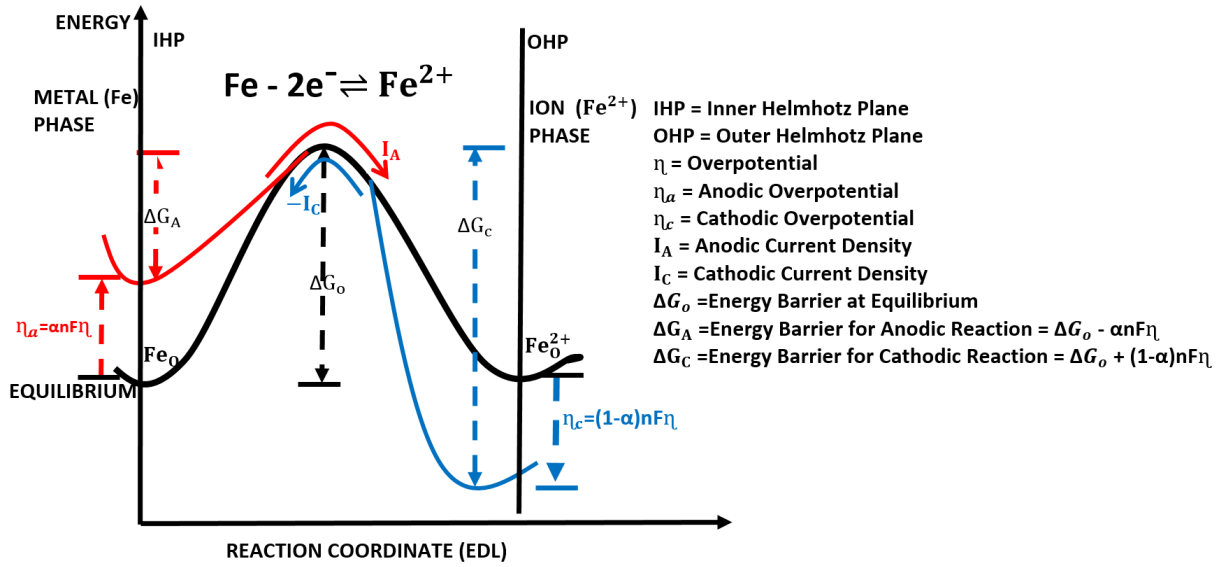


Figure 2.8: Modified energy diagram (reaction barrier) for corrosion reactions in Fe [88]

2.4.2 Pourbaix diagram for Fe-H₂O and Fe-CO₂-H₂O systems

The Pourbaix (Potential-pH) diagram, otherwise termed as stability diagram employs theory of thermodynamics to predict stable corrosion product (metal stability) as potential and pH function. It is similar to equilibrium diagram where various phases stability can be determined as a function of temperature and metal composition. The Pourbaix diagram entails plotting of redox potentials against pH axis. Potential-pH diagrams are products of solubility data and calculations

obtained from Nernst equations [72, 85]. Figure 2.9 shows a typical pH diagram for Fe-H₂O system. Metallic iron could corrode in regions where hydrated Fe²⁺, Fe³⁺ and FeOH⁻ remain stable. Immunity (no corrosion) occurs in region of metallic iron stability which corresponds to higher negative potentials. No corrosion is expected at stable regions of metallic oxides where iron surface is covered with oxide films. Atmospheric oxygen could corrode iron at potential ranges lower than oxygen equilibrium potential while Hydrogen ion presence in aqueous phase could cause corrosion at potential ranges lower than Hydrogen equilibrium potential [75].

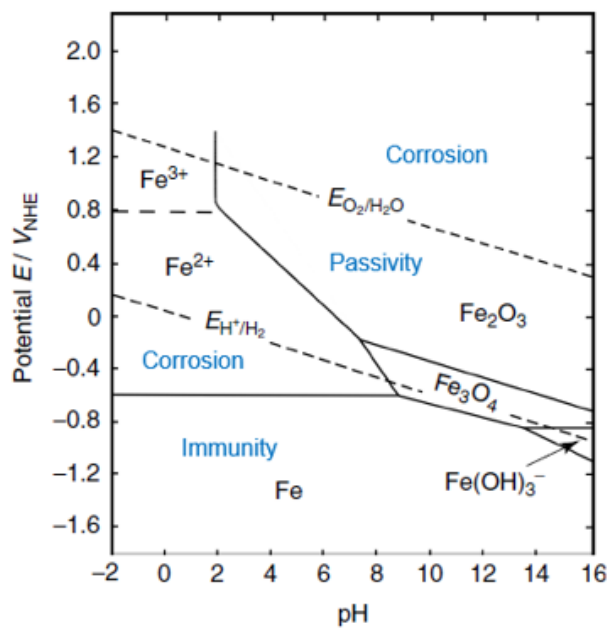
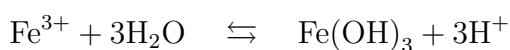
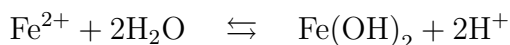


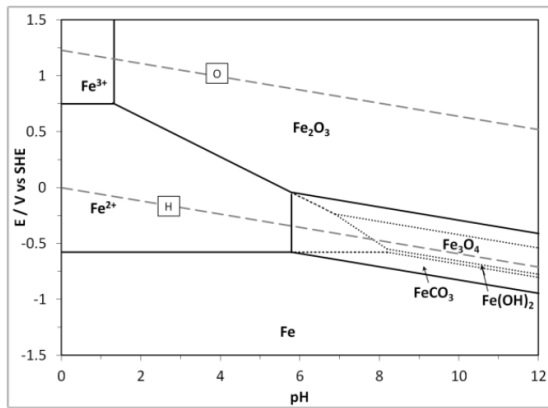
Figure 2.9: Potential-pH diagram for Fe-H₂O System [75]

Reactions involving electron transfer only (eg Fe and Fe²⁺) are potential dependent. These are represented in horizontal lines. Reactions that do not involve electron transfer (potential independent) but pH dependent are represented with vertical lines. Examples of such reactions include;

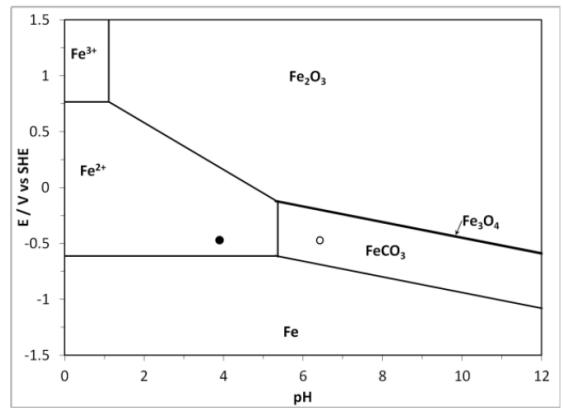


Reactions such as $Fe_2O_3 + 6H^+ + 2e^- \rightleftharpoons 2Fe^{2+} + 3H_2O$ entails pH change and electron transfer and are thus represented as inclined lines. The dotted lines represent Oxygen and Hydrogen lines. The Pourbaix diagram separates the

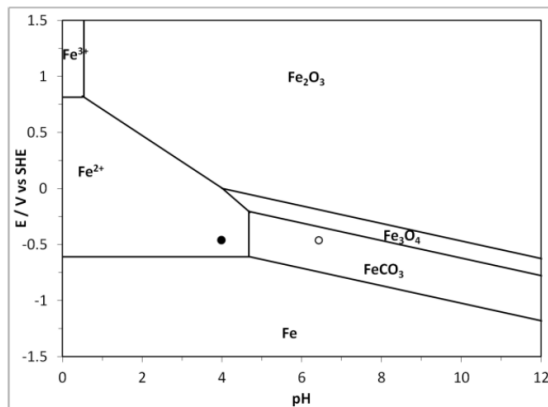
plots into **immunity**, **corrosion** and **passivation** regions which can be used to predict metal corrosion tendency [85]. Tanupabrungsun et al. [70] developed a more revealing Pourbaix diagram of Fe-CO₂-H₂O system that took cognisance of dissolved CO₂ in solution chemistry for formed mild steel at temperatures ranging through 25°C, 80°C, 120°C, 150°C, 200°C and 250°C. Tanupabrungsun et al. [70] constructed Pourbaix diagram of Fe-CO₂-H₂O in Figure 2.10 using Nernst equation for electrochemical reaction.



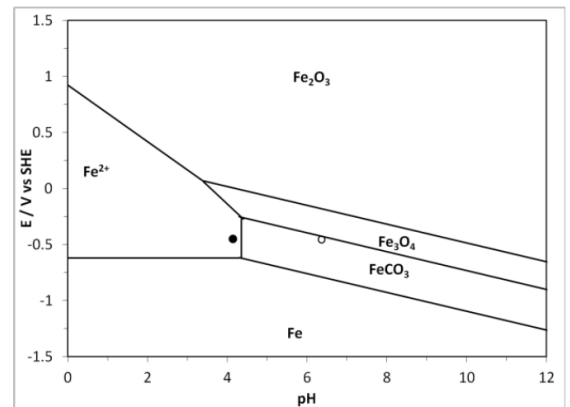
a. 25°C



b. 80°C



c. 120 °C



d. 150 °C

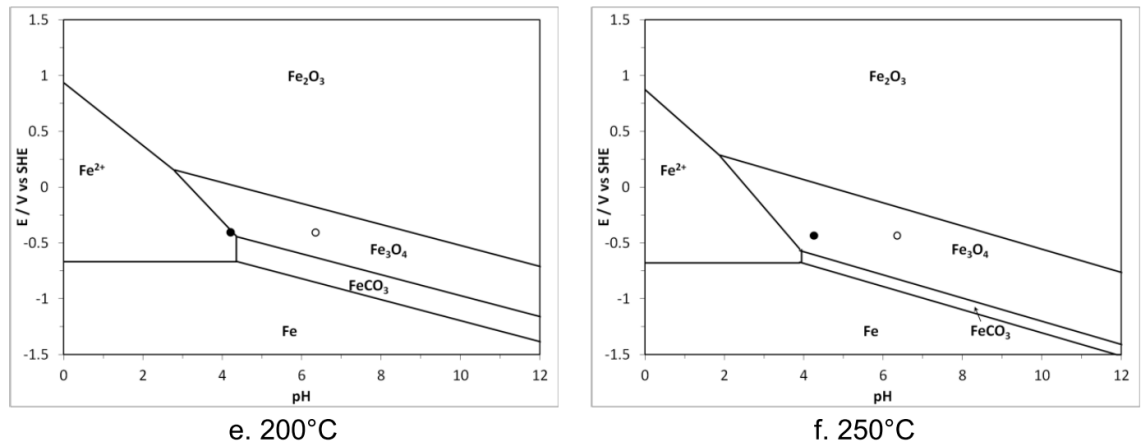


Figure 2.10: Generated Potential-pH diagrams at: (a) 25 °C (b) 80 °C (c) 120 °C (d) 150 °C (e) 200 °C and (a) 250 °C (Key: \circ - surface pH, \bullet - bulk pH) [70]

2.5 Electrochemical corrosion testing

Electrochemical testing is a useful tool in corrosion management that involves the use of array of equipment and methods to interpret corrosion test results. Electrochemical tests are designed to control parameters such as potential, current and voltage which govern corrosion processes. One or more of these parameters is often controlled to measure the other. The key corrosion parameters are potential and current as the former gives the driving force for corrosion occurrence while the later provide information on corrosion progress. Corrosion thermodynamic concepts are based on potential terms, which drive electrochemical reactions while corrosion kinetics concerns the rate of electrochemical reactions which is a function of current [81].

2.5.1 Galvanic coupling measurement

When dissimilar metals are coupled, a common corrosion potential is reached at a point between the corrosion potential of the individual metals. Galvanic coupling can also build on a metal when protective film on such metal is partially damaged.

The small exposed metal surface has more negative potential and hence anodic while the large protected surface becomes the cathode as featured in Figure 2.11.

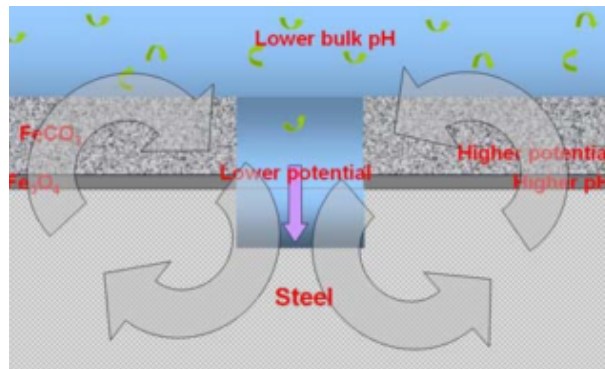


Figure 2.11: Galvanic Model in Compromised Film [63]

The galvanic effect produces measurable current which can be determined with the use of a zero resistance ammeter (ZRA). The ZRA converts measured current to voltage without imposing voltage drop on the external circuit.

2.5.2 Open circuit potential

Potentials are measured relative to a reference, or as a potential difference between anodic and cathodic reactions. When anodic and cathodic reaction occurs in same metal, they polarize towards a common potential. Open circuit potential is potential recorded when no external current is applied to a test electrode. Magnitude of measured potential is a measure of ionic concentration and EAS in the EDL [74].

2.5.3 Butler Volmer equation

A fully established EDL with no external potential applied has anodic and cathodic reactions occurring at the same rate (ie at equilibrium). Application of external potential to metal in a corrosive environment creates change in the EDL chemistry. Electron/ions from the metal/electrolyte as well as EAS perturb the EDL [74] thereby causing imbalance. Application of potential less negative than

the equilibrium potential favours cathodic reactions, while positive over-potential promotes anodic reactions. Deviation of EDL from equilibrium is a measure of net current densities of the anodic and cathodic reactions [89]. Current measurement is important in corrosion as it can be converted to determine the rate of metal penetration caused by corrosion [74]. The Butler-Volmer equation provides an expression that relates current density to changes in applied potential as expressed in Equation 2.12 [89].

$$i = i_o \left(\exp\left[\frac{\alpha_a n F \eta}{RT}\right] - \exp\left[\frac{\alpha_c n F \eta}{RT}\right] \right) \quad (2.12)$$

Where i and i_o are current density and exchange current density (mA/cm^2) respectively. α_a and α_c are anodic and cathodic charge transfer coefficient respectively, η = activation over-potential ($E - E_o$), n = number of electrons involved in reaction, R = Universal gas constant, T = absolute temperature (K), F = Faraday's constant. If anodic overpotential is made using a potentiostat, the anodic exponential term dominates the reaction and vice versa [74, 79]. A plot of potential versus current within overpotential range of $\pm 15mV$ gives a straight line while Plot of potential versus logarithm of current within $\pm 250mV$, known as Tafel Plot, gives inflected plots.

2.5.4 Tafel plots

Metallic corrosion often occurs as electrochemical reactions at electrolyte metal interface [79]. The corrosion rate depends on equilibrium attained between opposing anodic and cathodic reactions in which electrons are released and consumed respectively. OCP is a measure of the balance between the anodic and cathodic reactions when no external circuit is connected to the electrode. Relationship of potential and logarithm of corresponding current density within polarisation range of $\pm 250mV$ vs OCP can be depicted on Tafel plots [74]. The current is plotted on a logarithm scale due to wide range current measurement required in corrosion

experiment. A typical Anodic and Cathodic Tafel plot is indicated in Figure 2.12 where E_{corr} is the corrosion potential.

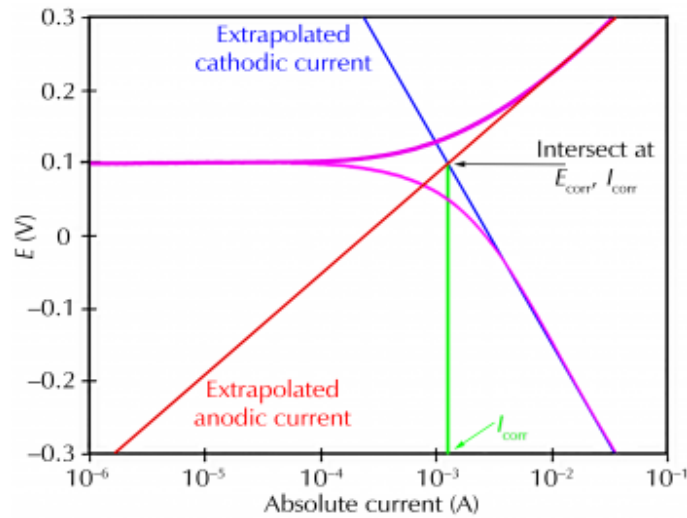


Figure 2.12: Typical Anodic and Cathodic Tafel Plot [79]

The positive polarisation curve is known as the anodic branch while the negative polarisation curve is the cathodic branch. The turning point on the curve indicate point at which current polarity reverses in both anodic and cathodic branches. Tafel slopes are obtained by calculating the gradient of best line of fit along the anodic and cathodic branches which are referred to as anodic Tafel (β_a) and cathodic Tafel (β_c) respectively [72] with unit in mV/decade. Tafel plots are used to study anodic and cathodic trend in metals placed in corrosive environment. The corresponding current (i_{net}) varies linearly with the value of overpotential of ($E - E_{\text{corr}}$). Advantage of the plot is that the corrosion current density i_{corr} can be obtained directly by extrapolating anodic and cathodic linear plots at OCP [74] .

2.5.5 Linear polarisation resistance and Stern-Geary's equation

Linear Polarisation Resistance (LPR) is a corrosion measurement technique capable of taking instantaneous measurement of corrosion rates over a defined surface area of a freely corroding metal [90, 91]. The LPR employs electrochemical concepts

to measure interfacial kinetics such as exchange current density and corresponding corrosion rate at the same time [91]. The general corrosion of a metal is related to the metal's polarisation resistance at ranges close to its corrosion potential, typically $\pm 10\text{mV}$ vs OCP [92]. LPR measurement technique is non-destructive and entails the use of a potentiostat to conduct stepwise polarisation of a test electrode within approximately $\pm 10\text{mV}$ vs OCP [74, 92]. Figure 2.13 features a typical LPR plot.

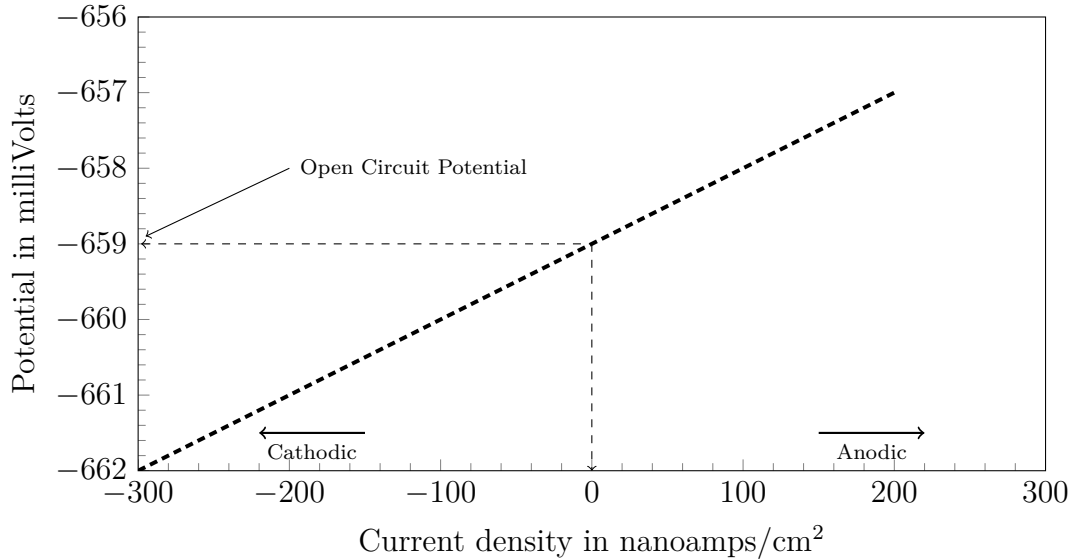


Figure 2.13: Typical LPR Plot [74]

The potential vs current density slope is referred to as polarisation or corrosion resistance R_p ie $R_p = \Delta E / \Delta i$. Sample area is determined prior to measurement of the R_p to ensure that measured value is not affected by the surface area. The unit of R_p is ohms-cm² which implies that if the surface area of same sample is halved, measured R_p value will be doubled and intrinsic R_p (ohms-cm²) remain the same [91]. The current response of applied potential is proportional to the corrosion current which is in turn converted to corrosion rate using a conversion factor. Having determined R_p , β_a and β_c , corrosion current density can be calculated instantaneously using the Stern Geary's expression shown in equation 2.13 [74, 92].

$$i_{corr} = \frac{1}{2.303R_p} \left(\frac{\beta_a \beta_c}{\beta_a + \beta_c} \right) \quad (2.13)$$

Where: i_{corr} = Corrosion current density (Amps/cm²) R_p = Corrosion (polarisation or charge transfer) resistance (Ohms-cm²). β_a and β_c are respectively Anodic and Cathodic Tafels in mV/decade. Stern Geary coefficient (B) = $\frac{1}{2.303}(\frac{\beta_a\beta_c}{\beta_a+\beta_c})$. Once i_{corr} is determined, corrosion rate (in mmpy) can be calculated using Equation 2.14 [23, 72, 92, 93].

$$\text{Corrosion rate (mmpy)} = 3.27 \times 10^{-3} \frac{i_{corr} \times E_w}{\rho} \quad (2.14)$$

Where:

0.00327 = constant for expressing in mmpy, i_{corr} = corrosion current density in $\mu\text{A}/\text{cm}^2$, ρ = metal density in (g/cm³), 27.5 g/cm³ for Fe), E_w = equivalent weight (27.56g for Fe).

Chapter 3

Literature Review

3.1 Carbon steel corrosion

Carbon steel remains the preferred choice for pipeline and petroleum installations while corrosion accounts for about 25% of recorded failures in the petroleum industry [61]. Over 50% of oil and gas corrosion failures emanate from sweet (CO_2) and sour (H_2S) fluid environments. Corrosion therefore plays a significant role when selecting materials for design in the oil and gas industry [37, 52]. Table 3.1 depicts percentages of failures attributed to corrosion in the oil and gas industry.

Table 3.1: Corrosion caused failures in Petroleum related industries [37]

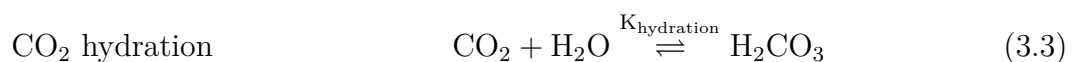
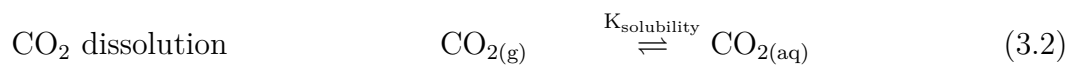
Failure Type	Total Failure (%)
CO_2 related	28
H_2S	18
Preferential weld	18
Pitting	12
Erosion control	9
Galvanic	6
Impingement	3

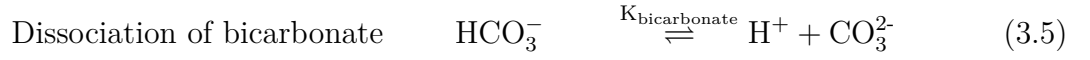
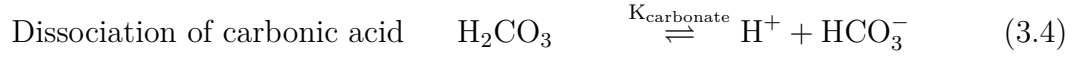
From Table 3.1, sweet corrosion accounts for a high failure rate in the petroleum industry. Carbon steel corrosion in oil and gas pipes can occur internally or on external surfaces of the pipe. External corrosion occurs when pipeline surface get

hydrated externally in an aqueous environment or ground water. The influence of flow constituents such as bicarbonate and carbonate ions also cause internal corrosion of steel pipelines [94]. Carbon steel corrosion in sweet environment therefore poses great challenge to the petroleum industry [95, 96, 97, 98]. Significant studies have been made on sweet corrosion since its first record in the 1940s [19]. Despite extensive studies, no acceptable model has been presented for carbon dioxide corrosion as the available semi-empirical models are not easily extrapolated [19]. Unlike H₂S, CO₂ alone does not cause catastrophic failure such as cracking. Its presence however causes high corrosion rate when dissolved in the aqueous phase by promoting electrochemical processes between contacting fluid phase and steel [37]. Carbon dioxide dissolves readily in water, brine as well as liquid and gaseous hydrocarbon [64]. Solution pH is reduced following CO₂ dissolution but research shows that solution acidification do not justify high corrosion rate of carbon steel in CO₂ environment [60, 95]. There seems to be a consensus that CO₂ presence accelerates corrosion electrochemical reduction processes. When carbon steel corrodes in carbon dioxide saturated solution, several reactions and processes take place concurrently around the surface of the corroding metal [24]. These include cation and electron release, mass transport of ions, hydrogen evolution and few other chemical and electrochemical processes. Equation 3.1 depicts hydration of CO₂ to form carbonic acid.



Only about 2% volume of the dissolved CO₂ forms carbonic acid (H₂CO₃) [50]. The chemical reactions that occur in a saturated solution of CO₂ are outlined in equations 3.2 to 5.4, where K denotes the equilibrium constant [50, 57].



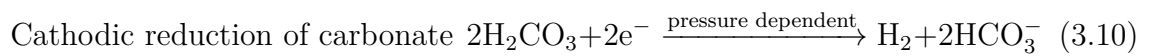
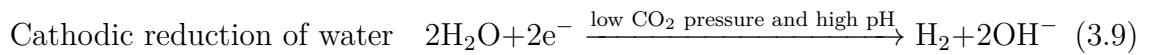
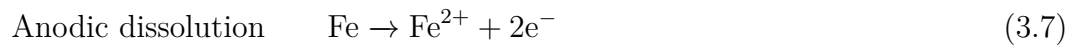


The chemical reactions do not proceed at the same pace. For instance, CO_2 dissolution (Equation 3.2) and CO_2 hydration (Equation 3.3) occur slowly while carbonic acid dissociation is fast; the former could become the rate determining-step (RDS) [24, 50]. Debate still exists on the likely rate-determining step (RDS) of the equilibrium reached in equation 3.1. Kermani and Morshed [10] summarised reactions as in Table 3.2 where hydroxyl adsorbates are believed to be replaced by carbonic adsorbates before dissolution of ferrous ions into solution.

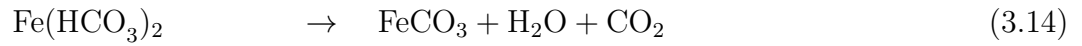
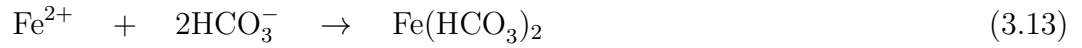
Table 3.2: Possible electrochemical reactions during the anodic dissolution of iron in CO_2 environment [10, 61, 99]

Reaction No.	Reaction or Equilibrium	pH<4	4<pH<5	pH>5
1a	$\text{HCO}_3^- \leftrightarrow (\text{HCO}_3^-)_{\text{ads}}$	1a	1a	1b
1b	$\text{CO}_2 + (\text{OH}^-)_{\text{ads}} \leftrightarrow (\text{HCO}_3^-)_{\text{ads}}$			
2	$(\text{HCO}_3^-)_{\text{ads}} \Rightarrow (\text{HCO}_3^-)_{\text{ads}} + \text{e}^-$			RDS
3	$(\text{HCO}_3^-)_{\text{ads}} \Rightarrow (\text{HCO}_3^+)_{\text{ads}} + \text{e}^-$		RDS	
4	$(\text{HCO}_3^+)_{\text{ads}} + \text{OH}^- \Rightarrow (\text{CO}_3)_{\text{ads}} + \text{H}_2\text{O}$	RDS		
5	$\text{Fe}-(\text{CO}_3)_{\text{ads}} + \text{H}_2\text{O} \Rightarrow \text{Fe}^{++} + \text{HCO}_3^- + \text{OH}^-$			
1→5	Tafel Slope (mV/log)	60/2 =30	60/1.5=40	60/0.5=120
1→5	H^+ reaction order	-2	-1	0
1→5	CO_2 reaction order	1	1	1

The anodic and cathodic reactions that occur during carbon steel corrosion in aqueous CO_2 solutions are listed in equations 3.7 to 3.11 [50].



In suitable conditions, the reactions in equations 3.7 to 3.11 can lead to the formation of FeCO_3 in two possible stages indicated in equations 3.12 to 3.14 [14, 48].



Carbon steel corrosion in CO_2 environment is generally controlled by cathodic reactions [97]. The anodic dissolution solely depends on temperature while the main cathodic reaction, which is hydrogen ion (H^+) reduction is pH dependent but limited by H^+ diffusion through the solution to the steel surface [50]. This implies that electrolyte flow has influence on H^+ evolution thereby aiding corrosion. Carbon dioxide can therefore primarily increase corrosion rate by setting free H^+ from H_2O to enhance cathodic reduction. The weak carbonic acid evolves free H^+ at a faster rate than that of a stronger acid at the same pH [24, 50]. Hydrogen evolution by direct reduction of water (Equation 3.9) is equivalent in thermodynamic terms with hydrogen evolution by reduction of free (dissociated) hydrogen ions (Equation 3.8) but the former's pathway is relatively slow, being kinetically hindered [50].

3.2 Effect of dissolved CO_2 on carbon steel electrochemical reactions

Steel corrosion in a CO_2 environment has been a great challenge in the oil and gas industry for decades [9]. Free water in presence of CO_2 naturally gets saturated to form carbonic acid (H_2CO_3) [100]. Carbonic acid dissolves to form bicarbonate (HCO_3^-) and hydrogen ion (H^+) [59]. The corrosion rate of carbon steel in CO_2 environment surpasses that experienced in strong acidic solution of the same pH as noted earlier [14, 101]. In fully dissociated acid, hydrogen evolution occurs as

indicated in Equation 3.8. Hydrogen gas evolution depends on transport to the steel surface to become reduced. That implies that hydrogen ion involvement is limited by mass transfer. The limiting effect is however negligible if carbon steel corrodes in solutions containing purged CO_2 due to high evolution of hydrogen gas as indicated in Equation 3.8. Additional cathodic currents emerge due to cathodic reduction of H_2CO_3 arising from hydrolysis of CO_2 [19]. Hydrolysis of CO_2 is a flow independent, chemical controlled step which also influences the diffusion limiting current [19, 64, 102]. Nescic et al. [19] noted a particular flow rate for CO_2 solutions while limiting current was separated into 3 components; hydrogen ion (H^+) diffusion, CO_2 hydration and H_2CO_3 diffusion. The presence of CO_2 in a corroding steel electrolyte increases the overall cathodic current while anodic current value is unaltered as shown in Figure 3.1. The limiting current observed on the cathodic branch in CO_2 system is caused by hydrogen ion depletion at the surface of the metal and slow rate of CO_2 hydration [101].

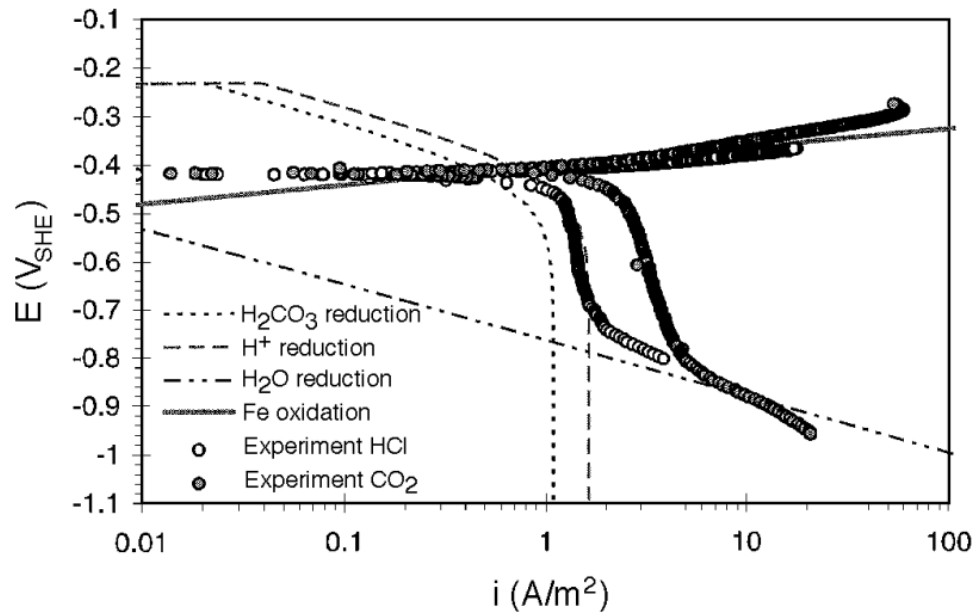


Figure 3.1: Effect of CO_2 on cathodic current [19]

3.3 Forms of CO₂ induced corrosion

Carbon dioxide corrosion normally emanates as uniform (general) corrosion, localised corrosion such as mesa attack, flow induced corrosion or pitting corrosion [37, 62]. Pits occur in the form of localised dissolution often with smooth tapered edges while stepped depressions with vertical sides that terminate into flat bottoms are referred as mesa attack [59]. pitting corrosion is often initiated in the open while crevice corrosion initiates at occluded or metal to non-metal junction [67].

3.3.1 Mesa attack

Mesa attack is a localised form of corrosion that occurs as a result of unstable corrosion products, predominantly FeCO₃ due to the environment or impinging operating conditions. Mesa attacks often feature as sharp edged, stepwise, flat bottom damage at low or medium flow [10]. Typical sample of mesa attack is featured in Figure 3.2. Some literature reported that pitting corrosion precedes the occurrence of mesa attack [62].



Figure 3.2: Typical picture of Mesa attack [10]

3.3.2 Flow induced localised corrosion

Localised attack that exhibits groove patterns in the direction of fluid flow is known as flow induced localised corrosion (FILC) [59]. FILC often develop from cracked

spots or corrosion pit sites in region of high flow intensities [62]. Flow turbulence propagates existing damage by removing corrosion products and hindering formation of further scales [10].

3.3.3 Galvanic corrosion

Galvanic corrosion is the corrosive damage that occurs in heterogenous metallic structures or when dissimilar metals are coupled in same corrosive electrolyte. Electron flows between the metals with preferential attack on the active (less noble) metal. Galvanic coupling often creates metallic polarisation which can be explained by the mixed potential theory [92]. Galvanic attack could result to uniform or localised corrosion and protective films may evolve to retard corrosion effect. The attack could however be severe when protective films are not formed. When two dissimilar metals are immersed in an electrolyte, the difference in corrosion potential causes preferential dissolution of the less noble metal (anode) while deposition takes on the noble metal (cathode).

3.4 Pitting corrosion

Metals such as Aluminium have the ability to form thin oxide layers (in nanometer scale) in normal environment where oxygen is abundant. Such films are however susceptible to breakdown thereby causing dissolution of underlying metal. Similar penetration of high magnitude could grow in typical CO₂ environment such as internal pipeline walls and remain unnoticed until failure occurs with its devastating environmental and health concerns [41, 57]. Pitting corrosion is a sort of extreme localised dissolution of metals which may be caused by breakdown of protective layer (passive film) [62]. Defects at inclusion point or heterogeneity of metallic structures could as well initiate pitting process. The exposed surface having small area corrodes

faster than the surrounding cathode having higher OCP [103]. Pitting corrosion can thus be defined as:

Form of localised corrosion that proceeds because of local cell action once the pitting potential has been attained under a given set of conditions for a given material in a given chemical environment [104].

Film breakdown and subsequent metallic dissolution is a common explanation for pitting corrosion. Pitting may as well be initiated when adsorbed chloride penetrate protective film at any point of film defect up to the bare steel surface [5, 105]. Cui et al. [106] found that breakdown of films by adsorbed chloride ions on carbon steel causes nucleation and growth of pit in neutral media. Pistorius et al. [107] categorized pitting to progress in stages namely; passivity breakdown, metastable/repassivation and stable pits. Espina-Hernandez et al. [108] however employed magnetic circuit to investigate pitting in mild carbon steel and described pitting corrosion to progress in 3 stages namely: passivity breakdown, early growth/repassivation and stable growth. Pitting corrosion of carbon steel is a form of electrochemical process that is generally accepted to progress in distinct stages namely pit initiation, pit propagation and possibly re-passivation [14, 56]. Hoepfner et al. [104] identified stress condition, solution chemistry, length of attack, material microstructure and composition as other factors governing pit growth. Similarly, Isaacs et al. [109] observed that pit survival depends on ability of surrounding film to harbour aggressive anolytes as it maintains contact with the bare steel such that anolyte concentration is not diluted to cause re-passivation.

3.5 Carbon steel pitting in sweet environment

Pitting could occur freely on carbon steel in CO₂ environment even without being polarised. High pitting susceptibility was reported in pipeline steels at temperatures

ranging from 60 to 80°C in sweet conditions [44]. Such attack could appear uniform when observed on the microscopic scale. Videm and Koren [60] suggested that passivation and breakdown potentials of carbon steel fall within the free corrosion range in sweet environments. The partial breakdown of film is referred to as **pit initiation**. Favourable conditions could cause carbon steel to passivate in sweet environment due to the presence of Fe_3O_4 beneath FeCO_3 , an important aspect of localised corrosion [110]. Pitting of mild steel in CO_2 environment is quite different from that observed in neutral or alkaline environment for a number of reasons:

- Differential aeration is ignored since CO_2 systems are free of oxygen [57].
- Pit acidification is not considered because CO_2 solution exhibits buffering effect and also due to the absence of ferric oxide and hydroxides in CO_2 systems [57].
- Point defect mechanism (seen in mesa attack) does not occur in oxygen free CO_2 systems [57].

There seems a consensus that carbon steel pitting occurs as a result of local dissolution of films formed on steel [56, 62, 111]. A lack of homogeneity of corrosion products, flow conditions, flow constituents and steel micro-structure could as well contribute to pitting in low carbon steels. Han et al. [112] experimented on the propagation of localised corrosion in sweet condition and observed that OCP decreases as protective films get damaged. The compromised area becomes the anode while the immediate surrounding becomes the cathode [59, 113]. Gao et al. [114] revealed that localised corrosion in mild steel could occur due to solubility changes in FeCO_3 caused by changes in solution ionic strength (due to operating environment). Iron carbonate (FeCO_3) film condition in the grey zone (FeCO_3 super saturation ranging from 0.5 to 2) favours propagation of localised corrosion [56]. The

grey zone condition is a state in film formation where neither FeCO_3 precipitation nor dissolution is expected in solution. The conditions beneath the FeCO_3 layer in turn promote the formation of magnetite (Fe_3O_4) which anchors the film to the steel surface [56]. In event of damage to the protected surface, galvanic effects could accelerate corrosion [51] as the underlying bare surface becomes the anode while the protected surrounding becomes the cathode [63]. The magnetite presence increases the potential on the film covered surface [63]. The early stage of pitting after local breakdown is referred to as metastable pitting where the initiated pits could either be repassivated or become a stable pit in the absence of repassivation [115, 107]. Initiation of pitting in passive alloys has been approached from different perspectives based on **film-break**, **penetration** and **adsorption mechanism** amongst others [116].

3.5.1 Carbon steel pitting initiation in sweet environments

The mechanism of film removal in single phase flow is still not fully understood but generally known to be caused by hydrodynamic forces or chemical dissolution (mass transfer) [15, 26, 117]. Mechanical impact is mainly responsible for film removal in multiphase flow systems and underwater impinging jets while film breakdown in single phase flow is mainly due to chemical dissolution or synergy between hydrodynamic effects and chemical dissolution [26]. Protective iron carbonate dissolution can be expressed in equation 3.15 where K_{sp} is the solubility product and it strongly depends on ionic strength and temperature [26]. Dissolution can occur only when the solution becomes under-saturated ($S < 1$) as indicated in equation 3.16. However, film may not dissolve under $S < 1$ in a metastable zone due to the energy barrier for dissolution.



$$S = \frac{(C_{\text{Fe}^{2+}})(C_{\text{CO}_3^{2-}})}{K_{\text{sp}}} \quad (3.16)$$

Carbon steel undergoing uniform corrosion could transit to pitting at a certain point probably due to structural defects or other factors. Carbon steel under uniform attack has equal anodic and cathodic current densities i_A and i_k in all points [118]. Anodic dissolution (Fe^{2+}) is as well accompanied by corresponding cathodic reductions (X^-) at the same point as featured in Figure 3.3.

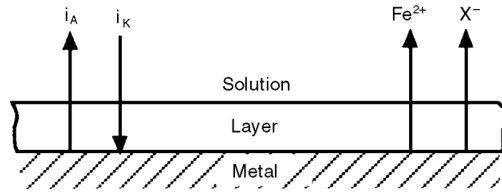


Figure 3.3: Carbon steel under uniform attack [118]

The magnitudes of anodic and cathodic current densities are similar but opposite for a sample under uniform corrosion. Equilibrium in current density ceases if local anode suffices on the metal at any spot possibly due to environment, mechanical or chemical influence. This causes Fe^{2+} dissolution to increase while HCO_3^- consumption decreases at the spot, therefore becoming a local anodic site. Protective films at the compromised spot diminish due to solubility of iron [118] thereby promoting faster film dissolution. Conversely, production of Fe^{2+} decreases at the cathodic site while HCO_3^- increases as shown in Figure 3.4. The galvanic effect created promotes anodic dissolution even without presence of HCO_3^- [118].

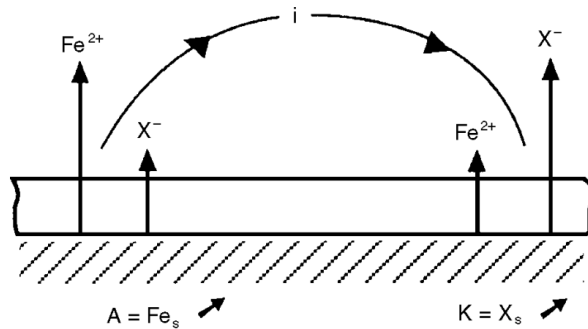


Figure 3.4: Localised attack in carbon steel [118]

Several other literature proposes pit initiation processes with the general consensus that passive film breakdown is key to such processes. Cheng and Luo [119] viewed

pitting corrosion from the divalent cation vacancy exhibited by iron. The duo proposed that pit initiation in carbon steel is a result of film rupture [119]. Steel micro-structure is as well attributed to influence corrosion performance in low carbon steel [120, 121]. Wei et al. [122] work on galvanic trend in low carbon steel suggested that localised corrosion evolves in low carbon steel due to the composition of steel matrix. There is yet no conclusive presentation on pit initiation processes in low carbon steel.

3.5.2 Propagation of carbon steel pitting

Initiated pits either grow or cease to grow depending on the environment. OCP difference between the anode and the cathode (Figure 3.5) is believed to be the driving force for propagation of localized CO_2 corrosion [56].

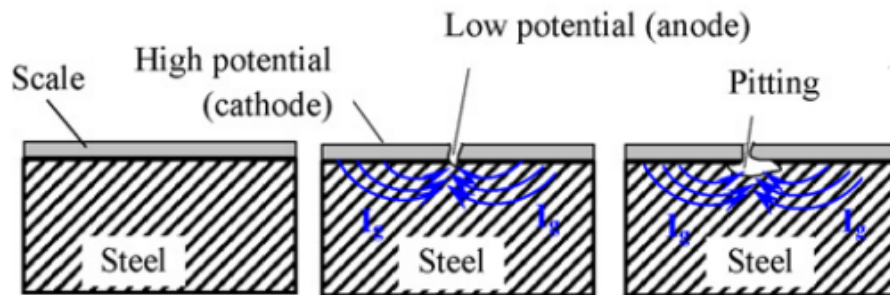


Figure 3.5: Galvanic model for CO_2 induced pitting corrosion in mild Steel [44]

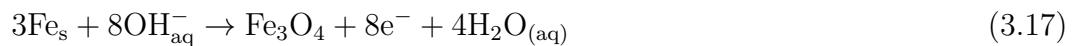
Pit propagation depends on film parameters such as CO_2 concentration, pH and temperature [55]. Fang et al. [123] attributed pit nucleation and growth in X-52 pipeline steel to passive film disruption and that pit sustenance depends on temperature, electrolyte and potential amongst other factors. Lou et al. [124] observed that pit growth on carbon steel is promoted in solutions of dissolved chloride and high acidity while dissolution is inhibited in alkaline conditions.

3.5.3 Pit termination

Propagation starts with growth of unstable pits called metastable pits as most initiated pits do not survive [45]. Some pits that do not meet the required conditions for self-sustenance may re-passivate. Burstein [42] reported pitting events as a function of pit size, geometry and iron cluster distribution. Meta stable pits that survive to grow large in size are termed stable pits which could repassivate or progress further depending on the environment [45]. As earlier noted, presence of halide anions such as chloride ions, promote the pitting process by stabilising anodic dissolution process. Change in electrochemical conditions such as reduced flow, higher temperature and pH that favours formation of dense protective film could promote the pit healing process.

3.5.4 Schematic representation of carbon steel pitting in a CO₂ environment

Han et al. [63] presented corrosion models featuring 3 cathodic entities. Figure 3.6 depicts a schematic representation of the corrosion process on bare surface (anode pit). The cathodic reactions involve proton reduction of hydrogen ions while dissolution of iron occurs at the anode. With the formation of FeCO₃, conditions beneath the film were assumed to favour formation of Fe₃O₄ in accordance to equation 3.17. This led to a greater film protection as featured in the vertical portion of anodic curve in Figure 3.7. The region where current density decreases with increase in potential is the passivation or iron carbonate forming process. The OCP value increases while corrosion rate decreases as a protective film forms on the metal surface [103].



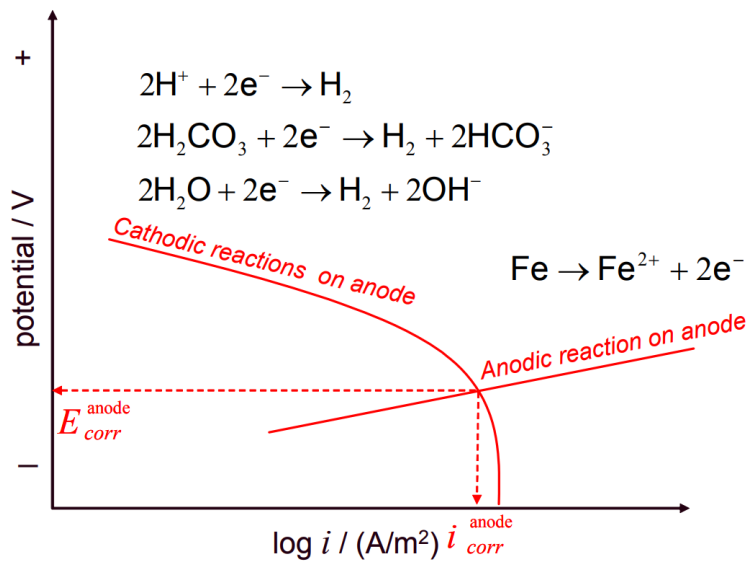


Figure 3.6: Schematic diagram of corrosion process at film free surface (pit anode) on carbon steel [63]

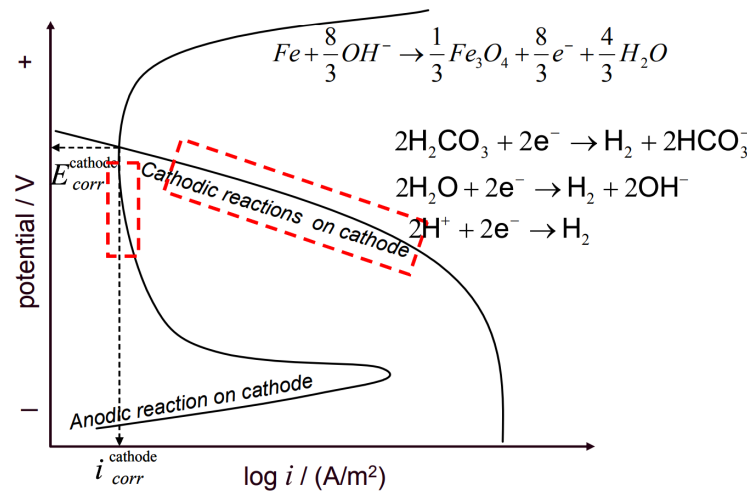


Figure 3.7: Schematic diagram of corrosion occurring on passive layer on protected surface (cathodic site) leading to formation of Fe_3O_4 [63]

The net anodic reactions are balanced by the net cathodic reactions at both surfaces while the measured coupled potential is the mixed potential as featured in Figure 3.8.

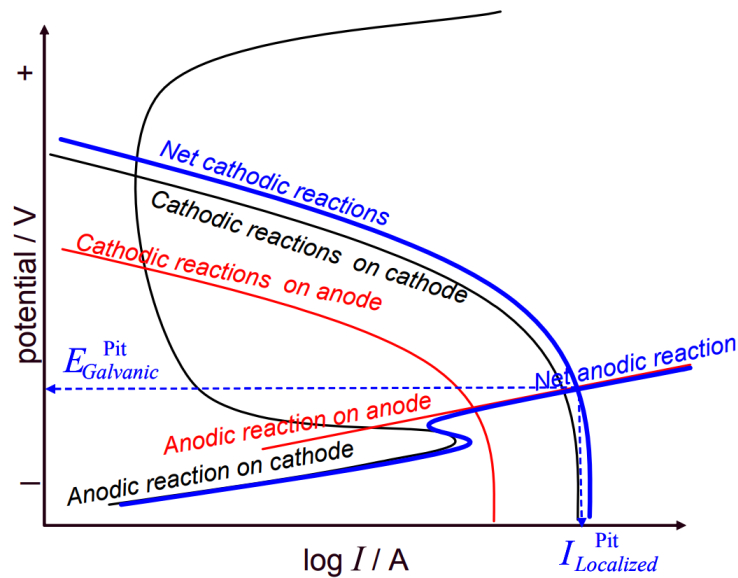


Figure 3.8: Galvanic cell schematic diagram featuring bare anode and protected cathode [63]

3.6 Identification and characterisation of corrosion pits

Addressing pitting corrosion problems would not be feasible without reliable means of identifying, estimating or measuring the extent of pitting [32, 104]. This calls for adoption of established standards for pit identification and measurement. Inspectors have over the years developed series of pit measurement devices such as J. Campbell Stirling pit gauge, lever type pit gauge, Thorpe pipe pit gauge (Figure 3.9) and bridging pit gauge amongst others [125]. Unacceptable discrepancies in measurement led to development of other measurement devices such as Machinist's depth gauge, Tri Pit gauge (Figure 3.10) and dial indicator pit gauges which requires high skills to operate [125].



Figure 3.9: William R. Thorpe Lever type Pit Gauge [125]

A number of other options are available for measuring the extent of pitting. This



Figure 3.10: Tri Gauge Pit Gauge [125]

includes visual inspection after sectioning, scanning electron microscopy, confocal microscopy and use of eddy current probes [104]. Other techniques used for measuring pitting extent include electrochemical noise, pitting index and ZRA technique [126]. Modern analysis technique entails the use of ultrasound and application of robotics to observe defects on metals in areas that are difficult to access.

3.6.1 Metal penetration and pitting factor

Researchers are often interested in pit depth measurement owing to the fact that the deepest pit is likely to perforate before others [104]. The ASTM standard categorise maximum pit depth of $25\mu\text{m}$ (0.025 mm) as a **Light Pitting** while pit depth of about $250\mu\text{m}$ (0.25 mm) is regarded as **Moderate Pitting** [104]. Inspectors however sometimes consider metal penetration to evaluate extent of pitting corrosion in either of 2 ways outlined below [127, 128, 129]:

- Height of deepest valley created or preferably, averaging the heights of 10 deepest valleys.
- Pitting Factor (Pf) defined as ratio of deepest valley depth to average metal penetration (measurable by weight loss)[130].

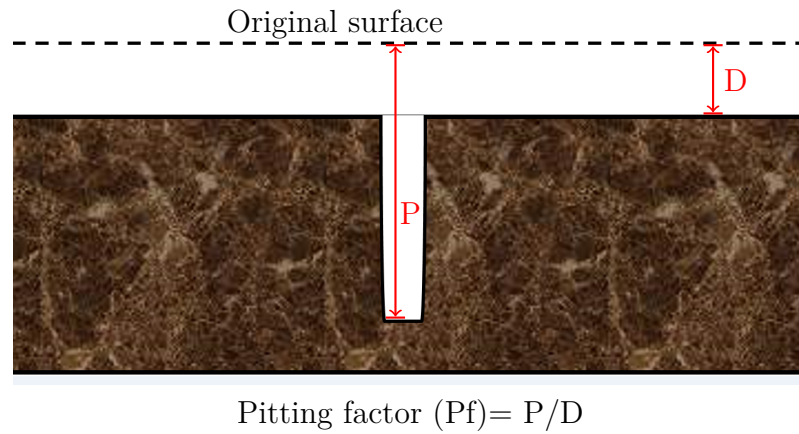


Figure 3.11: Schematics depicting pitting factor parameters

This can be expressed mathematically as depicted in Equation 3.18 [131] and illustrated in Figure 3.11.

$$\text{Pitting Factor (Pf)} = P/D \quad (3.18)$$

Where P = Deepest metal penetration (valley), D= Average metal penetration (measurable by weight loss)

This means that pitting factor of unit magnitude implies general corrosion while higher pitting factor indicates pitting corrosion presence [131]. Measuring of metal loss is however not suitable since uniform corrosion may occur with pitting [92]. Non-destructive inspection is often adopted by inspectors to assess corrosion damage. Aerial surface 2D and 3D profilometry could be employed for such measurements [132].

3.6.2 Characterisation of corrosion pits

The Annual Book of ASTM Standards provides guide on corrosion pit shapes as well as density, size and depth expected to confirm corrosion pit formation. Typical shapes of corrosion pits provided in ASTM standards are featured in Figure 3.12. The size, shape and density of corrosion pits are described in Annual Book of ASTM Standards is depicted in Figure 3.13. Column A describes pit as a function of pit

density (number of pits per unit area) while column B classify pit based on area (square metres covered). Column C categorise pits in terms of pit depth which is of significant interest to corrosion engineers as such parameter can reveal information on possible rupture of materials [104].

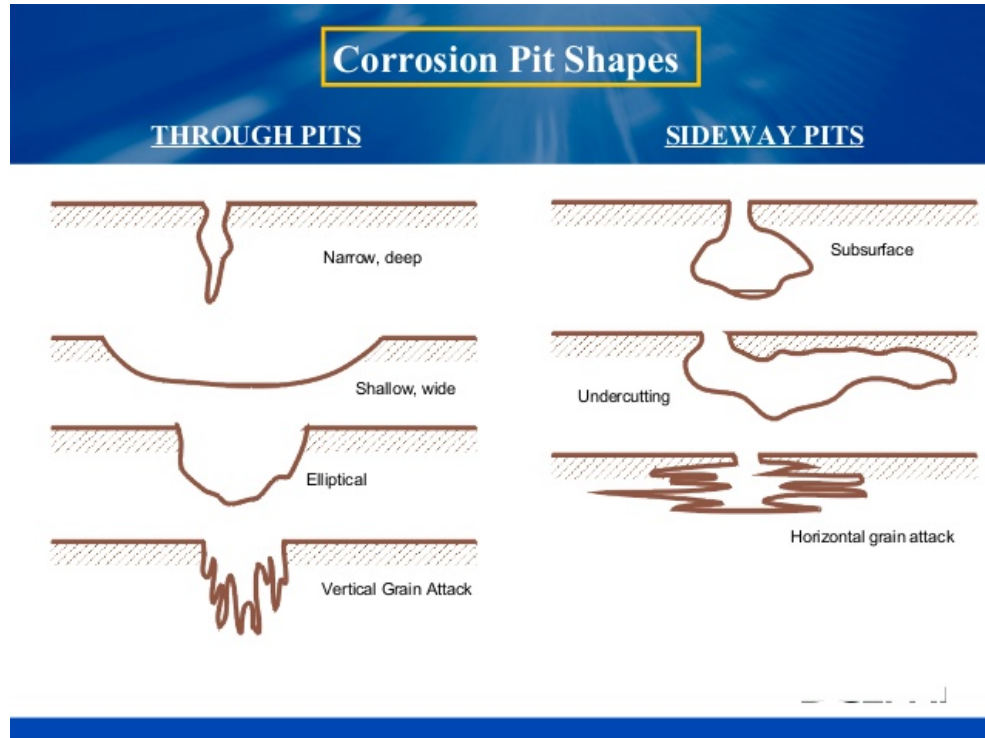


Figure 3.12: Cross section featuring corrosion pit shapes [133]

3.7 Corrosion products formed on carbon steel in sweet environments

Carbon steel is thermodynamically unstable in sweet environments [24]. Its ability to form protective films enables its application in the oil and gas industry. Corrosion products could retard or promote corrosion of carbon steel depending on prevailing circumstances [27]. The corrosion products that form on steel are a vital component of localised corrosion [32]. Knowledge of passive films formed on carbon steel vis-à-vis operating conditions is important in CO₂ corrosion. Conductivity or electrical properties of corrosion films are related to protectiveness

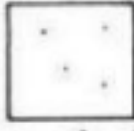
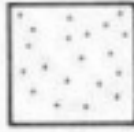
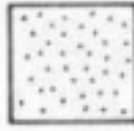
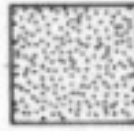
	<u>A</u> DENSITY	<u>B</u> SIZE	<u>C</u> DEPTH
1	 $2.5 \times 10^3/m^2$	 $0.5mm^2$	 0.4mm
2	 $1 \times 10^4/m^2$	 $2.0mm^2$	 0.8mm
3	 $5 \times 10^4/m^2$	 $8.0mm^2$	 1.6mm
4	 $1 \times 10^5/m^2$	 $12.5mm^2$	 3.2mm
5	 $5 \times 10^5/m^2$	 $24.5mm^2$	 6.4mm

Figure 3.13: ASTM Standard charts for rating corrosion pits [92]

and electrochemical behaviour of the film [134]. As films form on metal surface, the corrosion rate decreases while OCP increase in the positive direction [103]. The initial film formed tends to be non-protective with low galvanic coupling between the bare steel area and the covered surface. Further film build up becomes protective with significant rise in galvanic coupling. The film then acts as a barrier against anodic dissolution and cathodic reactions [44]. Films formed under certain conditions could offer protection while partial breakdown of films could lead to localised attack. Numerous parameters such as temperature, microstructure,

CO₂ partial pressure are vital in CO₂ corrosion. Carbon dioxide partial pressure and pH impacts on cathodic reactions while super saturation is necessary in the growth of scales. Scales can however breakdown for reasons such as **chemical dissolution, erosion, mechanical breakdown** or **flow effect** [135]. Morikawa et al. [32] investigated corrosion product formed in general and localised corrosion using infrared spectra and suggests that corrosion products around pit and general corrosion regions appear to have similar composition. Iron carbonate is a major product of mild steel corrosion in CO₂ environment particularly at grey zone conditions [8].

3.7.1 Grey zone conditions

At certain conditions of solution chemistry, Fe²⁺ (from anodic dissolution) and CO₃²⁻ (from dissolved CO₂) combine to form iron carbonate (FeCO₃) when their concentration exceeds the solubility limit as described in equation 3.19 [8, 56, 57, 58, 101, 103, 136]. K_{sp(FeCO₃)} is the solubility product limit for FeCO₃ which depends on ionic strength and temperature. As Fe²⁺ and CO₃²⁻ concentration exceeds the solubility limit, equilibrium in Equation 3.19 shifts towards super-saturation (SS_{FeCO₃}), leading to precipitation as stated in equation 3.20 [50, 58]. Sun and Netic [22] proposed that occurrence of pitting corrosion is best determined by the level of super-saturation; an approach embraced in many corrosion models [58].



$$\text{SS}_{\text{FeCO}_3} = \frac{(C_{\text{Fe}^{2+}})(C_{\text{CO}_3^{2-}})}{K_{\text{sp}}(\text{FeCO}_3)} \quad (3.20)$$

Protective scale forms as saturation exceeds unity [8]. Precipitation rate (R_{FeCO₃}) can be expressed as a function of super-saturation (SS_{FeCO₃}), temperature (T), surface area to volume ratio (A/V), and solubility limit K_{sp(FeCO₃)} as indicated in

Equation 3.21 [8, 137].

$$R_{\text{FeCO}_3} = \frac{A}{V} \times f(T) \times \text{FeCO}_3 \times f(\text{SS}_{\text{FeCO}_3}) \quad (3.21)$$

Field reports often present Fe^{2+} concentration in ppm and this is easily controlled during laboratory work. Similarly, bicarbonate concentration can be determined by solution pH and CO_2 partial pressure [57].

3.7.2 Iron carbonate and localised corrosion

Siderite (FeCO_3) which forms on carbon steel is of significant importance in oil and gas applications [138]. Anodic dissolution is the major source of ferrous components of the FeCO_3 film formed on metal surfaces [138]. Conditions favouring FeCO_3 formation include high CO_2 partial pressure, high pH, low flow and high Fe^{2+} concentration [101]. Han et al. [57] observed that the siderite film becomes stable at grey zone conditions, when there is no net precipitation or dissolution of FeCO_3 . This practically happens when the super saturation of FeCO_3 falls within 0.5 to 2. Siderite whose growth is highly dependent on precipitation kinetics is the major corrosion product formed when steel corrodes in CO_2 environment [15, 62, 97, 135]. FeCO_3 films can be rapidly formed in the laboratory by introducing ferric constituents into electrolyte but such early precipitation produces non protective films [139]. Unlike Fe_3C , Siderite does not conduct electricity and therefore hinders the chemical reaction [62]. The stages involved in the formation of FeCO_3 are not yet clear but Bian et al. [97] proposed the steps featured in Figure 3.14.

Bian et al. [97] noted that anodic dissolution creates cathodic sites which are occupied by dissolved cations. Fully occupied cathodic sites form film nuclei which continue to grow until the entire steel surface is covered with film [97]. The structure of a well formed FeCO_3 (Figure 3.15) remain stable upon exposure to dry air but rapidly formed FeCO_3 is unstable and easily decomposes to haematite (Fe_2O_3) when

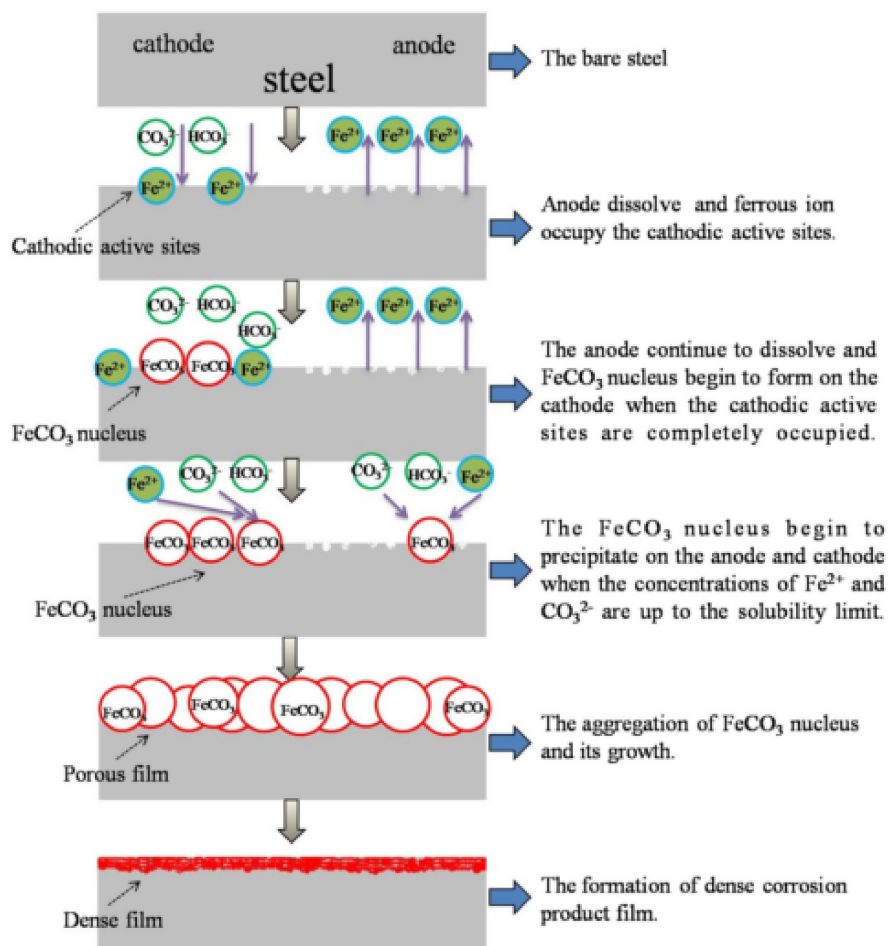


Figure 3.14: Steps involved in formation of FeCO_3 film [97]

exposed to air [140].

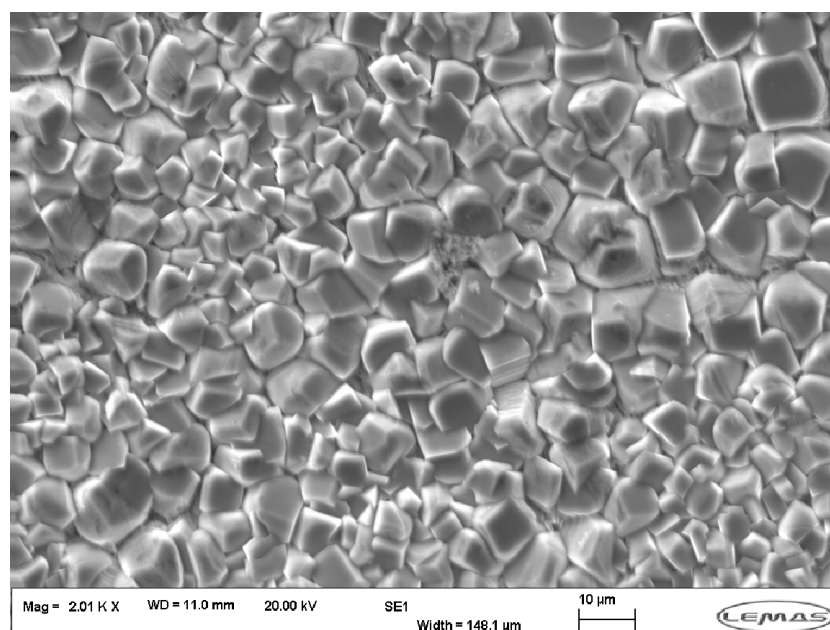


Figure 3.15: SEM Image showing FeCO_3 deposits on X65 carbon steel

Iron carbonate often lines the internal wall of carbon steel pipelines used for oil and gas application thereby retarding the flow of corrosion species [15, 51]. The processes leading to siderite formation and dissolution are of significant interest in sweet systems [24]. Based on the Dugstad [24] findings, formed scales may be porous if scale growth rate is less than the rate at which metallic dissolution occurs [24]. Some work submitted that cementite (Fe_3C) provides the needed anchor for siderite scales [10, 135]. An increase in temperature decreases solubility of FeCO_3 , thereby increasing its precipitation. Iron carbonate can nucleate when $S > 1$ and exists in different morphologies depending on the environment. FeCO_3 nucleation increases when saturation exceeds a critical super-saturation (S_c) [141]. A schematic representation of FeCO_3 morphology for low Cr-alloy steel is depicted as Figure 3.16.

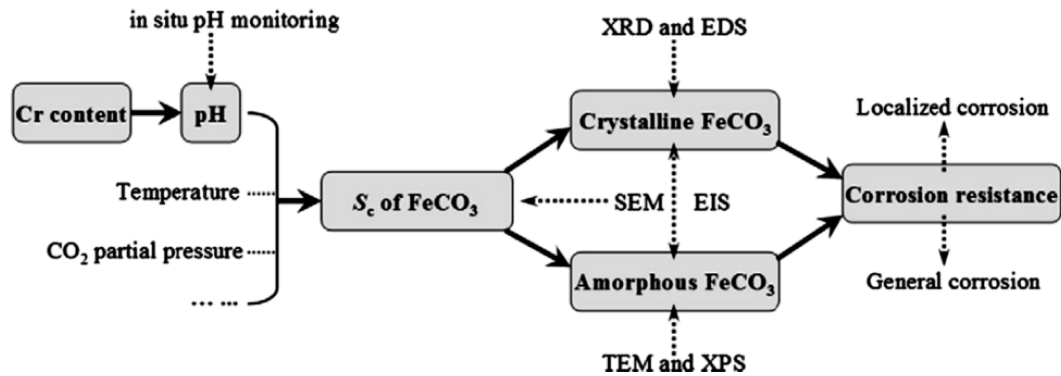


Figure 3.16: Schematics of properties of FeCO_3 morphology for low Cr-alloy steel [141]

Studies by Han et al. [103] led to rejection of the hypothesis suggesting FeCO_3 precipitation/ dissolution being the main explanation for passivation/de-passivation of carbon steel in sweet environment [103]. Carbon steel exhibits a significant drop in corrosion rate when fully covered with FeCO_3 films; this is often known as **pseudo-passivation** when it occurs and the solution pH is raised above pH7 [51]. Pseudo-passivation is thought to be caused by a layer of Fe_3O_4 formed beneath the FeCO_3 film, causing significant rise in OCP [51, 142]. A drop in pH level could lead to absence of pseudo-passivity due to dissolution of films [51]. An unstable pseudo-passive layer could cause galvanic effects resulting in localised corrosion [51].

Wei et al. [143] examined corrosion products formed on carbon steel and suggested that localised corrosion occurs during transition of amorphous scales to FeCO_3 scale. It was further revealed that under super-critical CO_2 conditions, amorphous layers initially form on steel surface and transform into dense inner FeCO_3 scales before being covered by a porous outer FeCO_3 film [143]. For low CO_2 partial pressure, dense FeCO_3 films form before formation of an inner porous FeCO_3 layer as shown in Figure 3.17 [143].

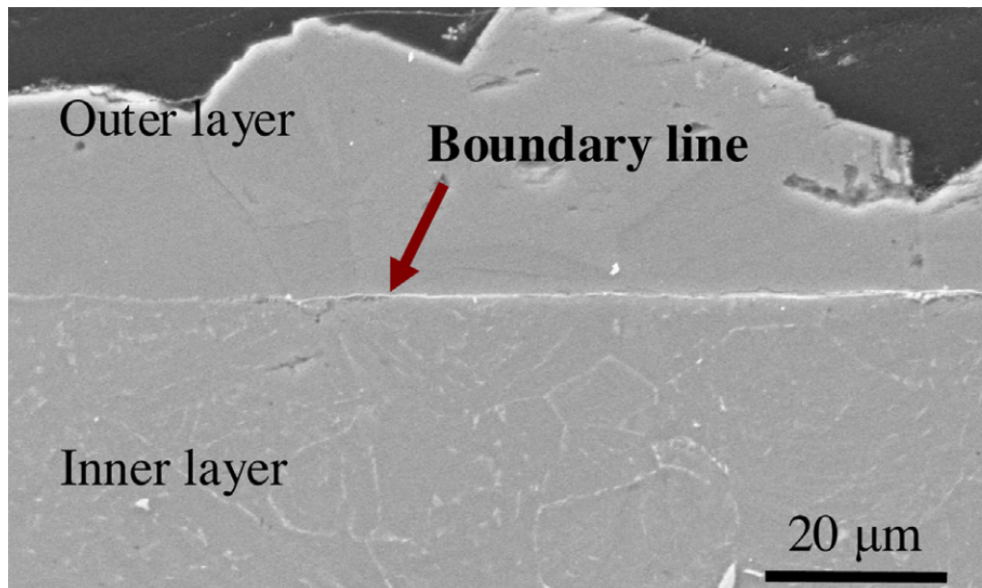


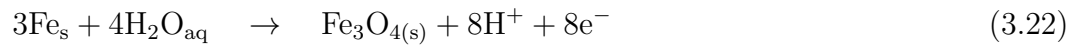
Figure 3.17: Image depicting boundary line between outer and inner FeCO_3 layers [143]

The outer scale offers high protection at low CO_2 partial pressure unlike the inner scale that offers better protection at higher CO_2 partial pressure [143]. The inner FeCO_3 layer plays a vital role in the protection, particularly in supercritical CO_2 conditions [143].

3.7.3 Magnetite (Fe_3O_4)

Han et al. [144] proposed a passivation scenario for mild steel in sweet environments. They explained that FeCO_3 formed on a mild steel surface becomes compact and hinders further reduction of protons. Proton deficiency increases the solution pH to

a level (beyond pH7) where iron oxide, known as **passivation magnetite**, forms on the metal surface as expressed in equation 3.22.



Magnetite (Fe_3O_4) could form as a result of electrochemical reaction of the steel with H_2O at over 110°C [62]. Formation of FeCO_3 also creates a favourable environment for the formation of underlying pseudo-passive films of Fe_3O_4 [51, 63]. Han et al. [144] also investigated passive film chemistry of mild steel in a sweet environment and suggested that Fe_3O_4 is the actual compound responsible for passivation of carbon steel in a sweet environment. This follows revelation of thick films of Fe_3O_4 underlying the FeCO_3 scales as shown in Figure 3.18 and Figure 3.19.

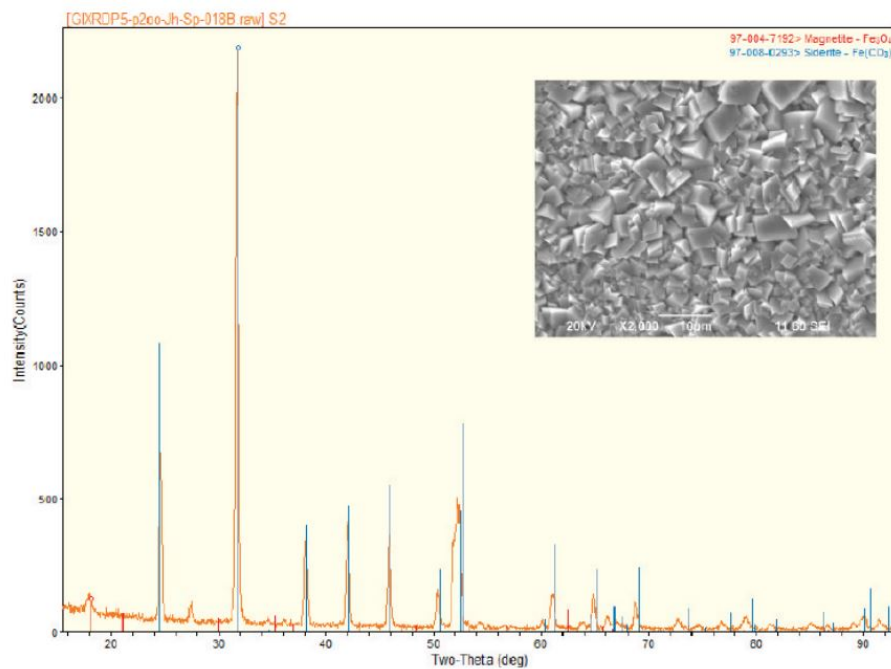


Figure 3.18: GIXRD and SEM indicating Fe_3O_4 presence in FeCO_3 Film [144]

3.7.4 Iron carbide (Fe_3C)

Cementite (Fe_3C) featured in Figure 3.20 is often revealed when ferrous region gets dissolved following the corrosion of steel. Iron carbide is electrically conductive and corrosion could occur on Fe_3C deposits typically as it does on carbon steel [118].

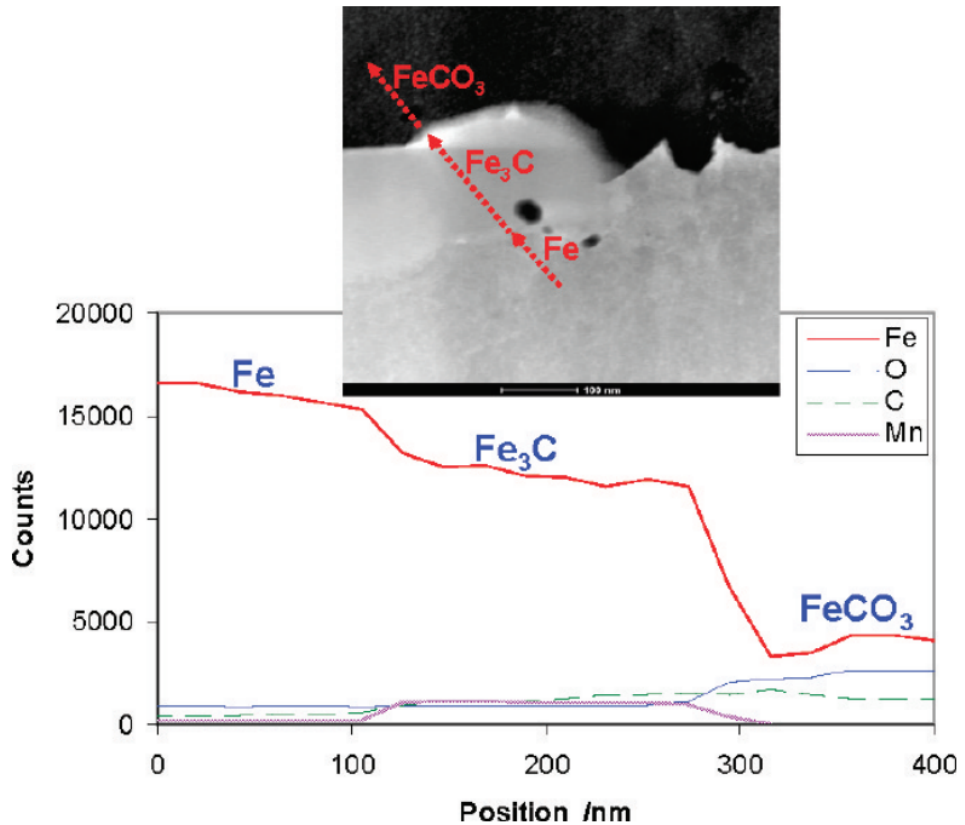


Figure 3.19: Element profile of EDX scan depicting likely Fe_3O_4 beneath FeCO_3 film [144]

The steel substrate could corrode while cementite acts as a cathodic site due to its conductivity with low hydrogen over-voltage [9]. The galvanic coupling therefore arises between Fe_3C and the substrate steel layer [118]. Crolet et al. [118] proposed that internal acidification following cementite formation is mainly due to galvanic coupling since bicarbonate ions exit the metal surface by electro migration. This was however disputed in the work of Han et al. [57] based on the buffering effect of CO_2 gas. Cementite films could induce corrosion since they are porous, conductive and act as large cathodes [61]. Solution chemistry also influences galvanic coupling as different stabilisation effect was recorded in water chemistry of different compositions [118, 145]. Localised corrosion could as well manifest due to lateral galvanic coupling [118]. Cementite when formed beneath FeCO_3 acts as an anchor for the latter [10, 25] as shown in Figure 3.21.

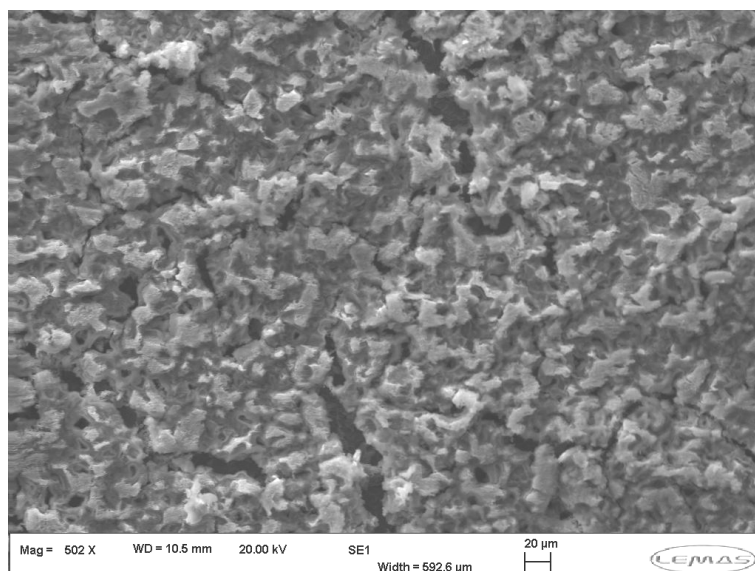


Figure 3.20: SEM Image of Fe_3C deposits

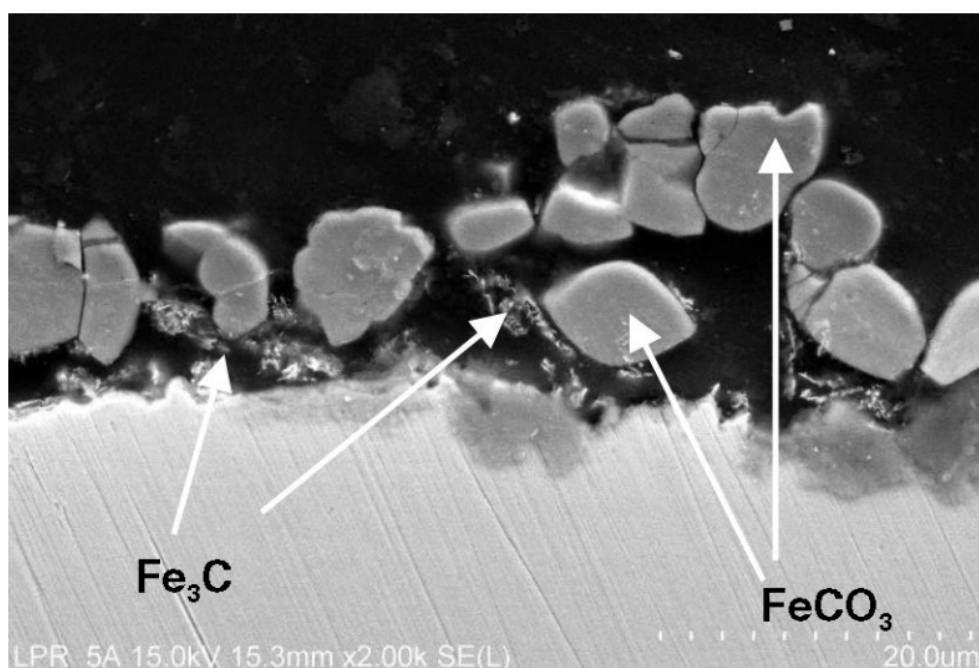


Figure 3.21: Image of Fe_3C anchoring FeCO_3 deposits [139]

3.7.5 Mixed $\text{Ca}_x\text{Fe}_{(1-x)}\text{CO}_3$ Films

Corrosion products formed in oil and gas environments often exist in the form of mixed carbonates due to the presence of metallic cations such as Ca^{2+} . Esmaeely et al. [146] conducted experimental investigations to understand how calcium influences protectiveness of FeCO_3 layers and concluded that mixed carbonate $\text{Fe}_x\text{Ca}_y\text{CO}_3(x + y = 1)$, forms in calcium-containing solutions and that calcium

influences corrosion rate in low carbon steel. Calcium scales also exist as a polymorph of CaCO_3 (such as calcite, aragonite and vaterite) in oil field environments [147, 148, 149, 150, 151, 152, 153, 154]. There is however no cited experimental work or theoretical model that has considered how the different CaCO_3 polymorph influences general or pitting corrosion in low carbon steel.

3.7.6 Calcium carbonate and localised corrosion

Steel tanks made of low carbon steel are vital components used to store crude oil in the petrochemical industry but recurrence of tank failures [155] calls for the need to understand events in environment similar to oil & gas storage tanks. Corrosion at tank floor which is more severe than tank wall, is difficult to inspect or remedy [156]. Corrosion of oil tanks is generally not due to organic compounds in crude oil but is often caused by water-brine constituents that settle at the base of the tank [157] with Ca^{2+} being among other metallic ions in crude sediments [158, 159, 160]. The corrosive effect of Ca^{2+} has also been reported in flow transport and saline aquifers [146]. Although operating conditions may produce CaCO_3 layers that cover steel surface, localised corrosion can still occur beneath the formed film [157] with catastrophic consequences. Sander et al. [161] reported that the Ca^{2+} ion level in water determines the corrosion rate in low carbonate concentrations while Tavares et al. [162] observed that calcium ingress alters morphology of FeCO_3 films formed on carbon steel thereby lowering film protection. This is in agreement with the work by Jiang et al. [163] who investigated how calcium ions affect pitting and observed that calcium increases pit initiation in both flowing and static conditions. Navabzadeh et al. [146] also studied how calcium influences FeCO_3 protectiveness and observed that corrosion rate increased with the addition of calcium. In a similar study, the work by Ding et al. [164] on the influence of Ca^{2+} on X65 carbon steel corrosion reported that corrosion rate could be enhanced when Ca^{2+} concentration is increased by 256 ppm to 512 ppm due to growth in crystal size and loose scale

structure.

3.8 Parameters governing pitting corrosion

The important factors governing pitting corrosion of carbon steel are cathode to anode area ratio, film formation, CO_2 partial pressure, pH, flow velocity, salt concentration and grey zone conditions [57, 63, 165]. Grey zone is a term used to define the electrochemistry condition when solution tends towards the precipitation of FeCO_3 . This is typical of FeCO_3 saturation in the range of 0.8 to 4 [57]. Other parameters affecting pitting corrosion include temperature, electrolyte composition, metal surface state and metal microstructure [30, 39, 166].

3.8.1 Area ratio of anode to cathode

Cathode to anode area ratio creates galvanic coupling for localised corrosion [44]. The rate of localised attack increases as cathode to anode area ratio increases [63, 135]. The OCP variation between the anode and relatively large cathode drives the localised attack [63, 103].

3.8.2 Salt concentration / Halides

Salt concentration also contributes to carbon steel corrosion in sweet environments. Salt concentration in most practical cases ranges between 1 to 3% weight ratio but higher concentrations to 20% are reported in literature [57]. Increase in salt concentration increases solubility of FeCO_3 thereby breaking down or hindering the formation of protective FeCO_3 films on the steel surface [57]. The grey zone widens with increasing salt concentration as shown in Figure 3.22.

Films are disrupted by halides depending on the halide concentration [94, 167] with

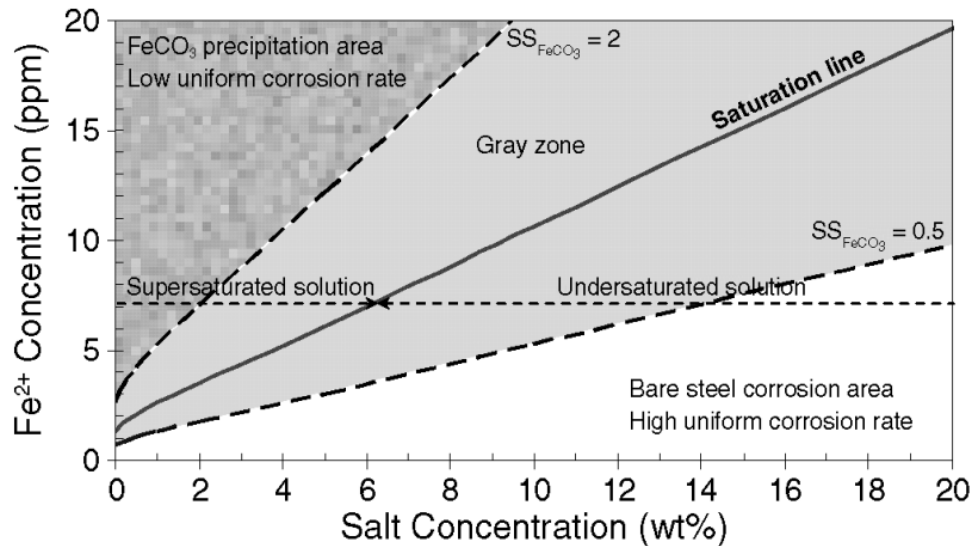


Figure 3.22: Effect of NaCl at grey zone condition (80°C, 0.53bar CO₂, and pH 6.0) [57]

chloride ion being the most aggressive pitting halide [167, 168, 169, 170] due to its small atomic diameter [127]. Pitting is retarded by chloride presence in low magnitudes up to about 10^{-4} m [171] but pitting is promoted at higher chloride concentrations [62, 171]. The chloride ions compete with carbonate films, adsorb on the film surface and become mobile anions to stabilise anodic reactions [94, 171]. The oxidation/reduction pair influences pitting process [94]. Jiang et al. [14] observed that Cl⁻ ions play no role in the corrosion rate of carbon steel once FeCO₃ is formed contrary to some literature but that chloride presence mildly influences pitting corrosion if film is broken. A review presented by Eliyan and Alfantazi [94] and work by Liu et al. [172] reported that an increase in chloride concentration increased the corrosion rate in sweet conditions to a level where further chloride concentration retarded CO₂ solubility and caused corrosion rate to decrease.

3.8.3 Acetic Acid (HAc)

Several constituents such as H₂O, CO₂, H₂S and organic acids form part of hydrocarbons in the field. Acetic acid (CH₃OOH), commonly referred as HAc, tops the list of volatile organic acids found in hydrocarbons while research also

identifies HAc as a major factor in localised corrosion occurrence in petroleum pipeline [11]. The effect of HAc is particularly pronounced at low pH [8]. Such organic acid alters electrolyte chemistry, FeCO_3 build up and film stability [24]. The anodic polarisation branch shifts towards the positive direction when acetic acid concentration is increased (anodic branch is inhibited) [52]. Studies conducted on the role of acetic acid on pit propagation of carbon steel in sweet environment indicated an increase in corrosion potential with increase in HAc concentration [52] while HAc depletion triggered pit growth but pits never grew in absence of HAc. Spherical pits manifested until certain pit radius when the pit begins to widen [11]. Acetic acid also caused pit growth in carbon steel subjected to sweet environment at room temperature [173]. The pit depth increased with increase in HAc concentration [11, 173]. It is difficult to distinguish reduction process of HAc from reduction of H^+ ion since acetic acid dissolution occurs very fast [24, 62]. It is therefore not yet certain if HAc is also reduced or only provides extra H^+ in sweet systems [24]. Carbonic acid (H_2CO_3) would however always be the main cathodic reactant in solutions of dissolved CO_2 and HAc since H_2CO_3 has greater reaction rate than HAc [24].

3.8.4 Temperature

Temperature generally accelerates corrosion at lower pH where films are absent. At high pH where film forms, temperature rise promotes film dissolution leading to increase in corrosion [49]. Pitting likelihood in carbon steel increases with temperature rise [127] while high pitting occurs within 75°C to 110°C [62, 171].

3.8.5 pH and flow velocity

The pH range often observed in oil and gas environment is from pH4 to pH6 [117]. Literature suggest that pitting is only feasible at pH range of 5.7 to 6.4 and that

pitting is unlikely at values less than pH5 [51, 57]. Pessu et al. [127] reported that FeCO_3 films form faster at high pH but pitting still progresses beneath the formed film. Galvanic effect that drives localised corrosion vanishes, causing pits to heal as pH increases beyond 6.6 [57, 94]. Steel generally tends towards passivity as pH increases due to slower H^+ ion reduction (cathodic) process [127]. At pH 10, pitting potential was reported to be independent of temperature [174, 175]. Increase in flow readily transport species such as H^+ ions to the metal surface for cathodic reactions thereby accelerating corrosion. This is more at low pH and low P_{CO_2} . At high P_{CO_2} , effect of flow is insignificant on corrosion rate due to high H^+ presence in the solution. Flow could as well cause partial dissolution particularly at conditions below FeCO_3 solubility limit, thereby paving way for localised attack [50].

3.9 Techniques for investigating pitting corrosion

Low carbon steel such as X65 is widely used as a pipeline material for oil and gas applications [176]. The limitation in carbon steel is in its corrosion resistance, which takes its toll on operations, economy as well as health and safety concerns. Most failures in the oil industry are not due to general corrosion but localised corrosion [177]. Pitting corrosion ranks among the highest level of corrosion defects while pitting in carbon-dioxide (CO_2) environment remains the most dangerous form of localised corrosion [178, 179]. Pitting is stochastic in nature, hard to predict [178] and can progress without being detected until catastrophe occurs. The danger of localised corrosion and how to effectively contain it is a growing challenge in the corrosion field [178, 180, 45]. Stochastic pits can be grown by conducting some long term corrosion tests in the laboratory. However, it is desirable to generate pits within a reasonable time frame for corrosion studies. Some pitting studies have been conducted using artificial pits [181] or by generating pits using mechanical indentation [182, 183] before conducting healing or pit propagation assessments. Other studies such as that by Fang et al. [184] used a needle to remove scales to

create pits. Pitting can also be created using indentation apparatus. Miresmaeili et al. [185] study on X65 steel weld hardness suggested that hardening could halt failure amidst hydrogen presence. Indented pits are however prone to minute cracks arising from deformation/and or residual stress from an indenter's penetration (Figure 3.23). Such crack tips or local stress state, particularly along grain boundaries could pave the way for hydrogen embrittlement [186, 187, 188].

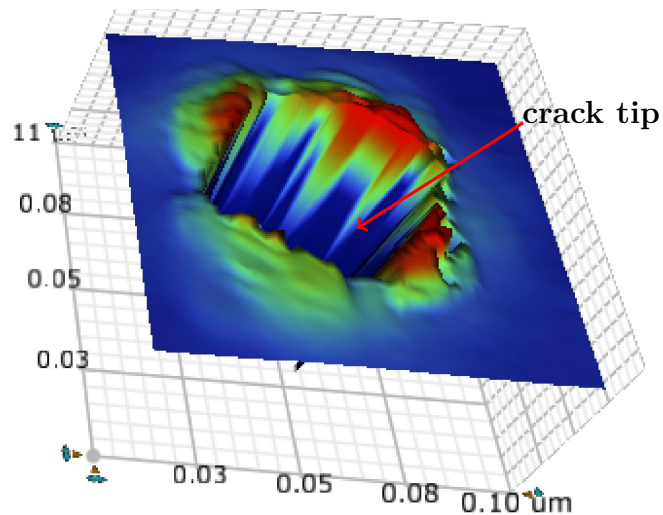


Figure 3.23: 3D morphology of a mechanical indented pit on X65 carbon steel featuring crack tips

A potentiostatic approach was utilised by Tian et al. [189] to investigate potential influence on stainless steel pitting in an oxygenated environment based on single pit examination and observed that pit depth increased with time and potential threshold. Tian's potentiostatic experiment was based on a single pit study which does not truly reflect the random properties of pitting in stainless steel. Corrosion in stainless steel could self-heal in certain instances but this is uncertain for low carbon steel which is more prone to corrosion but remains of high demand in oil and gas industry. There is yet no literature that presents a technique to generate reproducible stress free pits of predictable depths on low carbon steel for pit propagation/healing investigations. More so, not much is known about pitting/general corrosion relationships in low carbon steel.

3.10 Simulating pitting corrosion in the laboratory for corrosion test

Pitting process is stochastic and hard to predict [190]. Several models and experiments were conducted to study pitting corrosion. Electrochemical techniques are used to investigate pitting on metals [190]. Fang et al.[123] disrupted films on passivated X-52 carbon steel to investigate pitting corrosion and revealed that pit growth varies with corrosion environment. Fang et al.[123] work also created pits by using needles to break films, an approach likely difficult to re-enact. Pitting could be induced on metal by potentiostatic methods conducted in the work of Tian et al. [168] where steel was subjected to anodic polarisation to drive pits. Artificial pit techniques could also be used to study pitting. Several pitting experiments have been conducted using artificial pits by Newman [191], Turnbull [165], Palmer [55], Han et al.[63] and Amri et al. [52] pit model amongst others.

3.10.1 Newman artificial pit

Part of the early literature on artificial pits was by Newman [191] who studied passivation kinetics in corrosion resistant alloys using an artificial pit featured in Figure 3.24. The model entailed drilling through sample to create pit profile making it difficult to conduct repeated tests using the same rig for different pitting conditions.

3.10.2 Turnbull's pencil pit

Zhou and Turnbull [192] evolved a two compartment cell arrangement to study stress corrosion cracking in pre-pitted Ni-Cr-Mo-V steel. Turnbull et al. [193] utilised a similar method to evaluate an inhibitor's ability to retard localised corrosion. The design entailed separation of the anode and cathode compartment but electrically

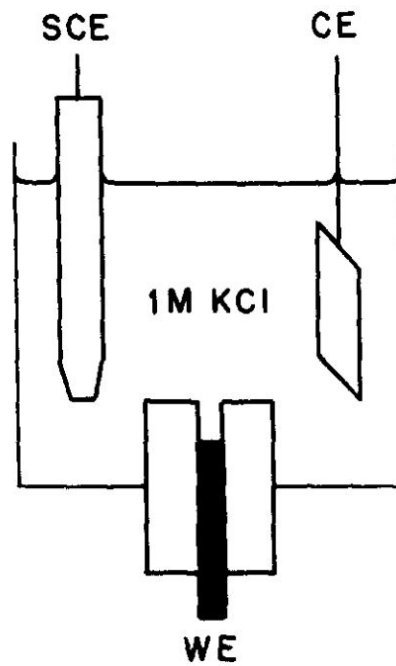


Figure 3.24: Schematics of Newman's artificial pit cell [191]

coupled with ZRA and agar salt bridge as depicted in Figure 3.25. Turnbull et al. [165] further utilised the two-compartment artificial pit in another work (Figure 3.26) to study the effectiveness of inhibitor in preventing localised corrosion. The cell housing the pit was set-up using a rotating electrode to increase cathodic current density in a diffusion-controlled cathodic reaction [165]. Physical separation of the anode and cathode in this model however, does not reflect the scenario expected in in localised corrosion concept.

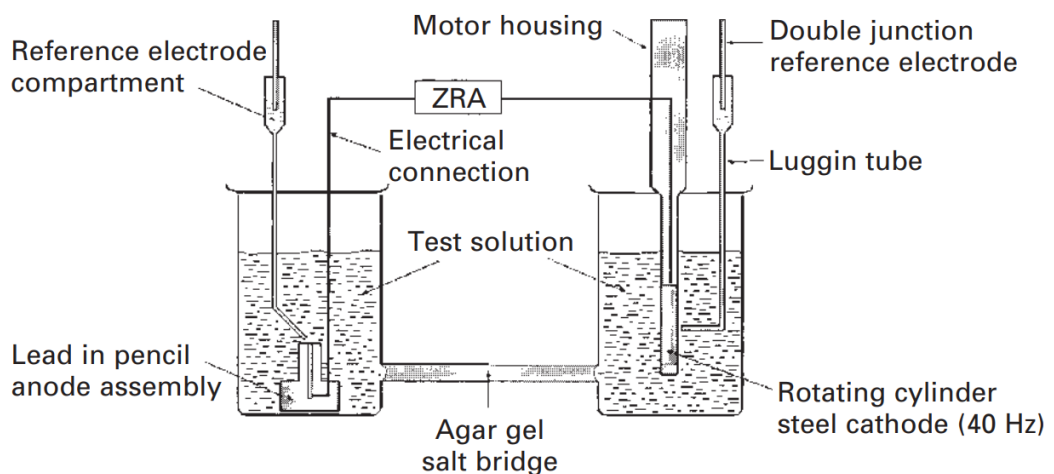


Figure 3.25: Diagram of two compartment cell with pencil pit assembly [193]

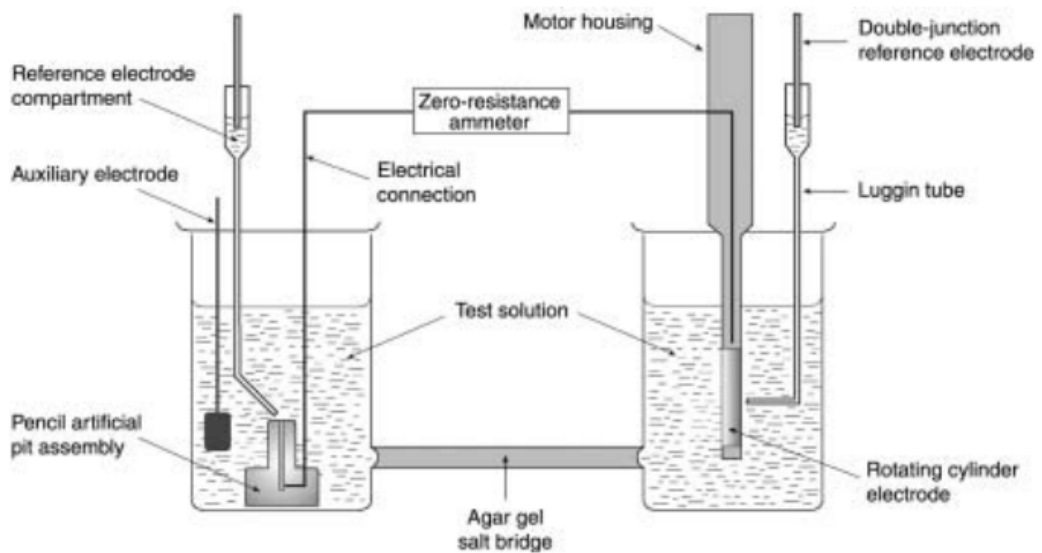


Figure 3.26: Schematic representation of Turnbull's 2-compartment pit cell [165]

3.10.3 Palmer's artificial pit

An artificial pit assembly was developed by Palmer et al. [55] to assess inhibitor performance in retarding localised corrosion. The design utilised a ZRA to measure the current between two electrodes of the same material but different surface areas. A schematic representation of the Palmer et al. [55] artificial pit is shown in Figure 3.27. The electrodes were periodically decoupled to conduct polarisation and depolarisation tests. Total corrosion rate in the pit was estimated by adding implied coupled current to the measured uncoupled current. The Palmer artificial pit however has no provision for flexibility in pit depth profile.

3.10.4 Han's artificial pit

Han et al. [56] developed an artificial pit to investigate localised corrosion of mild steel in a sweet environment. The design features insulated coupling of 0.018cm^2 cylindrical anode in 16cm^2 cylindrical cathode as depicted in Figure 3.28. Han's pit is suitable for corrosion pit test as anode and cathode units are encased in close proximity. The work indicated that artificial pits can be active or passive under certain film conditions as depicted in Figure 3.29 [57]. The result further revealed

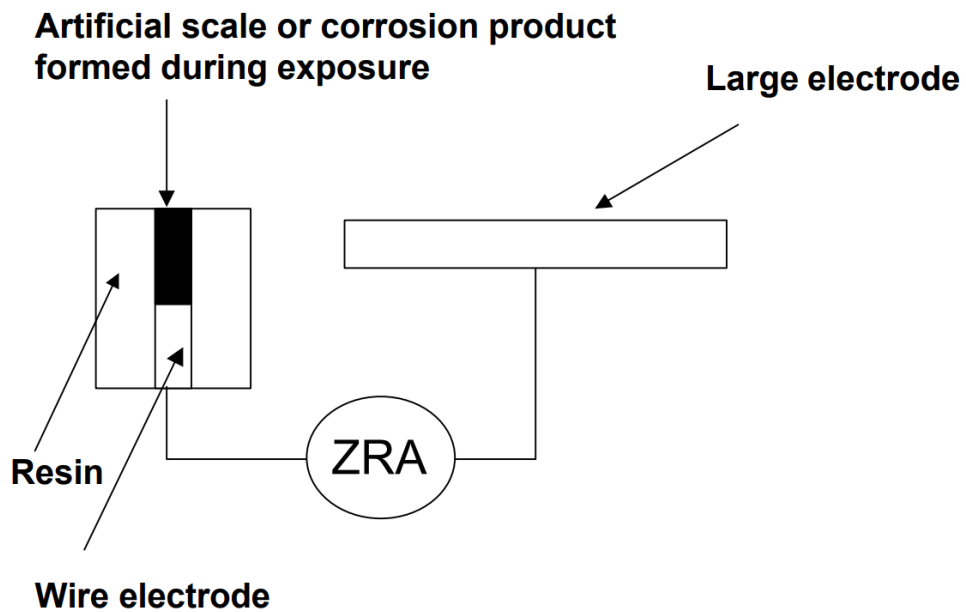
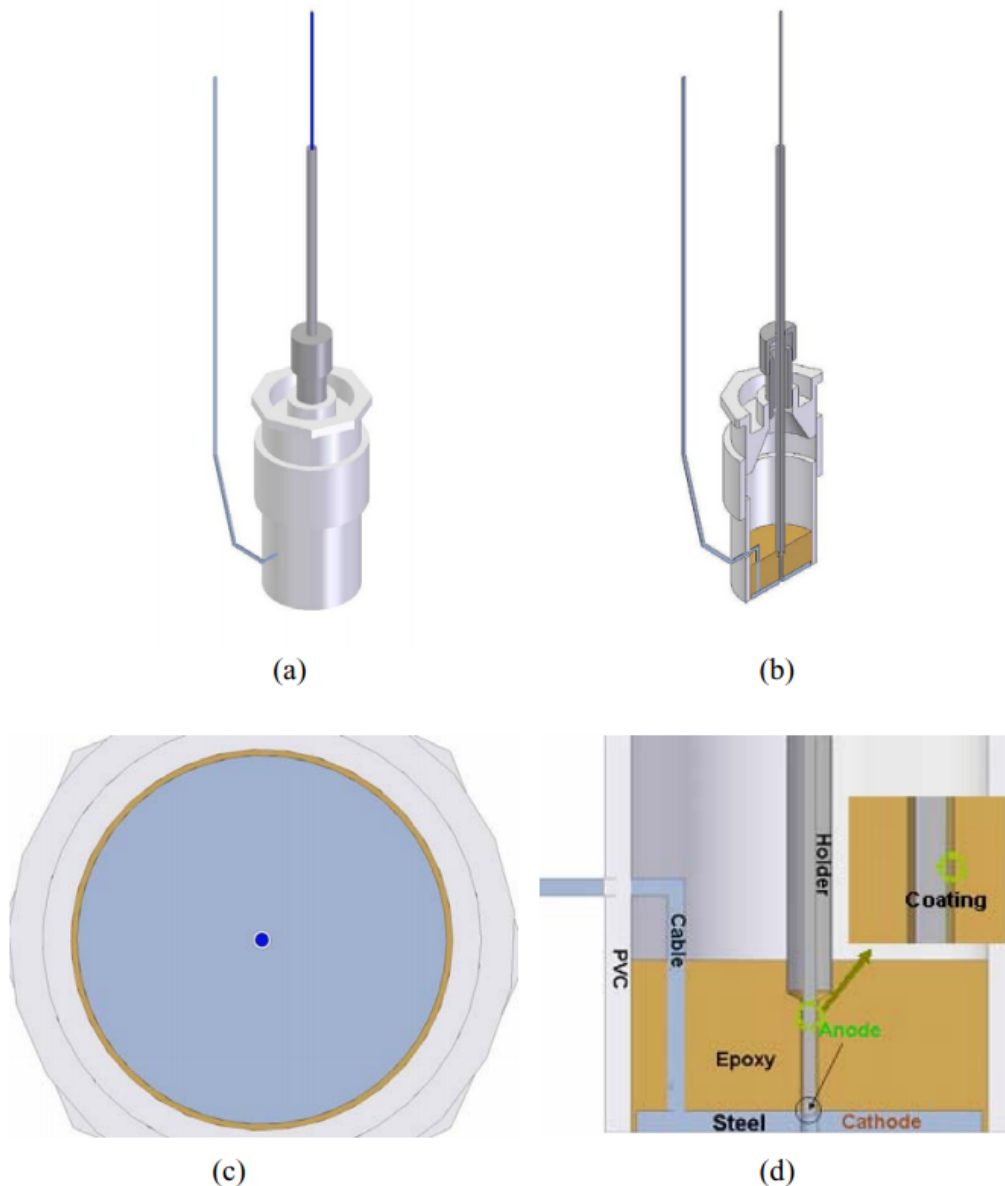


Figure 3.27: Schematic representation of Palmer's artificial pit assembly [55]

that localised propagation forms in CO_2 environment only at FeCO_3 supersaturation range of 0.5 to 2. This is typical of Figure 3.29 (c) [57] when neither significant precipitation nor dissolution of FeCO_3 is expected [56, 57]. The galvanic current was measured using ZRA while the coupling was decoupled occasionally for about 1 minute for LPR test. The work suggested that localised corrosion is propagated when FeCO_3 supersaturation falls within the range of 0.5 to 2.0.

Han's artificial pit [57] was further employed to investigate the galvanic mechanism in propagation of localised CO_2 corrosion under varying parameters that generated results featured in Figure 3.30 [57]. A pit depth of 2mm and flush position was considered in Han's work. Iron carbonate films propagate actively in the so-called grey zone such as $\text{SS}_{\text{FeCO}_3}$ of about 0.5 to 2, 80°C and P_{CO_2} of about 0.5 to 2 bar. About 200ppm Iron (II) Chloride (FeCl_2) [56] was added to the solution at the start of experiment to enhance formation of FeCO_3 film which forms after about 48Hrs when Fe^{2+} concentration in the solution drops to about 1 to 2 ppm [57]. The coupon was polished to 600 grit and LPR conducted on one of the coupons at $\pm 5\text{mV}$ at scan rate of $0.25\text{mV}\text{S}^{-1}$. The film was deemed completed when corrosion rate approached 0.1mmpy . The work reported that pH, temperature, flow velocity, salt concentration



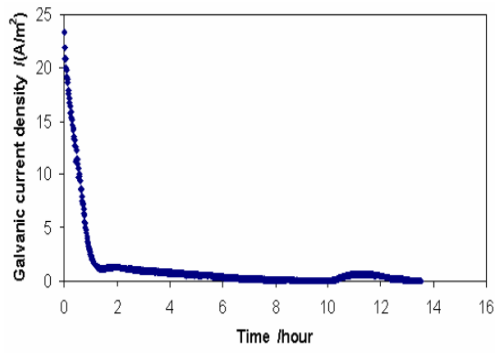
The artificial pit design (a), cutaway (b), enlarged bottom view of cathode (c), and detailed cross section view (d).

Figure 3.28: Han's artificial pit [56]

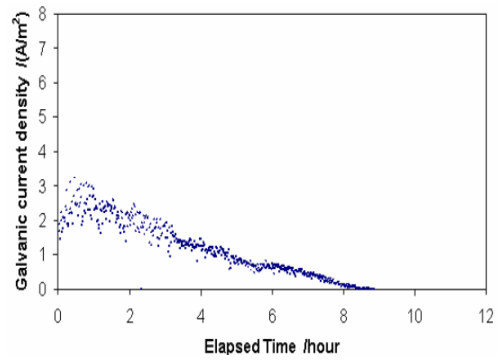
and CO_2 partial pressure are the key factors that promote localised corrosion in low carbon steel.

3.10.5 Amri et al. pit

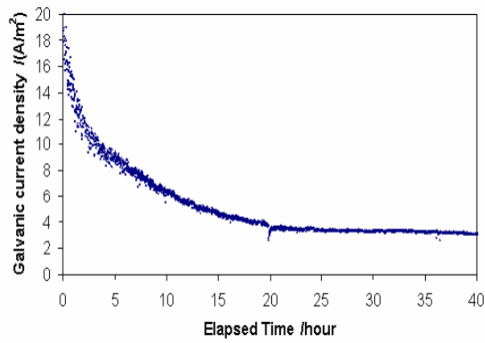
Amri et al. [52] also designed an artificial pit to study the effect of acetic acid on pitting and stifling of carbon steel in a CO_2 environment as featured in Figure



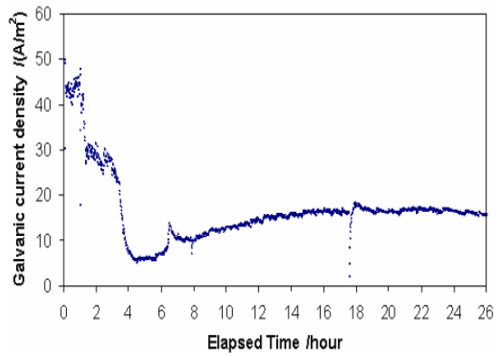
(a) Passive pit (FeCO_3 SS of 3-9)



(b) Passive pit (FeCO_3 SS of 0.2-0.5)



(c) Active pit (FeCO_3 SS of 0.4-4)



(d) Active pit (FeCO_3 , SS of 0.3-0.8)

Figure 3.29: Conditions favouring: (a) Passive Artificial Pit under high FeCO_3 SS of 3-9, 80°C , $0.53\text{bar } P_{\text{CO}_2}$, $\text{pH}5.5$ and $1\text{wt}\%$ NaCl (b) Passive Artificial Pit under low FeCO_3 SS of 0.2-0.5, 80°C , $0.53\text{bar } P_{\text{CO}_2}$, $\text{pH}5.8$ and $1\text{wt}\%$ NaCl (c) Active Artificial Pit under moderate FeCO_3 SS of 0.4-4, 80°C , $0.53\text{bar } P_{\text{CO}_2}$, $\text{pH}5.9$ and $1\text{wt}\%$ NaCl (d) Active Artificial Pit under low FeCO_3 , SS of 0.3-0.8, 80°C , $0.53\text{bar } P_{\text{CO}_2}$, $\text{pH}6.0$ and $10\text{wt}\%$ NaCl [56]

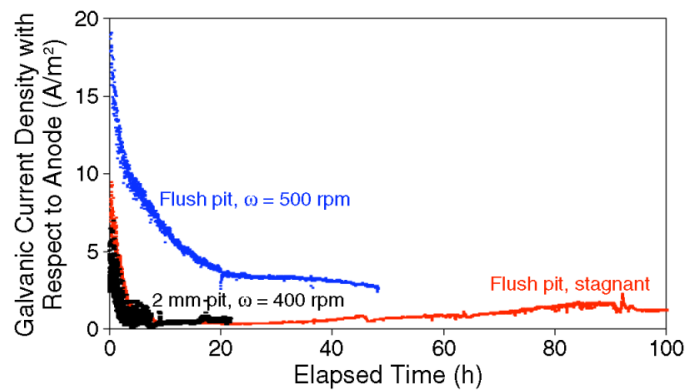


Figure 3.30: Current density recorded from coupled Anode/Cathode pit area ratio 1:1000, $\text{pH}5.85$, $\text{SS}_{\text{FeCO}_3}$ of 0.2-4 at 80°C and $1\text{wt}\%$ NaCl [57]

3.31. Amri's pit is unique for its ease in design and anode/cathode being in close proximity.

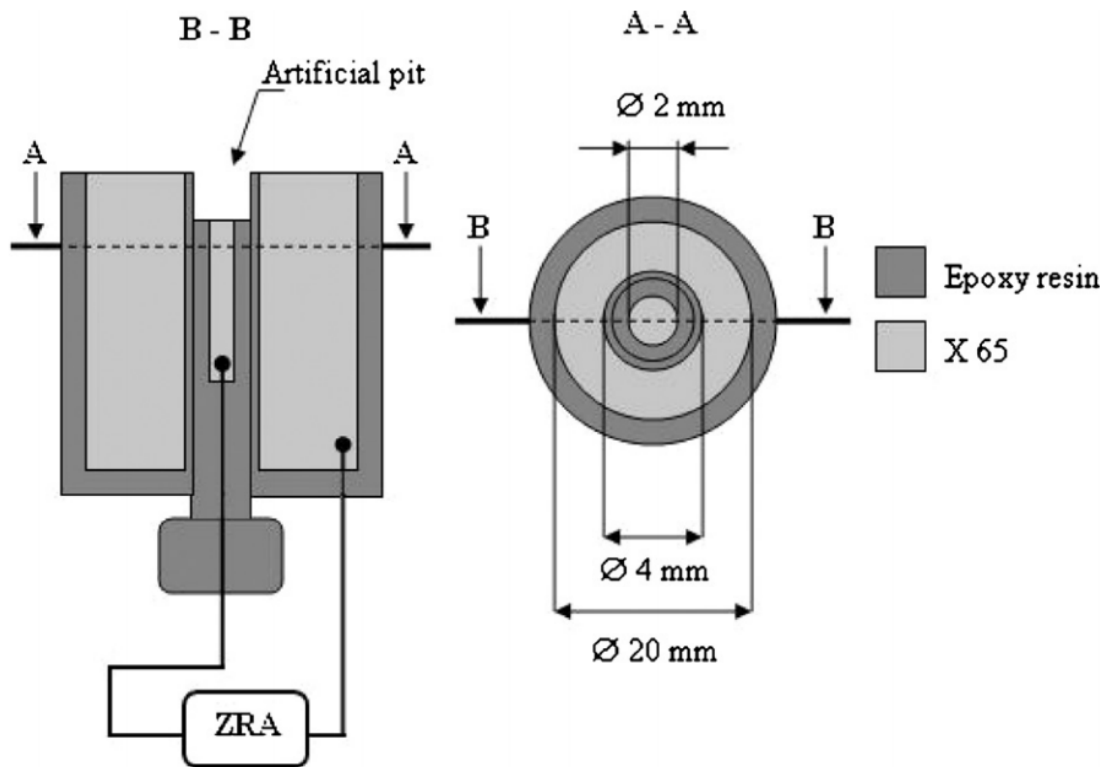


Figure 3.31: Amri et al. Artificial Pit[52]

Other pit models developed include Schmitt's model used to study flow induced localised corrosion (FILC) and Achour's model used for galvanic studies [63]. All the models described above were designed to fulfil experimental requirement for pitting investigations. Separation of anodic compartment from cathodic enables variation of parameters in the separate compartments as featured in Turnbull's model but Ohmic drop registered during measurement is a setback to this approach. For pitting investigation, it is desirable for the anode and cathode to be isolated but as close as possible in the same solution. Amri et al. [52] and Han et al. [56] models could be modified to suit pitting corrosion investigations due to close proximity of electrodes and ease of incorporating both electrodes within the same cell. Localised corrosion propagates when galvanic coupling exists between large film-covered cathode and tiny film free anode, a scenario suited by the artificial pit.

3.11 Application of artificial pits for pitting studies

Pitting corrosion is generally believed to evolve from localised disruption of films formed on metal. Disruption of passivated film is also a common cause of mesa attack recorded in the oil & gas environment [194]. The compromised site known as the anode possesses lower potential than the surrounding cathode with higher positive potential. Temperature drop in gas transport lines causes condensation in internal walls of pipes with consequence of top-of-line corrosion if dissolved CO_2 is present, as dissolved CO_2 creates acidic condensates typically in ranges of $\text{pH} < 4$ [178]. The stability of protective FeCO_3 films formed at high pH make it applicable in managing corrosive effect in top-of-line condensation. Such cost effective practice of retarding corrosion by forming protective FeCO_3 on steel surface is termed **pH stabilisation** [195]. High pH regime is also common in crude [196] storage and saline aquifers [197, 198] just as bacterial ureolysis could also cause rapid rise in pH level in saline aquifers [199]. High pH in a sweet (CO_2) medium decreases solubility (promotes precipitation/scaling) of FeCO_3 [178]. Corrosion products formed on carbon steel can retard the corrosion rate by disrupting anodic dissolution and forming a mass transfer barrier which blocks interaction of cathodic species on the metal surface [200]. Corrosion at high pH ($\text{pH} > 7$) yields a protective film characterised by a rise in open circuit potential and sharp drop in corrosion rate; a phenomenon termed as **pseudo-passivation** [200]. A typical pseudopassive trend is shown as Figure 3.32, where recorded potential spontaneously increased from -0.70V to -0.62mV . Low carbon steel corroded in saturated CO_2 solution beyond 48 h at high pH becomes pseudo-passivated recording potential increase up to about 400 mV compared to a freshly polished surface [200]. No clear explanation is available to date on pseudo-passivation. Many works however believe that formation of magnetite (Fe_3O_4) beneath FeCO_3 layers causes the pseudo-passive effect [201, 200]. Singer [202] is of the view that high pH of electrolyte trapped between steel substrate and

formed film influence formation of Fe_3O_4 [202]. Despite film protectiveness, pitting corrosion was observed to occur on passive surfaces as revealed by Pessu et al. [203] who investigated the influence of pH on localized corrosion behaviour of X65 carbon steel in CO_2 -saturated brines. Artificial pits can be employed to unravel event(s) that occur within an actively corroding pit. The artificial pit mimics actual pitting profile that could be controlled and as well designed to allow collection of data that suggests events within the pit. The artificial pit cathode can be passivated under high pH condition to create pseudopassive covering after which a freshly polished anode was inserted and the resulting galvanic trend was measured.

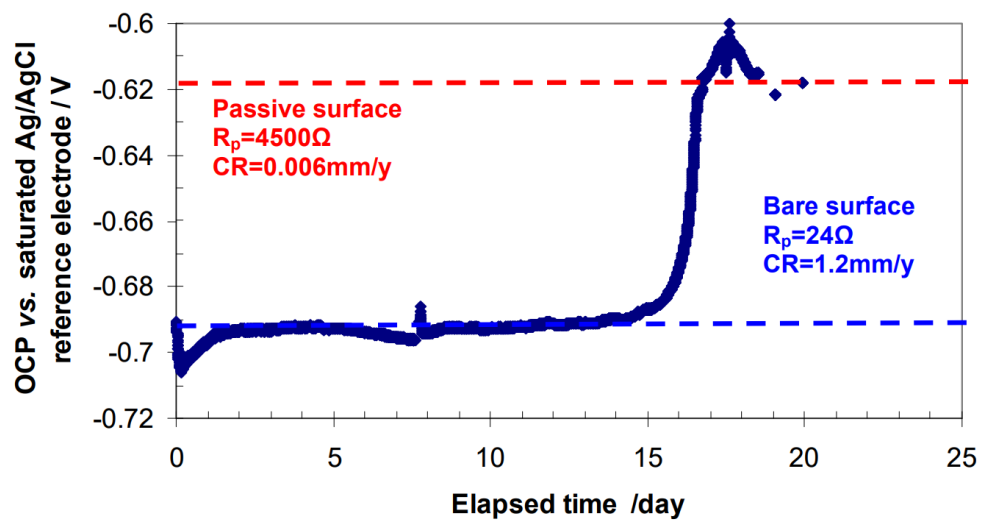


Figure 3.32: Pseudopassivation recorded at pH 6.6, 80 °C, 1 wt.% NaCl [63]

3.12 General and pitting corrosion

For active steel, significant general corrosion occurs as pitting progresses unlike in stainless steel [127]. Pitting is a form of induced corrosion at localised site in which metal beneath the local site maintains contact with the electrolyte [170]. Carbon steels in NaHCO_3 solutions are usually passive at approximately $0.65V_{\text{SCE}}$ and undergo pitting at potential of $0.50V_{\text{SCE}}$ and beyond [60]. Pitting is known to occur due to break down of passive films [170]. Meta stable pitting (pit breakdown and repair) is believed to occur at potentials below the pitting value [204].

The general corrosion that progresses around a pitting site contributes to the overall pitting process [127]. General corrosion implies uniformity in distribution of anodic and cathodic sites while stability of local anode within bulk cathode defines pitting survival [59]. Papavinasam et al. [59] reported that uniform corrosion is dominant on steel in absence of corrosion products while Pessu et al. [127] suggested that pitting extent is related to formation rate of film in situation where corrosion film is non-protective. Pessu [127] also observed that for a surface under uniform and localised attack, pit growth appears to decline if general corrosion increase and that measured pit depth could be marred in such instance. Cui et al. [106] compared general and pitting corrosion in carbon steel using constant and moving anodes in unstirred medium, typical of storage units but this does not reflect conditions in petroleum transport systems. Few other literature that delved on both general and pitting corrosion of carbon steel did not clearly define the relationship between general and pitting corrosion. The onset of localised corrosion does not necessarily imply seizure of general corrosion on steel substrate.

3.13 Summary of literature review

Several aspects of literature were studied to gain an insight into pitting corrosion of X65 carbon steel in a sweet environment. The literature revealed efforts made in the past on pitting corrosion study in sweet conditions. Pitting investigations differ from experiment to experiment and amongst available model options. There is the need for a standardized technique for pit growth and assessment. Potentiostatic polarisation techniques offer promise for generation of stochastic pitting patterns on steel.

Some artificial pit experiments provide conditions for steady propagation of localised

corrosion, known as grey zone conditions. Such pits are active at SS_{FeCO_3} of about 0.5 to 2, $80^\circ C$ and P_{CO_2} of about 0.5 to 2 bar. About 200 ppm Iron (II) Chloride ($FeCl_2$) is required at the start of experiment to enhance the formation of $FeCO_3$ film which forms after about 48Hrs after which the Fe^{2+} concentration in the solution drops to about 1 to 2 ppm. The influence of anode to cathode area ratio, protective film and a few other parameters on pitting progress has been extensively studied. Some aspects of the pitting mechanism however still cast doubts and require further study. Investigating a lower magnitude pitting (on film free surface) within a macro pit (artificial pit) could elucidate pitting initiation processes. More so, most artificial pit studies were based on $FeCO_3$ film environment whereas calcium and other impurities often present in oil & gas environment could interfere with pitting kinetics. Observed gaps are presented as questions which are intended to gain understanding on pitting corrosion.

3.14 Research questions and work approach

The research questions and the approach to the work contained in this thesis are featured in Table 3.3.

Table 3.3: Research question and work approach

Serial	Research Question	Approach in this thesis
1.	As a considerably long period of time is required to generate pits on steel naturally, there is the need to generate stochastic pitting for laboratory studies. The desired pitting pattern should be stress-free, producible in a practical time-frame and the average pit depths should be reproducible	X65 Carbon Steel to be subjected to 50mV, 100mV and 150mV potentiostatic. Interferometer to be utilised to establish repeatable trend in pitting (depths, volume, diameter etc.)

2.	Cations such as Ca^{2+} are present in the oil field and influence corrosion trends in low carbon steel. There is the need to understand how mixed carbonates ($\text{Ca}_x\text{Fe}_{(1-x)}\text{CO}_3$) influence pitting in low carbon steel	Corroded X65 carbon steel of known pitting depth (top-ten average) is to be subjected to calcium-containing solution under mixed carbonate conditions. SEM, EDX, XRD and profilometry check to be conducted on samples after the test to assess general corrosion and pitting trend.
3.	Calcium exists in several polymorphs such as calcite, aragonite and vaterite. How does the calcium polymorph influence general and pitting corrosion in low carbon steel?	Corroded X65 carbon steel of known pitting depth (top-ten average) is to be subjected to calcium-containing solution under calcite, aragonite and vaterite polymorph conditions. SEM, EDX, XRD and profilometry check to be conducted on samples after the test to assess general corrosion and pitting trend.
4.	Assuming galvanic current is responsible for pitting corrosion, how does calcium influence potential/galvanic trends and pitting in X65 carbon steel under mixed carbonate conditions?	Design artificial pit with cathode disc pre-passivated in mixed carbonate film. Insert freshly polished anode to measure mixed potential/galvanic magnitude. Conduct profilometry check to reveal events on pit anode after coupling test.
5.	Galvanic coupling between anode and cathode is attributed to driving pitting corrosion. What happens if the situation is reversed?	Explore the effect of applying external current (simulating galvanic current) to coupling of film-free cathode and anode in an artificial pit in 'grey zone' condition
6.	Do anodic and cathodic reactions occur at the same spot or are they separated during pitting process?	Design two models of artificial pit. Model 1 – Anode inserted through insulated cathode wall. Model 2 – Anode inserted through non-insulated cathode wall. Compare galvanic trend in both scenario

Chapter 4

Materials and Experimental Procedures

4.1 Materials

API X-65 (UNS K03014) grade carbon steel was used for this work. The composition of the steel is as contained in Table 4.1. The steel sample was polished in sequence up to 1200 grit using silicon carbide (SiC) paper and was further finished to $6\mu\text{m}$ using diamond paste for samples to be etched in Nital solution. The polished sample was etched in 5% Nital and characterised using the SEM. A micrograph of X65 carbon steel is shown as Figure 4.1. The micrograph of low carbon steel features pearlite (dark spots) in ca 15vol% and ferrite (bright portions) in about 85 vol%.

Table 4.1: Chemical composition (wt%) of X65 carbon steel

C	Si	Mn	P	S	Cr	Mo	Ni
0.12	0.18	1.27	0.008	0.002	0.11	0.17	0.07
Cu	Sn	Al	B	Nb	Ti	V	Fe
0.12	0.008	0.022	0.0005	0.054	0.001	0.057	Balance

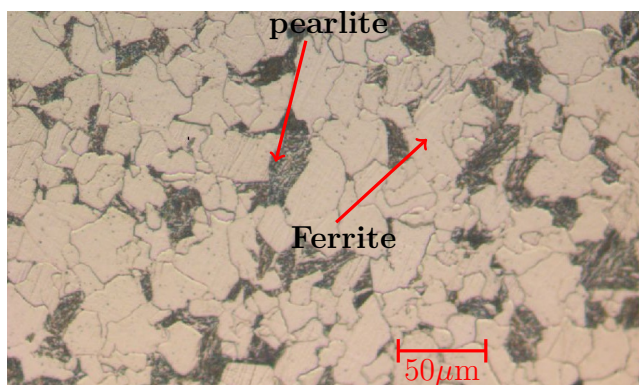


Figure 4.1: Micrograph of X65 carbon steel.

4.2 Sample preparation and procedure for potentiostatic polarisation tests

X65 carbon steel samples of 12mm diameter (surface area 1.131cm^2) were sectioned to 5mm thickness with the non-working surface soldered and masked in non-conductive epoxy. The test surface was wet abraded using silicon carbide (SiC) papers of 120, 320, 600, 800, 1,200 grit in sequence followed by degreasing in acetone and immediately air dried. The electrolyte was prepared in a glass vessel containing 1,000mL de-ionised water and 35g of sodium chloride (NaCl) to create a 3.5% NaCl solution. The solution was purged with CO_2 for over 6h at 30°C before the start of each experiment. The encased sample was then subjected to potentiostatic tests under conditions depicted in Table 4.2.

Table 4.2: Test matrix

Item	Description	Value
Metal specification	X65 carbon steel	
	Surface area	$2 \times 1.121\text{cm}^2$
	Test sample	2 per cell
Electrolyte condition	De-ionised water	1,000ml
	Salt concentration	3.5 wt% NaCl
	pH	pH 3.8 & pH 6
	Over potential	50mV, 100mV & 150mV
	Temperature	30°C & 75°C
	Duration	24h

The standard reference electrode used was Ag/AgCl in 3M KCl. The electrode was fitted with 2-way splitter connector for the reference and counter electrode connection. An Ivium multichannel potentiostat was used for the 3-electrode cell corrosion experiments. Temperature was maintained using a hot plate with magnetic stirrer set at 250rpm. A multichannel Ivium was used for electrochemical measurements. The first sample was polarised to 50mV vs OCP for 24 h and the process was repeated using a fresh sample. Other samples were subjected to 100mV and 150mV vs OCP for 24 h and also repeated. The 150mV potentiostatic tests were subsequently repeated covering durations of 24, 48 and 72 h. Repeatability of the potentiostatic experiment was validated by running repeated experiments in similar conditions using samples of different values of surface area. Similar electrochemical results were obtained under both conditions.

4.2.1 Post experiment analysis

Collected samples were immediately prepared for analysis or stored in a vacuum desiccated jar. Scanning Electron Microscopy (SEM) and X-Ray Diffraction (XRD) analyses were conducted on corroded surfaces to reveal information on products formed under experimental conditions. This was followed by detailed white light interferometry analysis. The samples for interferometry analysis were thoroughly cleaned in Clarke's solution and immediately rinsed in de-ionised water before analysis. The Clarke's solution comprised of 1000 mL Hydrochloric acid (HCl), 50g stannous chloride (SnCl_2) with 20g antimony trioxide (Sb_2O_3) in line with the American Standard of Test and Measurements (ASTM) practice standard G1-03 [205].

4.3 Test procedure for pit propagation tests

Pits were induced on X65 carbon steel using a methodology presented in an earlier publication [206]. The potentiostatic approach for generating repeatable pits was performed by applying 150mV potentiostatic polarisation on 2.242cm² samples in 1,000ml solution containing 3.5 wt% NaCl at 30 °C in saturated CO₂ for 24 h. Top-10 average of pits recorded after 150mV potentiostatic polarisation was applied on X65 carbon steel for 24 h was 70µm [206]. Corrosion products formed on pitted samples were immediately cleaned using pressurized de-ionized water and dried with air gun before immersing in test solution for electrochemical test. The experimental test matrix is presented in Table 5.5. The solution consisted of 1,000ml de-ionized water sparged with CO₂ until the pH drops to 3.8 after about 6 h. The solution pH was later adjusted using NaHCO₃ or dilute HCl. The working electrode (WE) was coupled using a three-electrode cell comprising a Ag/AgCl reference electrode (RE) with a platinum counter (auxiliary) electrode (CE) in a glass beaker. Linear Polarisation Resistance (LPR) and Open Circuit Potential (OCP) measurements were made using an Ivium potentiostat. The LPR scan was done from ±15mV vs OCP with scan rate of 0.25mV/s. The Stern-Geary constants (B), presented in Table 7.2 were derived from Tafel plots (Figure C.1) and later used to calculate the corrosion rates.

Table 4.3: Test matrix

Item	Description	Value
Metal specification	X65 carbon steel	UNS K03014
	Surface area	2.242 cm ²
Electrolyte condition	De-ionised water	1,000 ml
	Ca ²⁺ concentration	0 & 5,000 ppm Ca ²⁺
	Fe ²⁺ concentration	8.5ppm Fe ²⁺
	Brine conc	2 wt% NaCl
	pH	pH 3.8 & pH 6
	Temperature	80 °C
	Flow speed	100 rpm
	Duration	up to 96 h

Pitting and general corrosion could occur together depending on the operating

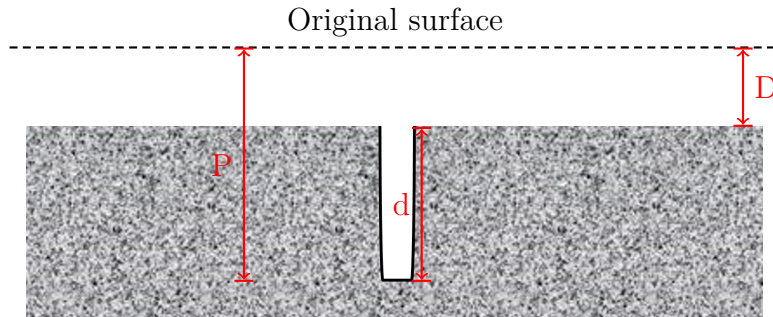
Table 4.4: Matrix of Tafel constants obtained under experimental conditions

pH	Temp (°C)	β_a (mV/decade)	β_c (mV/decade)	B(mV/decade)	I_{corr} (mA/cm ²)
*pH 3.8	80 °C	65	145	19	0.270
**pH 3.8	80 °C	85	205	26	0.380
*pH 6	80 °C	70	40	11	0.042
**pH 6	80 °C	75	75	16	0.060

* 0 ppm Ca²⁺

** 5,000 ppm Ca²⁺

environment. The pitting extent can be quantified in terms of a pitting factor (P_f). A schematic showing parameters used for calculating P_f is shown in Figure 4.2. P_f is defined as ratio of deepest pit to general metal thinning. This is expressed mathematically as depicted in Equation 4.1 [207]. Pitting factor of unit magnitude implies general (uniform) corrosion while pitting is said to occur when $P_f > 1$. Higher pitting factor indicates more pitting [207]. Average metal penetration (D) in this work was calculated using LPR measurements taken during corrosion tests since pitting contribution was significantly lower than general corrosion as reported in Section 6.4.2. Surface profilometry was conducted to determine top-ten pits, which were averaged to obtain the pit depth relative to corroded surface, d .



P = Deepest metal penetration (valley)

D = the average metal penetration

d = pit depth relative to corroded surface

Figure 4.2: Schematic representation depicting parameters for calculating pitting factor

$$Pitting\ factor(P_f) = \frac{P}{D} = \frac{D + d}{D} \quad (4.1)$$

4.3.1 Post experiment analysis

Corroded samples were rinsed mildly with de-ionized water and dried using a hot air gun. X-ray diffraction (XRD), scanning electron microscopy (SEM) and Raman analysis were conducted to examine corrosion products formed on steel samples. Samples were later cleaned of corrosion product using Clarke's solution as prescribed in ASTM G1-03 [205] before conducting robust interferometry analysis to profile pits formed on sample surface. Profilometry was by the use of a white light interferometer to scan the entire sample surface beginning from the sample centre in anti-clockwise direction in bits of $1118 \mu\text{m} \times 637 \mu\text{m}$, taking a total of 172 measurements per sample. Scans were thereafter stitched with 25% overlap using automated inbuilt features of the profilometer [206]. Pit depth measurement utilised in this work was based on averaging of top-10 pits for two set of experiments since deepest pits are likely to rupture first amongst other pits.

4.4 Artificial pit and test procedure for artificial pit experiments

The crux of this research is to improve knowledge on the understanding of the pitting process in API-X65 carbon steel. Electrochemistry conditions tend to vary from the pit mouth to the deepest point of the pit and this could influence pitting kinetics on metals. An improved artificial pit was designed to understand how corrosion products influence pitting in an actively corroding pit.

4.4.1 Artificial pit design

Section 3.10 covered range of artificial pit in use. Separation of the anodic compartment from the cathodic enabled parameters to be varied in separate

compartments as featured in Turnbull's model but Ohmic drop registered during measurement was a setback to this approach. For pitting investigations, it is desirable for the anode and cathode to be isolated but as close as possible in the same solution. Localised corrosion propagates when galvanic coupling exists between large protected cathode in close proximity with tiny film - free anode. The Amri and Han models are suitable for investigating pitting corrosion due to close proximity of electrodes and ease of incorporating both electrodes within the same cell. An improved artificial pit was designed in this work to mimic events in a corrosion pit. The anode pin and cathode disc are two important components of the artificial pit model featured in Figure 4.3.

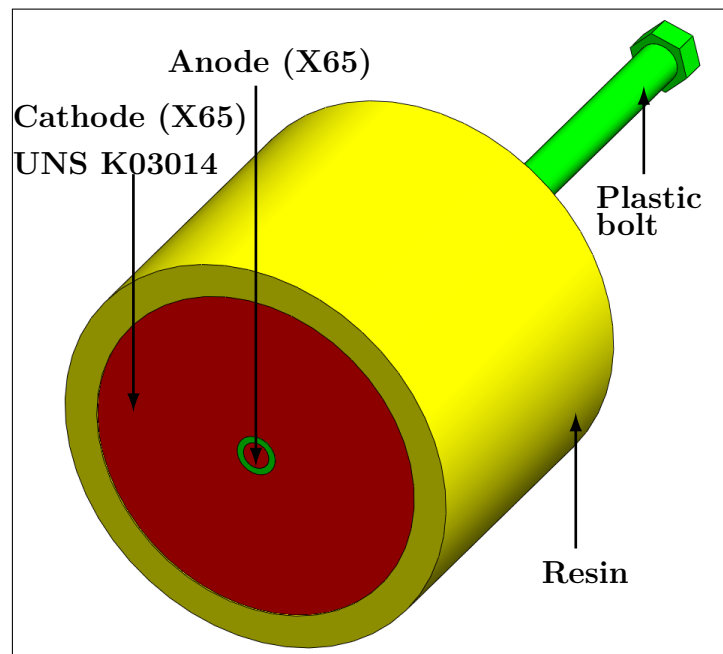


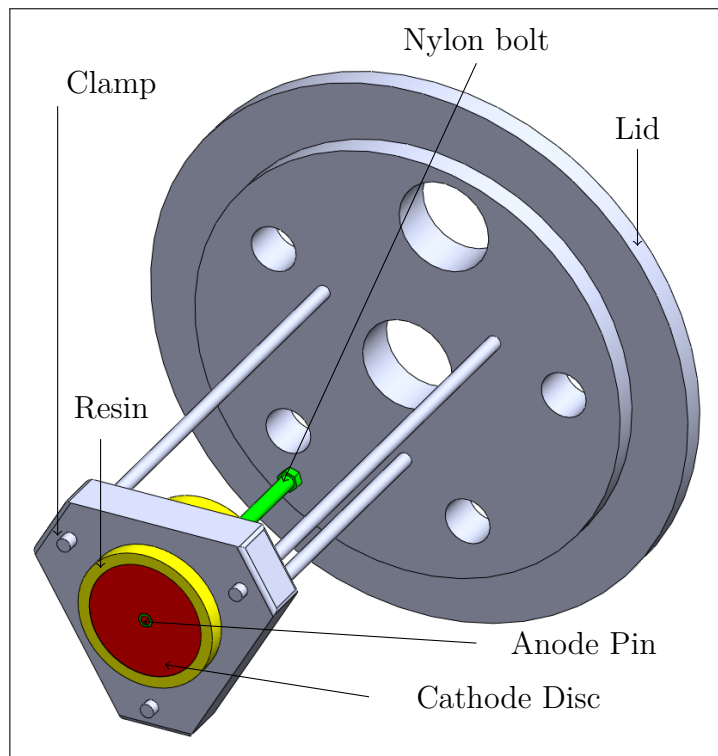
Figure 4.3: Artificial pit showing materials components of artificial pit

The artificial pit designed for this work was inspired by Amri's model [52] while adopted methodology was pioneered by Han et al. [208] work on localised corrosion propagation in CO₂ systems. The pit design features variable anode pins (1mm, 2mm and 3mm diameter) enclosed in a nylon bolt where thread pitch was used to control anode displacement (pit depth). Complete turn of the nylon bolt displaces the anode by 1.25mm. The design was aimed at mimicking localised corrosion environment with the aid of laboratory apparatus. The anode and cathode of the

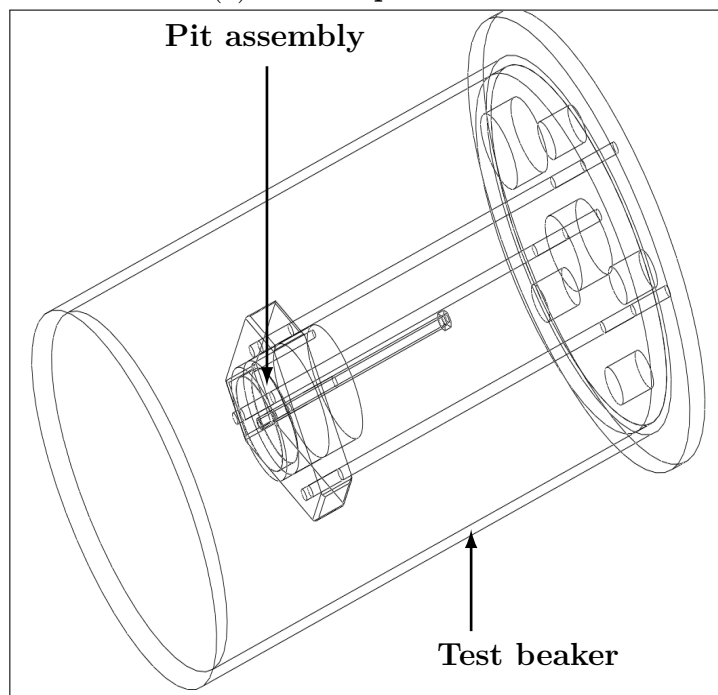
artificial pit shown in Figure 4.4(a) were made of X65 (UNS K03014) carbon steel. The cathode was machined from a cylindrical bar to disc shape of 4.9cm² (diameter of 25mm with thickness of 5mm) and masked in a heat resistant resin. A 9mm hole was drilled all through the centre of the cathode and filled with resin. The anode pin was machined in sets of 1mm, 2mm and 3mm diameter. A 4.2mm centre hole was drilled all through the length of a nylon bolt to accommodate the anode pin and connection cable. The anode pin with its cable was further insulated in resin sheath inside the nylon bolt. The artificial pit assembly was immersed in electrolyte contained in 1,000ml glass beaker featured in Figure 4.4(b). Solidworks drawing and image of the artificial pit is featured as Figure 4.5.

4.4.2 Samples preparation and experimental approach

Cathode disc samples were wet polished using silicon carbide (SiC) abrasive grits in sequence of 120, 320 and 600 after which the surface was degreased using acetone before immersing in test solution. The electrolyte comprise of 1,000 ml de-ionised water containing NaCl as required with over 12 hours purging in CO₂ until oxygen level drops below 5 ppb. The solution pH and temperature was set in line with test matrix contained in Table 7.1. LPR and OCP measurements was conducted for up to 4 days to produce pseudo-passive films. Anode pin was then polished using SiC in grit sequence from 120 to 1,200 and then coupled to a passivated cathode. An ACM Gill AC potentiostat was utilised for measuring galvanic (mixed) potential/current density established after screwing a freshly polished anode (with relatively lower potential) onto the cathode (having higher potential). As a baseline, an initial test was conducted in a Ca²⁺ - free solution to compare with experiments conducted in a Ca²⁺ solution. Although calcium content in formation water can exceed 3,000 ppm [146] experiments in this work were conducted using 682 ppm Ca²⁺ for artificial pit investigations for ease in taking galvanic measurements. Preliminary tests were conducted using 3.3 wt.%, 3.1 wt.%NaCl separately in 682 ppm & 1364 ppm Ca²⁺

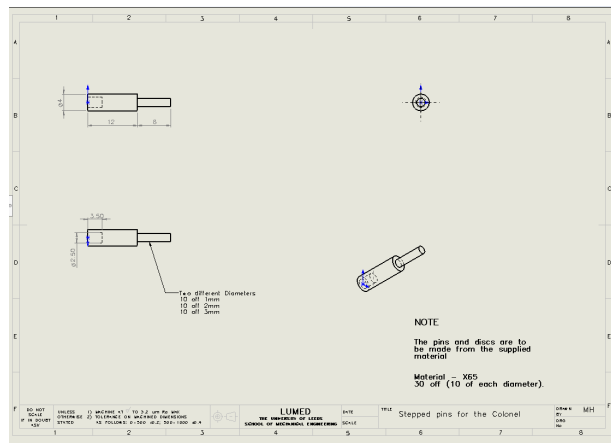


(a) Pit components

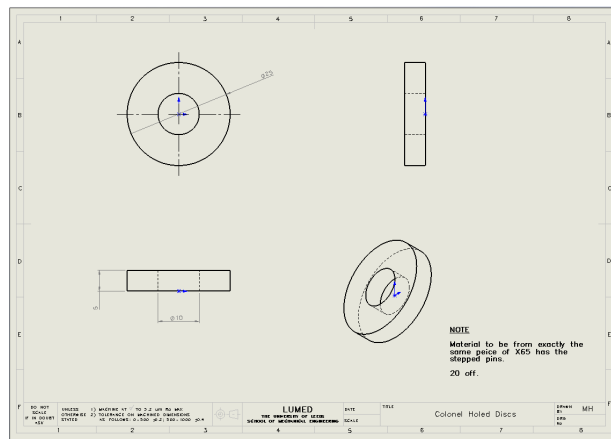


(b) Pit assembly in test beaker

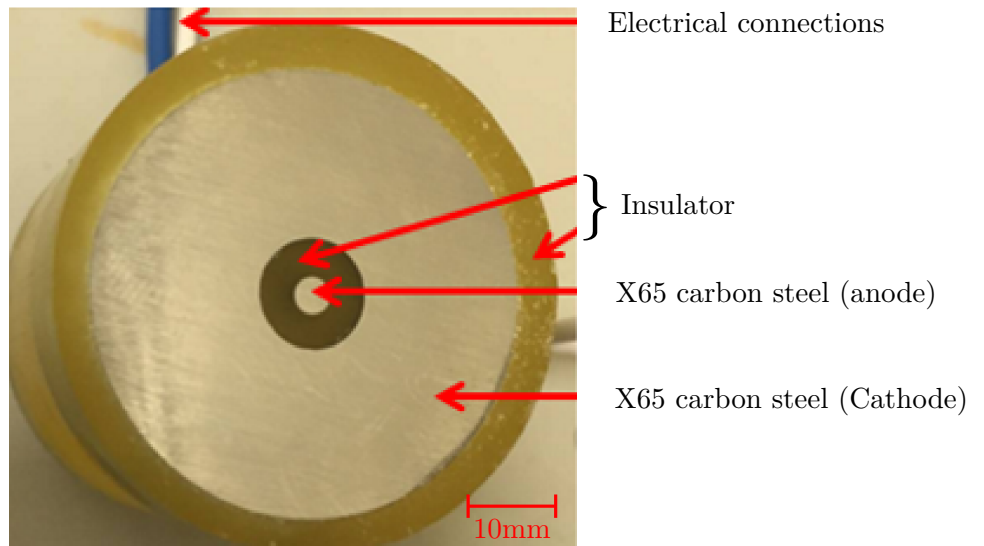
Figure 4.4: Artificial pit for pitting corrosion test featuring (a) pit components and (b) pit assembly in test beaker.



(a) Anode pin



(b) Cathode disc



(c) Coupled artificial pit

Figure 4.5: Artificial Pit design showing: (a) Solidworks drawing of anode pin (b) Solidworks drawing of cathode disc and (c) coupled artificial pit

solutions to determine suitable conditions for the artificial pit test. Since CaCl_2 was used as calcium source for the solution, overall chloride concentration was adjusted in order to maintain 21,233 ppm chloride concentration for both test conditions. Solution containing 682 ppm Ca^{2+} offered more protective scale coverage and was therefore utilised for the artificial pit investigations.

4.5 Corrosion measurement set-up

Localised corrosion occurrence is stochastic [58] in nature and therefore difficult to monitor using corrosion probes [90]. Electronic measurement of pitting process could be noisy due to pit coverage by corrosion deposits [204]. Linear polarisation, Tafel polarisation and potentiostatic techniques were utilised for electrochemical tests in this work. The three-electrode cell (Figure 4.6) comprising Ag/AgCl reference electrode (RE) coupled with platinum counter (auxiliary) electrode (CE) was set up in a 1,000ml glass beaker. The LPR was set for $\pm 15\text{mV}$ vs OCP with scan rate of 0.25mV/S . Cathodic Tafel plots were conducted within $+15\text{mV}$ to -500mV vs OCP at scan rate of 0.5mV/S while anodic Tafel plots were conducted within -15mV to 250mV vs OCP at scan rate of 0.5mV/S . A multichannel Ivium potentiostat (Figure 4.7) connected to a computer system was used for the electrochemical measurements. All channels of the multichannel Ivium potentiostat were dedicated for potentiostatic polarisation experiments conducted in this research work. ACM potentiostat was used for galvanic measurements taken during artificial pit experiments featured in Chapter 7. A schematic representation of the entire experiment set up is shown in Figure 4.8. A 99.9% CO_2 cylinder was connected through network of pipes, valves and flow meter to supply and regulate CO_2 gas used for experimental work. Hot plates fitted with magnetic stirrer and thermocouple were used to maintain temperature and flow condition of electrolytes.

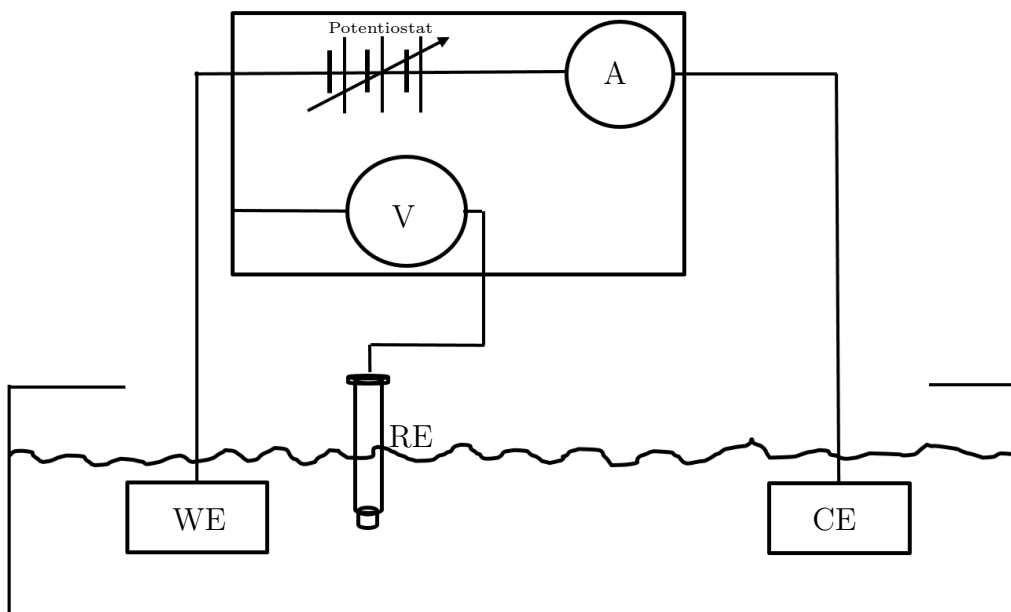


Figure 4.6: Schematic representation of the 3-electrode cell

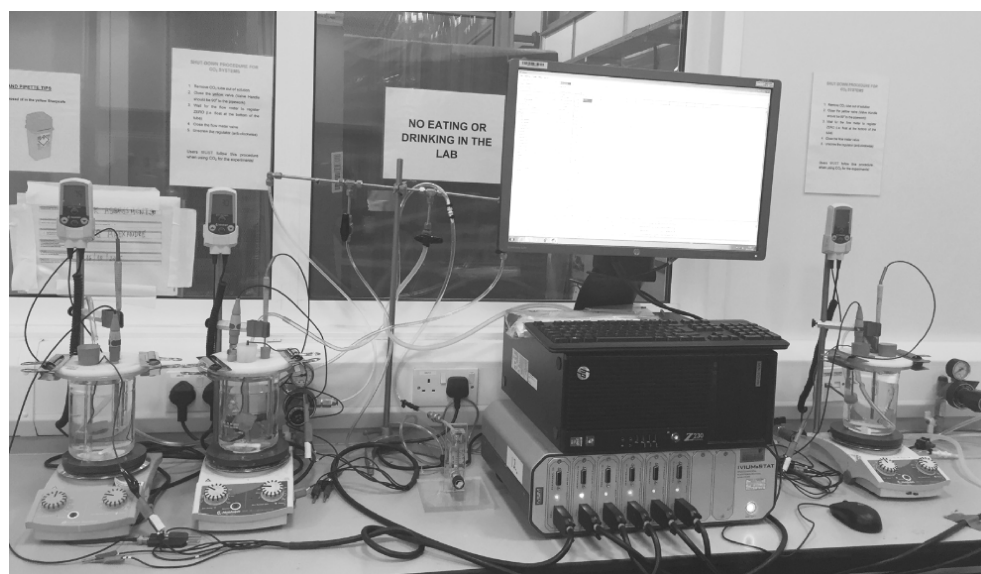


Figure 4.7: Corrosion test using multi-channel Ivium Potentiostat

4.6 Analysis tools

Pitting corrosion usually initiates and propagates on nano scale and therefore require array of equipment to interpret generated result. Consequently, array of equipment such as the PHILIP X-Pert X-Ray Diffraction (XRD), Bruker D8 XRD, MA15 ZEISS SEM, RENISHAW Raman and Bruker NPFLEX machine were utilised for post-experiment analysis.

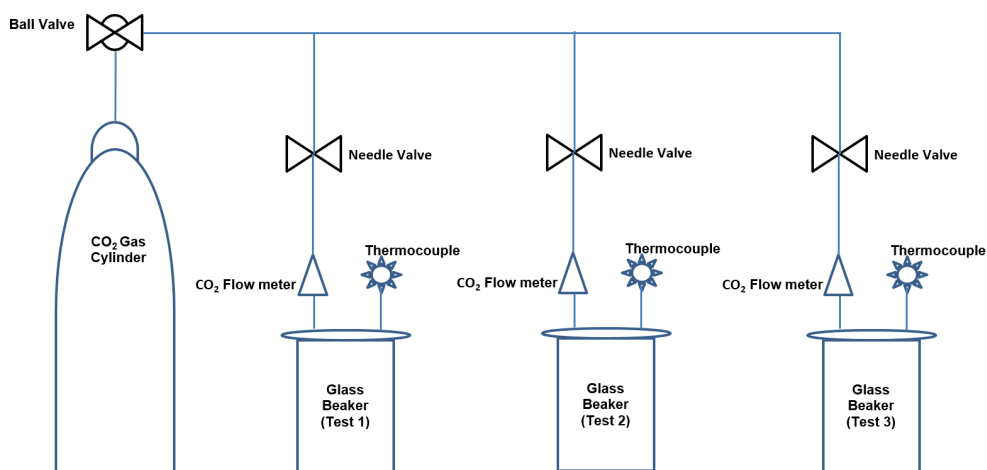


Figure 4.8: Schematic representation of the experimental set-up

4.6.1 PHILIPS X-Pert X-Ray Diffraction analysis

X-Ray Diffraction (XRD) is a research tool that can be used to identify the crystal structure of corrosion products that form on test samples. A photograph of the PHILIPS XPert XRD machine used for analysis is shown in Figure 4.9. The XRD provides information on crystallography of products formed on the steel surface based on diffraction of incident X-Ray beams as they strike the crystal structure. Electrons from heated filaments are often accelerated (using voltages) towards the target metal. The XRD machine measures angles and intensities of deflected/reflected rays. These are then matched with known standards to obtain information about the crystals. Crystal information such as lattice parameters (coordinates) and lattice spacing (Miller indices; h,k,l) can be obtained using the XRD technique. The technique is based on the application of Bragg's law which relates incidence angle of X-Ray beam to the scattering angle.

4.6.2 Scanning Electron Microscope (SEM) analysis

Scanning Electron Microscope (SEM) uses an electron beam on a sample to generate signals that reveal information about the sample. SEM measurements are taken in a vacuum chamber. The basic components of the SEM are the electron gun, anode



Figure 4.9: PHILIPS XPert XRD machine

plate, magnetic lenses, scanning coils, objective lens and detectors. The electron gun contains a tungsten filament heated to about $2,400^{\circ}\text{C}$ to emit electrons which are accelerated down a column by an anode (positive charge). The magnetic lenses focus the electrons to a narrow beam before reaching the conical objective lens that permits electron sweep in direction of interest. Final focusing of electron beam is done by the objective lens where the beam is struck on the sample. The detectors consist of positively charged collectors that pick emitted signals from the sample. The EVO MA 15 Scanning electron microscope pictured at Figure 4.10 was used to analyse the experimental samples.



Figure 4.10: EVO MA15 Scanning Electron Microscope

4.6.3 Raman Analysis

The light source directed onto a material (surface) can be reflected, absorbed, transmitted or scattered depending on the nature of the material and the wavelength (colour) of the light source. The study of such light behaviour is known as **spectroscopy**. Raman spectroscopy was employed to analyse films formed on X65 carbon steel. The RENISHAW Raman spectroscopy used is featured in Figure 4.11. Raman spectroscopy operates based on wavelength shift of scattered light by a vibrating molecule placed in the path of a monochromatic light source. RENISHAW Raman spectroscopy entails vibrating molecule of test sample while being illuminated using a monochromatic laser as light source. Some of the scattered lights have their energy unaltered and are termed as, **Rayleigh scatter**. About 1ppm of the scattered light however exhibits colour change and tend to gain or lose energy, and are referred to as, **Raman scatter**. Situation where energy is lost is termed as, **Stokes** while a state of energy gain is referred to as, **Anti-Stokes**. Raman shift occurs due to change in the energy path of light particles (photons) as a result of the vibration of the molecule of the test specimen. The Raman spectroscopy

consists for the following:

- a. Monochromatic light source.
- b. Motorised lenses: To auto-focus on sample and concentrate scattered light.
- c. Filters: To screen light and ensure that only Raman light is picked.
- d. Detectors: To sense light to be collected.
- e. Personal computer: for collecting and analysing data.

Special tools of RENISHAW Raman enabled baseline subtraction, polynomial fitting, cubic spline interpretation and curve fitting applications on derived data.



Figure 4.11: RENISHAW Raman

4.6.4 Coherence Scanning Interferometry

Coherence scanning interferometry (CSI) is a non-contact 3D measurement and surface characterisation technique that utilise optical coherence of fringes to reveal

complex details such as discontinuities, skewness, steps, valleys, hills and other features existing on a profiled surface [209]. The CSI utilise interference of light beams that exit from same source to reveal details on a sample. Typical interferometer layout is at Figure 4.12.

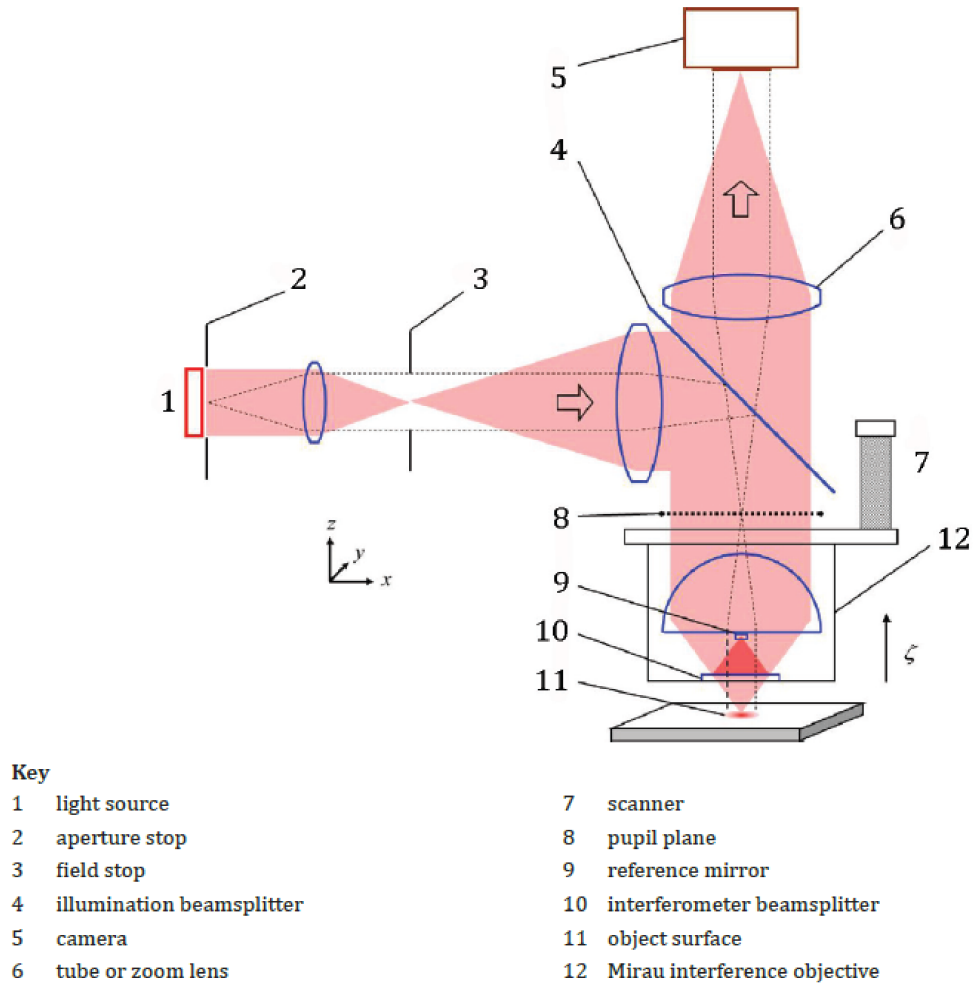


Figure 4.12: Schematics of Coherence Scanning Interferometry Layout [210]

A light beam from the same source is divided by a beam splitter into 2 paths, one to a reference mirror and the other to the sample [211]. The two beams are recombined by the beam splitter to interfere on an imaging lens which images the interferogram onto a camera [212]. The camera then measures optical path difference between the two reflected beams. Figure 4.13 captures Bruker NPFLEX used for analysing pitting in this work. The NPFlex is an automated CSI instruments that acquire data signal in image pixel relative to scan position. This ability enables precision scanning of tiny areas of a sample and integrating the scanned bits in stitches to

cover a large scan area. The NPFlex CSI was utilised in this study due to its powerful automated ability to accurately perform robust profilometry of a surface. The CSI enables measurement of corrosion defects such as pit depths, skewness, pit diameter (in X and Y plane), pit void details (such as pit volume and area), pit spacing as well as information on average thickness loss. Some CSI terms applied in investigating pitting profile include R_v , R_p , R_t , R_{sk} , X Diameter, Y Diameter and Full Diameter. Brief description of these terms are given in Table 4.5. Two dimensional representation of some amplitude parameters are presented in Figure 4.14 and Figure 4.15.

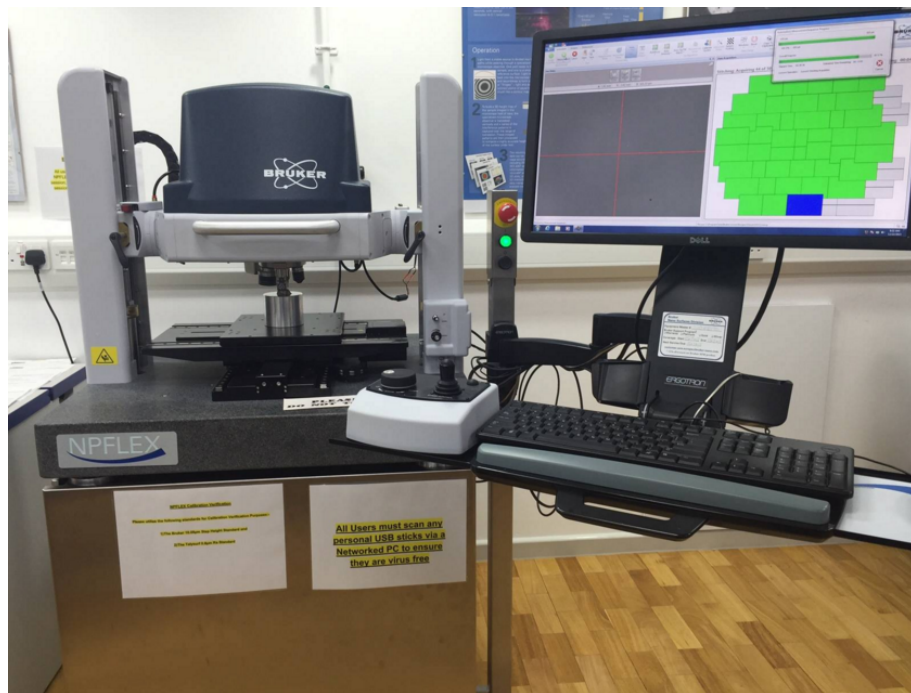


Figure 4.13: Bruker NPFLEX used for pitting analysis

4.6.5 Identification of pits and profiling technique

Addressing pitting corrosion problems would not be feasible without a reliable means of identifying, estimating or measuring the extent of pitting [32, 104]. The size, shape and density of corrosion pits are described in ASTM G46-94, Standard guide for examination and evaluation of pitting corrosion [214]. Researchers are more often

Table 4.5: Some NPFlex terms used for pitting analysis

Term	Description
Roughness Valley (R_v)	Valley (dane) depth from a reference peak height within the sample.
Roughness Peak (R_p)	Peak height from a reference peak height within the sample.
Roughness skewness (R_{sk})	Symmetry of height distribution about the distribution mean which serve as reference plane. Positive skew infers peak (hill) while negative skew represents valley (pit).
X Diameter	Lateral dimension of an imperfect circle circumscribed at pit mouth.
Y Diameter	Vertical dimension of an imperfect circle circumscribed at pit mouth.
Full Diameter	Diameter of an imaginary circle circumscribed at pit mouth.

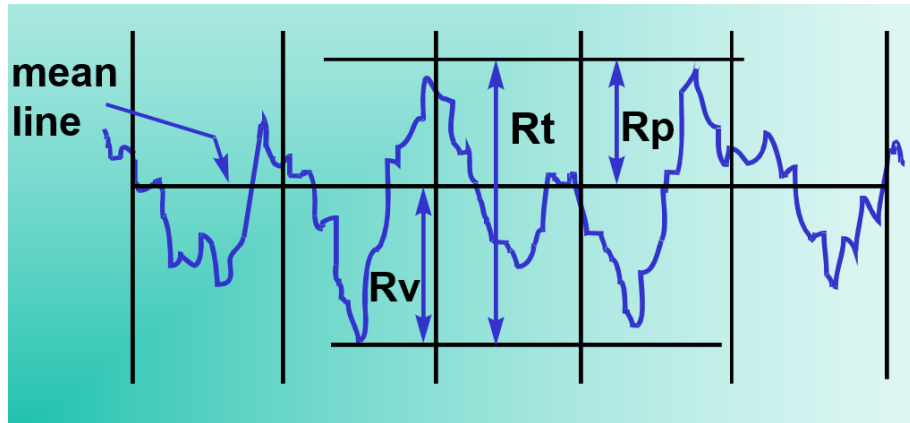


Figure 4.14: Schematic of amplitude parameters featuring Roughness Peak (R_p), Roughness Valley (R_v) and Roughness Peak to Valley (R_t) with reference from Mean Line [40].

interested in pit depth measurement owing to the fact that the deepest pit is likely to perforate before others [104]. The ASTM standard categorises a maximum pit depths of $25\mu\text{m}$ (0.025mm) as "light pitting" while pit depth of about $250\mu\text{m}$ (0.25mm) is regarded as "moderate pitting" [104]. Inspectors sometimes consider metal penetration to evaluate the extent of pitting corrosion in either of 2 ways outlined below [128, 129]:

- Height of deepest valley created or preferably, averaging the heights of 10 deepest valleys.

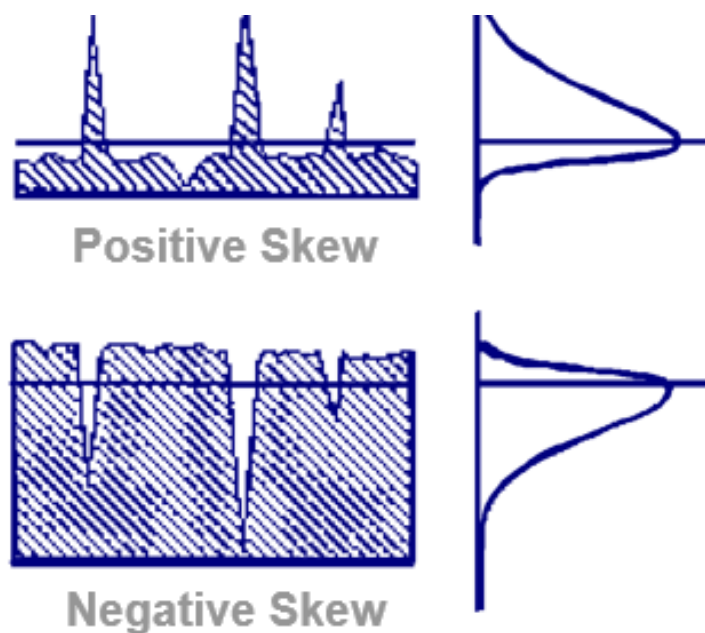


Figure 4.15: Depiction of Positive and Negative Skew [213]

- Pitting Factor (Pf) defined as the ratio of deepest valley depth to average metal penetration (determined by weight loss)[130].

Weight loss contribution has often been attributed to general corrosion while ignoring the pitting component. Pitting factor cannot be determined by electrochemical means alone. Electrochemistry / weight loss is needed to measure the general corrosion while pit details can be obtained using profilometry technique. For accuracy, this work took cognizance of weight loss due to pitting, which forms part of overall weight loss component. Accuracy of the calculation is high enough for the study of pitting factor as values obtained for 50mV, 100mV and 150mV are reasonably consistent in the repeated test featured in Tables 5.1 and 5.2. Pit identification in this work was based on averaging the 10 deepest pits after detailed, repeated systematic scanning of the entire corroded surface as well as reporting the maximum pit depth, in alignment with the ASTM standard.

4.6.6 Profiling technique for pit analysis

The ASTM standard envisaged the identification and averaging of 10 deepest pits in assessing pitting damage among other suggested approaches as presented in paragraph 3.6.1. Circular sample of 12mm diameter was considered suitable for pitting investigation due to in-built automated capability of the NPFlex to perform optimised circular scan covering a diameter of 10mm and beyond without operator's interference once a reference point is set. This saves time and reduce likelihood of human error in measurement process. For pitting investigation, it is important to capture the entire surface of a corroded sample to ensure that that no pit is missed during the scanning process. A 10mm scan diameter was set for NPFlex analysis leaving out only 1mm edge that was covered in resin during the corrosion test. The overall sample area was scanned in bit area of $1118.1\mu\text{m} \times 838.6\mu\text{m}$. Interface of scan process is shown in Figure 4.16 while description of 172 stitched areas representing entire 10mm diameter of the sample is featured in Figure 4.17.

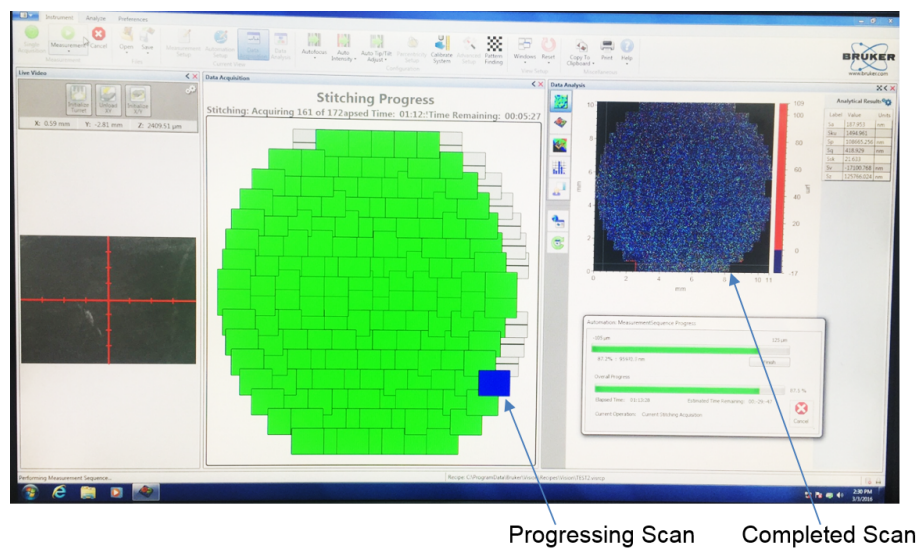


Figure 4.16: Interface showing data collection process

The measurement was programmed to commence from the centre of the sample and scanned outwards in anti-clockwise direction covering minute area ($1118.1\mu\text{m} \times 838.6\mu\text{m}$) that extends over the entire area of the sample in 172 measurements with 25% area overlap. The scan pattern employed is featured in Figure 4.18.

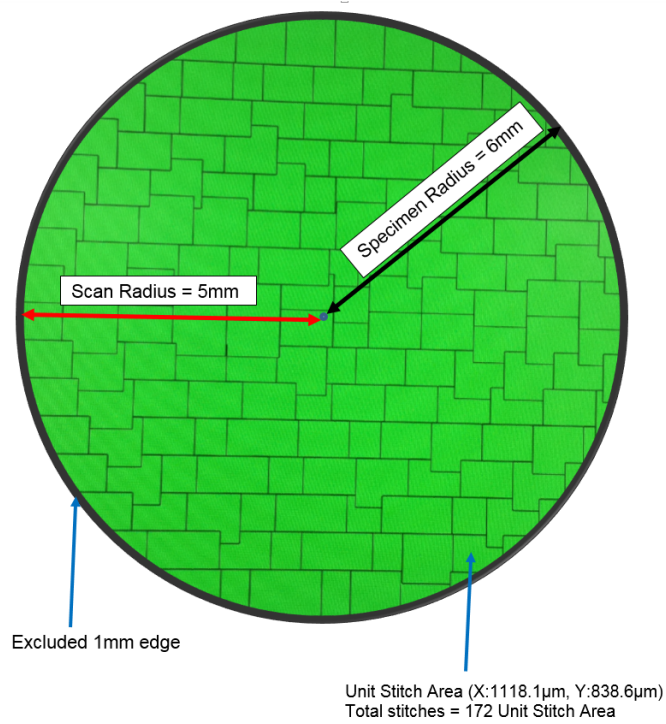


Figure 4.17: Description of Sample Scan area comprising 172 stitches in 10mm diameter

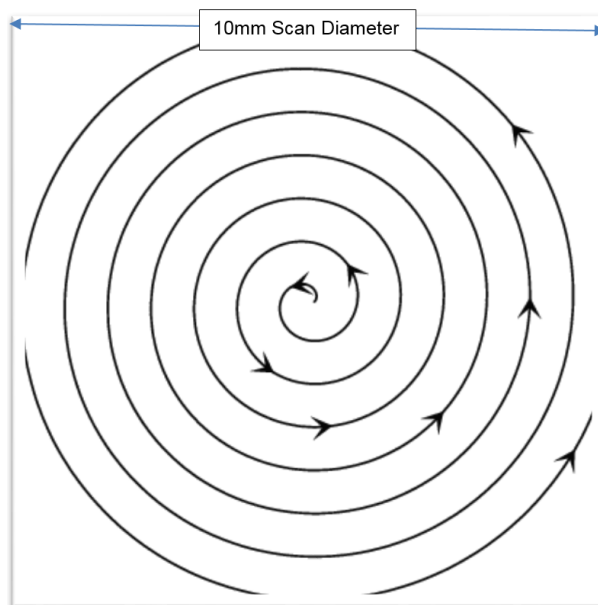


Figure 4.18: Spiral scan pattern adopted for CSI analysis

4.6.7 Application of NPFLEX CSI for pitting corrosion measurement

Inspectors and corrosion engineers have over time evolved methods for categorising pitting corrosion damage which could vary based on material, application and

environment amongst others. ASTM G46-94 [92] however offered a generally accepted standard for categorising pitting damage by considering the depth of top ten pits as well as maximum pit depth from cleaned corroded surface. The ASTM standard also provides description of pit in terms of density, size and depth [92]. This provision guides the technique applied in categorising pitting in this work. Outliers could be recorded in measured data due to the combination of relatively rough specimen surface with ultra-precision processing tools of CSI instrument [215]. An array of filter options is available in NPFLEX CSI to allow users to get rid of such roughness or waviness. The NPFLEX offers unique applications such as terms removal, data analyser, multiple region analysis, amongst other tools suitable for analysing corrosion damage in steel samples. The multiple region analysis provides statistics and location of pits, size, volume, diameter, skewness and other parameters suitable for validating identified pits. Interface of typical multiple region analysis is featured at Figure 4.19. Advance stitching capability of the NPFLEX enables scan of large area (within optimal fringe caption) by adding series of small datasets in the scan area of any dimension. Required data range is determined by selecting suitable threshold for pit depth and pit pixels. Detail of profilometry technique applied is in Appendix A while sample of some 2D images are presented in Appendix B.

Tools such for pixel, R_{sk} and R_v measurements amongst others enable further screening of generated data which could be logged on excel compatible format after ranking in accordance with the provisions of ASTM G46-94 [92] standard for pit analysis. Analysis conducted on the NPFLEX were as well guided by the provisions contained in the Measurement Good Practice Guide No.108 provided by the National Physical Laboratory [215] and other International Organization for Standardization (ISO) literature. Tests and measurements were repeated to validate data which are germane in arriving at findings presented in this work.

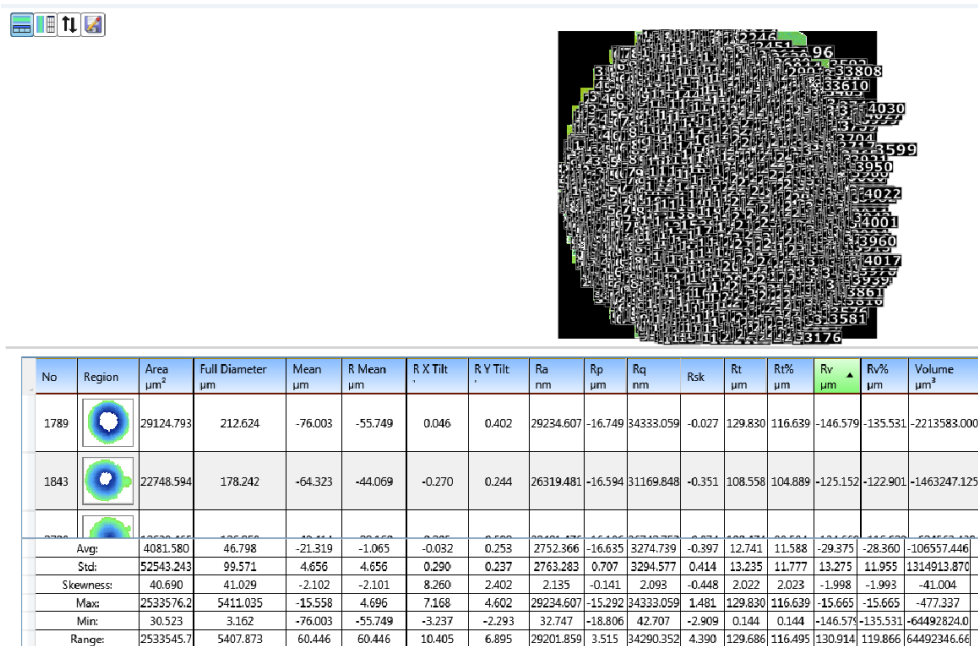
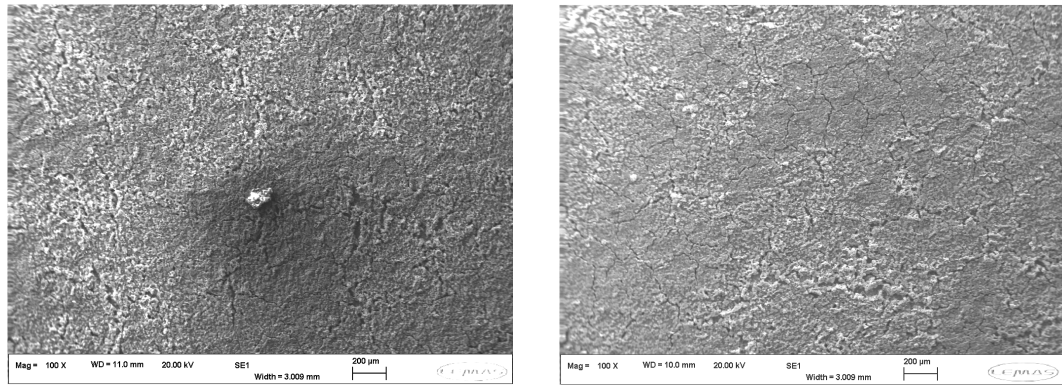


Figure 4.19: Computer interface featuring a multiple region analysis of corrosion pits formed on X65 carbon steel under 150mV potentiostatics in 3.5% NaCl solution, unbuffered, 30°C, P_{CO_2} of 1bar for 72 Hrs.

4.7 Confirmation of electrochemical response

Potentiostatic polarisation was employed to induce pitting on API-X65 carbon steel as presented in Chapter 5. The effect of polarisation on pit acidification is ignored due to the absence of oxygen and buffering effect of CO_2 system [57]. Formed corrosion products were analysed to appraise the effect of polarisation on corrosion chemistry. SEM analysis of corrosion products formed on a freely corroding X65 samples and polarised film-free environment were compared. SEM images of X65 carbon steel under 150mV potentiostatic (at pH3.8, 30°C) and in absence of polarisation are shown in Figures 4.20(a) and 4.20(b) respectively. Both images show strong similarities which suggests similar composition of corrosion products on polarised and freely corroded sample. The main difference being compromised spots which indicate pit sites on the polarised sample. It is however unclear if pitting preferentially occurs at pearlite, ferrite or grain boundaries of the corroded sample.

Figure 4.21 shows the SEM image of a polarised sample under a protective film environment. In this case, pits are not clearly visible on the SEM image even



(a) SEM image after 150mV potentiostatic in 3.5% NaCl solution, pH3.8, 30°C for 24h.

(b) SEM Image of Free corroding X65 sample in 3.5% NaCl solution, pH3.8, 30°C for 24h.

Figure 4.20: SEM image of corrosion product formed on X65 carbon steel under (a) 150mV potentiostatic and (b) free corrosion in sweet environment.

at higher magnification. Details on potentiostatic polarisation under FeCO_3 film condition is presented in Section 5.4.

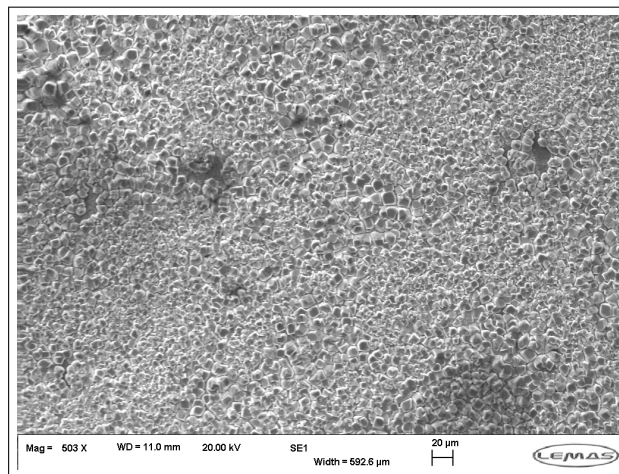
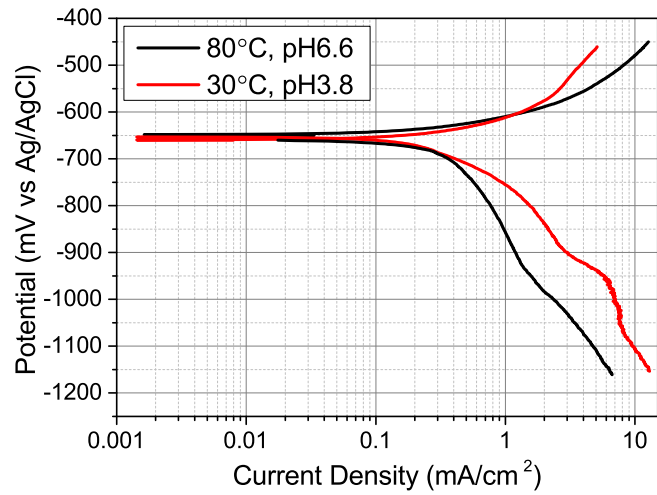


Figure 4.21: SEM Image after 150mV potentiostatic in 3.5% NaCl solution, pH of 6.6, 80°C for 24h.

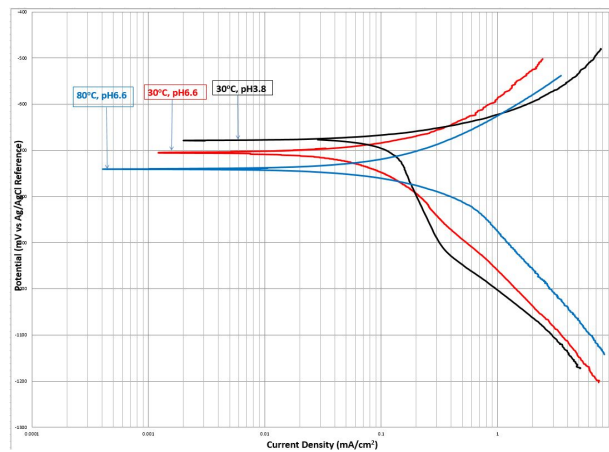
4.8 Tafel plot on test conditions

Tafel measurements can serve to characterise the electrochemical response of a corrosion process. Measured anodic and cathodic values vary with electrolyte conditions. Tafel polarisation was conducted after 7 h exposure of X65 carbon

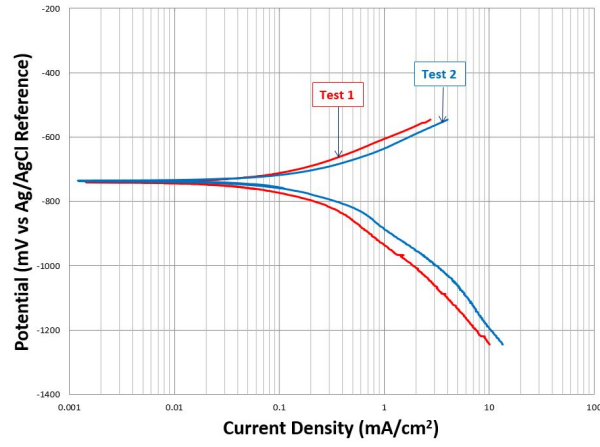
steel to LPR and OCP tests, when corroding surface does not mask the likelihood of cathodic reactions [127]. Tafel plot values taken after 7 h were therefore adopted for LPR experiments for ease of reference. LPR tests were conducted for each set of experiments with the aid of a multichannel Ivium potentiostat. Figure 4.22(a) features Tafel plots for some potentiostatic experiments while Tafel constants applied for corrosion experiments were derived from Tafel plots shown in Figure 4.22(b-c).



(a)



(b)



(c)

Figure 4.22: Tafel curves after 7h tests on 4.9cm² X65 carbon steel in 3.5%NaCl and atmospheric pressure under (a) 150mV potentiostatic (b) LPR and OCP measurement on cathode disc (c) LPR and OCP measurement on 3mm anode pit.

The anodic and cathodic Tafel slopes were carefully drawn through points approximately ± 50 mv from OCP respectively. The current axis coordinate of the extrapolated anodic and cathodic linear plot at OCP measures the absolute i_{corr} value. A typical Tafel plot featuring anodic and cathodic linear extrapolation is depicted in Figure 4.23(b). The Tafel plots were repeated for reproducibility. Further detail on derived Tafel calculations for calcium tests extrapolations in this work are at Appendix C. Anodic Tafel (β_a) and cathodic Tafel (β_c) constants were utilised to calculate the Stern Geary coefficient (B) by substituting into the following Equation 4.2.

$$B = \frac{1}{2.303} \left(\frac{\beta_a \beta_c}{\beta_a + \beta_c} \right) \quad (4.2)$$

Corrosion current density (i_{corr}) could be measured directly from Tafel plot or derived by combining the Stern Geary coefficient (B) with the polarisation resistance from the LPR as provided in Equation 4.3.

$$i_{corr} = \frac{1}{2.303R_p} \left(\frac{\beta_a \beta_c}{\beta_a + \beta_c} \right) \quad (4.3)$$

Corrosion rate in mmpy was calculated by substituting the i_{corr} values into Equation

4.4 [23, 72, 92]

$$\text{Corrosion rate (mmpy)} = 3.27 \times 10^{-3} \frac{i_{corr} \times A_w}{n \rho} \quad (4.4)$$

Where A_w , n and ρ are respectively the corroding metal atomic weight, number of transferred electrons and density.

4.8.1 Tafel properties of X65 carbon after 24 h polarisation test

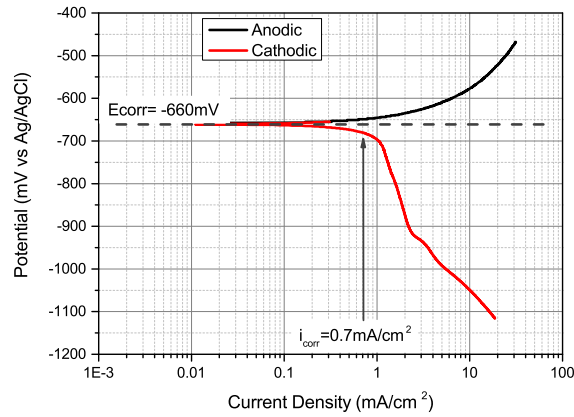
Tafel extrapolation of plots after 24h potentiostatic polarisation was utilised to derive corrosion current density under the two film conditions; when FeCO_3 forms and when corrosion product was predominantly Fe_3C scale. Corrosion current density derived from anodic and cathodic linear extrapolation plots at OCP are shown in Figure 4.23. Higher corrosion current density ($0.7\text{mA}/\text{cm}^2$) was recorded for the extrapolated Tafel plot after 24h polarisation in film-free conditions. Current density of about $0.03\text{mA}/\text{cm}^2$ was however recorded under protective film (FeCO_3 favoured) condition hitherto referred as **scaled condition**.

Table 4.6: Derivations from Tafel Extrapolation

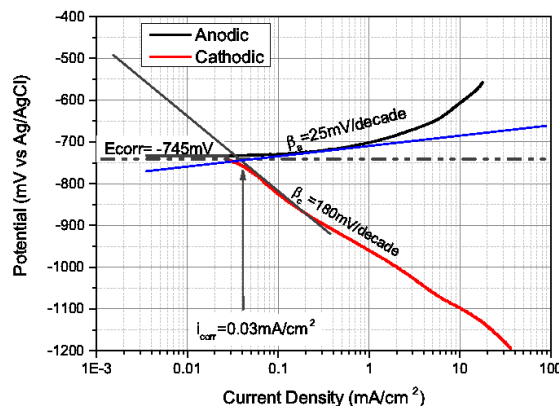
	E_{corr} (mV)	β_a (mV/dec)	β_c (mV/dec)	i_{corr} (mA/cm ²)
*	-660	60	200	0.7
**	-745	25	180	0.03

* Film free condition

** Protective film condition



(a)



(b)

Figure 4.23: Tafel plots after 24h, 150mV potentiostatic test in (a) 3.5% NaCl solution, pH of 3.8, 30°C. (b) 3.5% NaCl solution, pH 6.6, 80°C.

FeCO_3 and steel impurities such as non-protective Fe_3C are common corrosion products formed on carbon steel in sweet environment. Iron carbonate forms at high temperature and high pH while non-protective iron carbide impurity is predominant at relatively low temperature. Experimental conditions (3.5% NaCl, 30°C, pH 3.8, in CO_2 saturated solution) where Fe_3C predominantly forms on metal surface is termed in this work as **non-scaled condition**. Experimental conditions (3.5% NaCl, 80°C pH6.6 in CO_2 saturated solution) where iron carbonate forms on the metal surface thereby retarding corrosion progress is herein termed as **protective-film condition**.

Chapter 5

Effect of potentiostatic polarisation on carbon steel corrosion

5.1 Introduction

This chapter aimed to establish a procedure for producing stress-free reproducible shallow pits suitable for studying pitting corrosion kinetics in a controlled environment. The objective was to come up with a set of conditions where active pits can be established and then transferred into desirable electrochemical environment to examine their growth. Potentiostatic polarisation can be employed to induce pitting for corrosion investigation [216]. The electrochemical reactions in a polarised system comprise **charge transfer** and **mass transfer** processes [217]. Charge transfer occurs at the electrolyte / electrode interface while mass transfer entails movement of electrochemical active species such as H^+ ions through the bulk solution. Current density recorded is an aggregate of both anodic and cathodic entities involved in the corrosion process [218]. Anodic polarisation curves are therefore a sum of oxidation and reduction reactions that

become activation-controlled when the over-potential exceeds 50mV [218]. Anodic polarisation causes an increase in the recorded anodic current density which subsequently increases the metal dissolution rate [219, 220]. Anodic polarisation can be used to obtain a high corrosion rate in a relatively short time and also has the ability to control corrosion rate through applied potential [216]. The application of a potentiostatic polarisation method to induce pitting in low carbon steel is yet to be fully explored. This prompted the need to investigate pitting corrosion of X65 carbon steel using potentiostatic polarisation. The merits of this approach are as follows:

- Ability to induce high corrosion rate in relatively short time [216].
- Ability to control corrosion rate through applied potential threshold [216].

This chapter explores the potentiostatic polarisation approach in its ability to generate pitting in low carbon steel. This is supported by robust post-test surface analysis. Experiments were performed under electrochemical conditions suitable for generating reproducible stress free pits. Since the emergence of pitting does not imply the absence of general corrosion with regards to carbon steel, this work further explores profilometry and potentiostatic application to establish the relationship between general and pitting corrosion in low carbon steel. This chapter covers the effect of applied potential on pitting and comparison of pitting trend under film free & protected film conditions as well as statistical trend of discrete pit profiles.

5.2 Effect of applied potential on pitting

The current density transient response of samples subjected to 50mV, 100mV and 150mV potentiostatic (Figure 5.1) was observed to fluctuate at the start of the

experiment and equilibrate after about 7h. For passive steel, Pagitsas et al. [170] suggested that high and low current measured during potentiostatic polarisation respectively reflect the non-protective and protective states of a metal where drop in current would normally imply significant transition of a metal from an active to a passive state. This however does not apply to carbon steel in this instance, as it remains an actively corroding material throughout the duration of the experiment. At the end of each experiment, distinct pits were visible on each steel surface using SEM. An example of the nature of pits observed under SEM for conditions of 150mV after 24h is provided in Figures 5.2 and 5.3. Fe_3C line the pit walls while profilometry of revealed pits suggests that pit walls widens as pit depth increased.

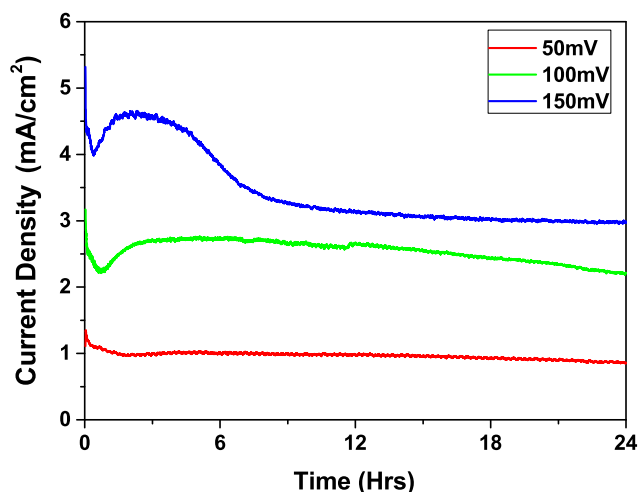


Figure 5.1: Current transient plot of 50mV, 100mV and 150mV potentiostatic polarisation on X65 carbon steel over a duration of 24h in a 3.5 wt.% NaCl solution saturated with CO_2 at 30°C at pH3.8.

SEM images of polarised samples revealed that pitting was more and most prominent at 150mV polarisation. This is sensible given that there is a greater driving force to propagate localised attack. XRD analysis of the surfaces of steel samples subjected to 50mV, 100mV and 150mV potentiostatic revealed presence of Fe_3C (Figure 5.4) which was revealed due to the preferential dissolution of the ferrite phase within the steel microstructure. The quantity of Fe_3C becomes more abundant with increase in the applied potential.

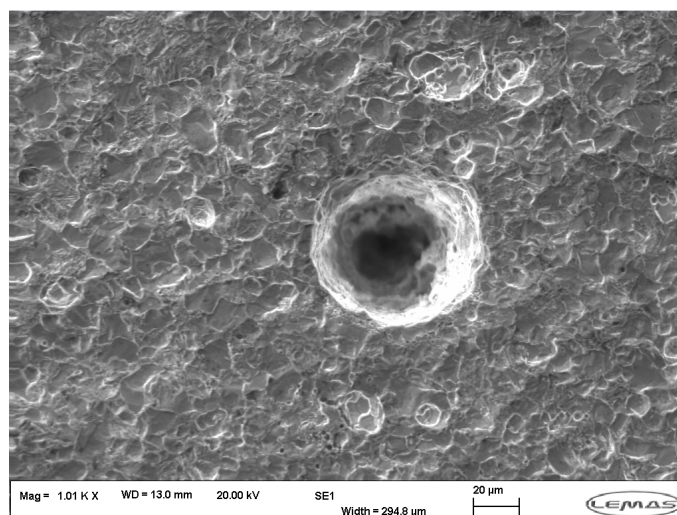


Figure 5.2: SEM image of pit formed through carbide films on X65 carbon steel under 150mV potentiostatics in 3.5% NaCl solution, pH of 3.8, 30°C for 24h after cleaning with Clarke's solution.

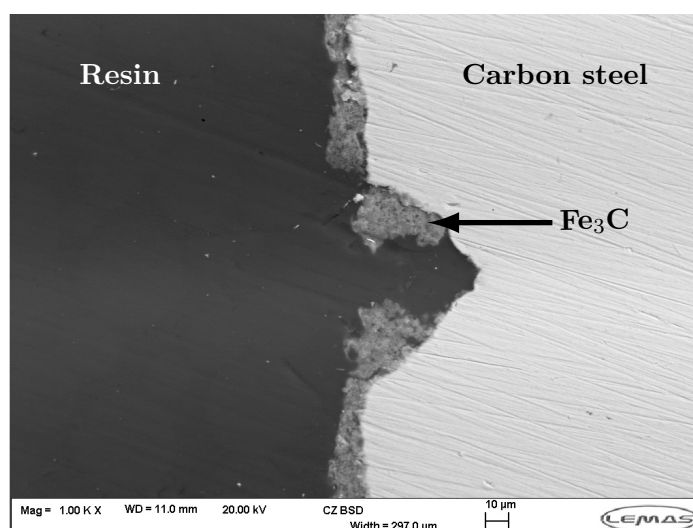


Figure 5.3: Cross section of pit formed through carbide films on X65 carbon steel under 150mV potentiostatics in 3.5% NaCl solution, pH of 3.8, 30°C for 24h.

Pits were observed to grow beneath the seemingly fragile and porous Fe₃C network as shown in Figure 5.2. This affirms that the Fe₃C formed was not protective. From the SEM and XRD analysis conducted, iron carbonate (FeCO₃) was not present in the corrosion film as expected under the experimental conditions (i.e. the low pH and low temperature make the FeCO₃ precipitation unfavourable). The environment favored formation of Fe₃C films as revealed in the XRD pattern.

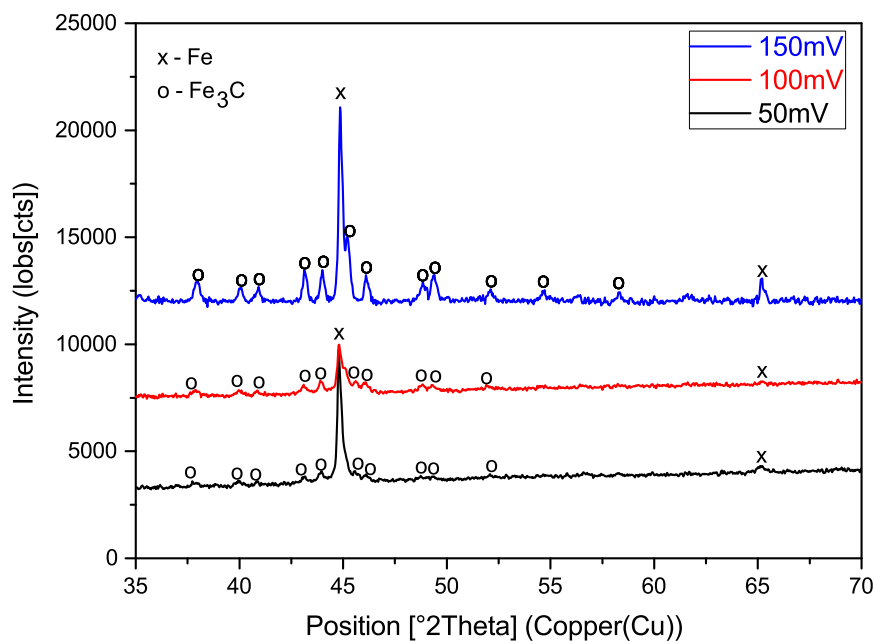
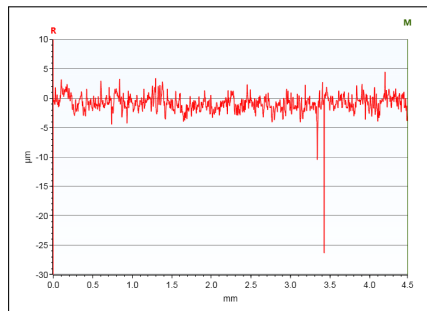


Figure 5.4: XRD pattern showing Fe₃C deposit on X65 carbon steel after 50mV, 100mV and 150mV potentiostatic in 3.5% NaCl solution, pH of 3.8, 30°C for 24h

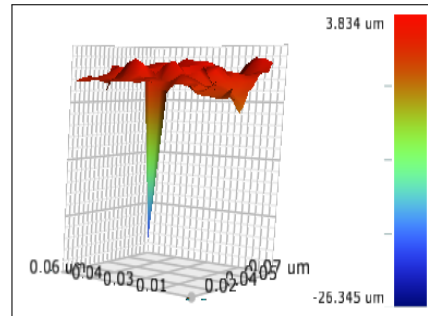
5.2.1 Analysis of pitting trend

Profilometry analysis was conducted to determine and quantify the extent of pitting on the polarised X65 carbon steel samples. Pit ranking was done based on pit depth obtained from the multiple region analysis tool of the profilometry software. The morphology of deepest pits recorded under 50mV, 100mV and 150mV polarisation of X65 carbon steel at 30°C, pH3.8 for 24h were 25µm, 55µm and 120µm respectively as shown in Figure 5.5. The result revealed that pit depth increased with applied anodic potential similar to the pitting trend reported for passive steel polarisation by Tian et al. [168].

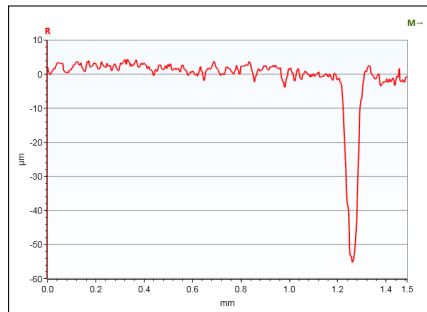
The skewness value recorded for generated pits were near zero which indicates a symmetrical pit profile. The interferometry analysis was conducted twice for each set of corroded samples after potentiostatic experiment to ascertain repeatability. Pit depth statistics recorded in Fe₃C growth conditions under 50mV, 100mV and 150mV potentiostatic is shown in Figure 5.6. It shows that pit depth increased with



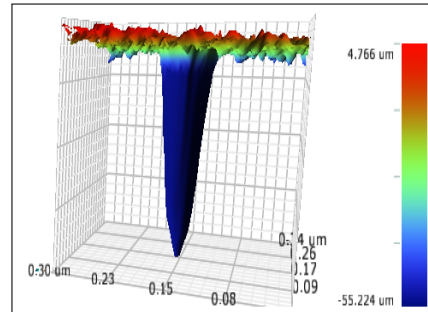
(a) **25 μm** pit (2D) for **50mV** potentiostatic



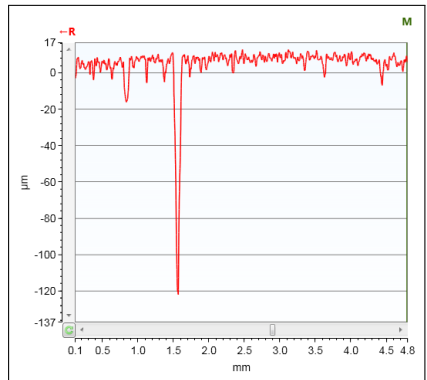
(b) **25 μm** pit (3D) for **50mV** potentiostatic



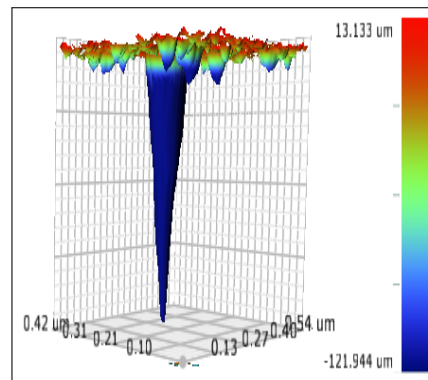
(c) **55 μm** pit (2D) for **100mV** potentiostatic



(d) **55 μm** pit (3D) for **100mV** potentiostatic



(e) **120 μm** pit (2D) for **150mV** potentiostatic



(f) **120 μm** pit (3D) for **150mV** potentiostatic

Figure 5.5: White light profilometry images showing maximum pit depth recorded on X65 carbon steel after 24h exposure in CO₂ saturated, 3.5% NaCl solution, pH3.8, 30°C under (a&b) 50mV, (c&d) 100mV and (e&f) 150mV polarisation.

increase in applied potential and that pitting progressed beneath the revealed Fe_3C as seen in Figure 5.7. The base of the pit featured in Figure 5.3 was free of Fe_3C film unlike that shown in Figure 5.7. This suggests that Fe_3C detach and collapse at the base of pit as pit depth increased.

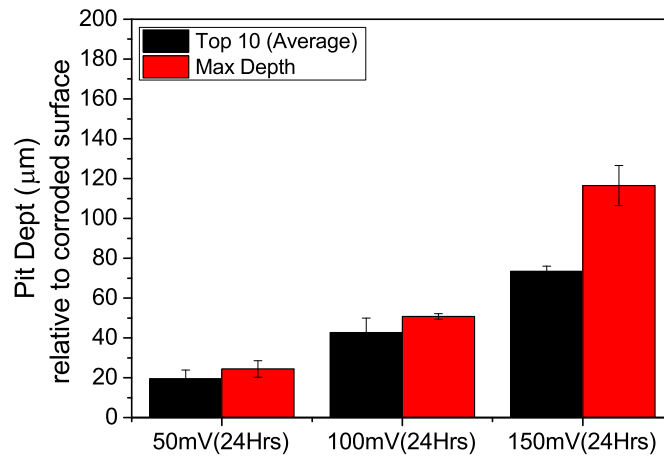


Figure 5.6: Pit depth chart depicting top-10 average and maximum depth recorded for samples subjected to 50mV, 100mV and 150mV potentiostatic polarisation at 30°C, pH3.8, 3.5wt% NaCl, CO_2 saturated for 24h. (Note: Max depth (red bars) indicates deepest valley; average of top ten pits (black bars) is termed top-10 average; error bars are based on standard deviation of two set of tests).

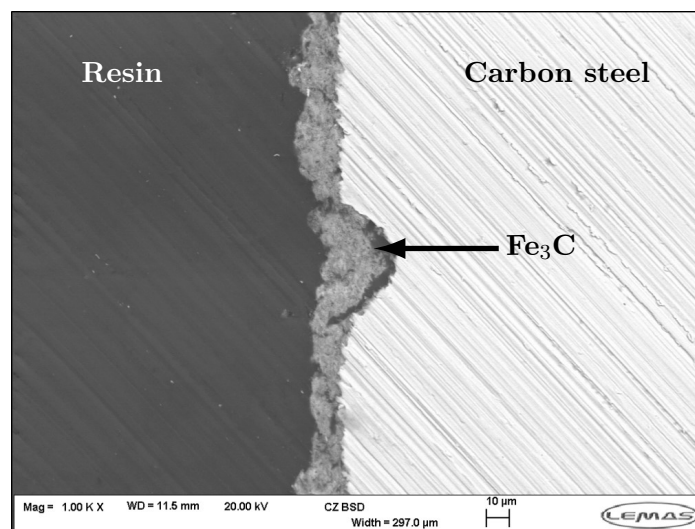


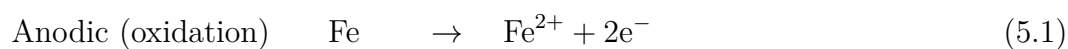
Figure 5.7: Cross-section morphology of pit formed after 150mV at 3.5% NaCl, 30°C, pH3.8, 24h.

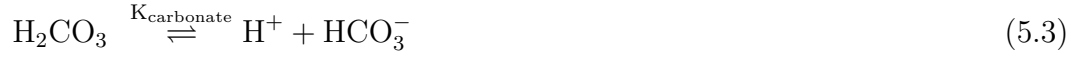
5.2.2 Application of Faraday's law of electrolysis to potentiostatic test result

The Butler-Volmer equation provides expression that relates current density to applied potential [221, 222]. Since anodic overpotential of 50mV and beyond were utilised in this work, the anodic exponential term predominates [221, 223, 224] which implies that measured current was solely a measure of applied anodic potential [223] that caused metallic dissolution. The interferometry software was used to calculate discrete pit volumes. Screened pits in the threshold of $25\mu m$ and beyond were considered as true pits in line with ASTM standard for evaluating corrosion test specimens [214]. Pit volume, otherwise termed void volume is the volume of cavity or space created by pit.

Current density measured under potentiostatic conditions accounts for general and pitting corrosion. Void volume derived was then resolved to a mass component based on the density of the steel. Total charge equivalence was obtained by integrating the current transient measurement while Faraday's law was applied to relate charge to associated mass loss. Mass equivalence of void volume was deducted from the overall mass obtained from Faraday's relationship to obtain a mass due to general corrosion.

The potential applied during potentiostatic polarisation perturbs equilibrium thereby forcing electron flow from the anodically polarised electrode which results in accelerated corrosion. Anodic polarisation causes oxidation of the electrode (loss of electrons) in accordance with the Equation 5.1 while corresponding cathodic reactions may be complex, but mainly influenced by reactions featured in equations 5.2 to 5.4 .





Progressive charge from the electrochemical reaction was calculated from the corrosion current density response recorded during 24h potentiostatic experiment by integrating the product of measured current (I) with time (t) as presented in Equation 5.5. Electrochemical measurements were taken at intervals of 10 seconds covering 24h test duration.

$$Q = \int_0^{24h} I dt = \int_0^{24h} i A dt \quad (5.5)$$

Where Q is the total charge recorded after 24h potentiostatic test measured at intervals of 10 seconds, 'i' is current density (A/m²) and 'A' is test surface area (m²). Faraday law was applied to the electrochemical reaction to express relationship between mass and current as given in Equation 5.6.

$$Q = It = zFn \quad (5.6)$$

Where Q (Coulombs) is charge involved in the electrochemical process, I is current (Ampere), t is time (seconds), z is number of electrons in one molecule of Fe, F (Faraday's constant) = 96,485 Coulombs/mole and n is the number of reacting mole = reacting mass (m)/molar mass (M). Equivalent weight (E_w) is the mass of reacting species that utilises one Faraday charge. This implies that E_w = atomic or molecular weight (M) /valency(z). Substituting for n in Equation 5.6 gives Equation 5.7 [225].

$$m = \frac{MI t}{zF} = \frac{MQ}{zF} = \frac{(E_w)Q}{F} \quad (5.7)$$

Volume equivalence or void volume (V) can be obtained by substituting for mass in Equation 5.7 to derive expression in Equation 5.8, where ρ is density of carbon

steel.

$$Q = \frac{VF\rho}{E_w} = \frac{VFZ\rho}{M} \quad (5.8)$$

Q, represents the total charge utilised for the entire corrosion process which comprises of uniform and general corrosion. A similar expression was utilised in the work of Tian et al. [189] who investigated potential effect on stainless steel. The volume component therefore reflects void volume for uniform and pitting corrosion that take place on the steel. With $25\mu\text{m}$ minimum threshold set for pitting categorisation, pitting volume was deducted from the total volume derived from electrochemical results.

Total charge involved during the potentiostatic tests was calculated by integrating parameters in Equation 5.5. A total charge of approximately 200 Coulomb, 500 Coulomb and 700 Coulomb was involved under 50mV, 100mV and 150mV potentiostatic respectively as depicted in Figure 5.8.

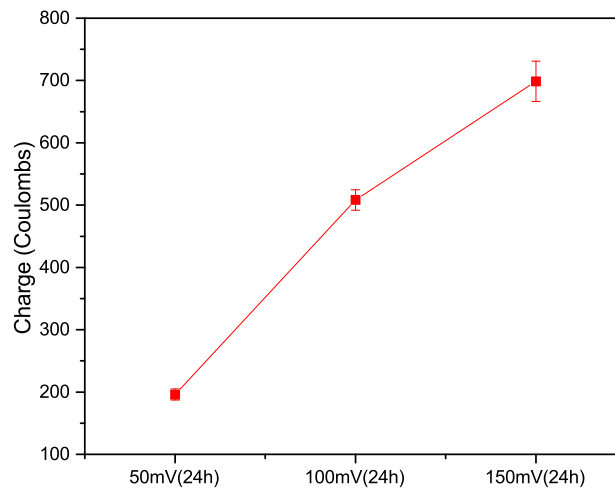


Figure 5.8: Plot depicting magnitude of charge expended for repeated test of 50mV, 100mV and 150mV potentiostatic at 30°C , pH3.8, 3.5%wt NaCl for 24h.

Figure 5.9 shows that no significant pitting was recorded under 50mV. Low pitting

but high general corrosion was recorded for 100mV potentiostatic. Pitting and general corrosion were both significant under 150mV potentiostatic. This implies that increase in potentiostatic range increases general corrosion as well as pitting but to different extents.

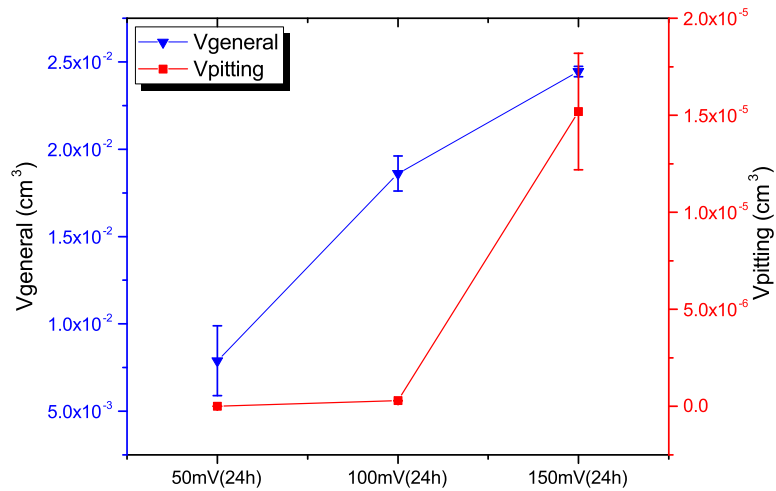


Figure 5.9: Plot of void volume depicting trend for general and pitting corrosion after 50mV, 100mV and 150mV potentiostatic at 30°C, pH3.8, 3.5%wt NaCl for 24h.

5.2.3 Derivation of pitting factor

An acceptable approach to relate pitting extent with general corrosion is by considering pitting factor (Pf) as provided in ASTM G46-94 [214]. Pitting Factor is defined as the ratio of deepest valley depth to average metal penetration [130].

Pitting factor of unit magnitude indicates general corrosion. Pitting factor basically increases as pitting extent increase. Since general corrosion takes place on the entire test sample surface, the volume of mass corroded ($Vol_{general}$) is expressed as indicted in Equation 5.9.

$$Vol_{general} = \pi r^2 D \tag{5.9}$$

Where r is the radius of test sample (ie 0.6cm). D was therefore calculated for 50mV, 100mV and 150mV potentiostatic tests as tabulated in Tables 5.1 and 5.2.

Analysis of the pitting factors contained in Table 5.1 features Pf of 1.41, 1.34 and 1.55 for 50mV, 100mV and 150mV potentiostatic polarisation. A repeated test recorded Pf of 1.21, 1.17 and 1.32 for 50mV, 100mV and 150mV as depicted in Table 5.2. This indicates that the extent of general corrosion thickness loss compared to pitting depth were quite similar. Interestingly, recorded pitting factor for all polarisation cases fell within values reported on the 7th day test of Pessu et al. [226] who compared pitting and general corrosion under 30°C, 50°C, and 80°C by naturally developing pits at OCP. Pessu used the same material, temperature (30°C), CO₂ partial pressure as this work but with a higher pH and a slightly higher NaCl concentration, which could lead to formation of amorphous FeCO₃. Such amorphous films do not tend to evolve into dense protective films at low temperature (30°C). Low temperature retards precipitation [227] which renders amorphous layer porous thereby allowing interaction of the surface with the bulk solution. Experimental conditions employed in this work are however reasonably close to the 30°C investigations made by Pessu et al [226]. This suggests that potentiostatic polarisation gives accelerated corrosion of both general and pitting corrosion instances in reasonable proportion. This implies that potentiostatic polarisation has the potential to be employed for accelerated corrosion processes.

Table 5.1: Parameters for determining pitting factor (Test 1)

Description	50mV	100mV	150mV
$Vol_{general}(cm^3)$	6.89×10^{-3}	1.81×10^{-2}	2.45×10^{-2}
D (cm) (Equation 5.9)	6.09×10^{-3}	1.60×10^{-2}	2.17×10^{-2}
Pit_{max} (cm) from interferometry	2.50×10^{-3} (25 μm)	5.50×10^{-3} (55 μm)	1.20×10^{-3} (120 μm)
P (cm) ($D + Pit_{max}$)	8.59×10^{-3}	2.15×10^{-2}	3.37×10^{-2}
$Pf = P/D$	1.41	1.34	1.55

Table 5.2: Parameters for determining pitting factor (Test 2)

Description	50mV	100mV	150mV
$Vol_{general}(cm^3)$	7.54×10^{-3}	1.93×10^{-2}	2.69×10^{-2}
D (cm) (Equation 5.9)	6.67×10^{-3}	1.71×10^{-2}	2.38×10^{-2}
$Pit_{max}(cm)$ from interferometry	2.50×10^{-3} (25 μm)	5.50×10^{-3} (55 μm)	1.20×10^{-3} (120 μm)
P (cm) (D + Pit_{max})	9.16×10^{-3}	2.26×10^{-2}	3.58×10^{-2}
Pf = P/D	1.21	1.17	1.32

5.3 Pit growth under active conditions

To evaluate the ability of pits formed from the potentiostatic technique to continue to propagate, a series of experiments were performed. The samples polarised at 150mV for 24h were transferred into an unbuffered test solution at 80°C and left for 24 and 48h. Pitting data gathered from extensive profilometry of the steel surface indicated that the pits continues to grow linearly in depth after immersion in the 80°C test solution. These results hold promise in that the technique can potentially be used to help in the understanding of pit propagation within laboratory tests repeatedly and in a reasonable time frame.

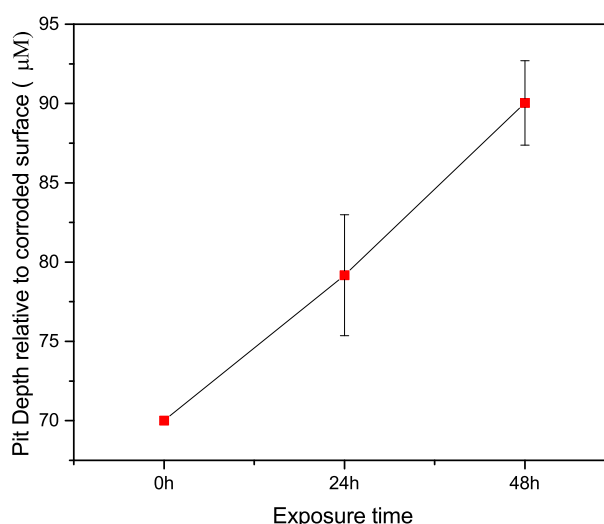


Figure 5.10: Plot depicting trend of pit from initial depth of 70 μm exposed to saturated CO₂ unbuffered solution at 80°C up to 48h.

Figure 5.10 depicts the growth of pit exposed to unbuffered, saturated CO₂ solution at 80°C. Pit with initial depth of 70 μ m (top-10 average) increased to about 78 μ m after 24h exposure with further incrementation to 90 μ m after 48h of exposure. This suggests that general and pitting corrosion progress linearly under the 2-day exposure.

5.3.1 Effect of potentiostatic duration on pitting trend

Figure 5.6 shows that pit depth increased with increase in applied potential under film-free conditions. Corrosion current density was observed to as well decrease steadily as exposure time increases. Electrochemical measurement of potentiostatic test in durations of 24h, 48h and 72h is shown in Figure 5.11. Pit depth in samples subjected to same potentiostatic (150mV) also increase with exposure time as shown in Figure 5.12. Pit propagation rate however reduce as exposure time increased. Coincidentally, this is in consistent with declining current density trend as exposure time increased. Pitting propagation rate could therefore be said to decline as exposure time increase. Figure 5.11 shows a consistent decline in pitting propagation rate under potentiostatic polarisation in threshold of 150 mV. From Ohms law, the drop in current trend under static potential condition implies that the system resistance increased as the polarisation progressed. With drop in current, pitting kinetics expectedly reduce and this is in agreement with the pit count statistics featured in Figure 5.12.

5.3.2 Polarisation curves under film-free and passive film conditions

Potential-dynamic curves were obtained by polarising X65 carbon steel from -15mV to 1,000mV vs Ag/AgCl at 0.25mV/s under film-free and passive film conditions. Polarisation curves of X65 carbon steel under film-free condition are shown in Figure

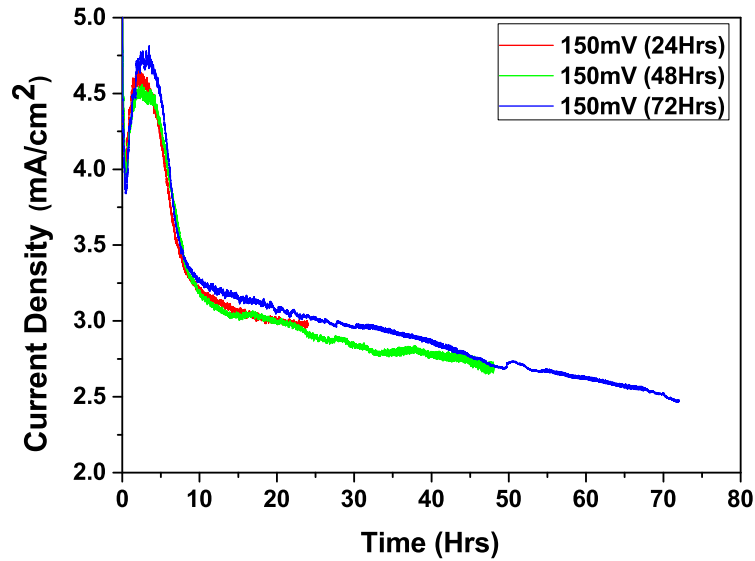


Figure 5.11: Current transient plot of 150mV Potentiostatic on X65 Carbon steel over a duration of 24h, 48h and 72h in unbuffered 3.5 wt.% NaCl solution saturated with CO₂ at 30°C.

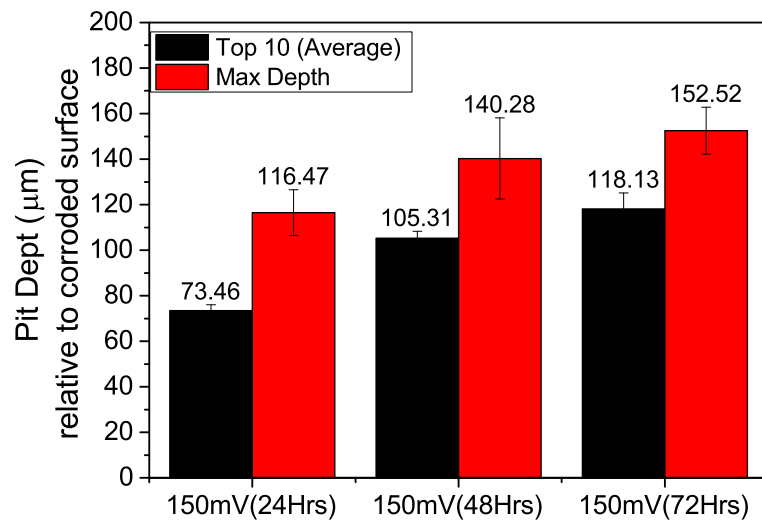


Figure 5.12: Pit depth analysis depicting average depth and maximum depth of samples subjected to 150mV potentiostatic at 30°C, unbuffered, 3.5wt% NaCl, CO₂ saturated for 24h, 48h and 72h.

5.13. The curve features an active trend with no passive region. Polarisation curve of X65 carbon steel under protective-film condition is at Figure 5.14. A polarisation curve under protective-film condition features active, pseudo-active and trans-active regions. The pseudo-active region of the potentiodynamic curve fell within potential

range of -600mV to -300mV vs Ag/AgCl. The measured OCP for the experimental condition was approximately -735mV vs Ag/AgCl. Setting the potentiostat to the over-potential range between 50mV to 150mV would conveniently be accommodated across the active and pseudo-active range in Figure 5.14. Hence, over-potentials of 50mV, 100mV and 150mV were applied to investigate effect of polarisation on passive trend. From the results featured in Chapter 5 of this work, 150mV potentiostatic polarisation perfectly suits the generation of repeatable stress-free pitting pattern of predictable depth on low carbon steel.

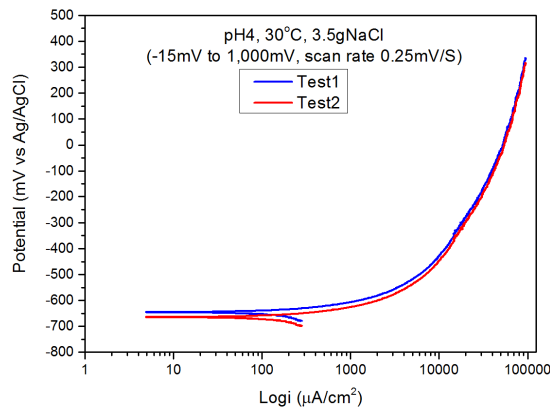


Figure 5.13: Polarisation curve of X65 carbon steel under film-free condition (pH 3.8, 30°C, 3.5wt% NaCl, -15mV to 1,000mV, scan rate 0.25mV/S, 250RPM).

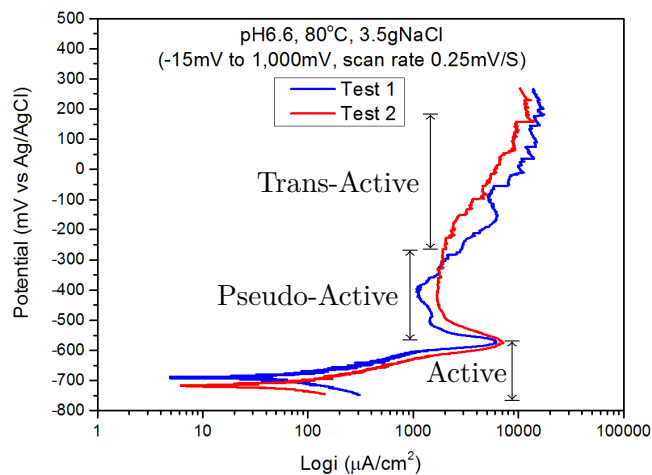


Figure 5.14: Polarisation curve of X65 carbon steel under protective film condition (pH 6.6, 80°C, 3.5%NaCl, -15mV to 1,000mV, scan rate 0.25mV/S, 250RPM).

SEM images of 50mV, 100mV and 150mV revealed pit formation was pronounced in samples polarised to 150mV (Figure 5.15). An increase in localised corrosion propagation amounts to higher current flow between anodic and cathodic sites

(Figure 5.1) while current drops implies less or no driving force to propagate localised attack [90]. XRD analysis of films formed on samples subjected to 150mV, where clear pitting was observed revealed presence of Fe_3C deposits. This matched with reference code 04-013-0091 in Highscore plus XPert analysis tool. The XRD image is shown in Figure 5.16.

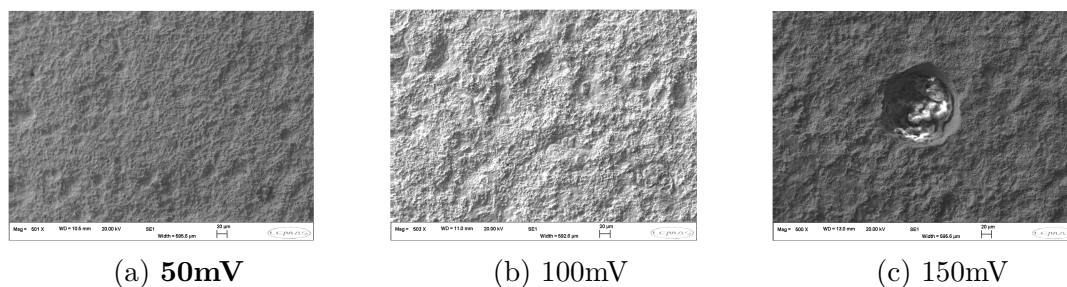


Figure 5.15: SEM images of corrosion pits formed on X65 carbon steel under (a) 50mV, (b) 100mV and (c) 150mV potentiostatics in 3.5% NaCl solution, pH 3.8, 30°C, P_{CO_2} of 1bar for 24h.

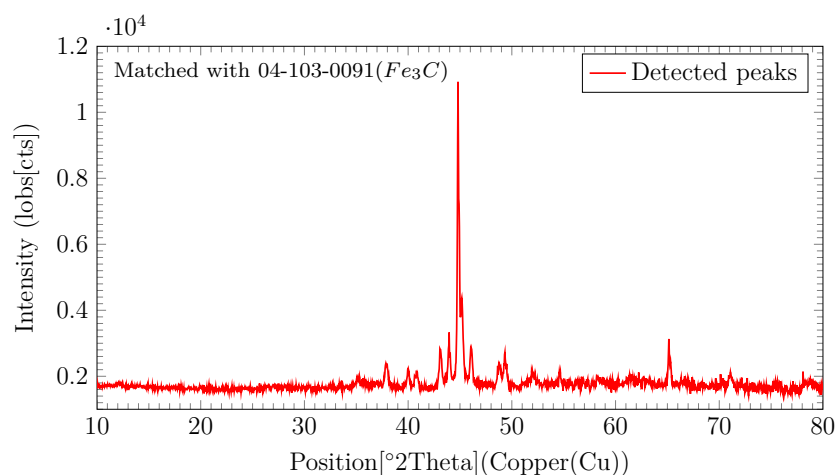


Figure 5.16: XRD pattern images of corrosion product formed on X65 carbon steel under 150mV potentiostatic in 3.5% NaCl solution, pH of 3.8, 30°C for 24 Hrs

SEM and Raman analysis were conducted to reveal information on corrosion products formed on the steel. SEM Images of corrosion film formed under 150mV potentiostatic is shown in Figure 5.17 while image obtained from Raman analysis is featured as Figure 5.18.

The two peaks featured at about 1345 and 1580 cm^{-1} are identified as D and G band of the Raman shift which indicate presence of Fe_3C deposits [228, 229]. $FeCO_3$ is not present in the film since no clear peak was observed within 1090 cm^{-1} Raman

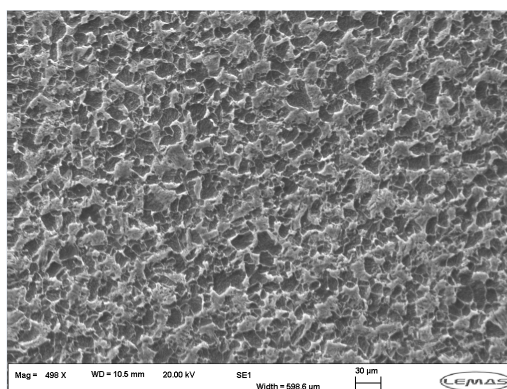


Figure 5.17: SEM image of corrosion products formed on X65 carbon steel under 150mV potentiostatics in 3.5% NaCl solution, pH of 4.0, 30°C for 24h.

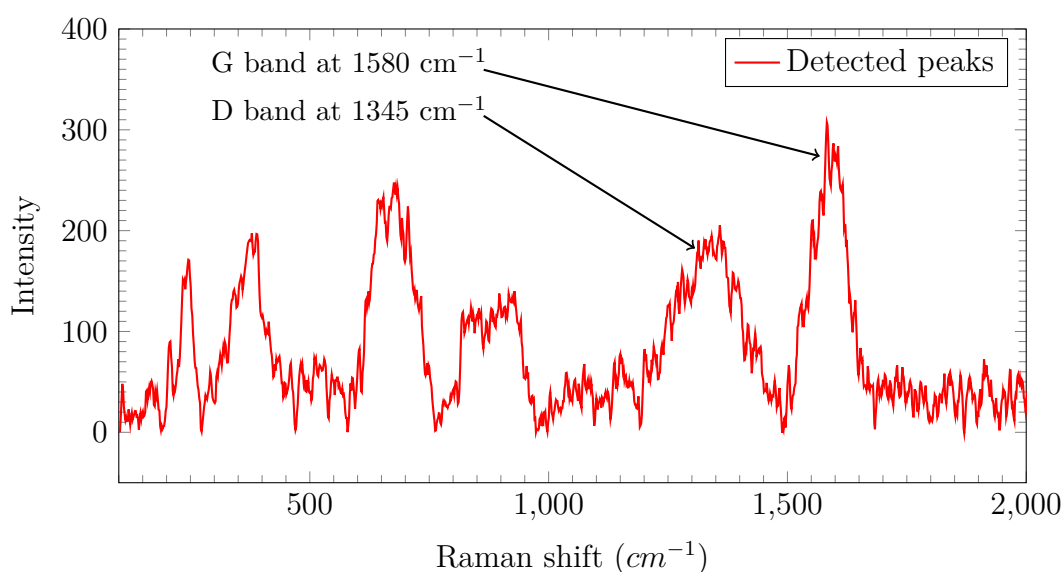


Figure 5.18: Raman image of corrosion products formed on X65 carbon steel under 150mV potentiostatics in 3.5% NaCl solution, pH of 4.0, 30°C for 24 Hrs.

shift [230, 231]. Pits were observed to grow through densely covered Fe_3C films as shown in Figure 5.19. This affirms that the Fe_3C layer formed was not protective. The non-protective nature of the Fe_3C film could be due to observed cracks in the morphology of Fe_3C film (Figure 5.20).

The presence of such gap affirms porosity on Fe_3C films [9] which could be attributed to galvanic coupling in line with earlier findings of Crolet et al. [118]. The gap provides pathways through which electrolyte have direct contact with the steel surface. From the SEM, XRD and Raman analysis conducted, No FeCO_3 was detected in the corrosion film as expected under the experiment conditions. The

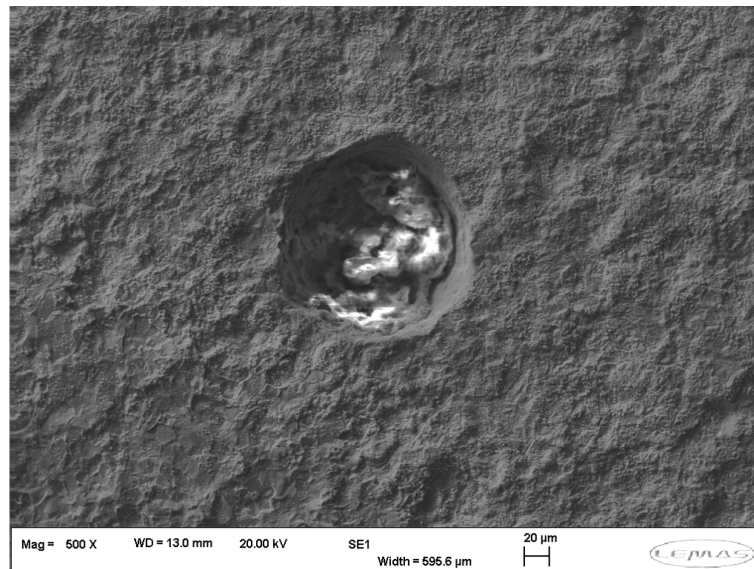


Figure 5.19: SEM images of corrosion products formed on X65 carbon steel under 150mV potentiostatics in 3.5% NaCl solution, pH of 4.0, 30°C for 24 Hrs under SEM Magnification of X500.

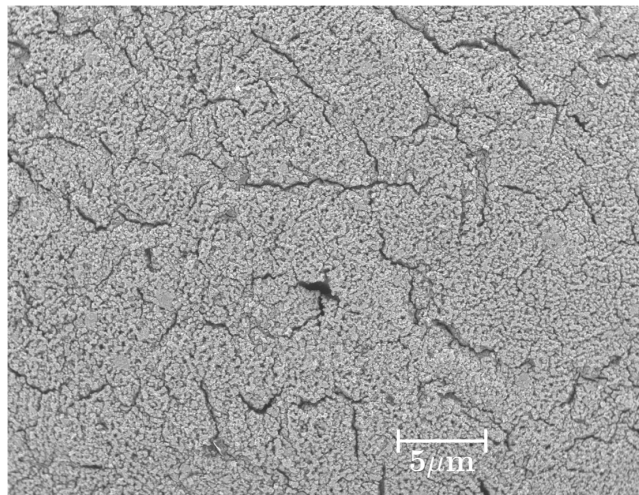


Figure 5.20: SEM images showing cracks in Fe_3C film on X65 carbon steel under 150mV potentiostatics in 3.5% NaCl solution, pH 3.8, 30°C for 24 h.

condition favours formation of Fe_3C films as revealed in the XRD and SEM images. The Fe_3C films covers the steel surface but did not prevent the electrolyte from making contact with the scale/steel interface. The Fe_3C rather produces coupling effect due to Fe_3C conductivity. Polarisation effect cause partial breakdown of the Fe_3C films which expose certain portions of the bare steel to the electrolyte. This creates additional coupling at the compromised site leading to deeper pit growth as exposure time increases. The high current density recorded at start

of the experiment could be attributed to high general corrosion before pitting became significant. The current decline particularly after 7 hours exposure under all test conditions suggest that general corrosion decrease significantly with time as enhanced pitting corrosion progresses on the test sample.

5.3.3 Statistical trend of discrete pit profiles

Profilometry analysis was utilised to obtain discrete data for statistical analysis of formed pits under 100mV and 150mV potentiostatic polarisation at 30°C where protective film is not expected. Only pits in thresholds above 5 μ m were considered for analysis. Table 5.3 depicts average value of roughness (R_a), pit depth (R_v), volume and diameter under selected experimental conditions. A summary of the major attributes of pit profile for 100mV and 150mV polarisation are provided in Table 5.3. It shows that average pit roughness, pit mouth diameter and void volume increase as applied potential and/ or exposure time increase. Details of discrete statistical plot of generated pit profiles for selected experimental conditions are provided in figures 5.21 to 5.23. Comparison of Figure 5.21 and Figure 5.22 shows that pit mouth diameter increase as applied potential increased. Maximum Pit mouth diameter of about 80 μ m (Figure 5.21a) and 120 μ m (Figure 5.22a) was respectively recorded for 100mV and 150mV potentiostatic. Similarly, maximum void volume of approximately 100,000 μ m³ (Figure 5.21b) and 250,000 μ m³ (Figure 5.22b) was recorded for 100mV and 150mV respectively. Positive slope of regression fit on plots of R_v versus volume implies linear relationship between pit depth and pit mouth diameter in all instances. R^2 of 0.03839 recorded for 150mV potentiostatic after 72h exposure (Figure 5.23a) suggests the tendency for non-linear relationship between pit mouth diameter and pit depth as exposure time increased. On roughness scale, R_a values of 150mV potentiostatic doubles that of 100mV (Figure 5.21c and (Figure 5.22c).

Effect of exposure time (under fixed potential) on pit profile value was considered by

Table 5.3: Applied potential and pit attributes

	R_a^* (μm)	R_v^{**} (μm)	Diameter* (μm)	Volume* (μm^3)
100mV(24h)	397.87	-50.74	15.279	-1945.34
150mV(24h)	1379.81	-141.44	23.89	-9785.25

* Average

** Maximum

R_a is the average of pit roughness, R_v is valley (dane) depth from reference plane, volume is a measure of void space created by pit while measured diameter is that of an imaginary circle circumscribed at pit mouth.

comparing Figure 5.22 and Figure 5.23. Table 5.4 summarise details of measured pit profile for 150mV potentiostatic over durations of 24h and 72h for ease of comparison. The trend shows that average pit roughness, pit mouth diameter and volume increase as application duration of potentiostatic polarisation is increased.

Table 5.4: Exposure time and pit attributes

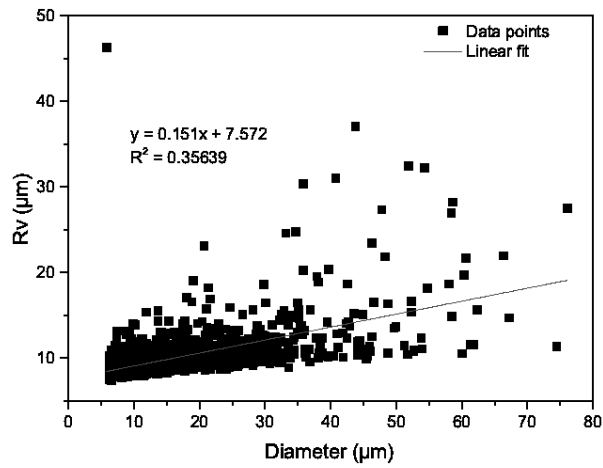
	R_a^* (μm)	R_v^{**} (μm)	Diameter* (μm)	Volume* (μm^3)
150mV(24h)	1379.81	-141.44	23.89	-9785.25
150mV(72h)	2562.91	-176.08	46.84	-21793.84

* Average

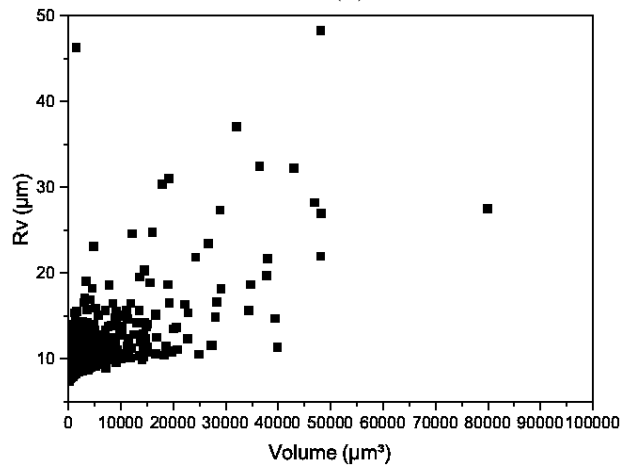
** Maximum

5.4 Potential induced pitting under protective film conditions

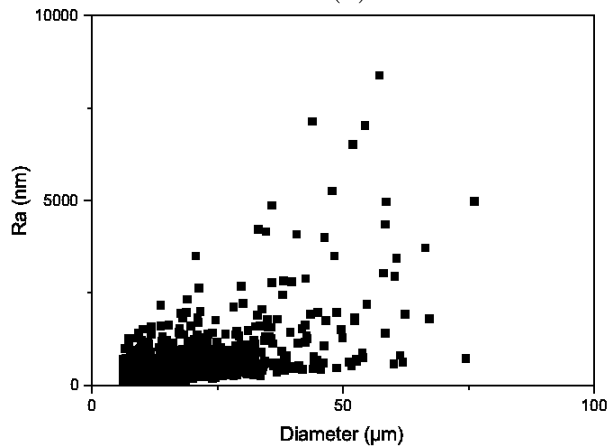
A test matrix for polarisation tests under protective film conditions is contained in Table 5.5. Potentiostatic experiments were conducted in conditions favouring $FeCO_3$ formation since such conditions are important in film build/repair process. The electrochemical response obtained after 24h of 50mV, 100mV and 150mV potentiostatic polarisation on X65 carbon steel samples at pH6.6, 80°C is shown in Figure 5.24. For 50mV potentiostatic, the current density attained a peak of



(a)



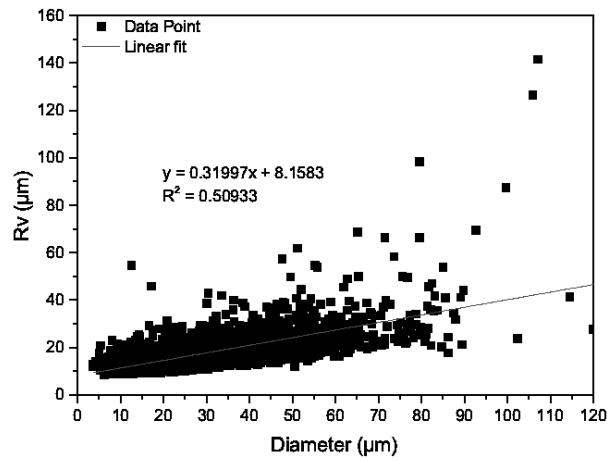
(b)



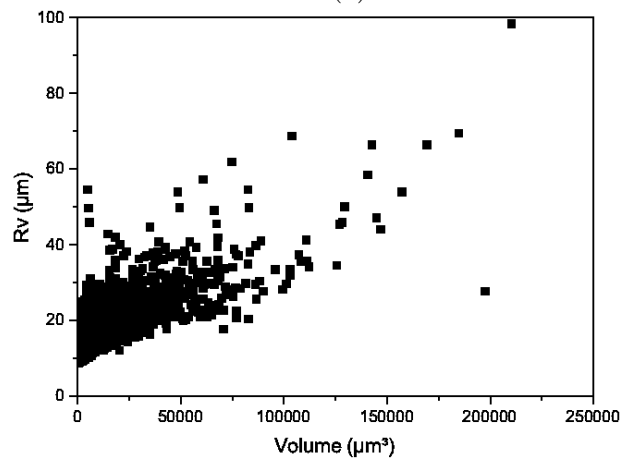
(c)

Figure 5.21: Statistical data showing discrete plots of (a) R_v versus Diameter, (b) R_v versus Volume and (c) R_a versus Diameter of corroded sample after 100mV polarisation in 3.5% NaCl solution, unbuffered, 30°C, P_{CO_2} of 1bar for 24h.

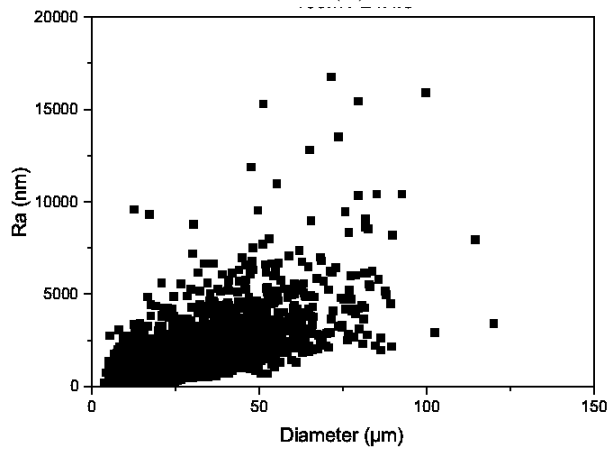
approximately $0.5\text{mA}/\text{cm}^2$ before dropping to zero while 100mV and 150mV attained peaks of $2\text{mA}/\text{cm}^2$ and $6.2\text{mA}/\text{cm}^2$ respectively. The higher peak trend however dropped to zero faster than lower peak trend. For instance Figure 5.24 shows that



(a)



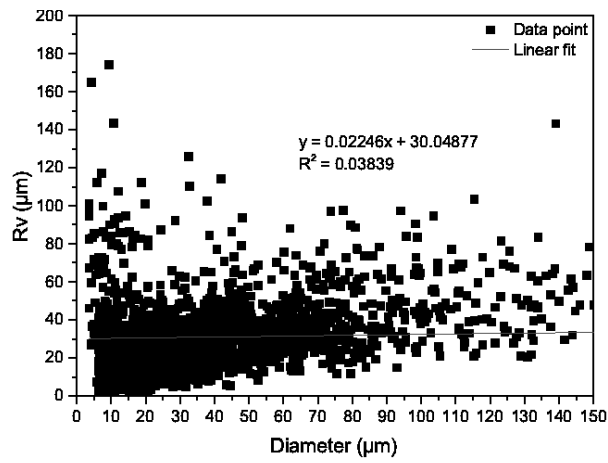
(b)



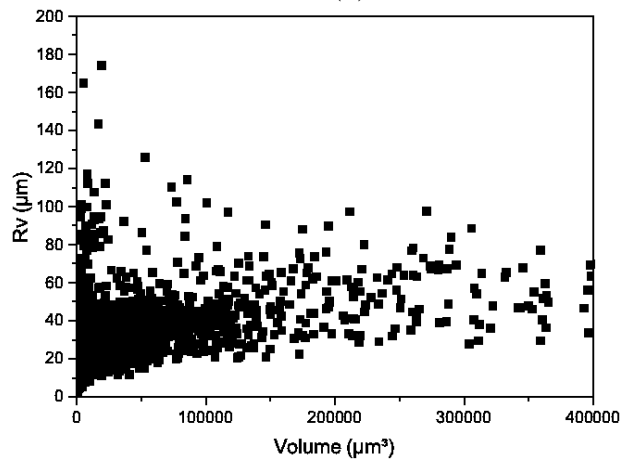
(c)

Figure 5.22: Statistical data showing discrete plots of (a) R_v versus Diameter, (b) R_v versus Volume and (c) R_a versus Diameter of corroded sample after 150mV polarisation in 3.5% NaCl solution, unbuffered, 30°C, P_{CO_2} of 1bar for 24h.

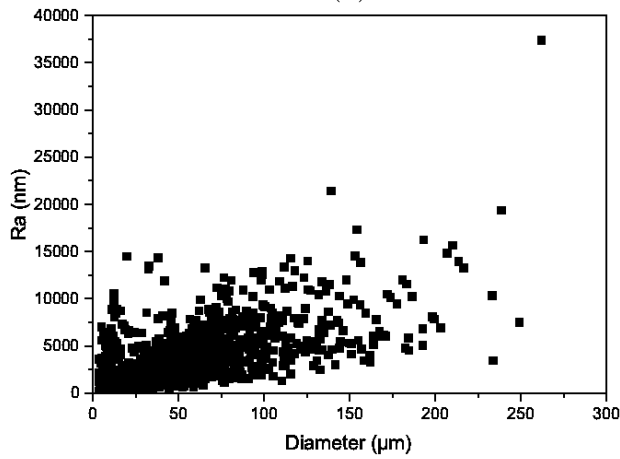
150mV potentiostatic attained peak of 6.2mA/cm² but dropped to zero value after about 10 minutes, 100mV dropped after 15 minutes while 50mV dropped to zero after about 1h. Under the three polarisation threshold (50mV, 100mV and 150mV),



(a)



(b)



(c)

Figure 5.23: Statistical data showing discrete plots of (a) R_v versus Diameter, (b) R_v versus Volume and (c) R_a versus Diameter of corroded sample after 150mV polarisation in 3.5% NaCl solution, unbuffered, 30°C, P_{CO_2} of 1bar for 72h.

current density approached zero magnitude barely 1 hr of tests conducted at 80 °C, pH 6.6. This suggests that high pH retards pitting process since higher pitting was recorded at higher temperature under same pH condition.

Table 5.5: Test matrix for polarisation tests under protective film condition

Item	Description	Value
Metal specification	X65 carbon steel	
	Surface area	2 x 1.121cm ²
	Test sample	2 per cell
Electrolyte condition	De-ionised water	1,000ml
	Brine conc	3.5 wt%
	pH	pH6.6
	Over potential	50mV, 100mV & 150mV
	Temperature	80°C
	Duration	24h

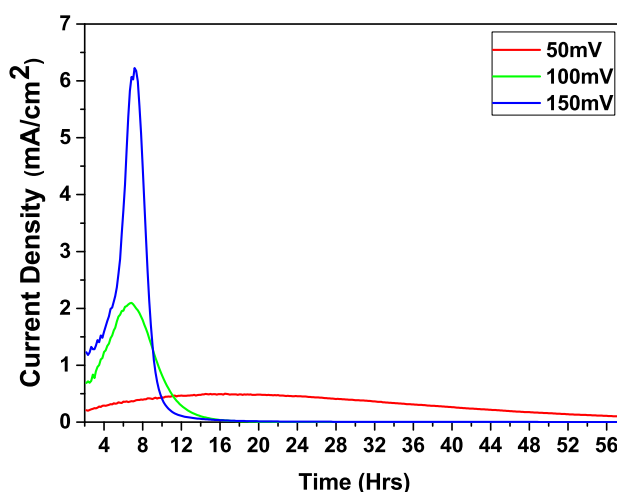


Figure 5.24: Current transient plot of 50mV, 100mV and 150mV Potentiostatic on X65 Carbon steel over a duration of 1h in 3.5 wt.% NaCl solution in saturated CO₂ at pH6.6, 80°C.

5.4.1 Analysis of pitting under protective-film conditions

The current density in the iron carbonate film conditions dropped sharply to zero after about 10 min, 15 min and 60 min respectively for 50 mV, 100 mV and 150 mV potentiostatic test. To further this investigation, 150 mV potentiostatic tests were conducted at conditions favouring FeCO₃ as well as other film-free conditions. The electrochemical responses are depicted in Figure 5.25.

Figure 5.25 shows that current density increases as temperature increases at low pH while current density decreases as temperature increases at high pH. Current density immediately attained zero value as FeCO₃ films build up at pH6.6, 80°C.

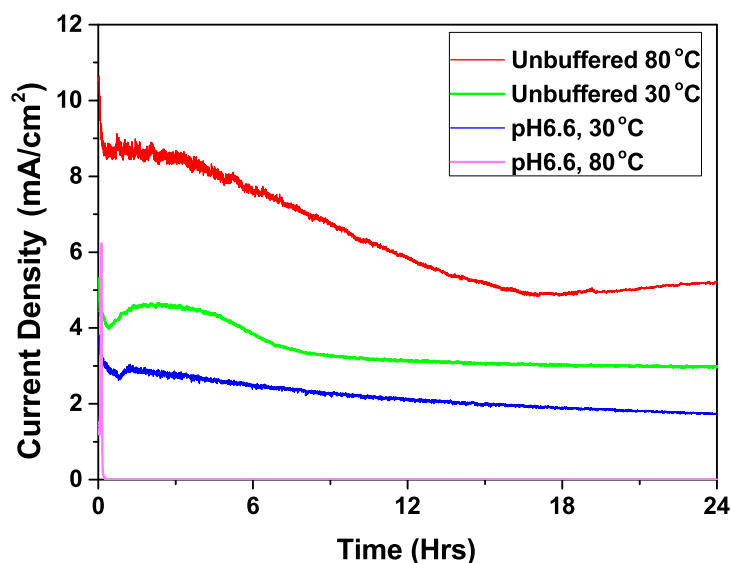


Figure 5.25: Current transient plot of 150mV potentiostatic on X65 Carbon steel over a duration of 24h in 3.5 wt.% NaCl in saturated CO₂.

This confirms the protective nature of FeCO₃ films. Similarly, pit count from NPflex showed that no significant pitting was recorded on samples subjected to 50 mV, 100 mV and 150 mV potentiostatic polarisation for 24 h under FeCO₃ build-up condition as depicted in Figure 5.26. This implies that unlike in non-scaled conditions, no significant pitting was recorded under FeCO₃ build-up condition. An increase in applied potential also has a negligible effect on pitting.

The red and green trend featured in Figure 5.25 are current density magnitude for 150mV potentiostatic polarisation in unbuffered solution at 80°C and 30°C respectively. Higher current density was recorded at high temperature indicating that temperature rise promotes pitting at low pH. The blue and pink trend in Figure 5.25 show magnitude of current density trend for 150mV potentiostatic at pH6, 30°C and pH6, 80°C respectively. Protective FeCO₃ film formed on sample surface in the latter due to high temperature at pH6. Interestingly, current density recorded under conditions favouring formation of FeCO₃ was of null magnitude (pink trend). Low pit depth recorded after test suggests that the electro-chemistry in FeCO₃ film condition offers resistance for pit initiation and growth despite with polarisation

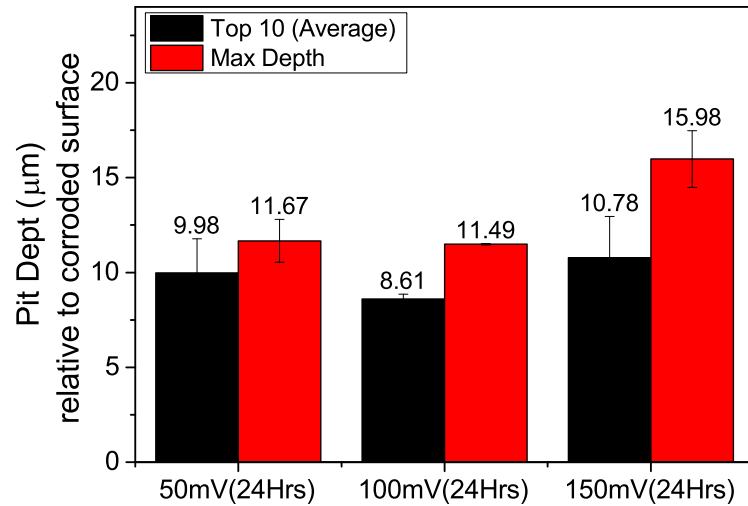


Figure 5.26: Chart depicting average pit depth and maximum depth of samples subjected to 50mV, 100mV and 150mV potentiostatic at 80°C, pH6.6, 3.5wt% NaCl, CO₂ condition for 24h.

threshold of 150mV. Pitting is however likely to be well pronounced under higher polarisation range. The green and blue trend lines in Figure 5.25 can be interpreted to explain the influence of pH on pitting trend. With both temperature at 30°, The green trend line (unbuffered solution) recorded higher current than the blue (pH6). This implies that pitting threshold reduces as pH increases.

5.5 Conclusions

Potentiostatic polarisation was investigated for its application to generate reliable stress-free stochastic pitting of predictable depth. The following key findings were made:

- a. The application of anodic potential was shown to accelerate both general and pitting corrosion, but to different extents (depending upon applied potential) in relation to their contribution towards total material loss from the steel surface.

- b. Potentiostatic polarisation between 50 and 150mV at pH 3.8 and 30°C in a CO₂ environment was shown to generate reproducible pits, which were stress free.
- c. Average pit depth increased linearly with increase in applied potential in the range of 50 to 150mV, with 150mV producing the more repeatable and deepest pits averaging 70µm.
- d. The pitting factors associated with polarised samples agreed with those obtained in literature in similar CO₂ environments, demonstrating that the polarisation effect produces the correct balance between the relative thickness losses associated with both general and pitting corrosion on the steel surface for pit propagation studies.
- e. Transfer of the polarised samples into test solutions at 80°C for 48h showed that the developed pits continued to propagate, indicating the potential of this technique in performing pit propagation studies in reasonable time-frames.
- f. Potentiostatic polarisation is suitable for generating repeatable shallow pits in low carbon steel.
- g. Pitting in low carbon steel reduces as pH increases at low temperature.
- h. Pitting in low carbon steel increase with rise in temperature under film-free conditions.
- i. Pitting increase with increase in applied potential at conditions where FeCO₃ film is not favoured.
- j. Pitting propagation rate reduce as exposure time increase.
- k. Pitting in low carbon steel reduce significantly under protective film conditions.

Chapter 6

Effect of calcium on X65 carbon steel corrosion in saturated CO₂ environment

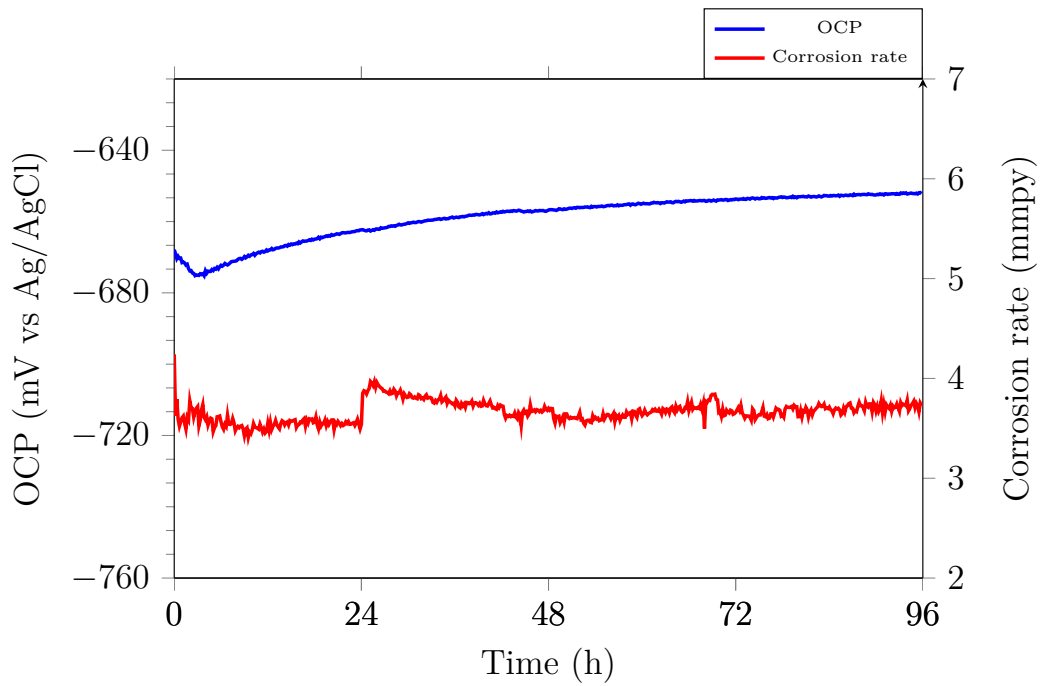
6.1 Introduction

Events in storage tanks and down-time in liquid aquifers promote pit growth beneath calcium rich layers. Pits could manifest from electrochemical events or manufacturing activities such as turning operations, finishing or handling [232] and later propagate during in-service life in a Ca²⁺ rich environment. Similarly, lines and tanks are often cleaned during product interchange or after maintenance shut-down where undetected pits could eventually lead to rupture as production resumes. This lends credence for the need to understand how Ca²⁺ influences pitting kinetics of pre-existing pits, which is likely to be different from that in which initiation and propagation occur under same environment or condition. In addition, Ca²⁺ exists as CaCO₃ and as mixed $Ca_xFe_{(1-x)}CO_3$ in oil field environments. Different polymorphs of CaCO₃ have been reported [147, 148, 149, 150, 151, 152, 153, 154] in literature but no experimental work or theoretical model that has considered how the

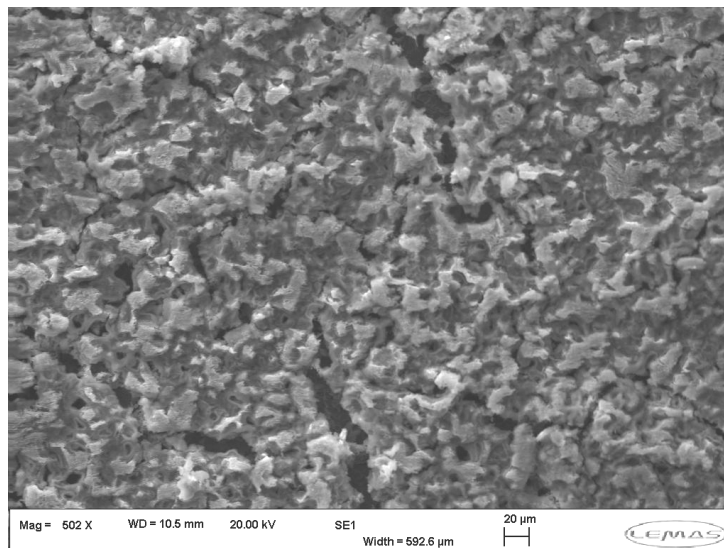
different CaCO_3 polymorphs influence pitting in low carbon steel. In this work, an experimental investigation was conducted to unravel the influence of Ca^{2+} on growth of stochastic micro pits in order to understand how some CaCO_3 polymorphs affect carbon steel pitting. Investigations were conducted under near static conditions to mimic events in crude oil storage environment and down time scenarios in saline aquifers and other oil & gas exploration settings.

6.2 Pitting in 0 ppm Ca^{2+}

Stochastic pits whose top-10 average measures $70\mu\text{m}$ were generated using the technique presented in Chapter 5 of this thesis. The pitted samples were later transferred into calcium and calcium-free solutions to access the pit growth. As a base-line measurement, pit growth was examined for pitted samples in solutions with 0 ppm Ca^{2+} at 80°C in pH 6 as well as solution at pH 3.8. A corrosion rate of about 3.67 mmpy was recorded on pitted samples at pH 3.8 while the potential increased slightly as corrosion product began to form on the sample surface as shown in Figure 6.1. The LPR/OCP plots for samples in the solution at pH 6 are shown as Figure 6.2. The potential level was observed to increase progressively as protective FeCO_3 forms on the sample surface. The corrosion rate of the pitted sample drops below 0.05 mmpy as films became more protective. Films formed at pH 6 are more protective than the Fe_3C network observed at pH 3.8. Profilometry results on the corroded surface revealed higher pitting at pH 3.8 than at pH 6. A bar chart depicting the pitting trend based on the top-ten average measurement of pits is shown in Figure 6.3. Low corrosion current density and low pitting recorded at pH 6 was due to the formation of protective FeCO_3 which created a barrier between the sample surface and the bulk solution. Corrosion product formed at pH 3.8 was not protective thereby enabling the bulk solution to interact freely with the metal. Hence high corrosion current and pitting are recorded at low pH.



(a) LPR/OCP (pH 3.8)

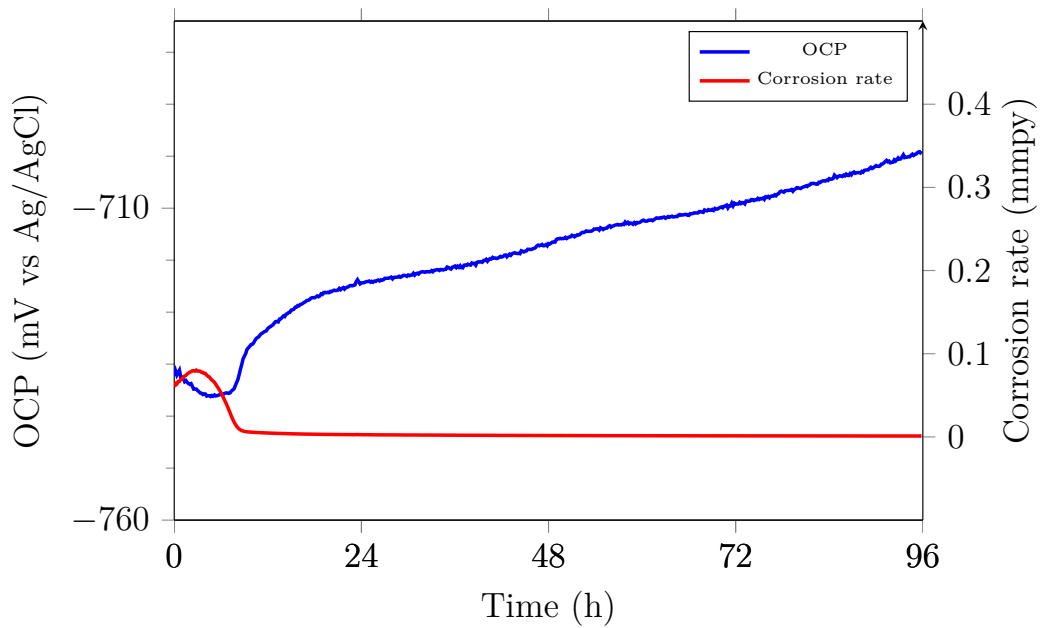


(b) Top-view SEM (pH 3.8)

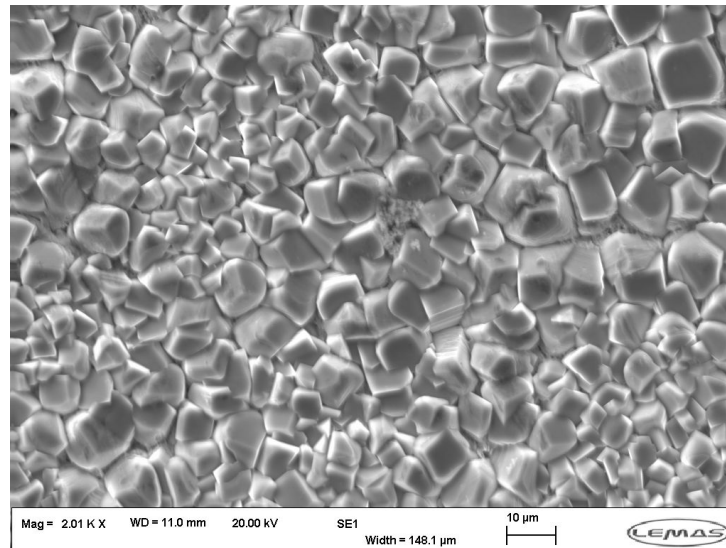
Figure 6.1: LPR/OCP and top view SEM image featuring corrosion products formed on pitted X65 carbon steel in saturated CO_2 , 3.5 wt% NaCl, 0 ppm Ca^{2+} , 80 °C over a duration of 24 h for pH 3.8

6.3 Effect of pH on Calcium Pitting at 80 °C

The effect of pH on calcium pitting was investigated by corroding pitted samples in 5,000 ppm Ca^{2+} at 80 °C, pH 3.8 and pH 6 for 96 h. LPR/OCP plots for the calcium tests at 80 °C are as shown in Figure 6.4. Corrosion rates of about 5.06 mmpy and



(a) pH 6



(b) Top-view SEM (pH 6)

Figure 6.2: Corrosion rate plot and top view SEM image featuring corrosion products formed on pitted X65 carbon steel in saturated CO_2 , 3.5 wt% NaCl, 0 ppm Ca^{2+} , 80 °C over a duration of 24 h for pH 6

0.788 mmpy respectively were recorded for pH 3.8 and pH 6 in the presence of calcium. Comparing Figure 6.4 to Figures 6.1 and 6.2, corrosion rates measured in Figure 6.4, containing Ca^{2+} are higher. This was probably due to the porous nature of the mixed $\text{Ca}_x\text{Fe}_{(1-x)}\text{CO}_3$ film that formed on the steel surface. The porosity permits the interaction of the bulk solution with the steel surface, therefore recording

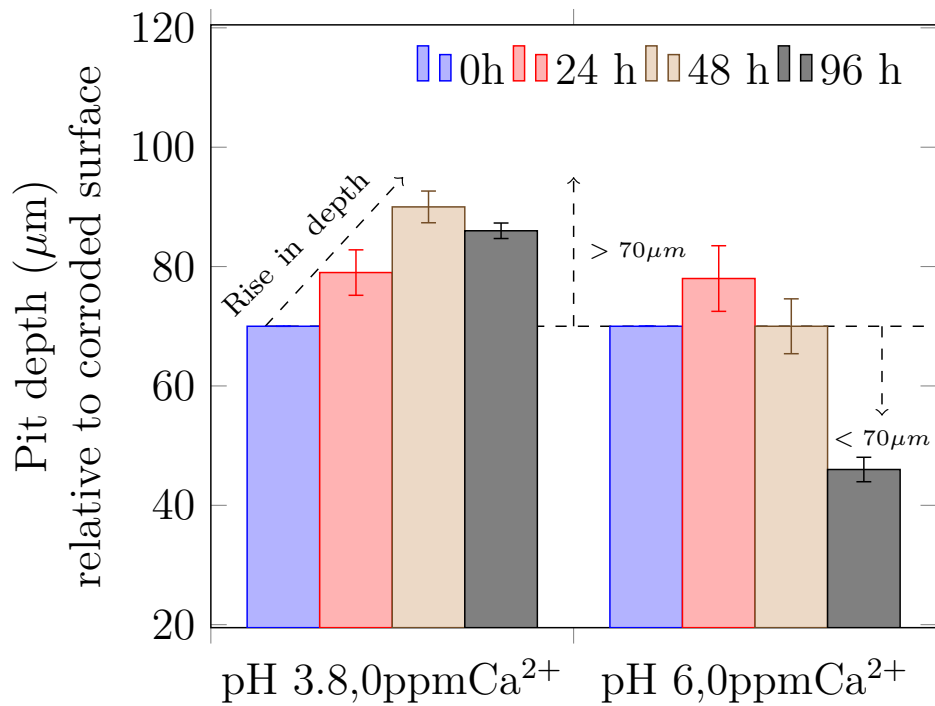
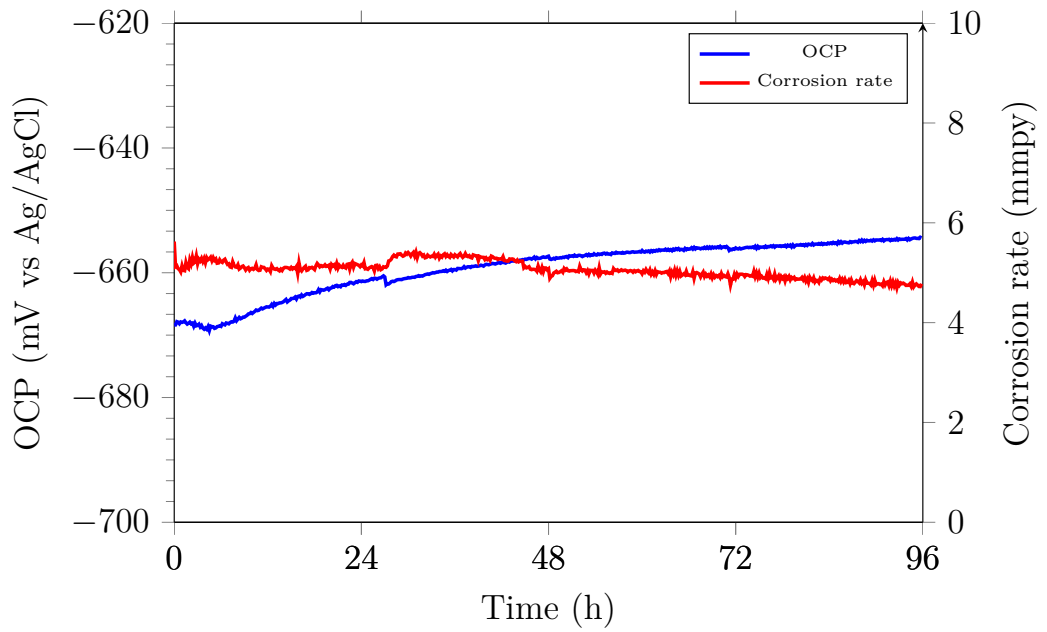
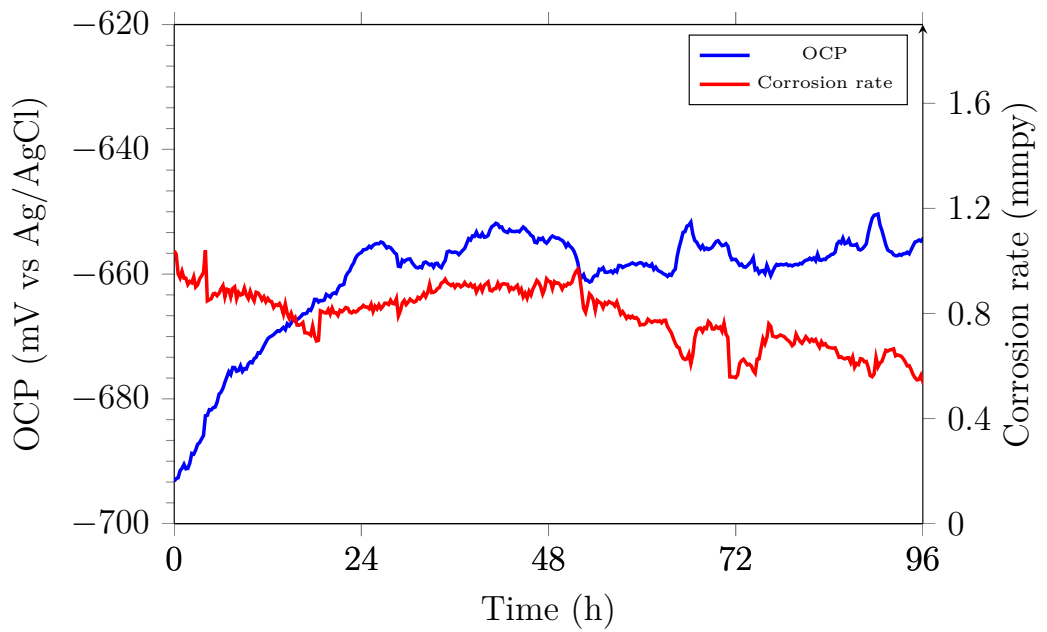


Figure 6.3: Bar chart depicting pitting trend (top-10 average) of pits from initial 70 μm depth in saturated CO_2 , 3.5 wt% NaCl, 0 ppm Ca^{2+} , 80 $^\circ\text{C}$ over a duration of 4 days at pH 3.8 and pH 6

a higher corrosion rate compared to when FeCO_3 films formed on the steel surface. A look at Tafel plots featured in Appendix C also show higher current density for solutions containing Ca^{2+} than for solutions without Ca^{2+} . This implies that calcium increases the corrosion rate as reported in other literature [233]. This suggests that Ca^{2+} influence anodic dissolution of Fe^{2+} in Ca^{2+} rich solutions. A bar chart showing the depths of the top-10 average pits in Ca^{2+} conditions for tests conducted at pH 3.8 is shown along with pH 6 results in Figure 6.5. Pit depth measured at this point was relative to corroded surface. Pit growth was generally higher at pH 3.8 than at pH 6 except for that at 96 h. A slight drop in pitting that was observed after 96 h at pH 3.8 was probably due to the growth of aragonite which started forming after 48 h exposure (covered in section 6.3.1). A look at Figure 6.4(a) reveals a higher corrosion rate than Figure 6.4(b), where $\text{Ca}_x\text{Fe}_{(1-x)}\text{CO}_3$ tends to form on the steel surface [159]. This is in line with findings by Tavares et al. [153] who recorded high anodic polarisation resistance and low i_{corr} for $\text{Ca}_x\text{Fe}_{(1-x)}\text{CO}_3$ scales. Figure 6.1(a) (0ppm Ca^{2+} , pH 3.8) recorded lower corrosion rate than Figure 6.4(a)



(a) pH 3.8



(b) pH 6

Figure 6.4: LPR/OCP plot of X65 carbon steel corroded in 2 wt% NaCl, 5000 ppm Ca^{2+} at 80 °C for 96 h in (a) pH 3.8 (b) pH 6.

(5,000ppm Ca^{2+} , pH 3.8). This suggests that calcium plays significant role in the corrosion process. Similar trend was observed for Figure 6.2(a) (0ppm Ca^{2+} , pH 6) and Figure 6.4(b) (5000ppm Ca^{2+} , pH 6) where higher corrosion rate was recorded in the latter.

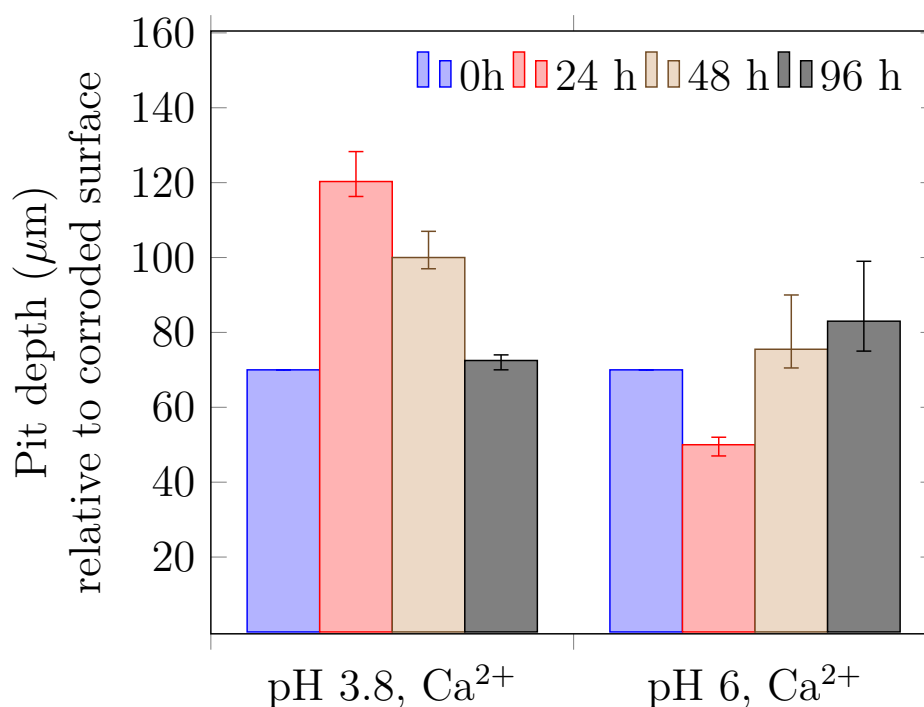


Figure 6.5: Bar chart depicting pitting trend (top-10 average) of pits from initial 70 μm depth in saturated CO_2 , 5000 ppm Ca^{2+} , 80 $^\circ\text{C}$ over a duration of 4 days at pH 3.8 and pH 6

6.3.1 Calcium pitting at low pH

Potentiostatic induced pits grew significantly from initial 70 μm to top-ten average depths of 120 μm , 100 μm and 72 μm after 24 h, 48 h and 96 h respectively after exposure in 5,000 ppm Ca^{2+} solution at 80 $^\circ\text{C}$, pH 3.8 (Figure 6.5). The interferometry profile of the maximum pit recorded under the calcium influence at pH 3.8 is shown in Figure 6.6. The maximum pit profile corroborates the top-ten average trend; that pits grow significantly after 24 h but pit depth begins to reduce beyond this point, probably due to high general corrosion on the surface of the metal. It is important to note that a drop in the measured pit depth is relative; actual depth can only be ascertained once penetration (metal thinning) due to general corrosion is accounted for. It is apparent that general corrosion can mask pitting rate with time.

XRD spectra of formed products were examined to understand the nature of film deposited on the corroded samples. The XRD patterns of corrosion products formed

at pH 3.8 are shown in Figure 6.7. The XRD peaks at $31.8^{\circ}2\theta$ reveals semblance of calcite [234, 235] on first 2 days of exposure while aragonite peaks were present after 4 days corrosion in Ca^{2+} solution at pH 3.8. Emergence of aragonite after 4 days of exposure was further investigated by SEM.

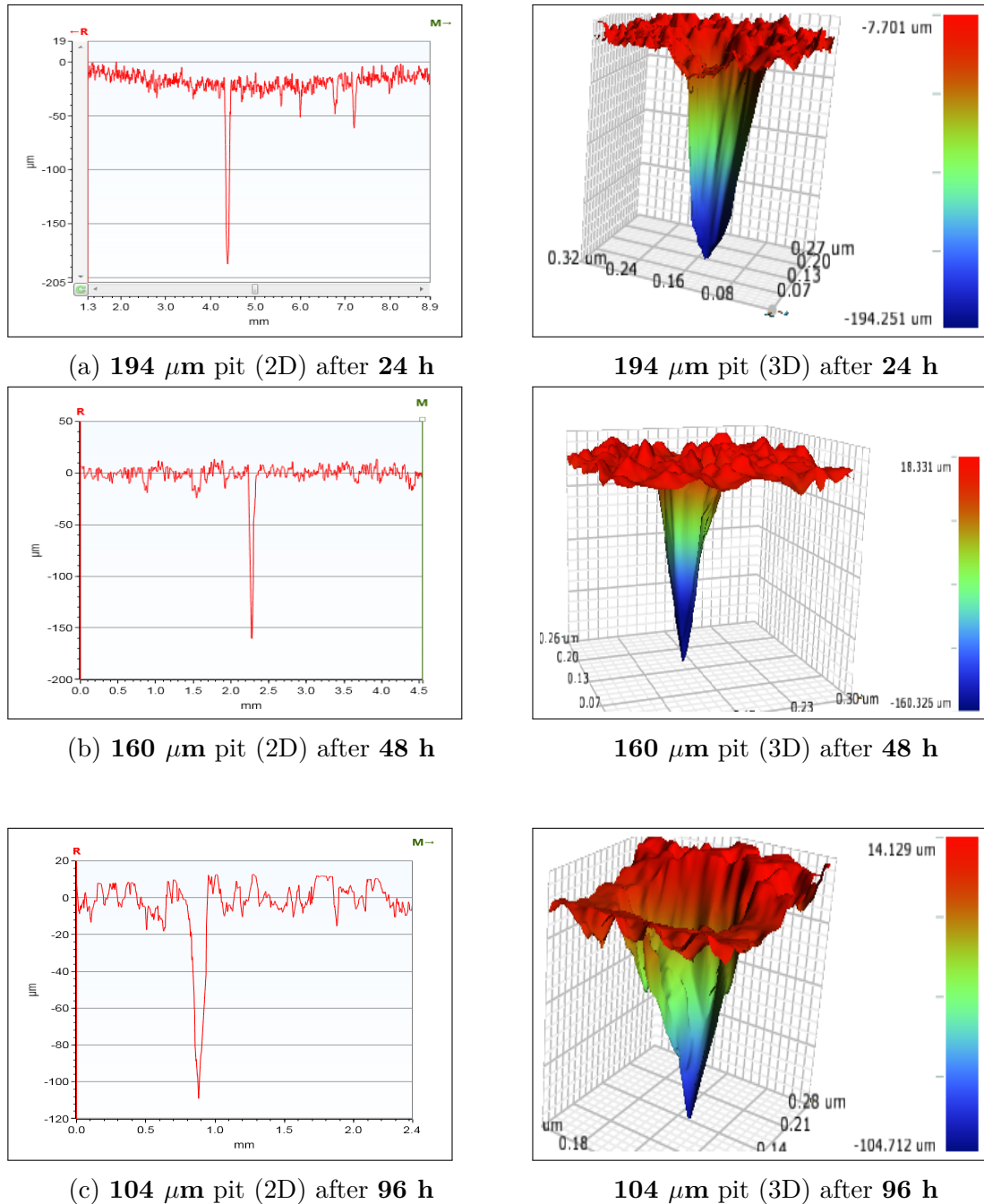


Figure 6.6: White light profilometry images showing maximum pit depth recorded after $70\ \mu\text{m}$ pit was corroded in saturated CO_2 , 2 wt.% NaCl, 5000 ppm Ca^{2+} , pH 3.8, $80\ ^{\circ}\text{C}$ for (a) 24 h, (b) 48 h and (c) 96 h exposure. Measurements relative to corroded surface.

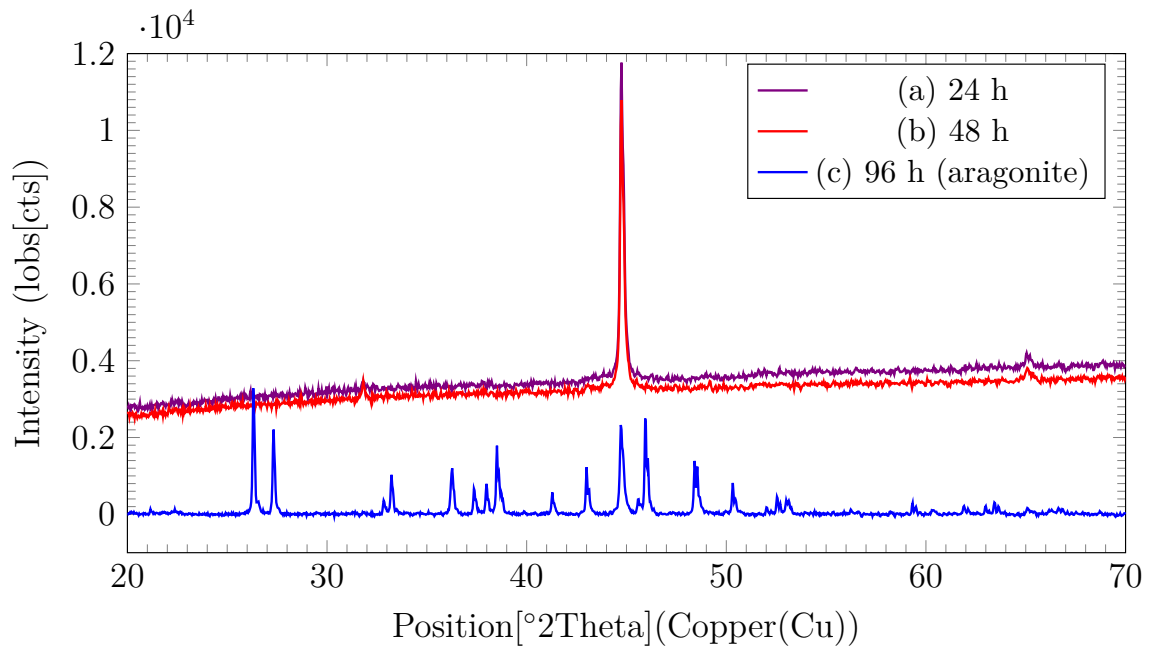
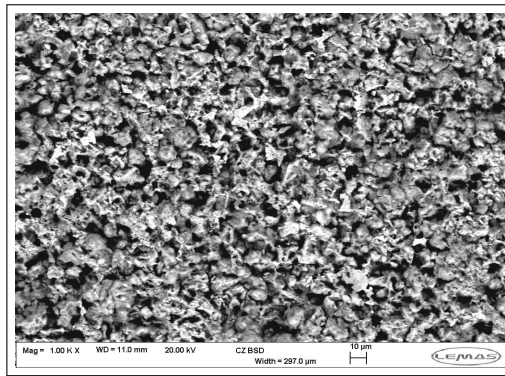
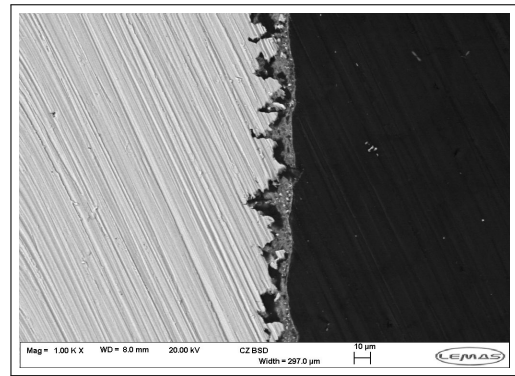


Figure 6.7: XRD scan pattern of formed product on X65 carbon steel corroded in saturated CO_2 , 2 wt% NaCl, 5,000 ppm Ca^{2+} , 80 °C, pH 3.8, for (a) 24 h, (b) 48 h, (c) 96 h.

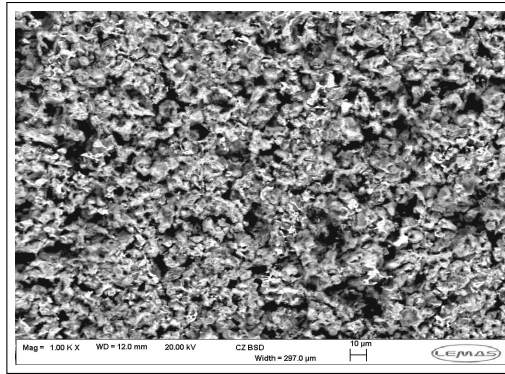
SEM images of corroded samples at pH 3.8, featured in Figure 6.8 do not give convincing information on products deposited after the first 48 h of exposure. Though the XRD pattern revealed traces of CaCO_3 after 48 h. This however fell within the noisy range in the scan. This was probably due to the fact that Fe^{2+} dissolution inhibited calcite formation on the steel surface [236, 237]. Raman investigation shown at Figure 6.9 however featured CaCO_3 peaks after 48 h of exposure. It implies that CaCO_3 formed after first 48 h was amorphous and not fully crystalline in nature. Needle-shaped aragonite was confirmed after 96 h exposure in Ca^{2+} solution at 80 °C, as Fe^{2+} does not inhibit formation of aragonite [236, 237]. The film formed shortly before emergence of crystalline aragonite was likely to be mainly amorphous CaCO_3 since amorphous precursor polymorphs often precede and determine growth of crystalline polymorph [238, 239]. Crystalline aragonite lines the pit walls tightly and limits interaction between pit and bulk electrolyte as shown in Figure 6.18(a). General corrosion however continues to progress thereby translating to apparent pit healing as pit measurement by interferometer was relative to corroded surface. From the cross section view shown in Figure 6.8, pits are seen



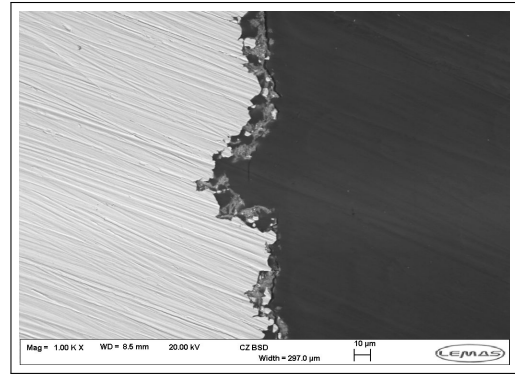
(a) 24 h - Amorphous CaCO_3



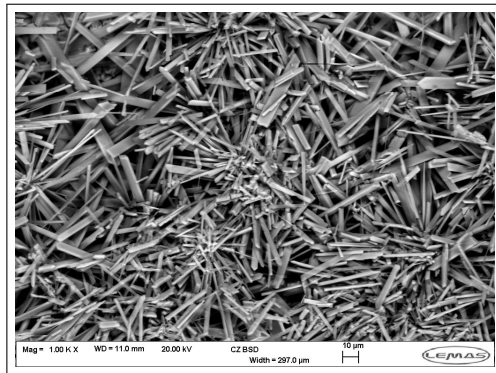
24 h - Cross section



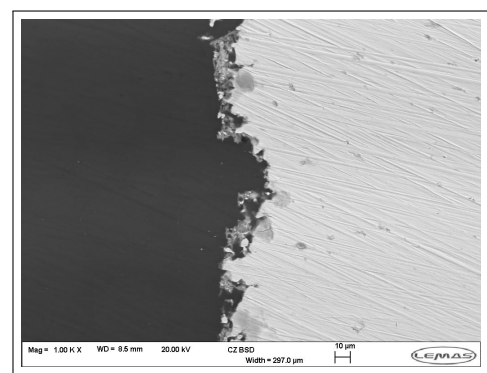
(b) 48 h - Amorphous CaCO_3



48 h - Cross section



(c) 96 h - Aragonite



96 h - Cross section

Figure 6.8: Top view SEM image and cross section featuring corrosion products formed on X65 carbon steel in saturated CO_2 , 2 wt.% NaCl, 5000 ppm Ca^{2+} , 80 °C, pH 3.8 over a duration of (a) 24 h (b) 48 h and (c) 96 h

to widen as exposure time increased. This could be due to presence of Ca^{2+} in corrosion products that lined the wall of pits. Comparison of calcite and aragonite molecular structure reveals hexagonal coordinate for calcite while aragonite forms in 9 coordinate environment as shown in Figure 6.10 [152]. Calcite hexagonal structure are less compact than that of aragonite which could be a possible explanation for the difference in pitting kinetics under both conditions.

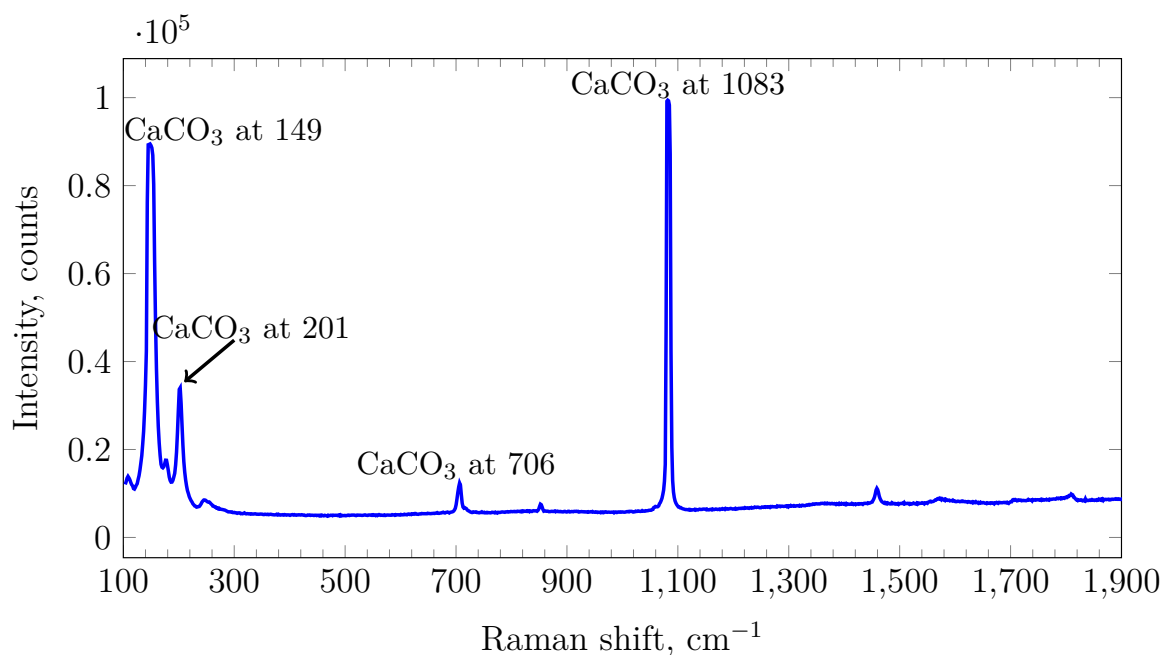
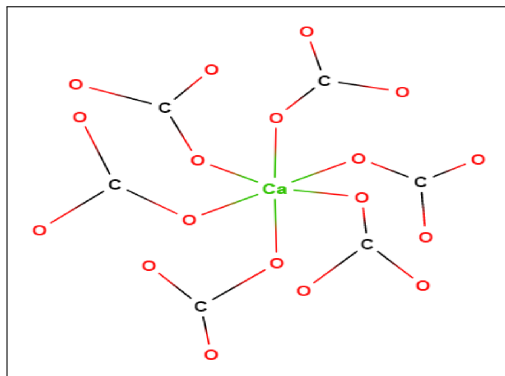
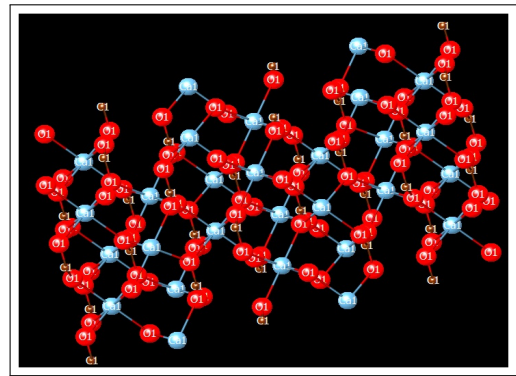


Figure 6.9: Raman image of corrosion product formed on X65 carbon steel corroded in saturated CO_2 , 2 wt% NaCl, 5,000 ppm Ca^{2+} , 80 °C over a duration of 72 h at pH 3.8

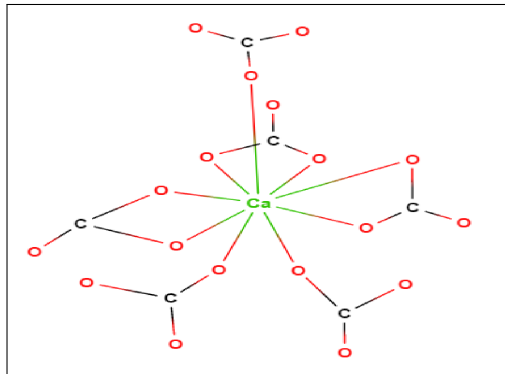
CaCO_3 features in several polymorphic forms while factors determining type of formed polymorph remain debatable [241, 242]. Calcite and aragonite are common CaCO_3 polymorphs which sometimes co-precipitate (Figure 8.9(b)) but high CO_2 bubbling is known to favour formation of aragonite [241]. Calcite and aragonite will normally precipitate at the same rate if both evolve together [243]. Concentrations of $\text{Ca}^{2+}/\text{CO}_3^{2-}$ are important parameters that determine the nature of crystalline polymorph formed on steel surface [244]. As calcium complexes form in solution, amorphous calcium carbonate (ACC) being the least stable polymorph will precipitate first in accordance with the Ostwald's step rule [239]. ACC however rapidly transforms into calcite which is a more stable polymorph [245, 239]. The electrochemical environment influences the morphology and attributes of the formed product [246]. Relating Figure 6.6 with Figure 6.8 reveals that pit growth declines as amorphous CaCO_3 transforms to aragonite. A cross section view of aragonite shown in Figure 6.11 shows aragonite densely lined the pit mouth and occupied the pit cavity probably due to its needle-like structure. EDX mapping across the deposited aragonite featured in Figure 6.12 and line scan (Figure 6.13) revealed



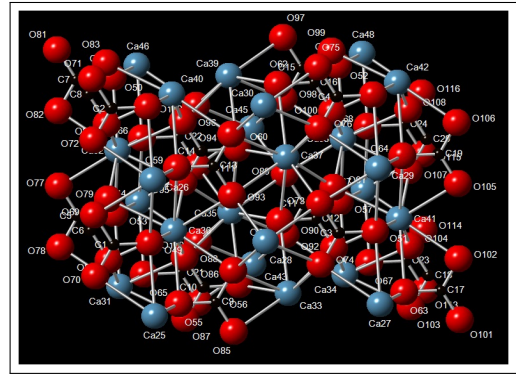
(a) Calcite structure



Calcite - 3D image



(b) Aragonite structure



Aragonite - 3D image

Calcite - Ca atom linked to six O₂ atoms from six different (CO₃²⁻) group

Aragonite - Ca atom linked to nine closely packed O₂ atoms from six different (CO₃²⁻) group [240]

Figure 6.10: Polymorphs of calcium carbonate showing (a) calcite in six coordinate and (b) aragonite in 9 coordinate environment. Images were generated using molview and CrystalMaker9

consistent Ca²⁺ presence from pit mouth to pit base. Reduced pitting beneath aragonite polymorph could therefore be due to needle-like aragonite that fills the entire pit and thereby disrupts electrolyte interaction with the pit wall. A look at Figure 6.12 shows pitting progressing in different directions making it difficult to accurately predict the likely axis of growth in the steel lattice structure. This suggests that the steel micro-structure influence pitting kinetics in low carbon steel. It could imply that pitting preferentially progress along ferrite-rich regions in the steel crystal while Fe₃C left from the pearlite region becomes obvious afterwards.

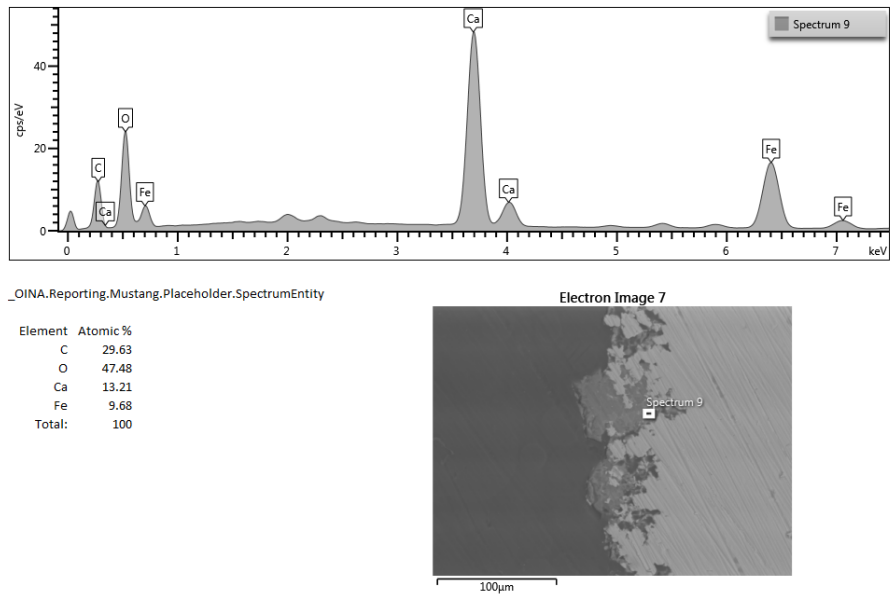


Figure 6.11: Cross section showing Ca^{2+} inside a pit on X65 carbon steel corroded at 2 wt% NaCl, 5,000 ppm Ca^{2+} , 80 °C for 96 h at pH 3.8

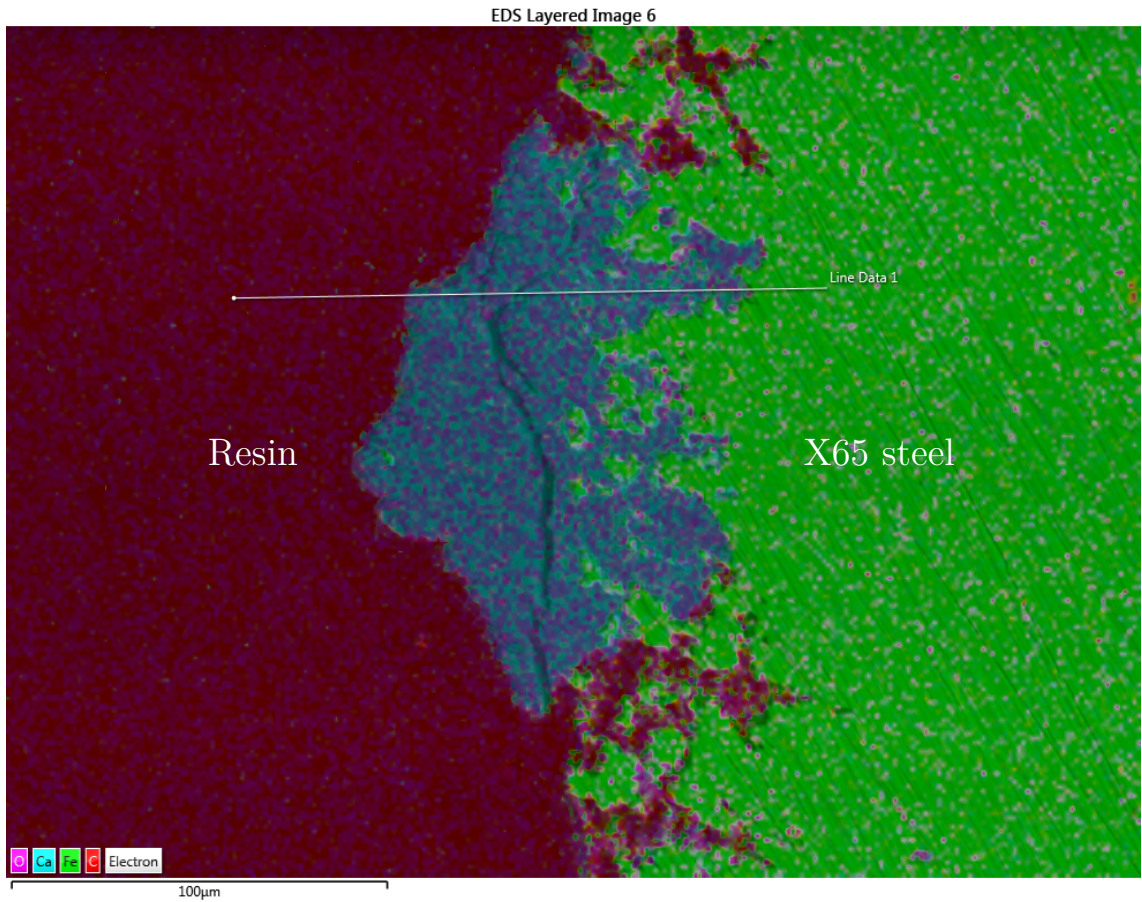


Figure 6.12: EDX mapping showing Ca^{2+} inside a pit on X65 carbon steel corroded at 2 wt% NaCl, 5,000 ppm Ca^{2+} , 80 °C for 96 h at pH 3.8

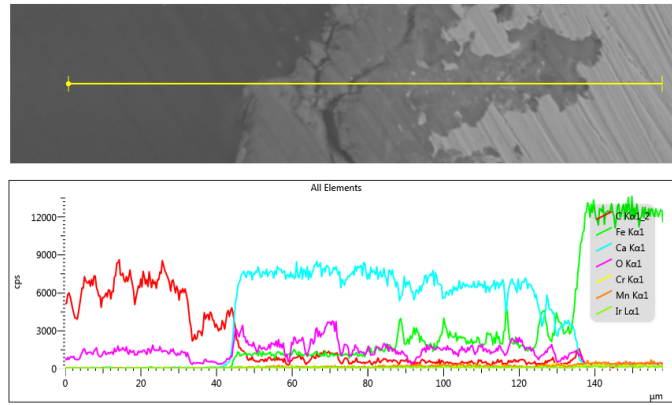


Figure 6.13: EDX line scan showing Ca^{2+} inside a pit on X65 carbon steel corroded at 2 wt% NaCl, 5,000 ppm Ca^{2+} , 80 °C for 96 h at pH 3.8

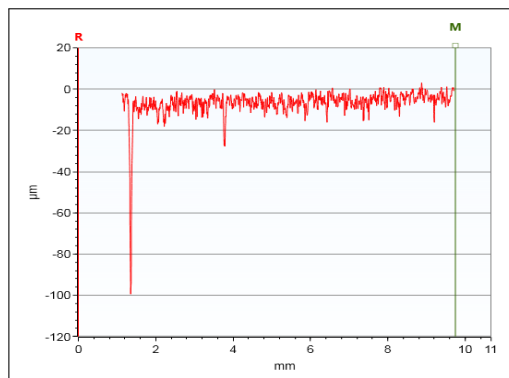
6.3.2 Calcium pitting at high pH

X65 carbon steel sample was first subjected to 150mV potentiostatic polarisation for 24 h and later transferred to calcium solution to investigate pit growth at pH 6, 80 °C. Solution pH was observed to drop progressively due to release of H^+ and Fe^{2+} resulting from corrosion [233] and as $\text{CaCO}_3(\text{s})$ precipitates when $\text{Ca}^{2+}(\text{aq})$ reacts with $\text{H}_2\text{CO}_3(\text{aq})$. This is in agreement with the work by Navabzadeh et al. [146] who investigated the influence of Ca^{2+} on FeCO_3 formation and protectiveness. Maximum pit recorded after 70 μm pits were corroded in Ca^{2+} solution at pH 6, 80 °C is shown in Figure 6.14. A bar chart depicting the top-ten average pits in comparison with that at pH 3.8 is featured in Figure 6.5. EDX analysis shows increasing atomic percentage of calcium on corrosion product as exposure time increased. This could infer that CaCO_3 dominates the mixed corrosion product formed as exposure time increased. Connecting this observation to progressive corrosion recorded (Figure 6.23) suggests that calcium influences corrosion process. Less pit growth recorded at pH 6 than at pH 3.8 was probably due to the presence of mixed $\text{Ca}_x\text{Fe}_{(1-x)}\text{CO}_3$ that forms at high pH [247]. FeCO_3 and CaCO_3 coexist as a porous mixture due to similar hexagonal crystal structures in which contributory ratio is a function of ionic concentration, pH, temperature amongst others [160]. Crystal peaks at 29.6 °2Theta position (Figure 6.16) is a slight shift from the calcite polymorph reported in literature [234, 235, 245]. There was however no trace of

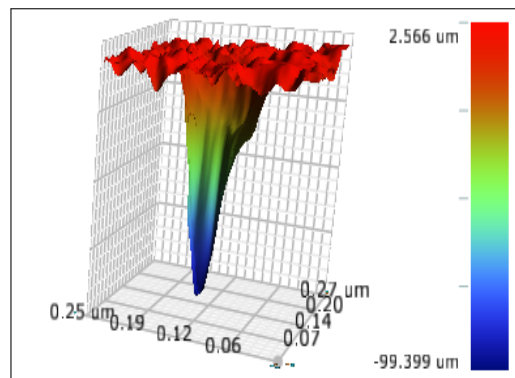
aragonite or FeCO_3 peaks on films deposited at pH 6. This implies that the crystal is CaCO_3 dominant and corroborates close proximity of the peak with a neighbouring CaCO_3 peak. This is also in agreement with Figure 6.15, top-view SEM image showing calcite crystals with no clear FeCO_3 crystal in the mixed structure formed. Fe^{2+} inhibits calcite deposition [236, 237] while the tendency of film formation at pH 6 consumes Fe^{2+} in solution to build films. Hence, calcite crystals [248] began to deposit at pH 6 as Fe^{2+} concentration drops in the solution.

6.4 Effect of pH on formed film

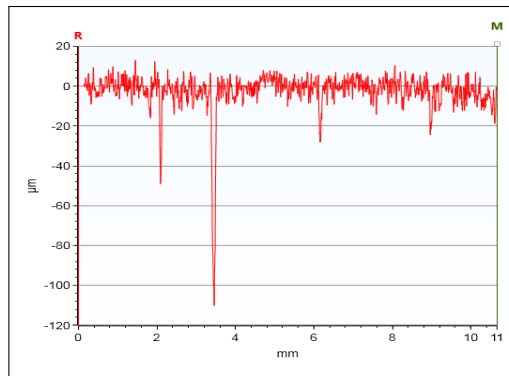
Growth of aragonite after a 4 day test at pH 3.8 indicate that aragonite is preferentially formed at low pH. XRD patterns identified calcite peaks only at pH 6. Crystals bearing calcite semblance interlaced with $\text{Ca}_x\text{Fe}_{(1-x)}\text{CO}_3$ were recorded in the SEM images of samples corroded at pH 6 (Figure 6.15). This points to the fact that calcite forms more easily at high pH where Fe^{2+} concentration is low. Revelation of $\text{Ca}_x\text{Fe}_{(1-x)}\text{CO}_3$ is in agreement with work conducted by Navabzadeh et al. [146] who reported porous [162] mixed iron and calcium carbonate scales in the proportion $\text{Fe}_x\text{Ca}_{(1-x)}\text{CO}_3$ for experiment conducted at pH 6, 80 °C. Increasing Cl^- was observed to influence CaCO_3 polymorph that forms on sample surface as depicted in Figure 6.17. While a mixture of needle-like and rod-like aragonite [249] formed in 2 wt% NaCl, pH3.8 solution after 4 days exposure. Patches of hexagonal platelet vaterite with rod-like aragonites [249] emerged on an amorphous layer in 3.5 wt% NaCl solution. Growth of aragonite and vaterite polymorph from the amorphous layer implies the layer was rich in CaCO_3 as amorphous CaCO_3 layers often precede growth of crystalline polymorphs [238]. Experimental conditions leading to the formation of product displayed in Figure 6.17(b) seems ideal for co-existence of aragonite and vaterite from the unstable amorphous layer. More aragonite coverage was observed probably due to lower stability of vaterite at high temperature [248]. The pit count of samples bearing corrosion products shown in



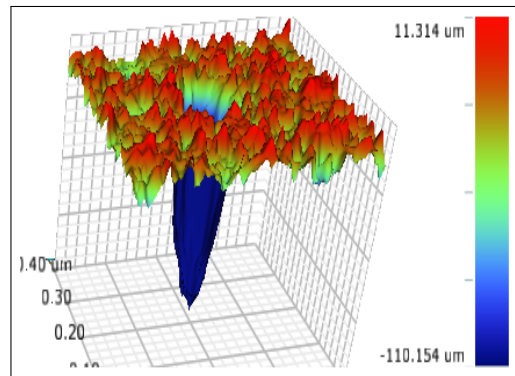
(a) 99 μm pit (2D) after 24 h



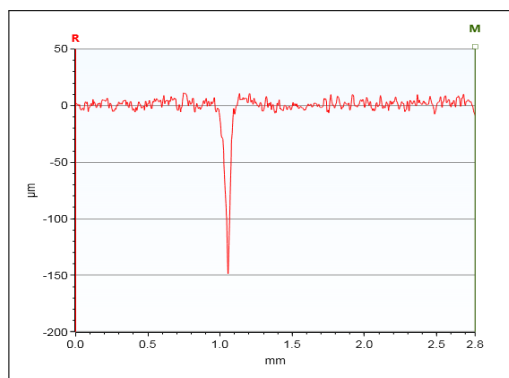
99 μm pit (3D) after 24 h



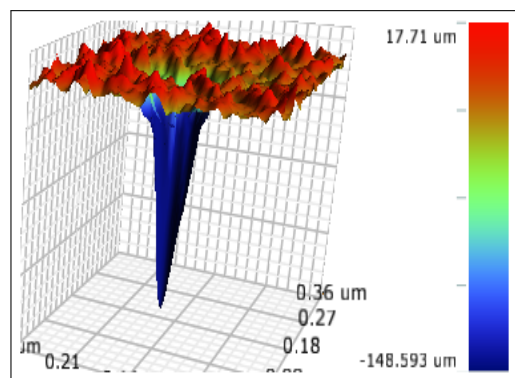
(b) 110 μm pit (2D) after 48 h



110 μm pit (3D) after 48 h



(c) 148 μm pit (2D) after 96 h



(d) 148 μm pit (3D) after 96 h

Figure 6.14: White light profilometry images showing maximum pit depth recorded after 70 μm pit was corroded in saturated CO_2 , 2 wt.% NaCl, 5,000 ppm Ca^{2+} , pH 6, 80 $^\circ\text{C}$ for (a) 24 h, (b) 48 h and (c) 96 h exposure. Measurements relative to corroded surface.

Figure 6.17(a) and 6.17(b) were identical which suggests that aragonite and vaterite have a similar influence on pit propagation. Corrosion products formed at high pH were observed to be compact and thin unlike that formed at low pH. This was probably due to high bulk precipitation at high pH which diminishes Fe^{2+}

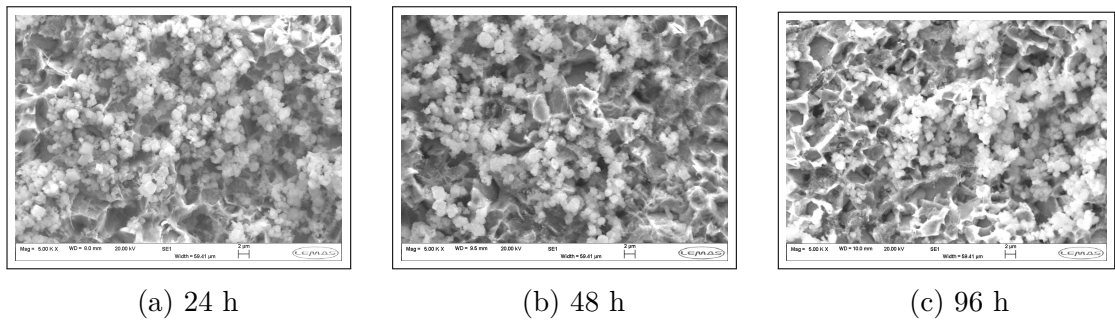


Figure 6.15: Top view SEM image and cross section featuring corrosion products formed on X65 carbon steel in saturated CO_2 , 2 wt.% NaCl, 5000 ppm Ca^{2+} , 80 °C, pH 6 over a duration of (a) 24 h (b) 48 h and (c) 96 h

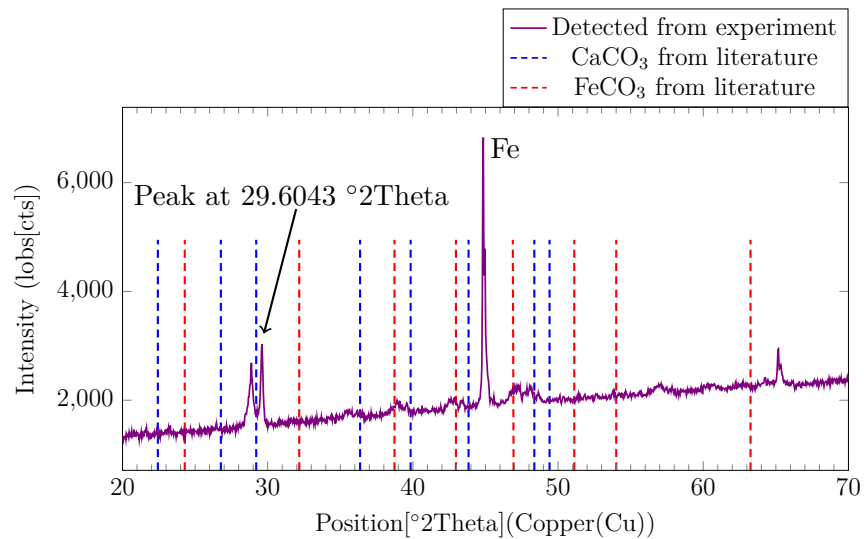
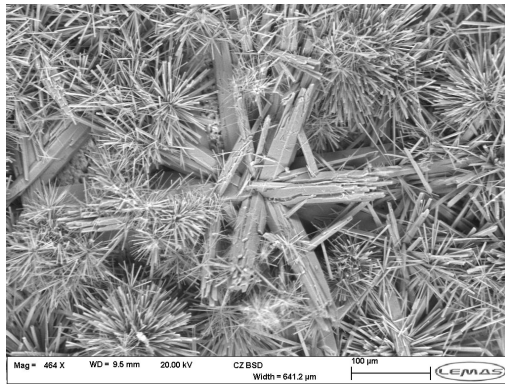


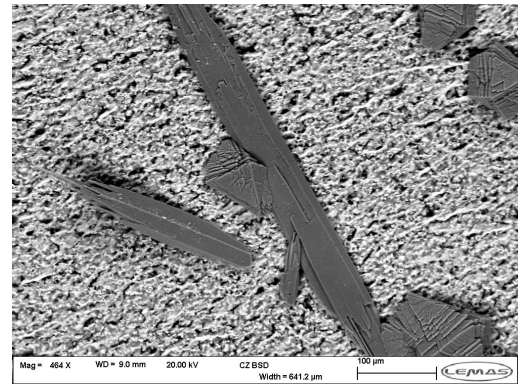
Figure 6.16: Plot depicting comparison of XRD $^{\circ}2\text{Theta}$ position of FeCO_3 and CaCO_3 from literature to that of detected peaks for X65 carbon steel corroded in 2 wt% NaCl, 5,000 ppm Ca^{2+} , 80 °C for 96 h at pH 6

concentration that would have contributed to film formation on sample surface. Top-view SEM images of products formed on corroded pit after 24 h exposure at pH 3.8 and pH 6 are shown at Figure 6.18. The thick films formed at low pH covers the pit mouth while thin films was observed to line pits at high pH. Cross section images of both conditions also revealed thin films and thick films at high pH and low pH respectively. Analysis of the pitting trend however show deeper pits at lower pH than at higher pH. This further strengthens the assertion that events beneath the Ca^{2+} rich films promote pit growth.

The lower corrosion rate recorded at pH 6 implies lower ferrite dissolution compared to that at pH 3.8. Although FeCO_3 precipitation is not expected at low pH, Ca^{2+}

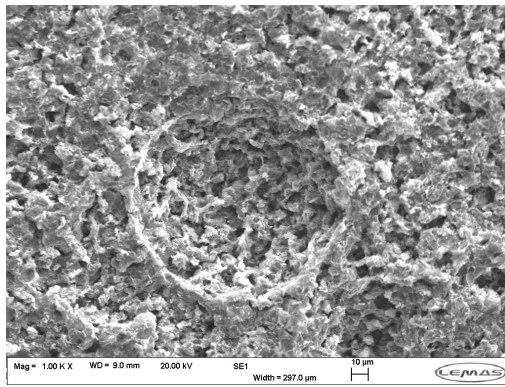


(a) Needle-like & rod-like aragonites

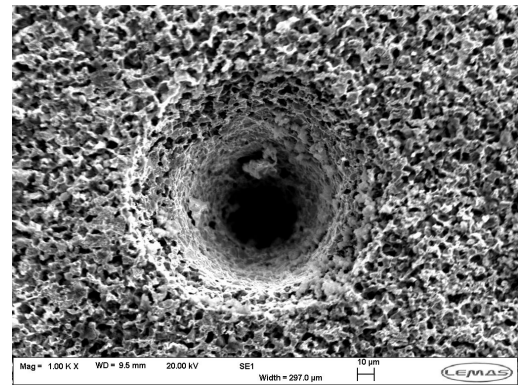


(b) Aragonites & vaterites on amorphous layer

Figure 6.17: Top-view SEM of film formed on pits in X65 carbon steel corroded in 5,000 ppm Ca^{2+} at 80 °C for 96 h in (a) 2 % NaCl, (b) 3.5 % NaCl,



(a)



(b)

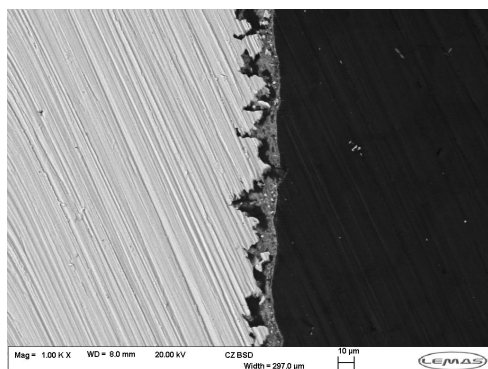
Figure 6.18: Top-view SEM of film formed on pits in X65 carbon steel corroded in 2 % NaCl, 5000 ppm Ca^{2+} at 80 °C for 24 h in (a) pH 3.8 (b) pH 6.

precipitated first and consumed carbonic anions to form CaCO_3 thereby further hindering the likelihood of FeCO_3 precipitation [237]. SEM images at high pH (Figure 6.15) revealed presence of calcite as Fe^{2+} concentration in solution was too low to interfere with calcite transformation since competition occurs in precipitation kinetics of cations [237].

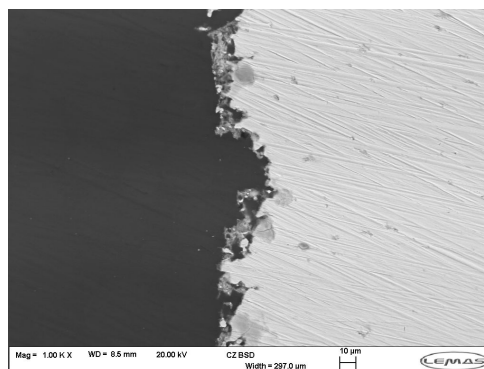
At low pH, CaCO_3 was observed to remain soluble with the solution remaining clear until after 48 h when aragonite began to grow. LPR/OCP plots at pH 3.8 (Figure 6.4(a)) indicated higher corrosion rate which signifies higher ferrite dissolution than experiments conducted at pH 6. SEM images of corroded sample (Figure 6.8) revealed no calcite deposited after 48 h exposure. This is in agreement with the

findings by [237] who reported that high Fe^{2+} concentration in solution inhibits calcite deposition. Aragonite dominated the sample surface after 4 day exposure at low pH as Fe^{2+} dissolution does not inhibit the growth of aragonite [250]. Pit growth statistics at pH 3.8 shown in Figure 6.5 indicated rapid growth after first 24 h while growth rate reduced as exposure time increased. Recorded pit depths after 48 h and 96 h were still relatively higher than the initial 70 μm depth.

Amorphous films form during the early stages of corrosion (less than 48 h) in Ca^{2+} solutions. The film adhered tightly to the steel surface for the solution at pH6 while dense films were observed at pH 3.8. The top-view SEM images showed the compactness of amorphous films for pH6 and unbuffered Ca^{2+} solutions (Figure 6.18). The cross-sectional view showing film thickness is in Figure 6.19. The thin film coverage recorded at pH6 could be attributed to high bulk precipitation observed during the test. This implies that pH increases bulk precipitation but does not contribute to film formation coverage. For tests conducted at pH 3.8, no bulk precipitation was observed but thick continuous films lined the sample surface. At pH 3.8, calcite emerges from amorphous layers and begins to transform to aragonite after about 48 h as shown in Figure 6.20. An increase in chloride concentration yielded a mixture of aragonite and vaterite (Figure 6.17(b)). At pH6, mixed $\text{Ca}_x\text{Fe}_{(1-x)}\text{CO}_3$ forms on the steel surface. The top-view SEM of products formed in pH 3.8 Ca^{2+} solution and at pH6 is shown as Figure 6.21. EDX analysis of products formed in the pits at pH 6 revealed higher Ca^{2+} concentration at the pit mouth but with near-zero Ca^{2+} presence inside pit as shown in Figure 6.22. For pH 3.8 solution, significant Ca^{2+} presence was recorded from the pit mouth all through the pit vertex as shown in Figures 6.11 to 6.13. This suggests that the needle-shaped aragonite (Figure 6.21(a)) fill up the entire pit cavity.

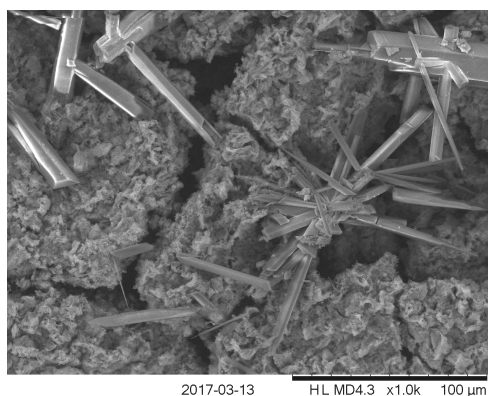


(a)

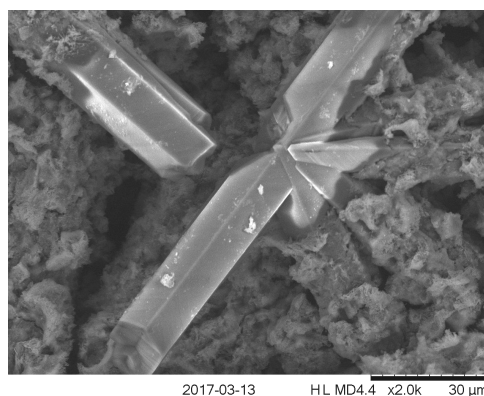


(b)

Figure 6.19: Cross-section view of film formed in 2 wt% NaCl, 5000 ppm Ca²⁺, 80°C for 96 h at (a) pH 3.8 and (b) pH6.

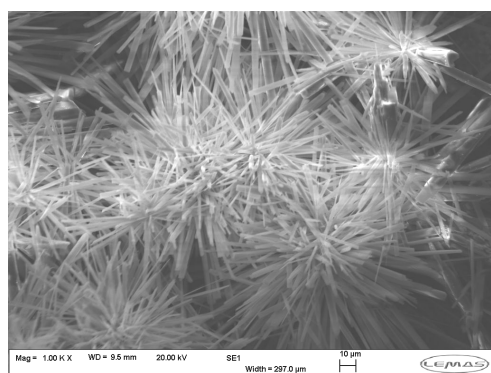


(a)

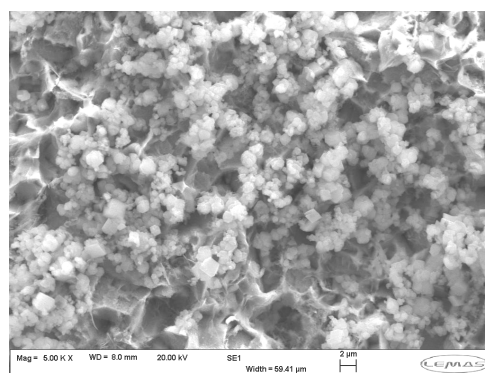


(b)

Figure 6.20: Top-view SEM depicting amorphous film transformation to aragonite in 2 wt% NaCl, 5000 ppm Ca²⁺, pH3.8, 80 °C under (a) X1.0 K and (b) X2.0 K magnification.

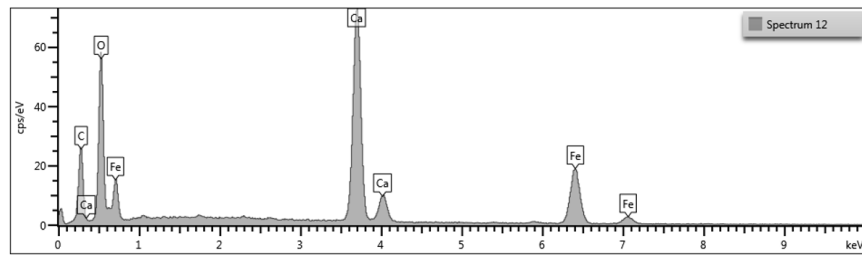


(a)



(b)

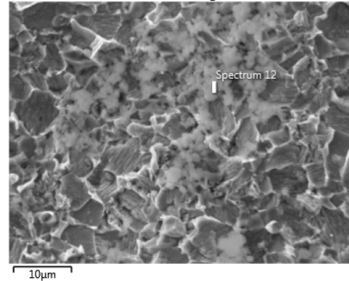
Figure 6.21: Top-view SEM depicting products formed under 2 wt% NaCl, 5000 ppm Ca²⁺, 80 °C for 96 h at (a) pH 3.8 and (b) pH6.



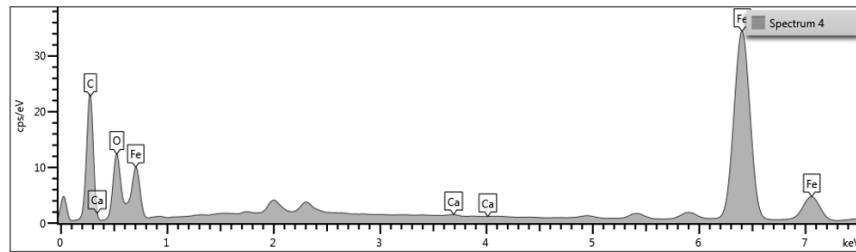
_OINA.Reporting.Mustang.Placeholder.SpectrumEntity

Element	Atomic %
C	30.16
O	54.28
Ca	10.04
Fe	5.52
Total:	100

Electron Image 6



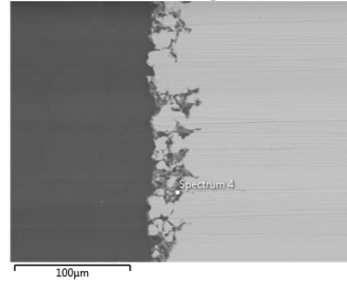
(a)



_OINA.Reporting.Mustang.Placeholder.SpectrumEntity

Element	Atomic %
C	65.36
O	15.88
Ca	0.06
Fe	18.7
Total:	100

Electron Image 4



(b)

Figure 6.22: EDX showing composition of products formed at (a) pit mouth and (b) inside pit under pH6 in 2 wt% NaCl, 5000 ppm Ca^{2+} , 80°C for 96 h

6.4.1 Metal thinning due to general corrosion

It is worthy to mention that general corrosion progresses along with pitting. Both forms of corrosion need to be accounted for in order to obtain the absolute (total) pit depth. All measured depths in the preceding sections of this Chapter were relative to the corroded surface. Pitting would be higher if general corrosion was taken into

account. Average metal thinning was therefore calculated from the corrosion rate measured during linear polarisation resistance (LPR) tests featured in Figures 6.1(a), 6.1(b) and 6.4. Corrosion rate and derived metal thinning for experiments conducted at pH 3.8 and pH 6 under 0 ppm and 5,000 ppm Ca^{2+} conditions are contained in Table 6.1. Metal thinning is metal penetration caused by uniform (general) corrosion, denoted as ' D ' in Figure 4.2. Metal thinning recorded under experimental conditions are contained in Table 6.1. Introducing 5,000 ppm Ca^{2+} increased the corrosion rate from 3.67 mmpy to 5.06 mmpy for experiments conducted at pH 3.8 while corrosion rate increased from 0.05 mmpy to 0.79 mmpy under pH 6 condition. This is in agreement with findings of other literatures that Ca^{2+} increases corrosion rate in metals [146, 233, 160]. Absolute pit depth, P can be obtained by adding pit depth, d (measured relative to the corroded surface) to metal thinning, D .

Table 6.1: Average metal loss obtained from LPR measurement under different pH conditions.

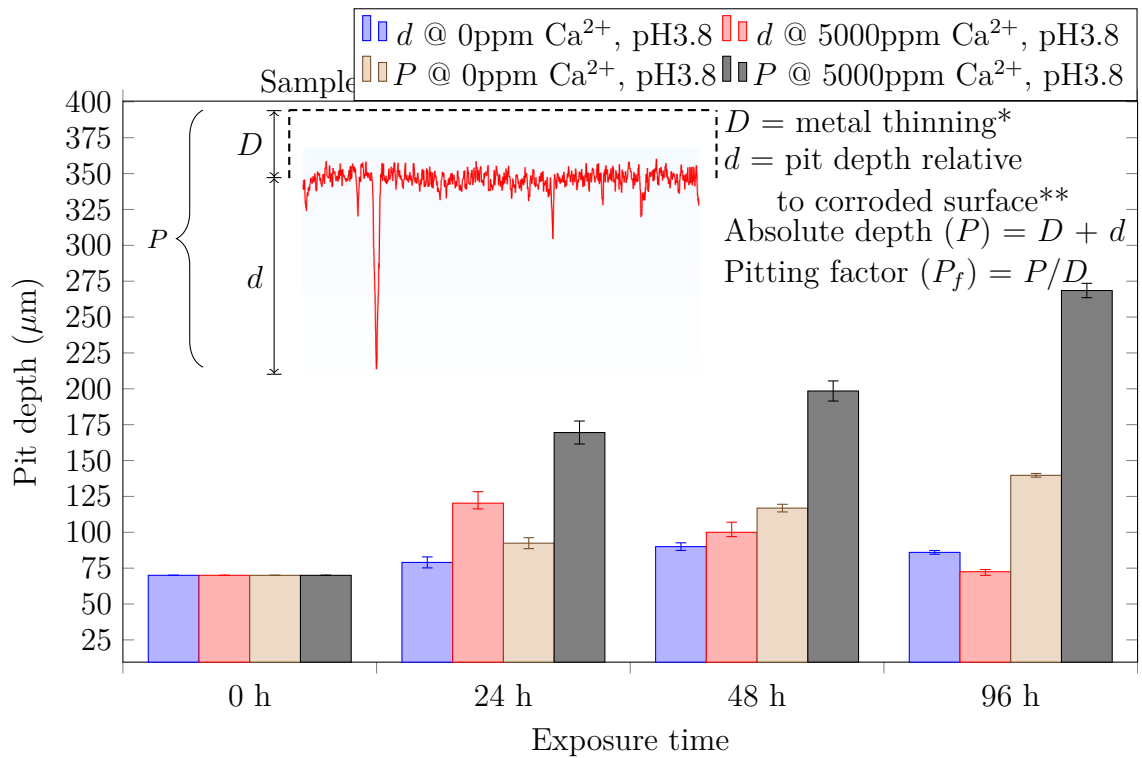
Description	Average corr rate	Metal thinning, D , after		
		24h	48h	96h
*pH 3.8, 80 °C (Figure 6.1(a))	3.67 mmpy	13.42 μm	26.85 μm	53.70 μm
**pH 3.8, 80 °C (Figure 6.4(a))	5.06 mmpy	49.23 μm	98.47 μm	196.93 μm
*pH 6, 80 °C (Figure 6.2(a))	0.007 mmpy	0.019 μm	0.038 μm	0.077 μm
**pH 6, 80 °C (Figure 6.4(b))	0.79 mmpy	3.59 μm	7.18 μm	14.36 μm

* 0 ppm Ca^{2+}

** 5,000 ppm Ca^{2+}

A bar chart showing the trend in absolute and relative pitting in Ca^{2+} and Ca^{2+} free solutions at pH 3.8 is in Figure 6.23. Pit depth relative to corroded surface in Ca^{2+} free solutions, d (depicted in blue), and that in Ca^{2+} solutions (red) increased after first 48 h while propagation rate declined after about 48 h exposure due to overriding uniform corrosion (metal thinning) as featured in Table 6.1. Absolute pit depth in Ca^{2+} free solution (brown) and in Ca^{2+} solution (black) both increased under all test durations as general corrosion was accounted for. Significant pitting was however observed for solution containing Ca^{2+} . It therefore becomes obvious that Ca^{2+} increases both general and pitting corrosion.

Increase in pH altered pitting kinetics in Ca^{2+} solutions. For solutions containing



* Uniform corrosion calculated from LPR measurement during corrosion test

** Pit depth obtained from white light interferometry

Figure 6.23: Bar chart depicting trend in relative and absolute pitting from initial $70\mu\text{m}$ depth in saturated CO_2 , 2 wt% NaCl, 80°C over a duration of 4 days at pH 3.8

5,000ppm Ca^{2+} at pH 3.8, amorphous CaCO_3 formed during first 48 h before transforming to aragonite as covered in section 6.3.1 of this Chapter. A look at Figure 6.5 and 6.6 shows that propagation rate was high within first 24 h of exposure. This could imply that amorphous aragonite layer that interacted with pit surface reacted with pit walls to increase pit depth. Pit growth (relative to corroded surface) however began to reduce after 24 h as amorphous layer increase in size and become densely packed. Beyond 48 h absolute pitting declines as crystalline aragonite grows on the steel surface and fills up the pit. The situation under low pH is totally different from pH 6 in which an unstable pitting trend was observed when $\text{Ca}_x\text{Fe}_{(1-x)}\text{CO}_3$ forms on steel surface.

6.4.2 Determination of pitting factor

The extent of pitting can be determined by calculation of pitting factor, ' P_f ' described in Figure 4.2 and mathematically expressed in Equation 4.1. Figure 6.24 shows P_f trend for experiments conducted. Figure 6.24(a) shows the trend under conditions where protective film was not formed on the sample surface while Figure 6.24(b) show P_f under 0ppm Ca^{2+} , pH 6, 80 °C where a protective FeCO_3 was formed on the sample. P_f was observed to generally decline with increase in exposure time due to overriding metal thinning (uniform corrosion) that mask pit depth (relative to corroded surface) with time in all cases. P_f under protective scale condition (Figure 6.24(b)) appear to be exceptionally high due to initial $70\mu\text{m}$ pits which was masked by FeCO_3 film that retarded general corrosion. A look at Figure 6.24(a) shows that P_f is high in Ca^{2+} solution at pH 6 (blue) but lesser at pH 3.8 (brown). Absolute pitting was however high at pH 3.8 as shown in Figure 6.23. Absolute pitting is an appropriate measure for assessing pitting damage as spot with deepest penetration would likely rupture first to signal failure.

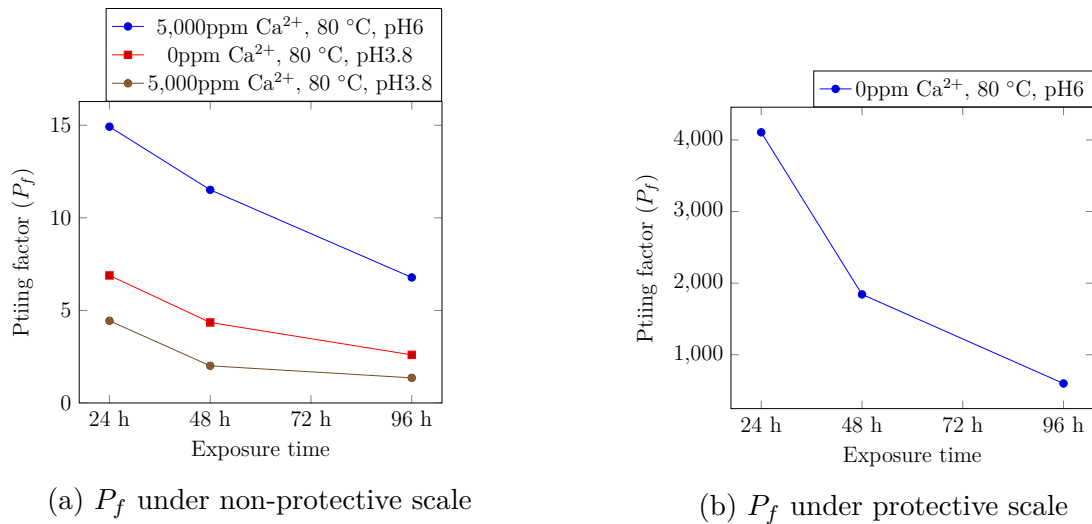


Figure 6.24: Plot showing trend in pitting factor P_f , derived for experiments conducted under (a) non-protective scale condition (b) Protective scale condition

6.4.3 Absolute metal thinning and pitting

Actual metal thinning and pitting extent was calculated from the average of results obtained from profilometry scan of repeated tests in calcium and calcium-free solutions at pH3.8. General corrosion recorded reflects metal thinning while relative pitting is measurement taken relative to the corroded surface of the metal. Initial pitting of $70\mu m$ (created by potentiostatic polarisation) was deducted from the measured values to assess pit growth. The objective of this approach was to compare actual metal thinning to pitting recorded after corrosion test. A summary of metal thinning and pitting is presented in Table 6.2. The result shows that general corrosion exceeded relative pitting in Ca^{2+} -free and calcium solutions for all tests conducted at pH 3.8. Absolute pitting (general + relative pitting) implies that pitting magnitude was masked by general corrosion and that actual pitting can only be observed when general corrosion is taken into account.

Table 6.2: General metal thinning and pitting of API-X65 carbon steel in Calcium-free and 5,000ppm Ca^{2+} solutions

Corrosion type	After 24 h		After 48 h		After 96 h	
	Ca^{2+} -free	Ca^{2+} soln	Ca^{2+} -free	Ca^{2+} soln	Ca^{2+} -free	Ca^{2+} soln
General corrosion (pH3.8)	$13\mu m$	$67\mu m$	$80\mu m$	$96\mu m$	$53\mu m$	$197\mu m$
Relative pitting (pH3.8)	$9\mu m$	$50\mu m$	$20\mu m$	$30\mu m$	$16\mu m$	$13\mu m$
Absolute pitting (pH3.8)	$22\mu m$	$117\mu m$	$100\mu m$	$126\mu m$	$69\mu m$	$210\mu m$

6.5 Comparison of Ca^{2+} pitting under pH 3.8 and pH 6

Comparing Figure 6.2(a) (0ppm Ca^{2+} , pH 6) and Figure 6.4(b) (5,000ppm Ca^{2+} , pH 6), the starting corrosion rate in the Ca^{2+} -free solution was significantly lower than that in 5,000 ppm Ca^{2+} solution. While $FeCO_3$ films formed in Ca^{2+} -free solution, mixed $Ca_xFe_{(1-x)}CO_3$ was detected in the Ca^{2+} -rich solution. This suggests higher

corrosion rate for solutions where saturation tends towards mixed $Ca_xFe_{(1-x)}CO_3$ formation than when $FeCO_3$ was favoured.

At pH 3.8, Figure 6.1(a) (0ppm Ca^{2+} , pH 3.8) recorded lower corrosion rate compared to Figure 6.4(a) containing 5,000 ppm Ca^{2+} at same pH. As expected, Fe_3C layer was detected at pH 3.8 in Ca^{2+} -free solution (Figure 6.1(b)) while aragonite deposits were recorded after a 4-day test in 5,000 ppm Ca^{2+} solution. Higher corrosion rate in the Ca^{2+} solution suggests that Fe^{2+} dissolution progressed significantly as aragonite began to deposit on the steel surface.

Higher corrosion rate in Ca^{2+} solution suggests that films form faster on the steel surface and as well cover the mouth of induced pits. The high corrosion rate in Ca^{2+} being sustained throughout the test duration suggests that Ca^{2+} promotes film porosity thereby allowing free interaction between the bulk and the steel surface. For pH 3.8 solutions, higher pitting was recorded in Ca^{2+} -rich solution compared to that in Ca^{2+} -free solutions Figure 6.23. EDX analysis of products formed in the pits at pH 6 revealed higher Ca^{2+} concentration at the pit mouth but with near-zero Ca^{2+} presence inside pit as shown in Figure 6.22. For pH 3.8 solution, significant Ca^{2+} presence was recorded from the pit mouth all through the pit vertex as shown in Figures 6.11 to 6.13. This suggests that the needle-shaped aragonite (Figure 6.21(a)) fill up the entire pit cavity.

6.6 Conclusions

The influence of Ca^{2+} on X65 carbon steel pitting has been investigated. The conclusions reached from the findings in this work are as follows:

- a. An amorphous layer forms on X65 carbon steel during the first 48 h in CO_2 saturated solution containing Ca^{2+} at low pH, 80 °C but transforms to aragonite polymorph after about 96h.

- b. Aragonite precipitates at low pH while calcite was identified with mixed $Ca_xFe_{(1-x)}CO_3$ that forms at high pH.
- c. Increasing Cl^- concentration at low pH reduces aragonite precipitation and promotes vaterite growth. Aragonite and vaterite have similar influence on pit propagation kinetics.
- d. Pit propagation at 80 °C, low pH is significantly higher than propagation at high pH due to the formation of mixed but porous $Ca_xFe_{(1-x)}CO_3$ that forms on the latter.
- e. Calcium generally increases pitting but the propagation rate is less beneath the aragonite film compared to the amorphous $CaCO_3$ film.
- f. The calcite hexagonal structure is less compact than that of aragonite which is a possible explanation for the difference in pitting kinetics under both conditions.
- g. Pit growth under amorphous $Ca_xFe_{(1-x)}CO_3$ films remains unpredictable and is likely to be influenced by molar constituent of cations in the mixture.
- h. Calcium preferentially displaces iron from mixed corrosion product formed as exposure time increases.
- i. Calcium influences both general and pitting corrosion in X65 carbon steel.
- j. A compact film lines the pit wall at high pH while thicker films form at low pH.

Chapter 7

Assessing the influence of calcium on X65 carbon steel pitting using an artificial pit

7.1 Introduction

Chapter 6 presents findings on how calcium polymorphs influence general and pitting corrosion. There are instances where products formed on carbon steel are not entirely CaCO_3 but a mixture of carbonates such as $\text{Ca}_x\text{Fe}_{(1-x)}\text{CO}_3$. This is expected in storage tanks harboring Ca^{2+} rich crude and down time scenarios in enhanced hydrocarbon recovery [163, 158, 159, 160, 146], in which pitting persists. Effects of flow, particles or chemistry change could limit protection of passive films by exposing bare steel to corrosive medium. Han's [194] work on roles of passivation and galvanic effects in localized CO_2 corrosion of mild steel reported that compromised spots in a passive layer can evoke galvanic coupling.

It is generally believed that the potential difference between the anode and cathode is responsible for pitting occurrence. Potential differences in the range up to 50 mV

have been utilised in several pitting studies conducted on low carbon steel using the artificial pit [177, 208, 251]. Several other investigations have been conducted on localised corrosion in carbon steel using an artificial pit [252, 194, 253]. Most artificial pit experiments conducted were based on deposited FeCO_3 ; knowledge is still lacking on how the galvanic trend influences pitting under mixed carbonate conditions which is common in oilfield brines. Similarly, the artificial pit is yet to be utilised to exhaustively unravel events on a compromised anode pin. This Chapter therefore investigated the effect of Ca^{2+} on X65 carbon steel pitting by forming mixed Ca^{2+} and Fe^{2+} carbonates on a cathode disc and later coupling to a freshly polished anode. The galvanic trend was measured and followed by comprehensive analysis of both anode and cathode electrodes.

7.2 Cathode disc passivation/results

The artificial pit cathode was pre-passivated before inserting a freshly polished anode for the galvanic experiment. The solution pH and temperature were set in line with the test matrix contained in Table 7.1. LPR and OCP measurements were conducted for up to 4 days to produce pseudo-passive films. The anode pin was then polished using SiC in grit sequence from 120 to 1,200 and then coupled to the passivated cathode. ACM Gill AC potentiostat was utilised for measuring galvanic (mixed) potential/current density established after screwing a freshly polished anode (with relatively lower potential) onto the cathode (having higher potential). As a baseline, an initial test was conducted in Ca^{2+} - free solution to compare with experiments conducted in a Ca^{2+} solution. Tafel plots and derivatives for electrochemical measurements conducted in 682 ppm Ca^{2+} solution are shown in Figure 7.1 and Table 7.2 respectively. Preliminary tests were conducted using 3.3 wt.%NaCl, 3.1 wt.%NaCl separately in 682 ppm & 1364 ppm Ca^{2+} solutions to determine suitable Ca^{2+} concentration for the artificial pit test, while maintaining 21,233 ppm chloride concentration. Chloride level was kept constant to ensure the

accuracy of pitting data collected as variation in chloride concentration could alter the pitting kinetics. Although calcium content in formation water can exceed 5,000 ppm, experiments in this Chapter were conducted using 682 ppm Ca^{2+} as higher Ca^{2+} concentrations diminish the magnitude of galvanic current needed to conduct artificial pit investigations. The trend observed under this condition can be inferred to solutions containing higher Ca^{2+} concentration. A pH of 7.5 was used to ensure faster precipitation of mixed $\text{Ca}_x\text{Fe}_{(1-x)}\text{CO}_3$ films at 50 °C.

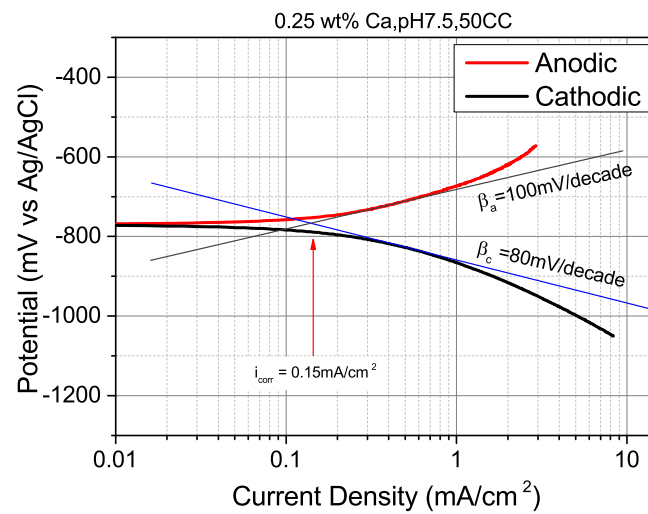


Figure 7.1: Tafel plots showing i_{corr} , β_a and β_c derivatives for experiment conducted in saturated CO_2 , 2 wt.% NaCl, 50 °C containing 682 ppm Ca^{2+} , pH 7.5

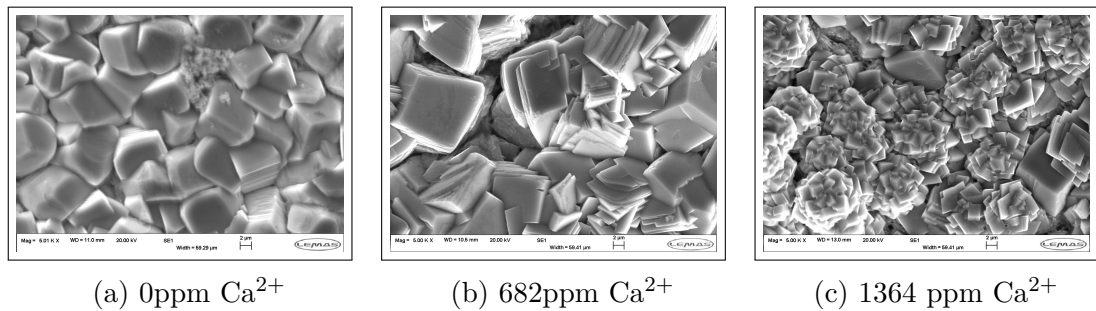


Figure 7.2: Top-view SEM image of mixed $\text{Ca}_x\text{Fe}_{(1-x)}\text{CO}_3$ formed on X65 carbon steel corroded for 96 h at pH 7.5, saturated CO_2 in (a) 3.5 wt% NaCl, 0 ppm Ca^{2+} (b) 3.3 wt% NaCl, 682 ppm Ca^{2+} and (c) 3.1 wt% NaCl, 1364 ppm Ca^{2+}

Top-view SEM and LPR/OCP plot of initial tests are shown in Figure 7.2 and Figure 7.3 respectively. Only FeCO_3 crystals of different sizes form in Ca^{2+} - free solution as expected and are shown in Figure 7.2(a). Mixed carbonate crystals ($\text{Ca}_x\text{Fe}_{(1-x)}\text{CO}_3$)

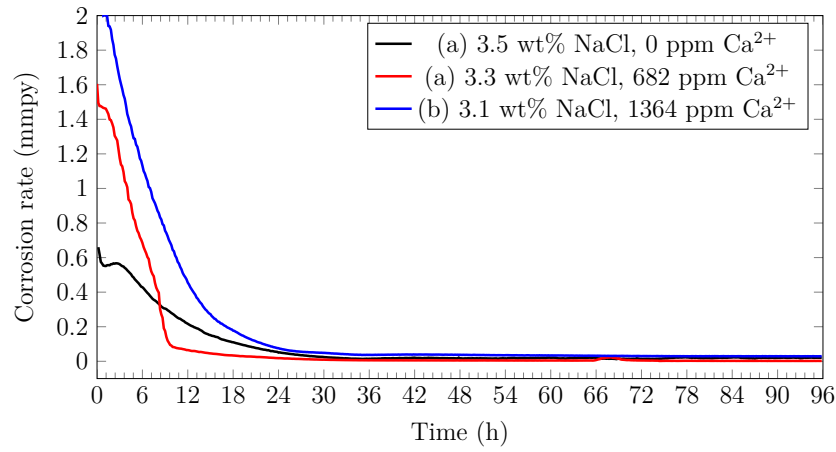


Figure 7.3: Corrosion rate plot for X65 carbon steel corroded for 96 h at pH 7.5, saturated CO₂ in (a) 3.5 wt% NaCl, 0 ppm Ca²⁺ (b) 3.3 wt% NaCl, 682 ppm Ca²⁺, (c) 3.1 wt% NaCl, 1364 ppm Ca²⁺

Table 7.1: Artificial pit test matrix

Item	Description	Value
Metal specification	X65	0.07 to 0.12%C
	Cathode diameter	25mm
	Anode diameter	1mm, 2mm and 3mm
	Anode/cathode ratio	1:625, 1:156 and 1:69
Film growth on cathode	Duration	96 h
	pH	pH7.5
	Temperature	50°C
	Magnetic stirrer	100 rpm
Test cell condition	Duration	24Hrs
	De-ionised water	1,000ml
	pH	pH7.5
	Temperature	50°C
	Pit depth	0.625mm
	Magnetic stirrer	Near-static
	Brine*	3.5 wt%NaCl, pH7.5
	Brine**	3.3 wt%NaCl, pH7.5 0.25 wt%CaCl ₂ .2H ₂ O

*21,233ppm Cl⁻ & 0 ppm Ca²⁺

**21,233ppm Cl⁻ & 682 ppm Ca²⁺

Table 7.2: Tafel constant

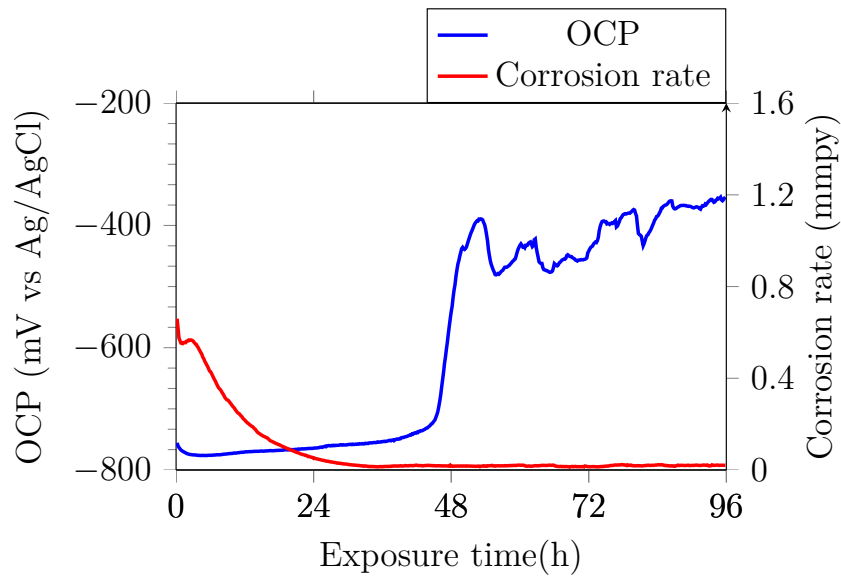
pH	Temp (°C)	β_a (mV/decade)	β_c (mV/decade)	B(mV/decade)	i_{corr} (mA/cm ²)
*pH 7.5	50 °C	70	75	15.72	0.04
**pH 7.5	50 °C	100	80	19.30	0.15

* 0 ppm Ca²⁺

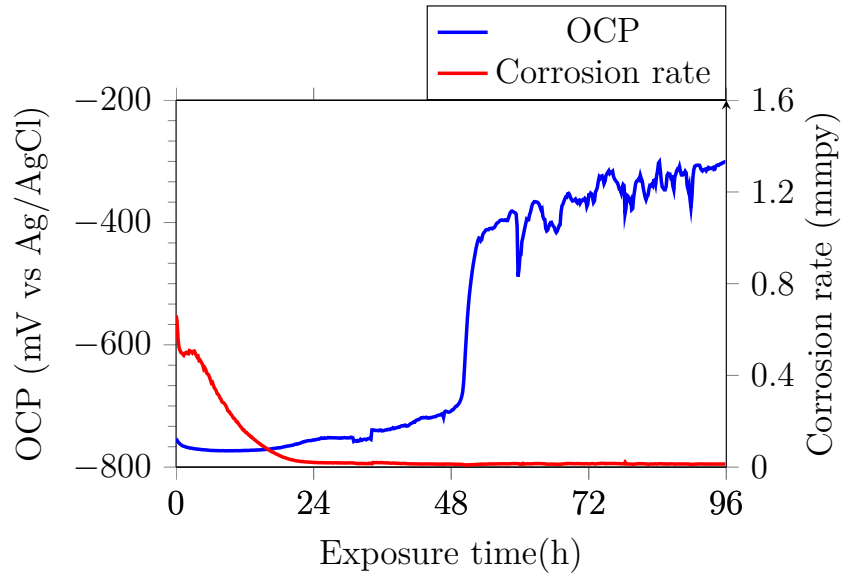
** 682 ppm Ca²⁺

were formed in 682 ppm Ca^{2+} -solution (Figure 7.2(b)). The crystal size however became smaller as calcium concentration was increased to 1,364 ppm as shown in Figure 7.2(c). The film formed on the passivated cathode plays a significant role in determining the galvanic trend of the artificial pit. Detailed SEM images of the film formed after corrosion tests in 682 ppm Ca^{2+} solution for 96 h are shown as Figure 7.6. Crystals with attributes similar to both Calcite and FeCO_3 crystals were recorded. This is in contrast to crystals observed for films in Ca^{2+} - free systems where smaller crystals fuse within cavities of larger crystals (Figure 7.2(a)). A look at the LPR results featured in Figure 7.3 shows that tests conducted in 3.3 wt% NaCl, 682 ppm Ca^{2+} (depicted in red) offered the lowest corrosion rate and therefore were considered appropriate for the artificial pit experiment since the highest galvanic currents were expected in the event of film break-down.

A pseudo-passive trend was observed on the steel surface after about 48 h in Ca^{2+} - free solution (Figure 7.4) while pseudo-passivation trend was delayed for solutions containing 682 ppm Ca^{2+} as shown in Figure 7.5. A delay in the emergence of the pseudo-passive trend for solutions containing 682 ppm Ca^{2+} suggests that calcium delays but does not hinder the formation of a pseudo-passive layer. Although several inconclusive reasons have been attributed to pseudo-passivity [200, 201], the revelation of pseudo-passivation in Ca^{2+} solution further broadens the scope of questions demanding answers for this phenomenon. For Ca^{2+} - free systems, the corrosion rate was observed to drop from about 1.5 mmpy to 0.15 mmpy after 24 h. OCP however increases spontaneously in magnitude of about 400 mV after 48 h. For solutions containing 682 ppm Ca^{2+} , a pseudo-passive trend was less rapid and became pronounced after about 72 h exposure. A delay in pseudo-passivation under 682 ppm Ca^{2+} suggests that Ca^{2+} retards the film building process.



(a) Test-1 (0 ppm Ca^{2+})

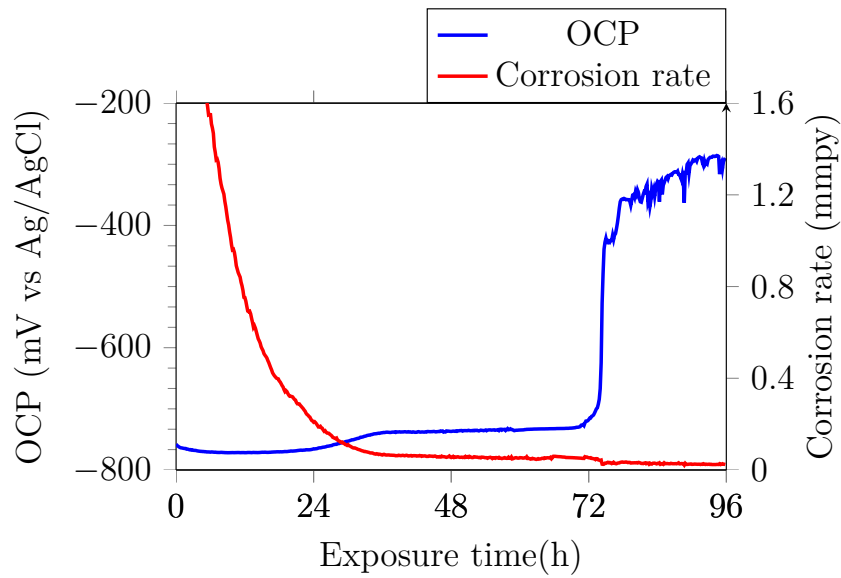


(b) Test-2 (0 ppm Ca^{2+})

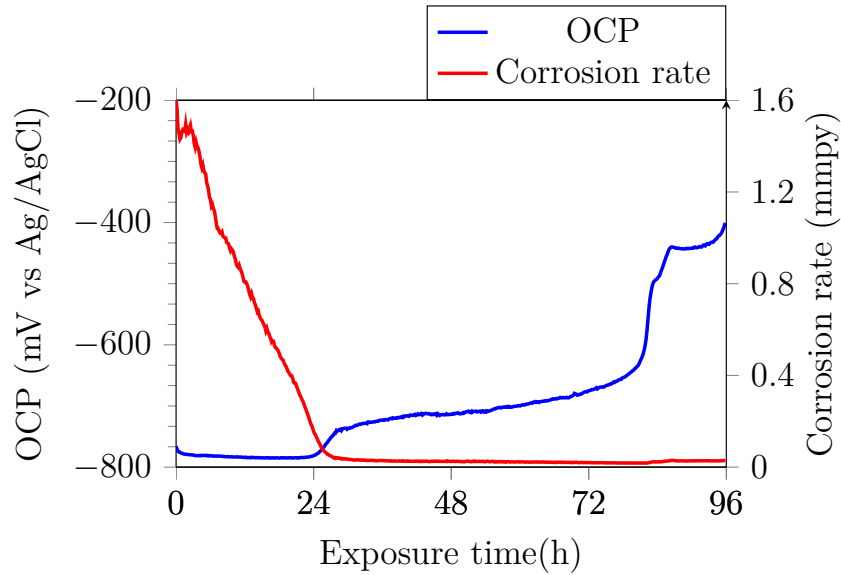
Figure 7.4: (a) Test 1 and (b) Test 2 result for LPR/OCP plot of X65 carbon steel corroded in 21,000 ppm Cl, at 50 °C, pH 7.5 for 96 h in 0 ppm Ca^{2+}

7.2.1 Analysis of mixed carbonate formed in 682 ppm Ca^{2+}

Figure 7.6 shows different magnifications of top-view SEM images of products formed on artificial pit cathodes before the anode pin was coupled. The images depict a mixture of crystals whose EDX elemental scan (Figure 7.7) suggests $\text{Ca}_x\text{Fe}_{(1-x)}\text{CO}_3$ hexagonal crystals. Ca^{2+} and Fe^{2+} were detected in net percentages of 3.05 and 19.61 respectively. This implies that molar fractions of Ca^{2+} to Fe^{2+} in the $\text{Ca}_x\text{Fe}_{(1-x)}\text{CO}_3$



(a) Test-1 (682 ppm Ca^{2+})



(b) Test-2 (682 ppm Ca^{2+})

Figure 7.5: (a) Test 1 and (b) Test 2 result for LPR/OCP plot of X65 carbon steel corroded in 21,000 ppm Cl, at 50 °C, pH 7.5 for 96 h in 682 ppm Ca^{2+}

mixture were 0.13 to 0.87 respectively. Detailed XRD analysis was conducted to corroborate the EDX scan results.

An XRD scan of the crystals formed on X65 carbon steel corroded in 682 ppm Ca^{2+} for 4 days before coupling the anode for galvanic measurement is shown as Figure 7.8. XRD analysis using the *highscore* software revealed the presence of a hexagonal crystal lattice whose properties lie between calcite and FeCO_3 . Matching experimental XRD peaks with literature results aligned in Figure 7.8

shows that peak detected at $31.7999^\circ 2\theta$ fell between CaCO_3 and FeCO_3 but much closer towards the latter. This suggests a higher proportion of Fe^{2+} in the mixed carbonate structure which is in agreement with the molar fraction revealed in the EDX result featured in Figure 7.7. Detailed composition of Ca^{2+} and Fe^{2+} was further investigated using cell parameters of XRD peaks detected at $31.7999^\circ 2\theta$.

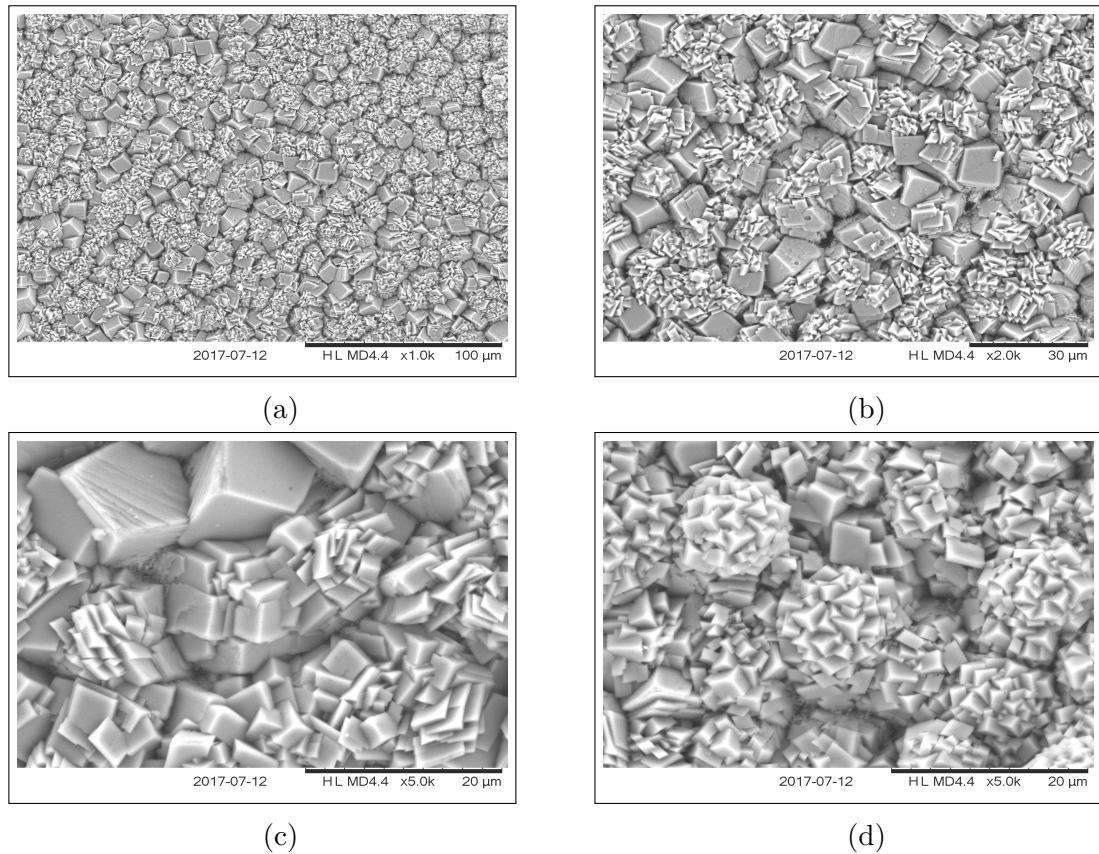
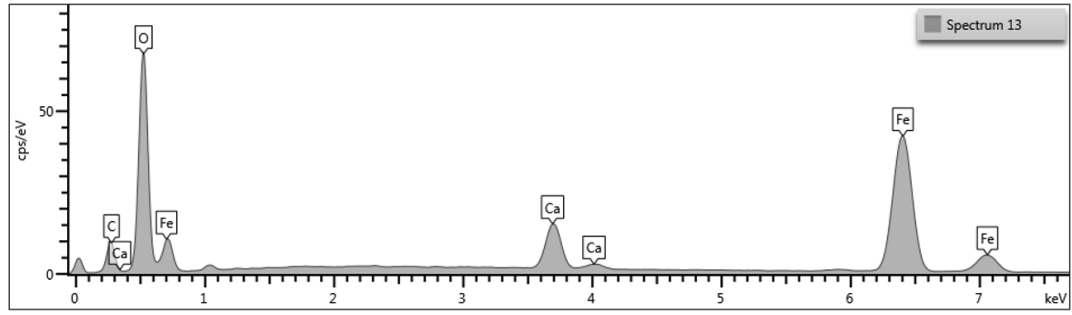


Figure 7.6: Top view SEM showing mixed FeCO_3 and CaCO_3 formed on X65 carbon steel corroded in 3.3 wt% NaCl, 682 ppm Ca^{2+} , 50°C for 96 h at pH 7.5 under (a) X1000 (b) X2000 (c) X5000 magnification and (d) calcite cluster zoom

A typical hexagonal diagram of CaCO_3 and FeCO_3 crystal is featured as Figure 7.9. Values of a and c were calculated using the d spacing equation for a hexagonal system featured in Equation 7.1 [254, 255] while unit cell volume, v , was obtained using equation 7.2, derived from Bragg's law [254, 255].

The Bravais lattice planes, expressed in terms of Miller indices h, k, l were obtained



_OINA.Reporting.Mustang.Placeholder.SpectrumEntity

Element	Atomic %
C	23.81
O	53.54
Ca	3.05
Fe	19.61
Total:	100

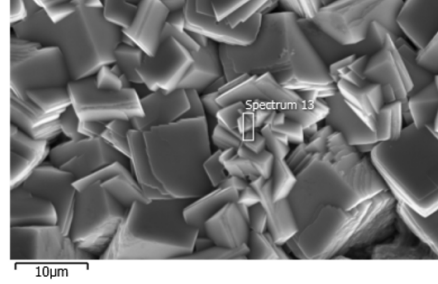


Figure 7.7: EDX showing percentage composition of elements detected on X65 carbon steel corroded in 2 wt% NaCl, 682 ppm Ca²⁺, 50 °C for 96 h at pH 7.5

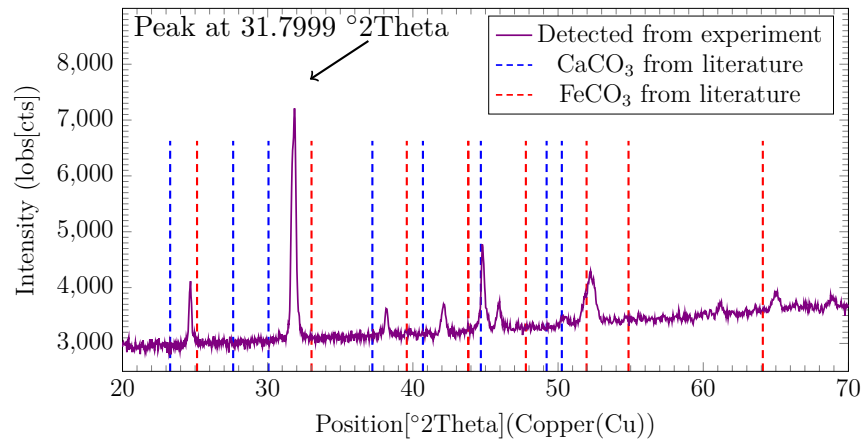


Figure 7.8: Plot depicting comparison of XRD $^{\circ}2\Theta$ position of CaCO₃ and FeCO₃ from literature to that of detected peaks for X65 carbon steel corroded in 3.3 wt% NaCl, 682 ppm Ca²⁺, 50 °C for 96 h at pH 7.5

from X-Ray scanned data. From XRD data obtained, $h = 1, k = 0, l = 4$ for peak at 31.7999 $^{\circ}2\Theta$ position. The terms "a" and "c" are unit cell edges, obtainable by substituting for known parameters in equations 7.1 and 7.2 [256]. The d-spacing, (d_{hkl}) was also obtained from XRD scan data. $d_{hkl} = 2.81745 \text{ \AA}$ for crystal peak detected at 31.7999 $^{\circ}2\Theta$ position.

$$\frac{1}{d_{hkl}^2} = \frac{4}{3} \left(\frac{h^2 + hk + k^2}{a^2} \right) + \frac{l^2}{c^2} \quad (7.1)$$

$$v = \frac{\sqrt{3}}{2}a^2c \quad (7.2)$$

Davidson et al. [257] provided data which relates cell parameters c and v of the hexagonal crystal structure with the molar fraction of constituting cations. Application of Davidson's data was demonstrated in a recent work by Esmaeely et al. [256] who investigated how the calcium presence influences carbonate film protectiveness. Figures 7.10 and 7.11 were plotted from c and v parameters provided by Davidson et al. [257]. The slope of regression lines obtained from points plotted from Davidson's data corresponds to molar fraction, x in $\text{Ca}_x\text{Fe}_{(1-x)}\text{CO}_3$ [257, 256]. Equations 7.3 and 7.4 derived from Figures 7.10 and 7.11 respectively, therefore provides an expression for presenting crystal parameters as a function of molar fraction, x .

$$\text{Lattice parameter, } c = 1.63x + 15.39 \quad (7.3)$$

$$\text{Unit cell volume, } v = 74.88x + 289.47 \quad (7.4)$$

Where " x " is the molar fraction of Ca in $\text{Ca}_x\text{Fe}_{(1-x)}\text{CO}_3$

The value of x can be derived by substituting equations 7.2, 7.3 and 7.4 into equation 7.1. The x value derived by solving equation 7.1 for peak detected at $31.7999^\circ 2\theta$ was 0.13. This implies that the crystal comprised of 0.13 and 0.87 molar fraction of Ca^{2+} and Fe^{2+} respectively. The result matches perfectly with molar ratio revealed from EDX investigation and it is in reasonable agreement with the position of the XRD peak detected at $31.7999^\circ 2\theta$ (Figure 7.8). This confirms that molar ratio of Ca^{2+} and Fe^{2+} in formed $\text{Ca}_x\text{Fe}_{(1-x)}\text{CO}_3$ film was 0.13 and 0.87 respectively.

7.2.2 Pitting trend in 682 ppm Ca^{2+}

The galvanic trend for coupled 1mm, 2mm and 3mm anodes in 682 ppm Ca^{2+} is shown in Figures 7.12, 7.13 and 7.14 respectively. Galvanic current was high at

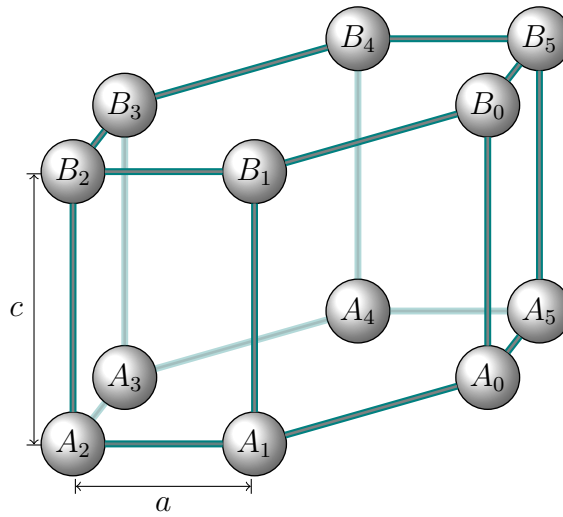


Figure 7.9: Schematic representation of a typical hexagonal lattice structure

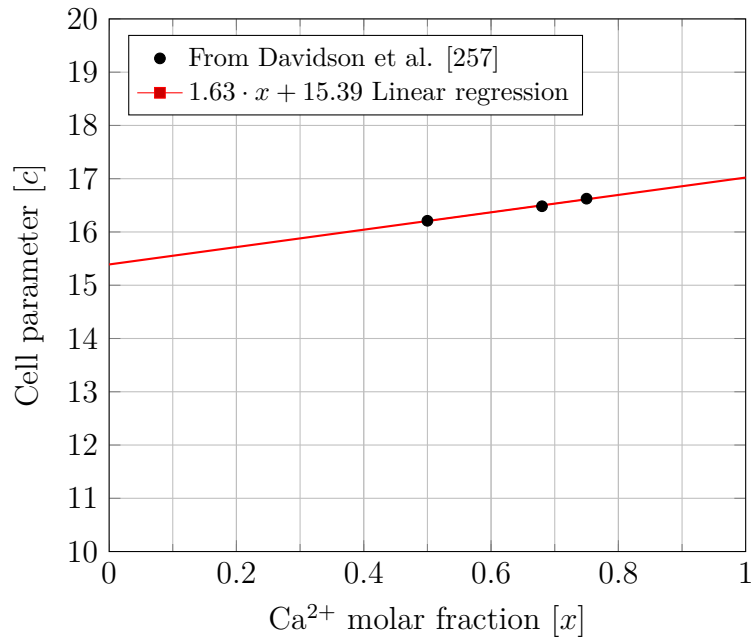


Figure 7.10: Plot of parameter "c" versus molar fraction of Ca²⁺

the start of experiments but rapidly declined during the first hour of exposure due to the high initial corrosion rate of the anode which was rapidly passivated. The current drops primarily due to the disruption in potential balance as the system got settled. Since measured galvanic current density is positive, the freshly polished pin (having less positive potential) is the anode in the pit coupling [253]. Spikes emerging from galvanic trend are likely attributed to pitting on the anode pin as the spikes trended in the positive direction. The potential of the large passivated cathode disc was about -400 mV (vs Ag/AgCl) while freshly polished anode pin was

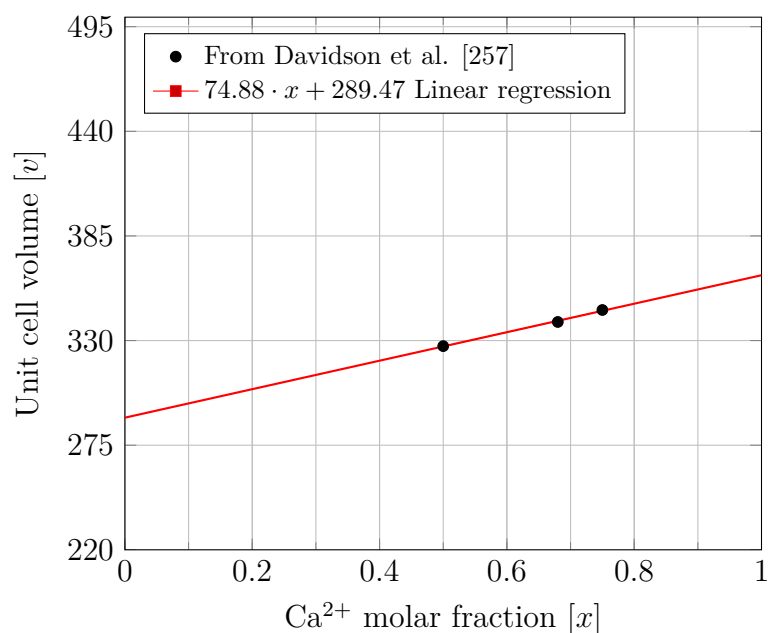


Figure 7.11: Plot of unit volume "v" versus molar fraction of Ca²⁺

about -750 mV (vs Ag/AgCl) in same solution when un-coupled. Upon coupling, mixed potential recorded was very close to that of the uncoupled cathode (-400 mV (vs Ag/AgCl)), due to the larger size of the cathode. As the anode pin corrodes in the coupling, its potential increases in the positive direction, but this event is masked by the overriding potential of the already passivated cathode disc.

The galvanic current generated by the coupling drops slowly as the potential of the anode increased. Relating figures 7.12, 7.13 and 7.14 to galvanic current recorded in Ca²⁺ - free solution (Figure 7.15) indicated higher current density for solution containing 682 ppm Ca²⁺. While average current density of 0.25 mA/cm², 0.12 mA/cm² and 0.02 mA/cm² were respectively recorded for 1mm, 2mm and 3mm pits in 682 ppm Ca²⁺ solution, average current densities of 0.1 mA/cm², 0.05 mA/cm², and 0.009 mA/cm² were recorded for 1mm, 2mm and 3mm anodes in Ca²⁺ - free solution. The top ten average pit depths on 1mm, 2mm and 3mm anodes coupled in artificial pit for 24 h in 682ppm Ca²⁺ solution were approximately 60μm, 34μm and 25μm respectively. Profilometry results of the maximum pit recorded on the anode electrodes after 24 h pit coupling in 682 ppm Ca²⁺ solution are featured in

Figure 7.16. Connecting these with the galvanic trend (Figures 7.12, 7.13 and 7.14) suggests that pit depth increases with a rise in galvanic current as expected. Though temperature was kept constant at 50 °C in this work, the pitting trend tallies with work by Han et al. [252] who reported an increase in localised attack with rise in temperature and cathode to anode area ratio (AR). AR of anode to cathode was observed to influence the magnitude of galvanic current. Average current density for 1 mm anode (AR 1:625), 2 mm anode (AR 1:156) and 3 mm anode (AR 1:69) in 682 ppm Ca^{2+} solution was 0.25 mA/cm², 0.12 mA/cm² and 0.019 mA/cm² respectively. This is in agreement with findings in other galvanic experiments [208, 252, 253]. For experiments conducted in Ca^{2+} - free solution, the maximum pit depth on 1mm, 2mm and 3mm anodes coupled pit for 24 h was 37 μm , 22 μm and 20 μm . A bar chart comparing pitting on anodes of coupled pit in 682 ppm Ca^{2+} and Ca^{2+} - free system is shown in Figure 7.21. Hence, higher galvanic current and pitting was recorded under mixed ($\text{Ca}_x\text{Fe}_{(1-x)}\text{CO}_3$) film conditions.

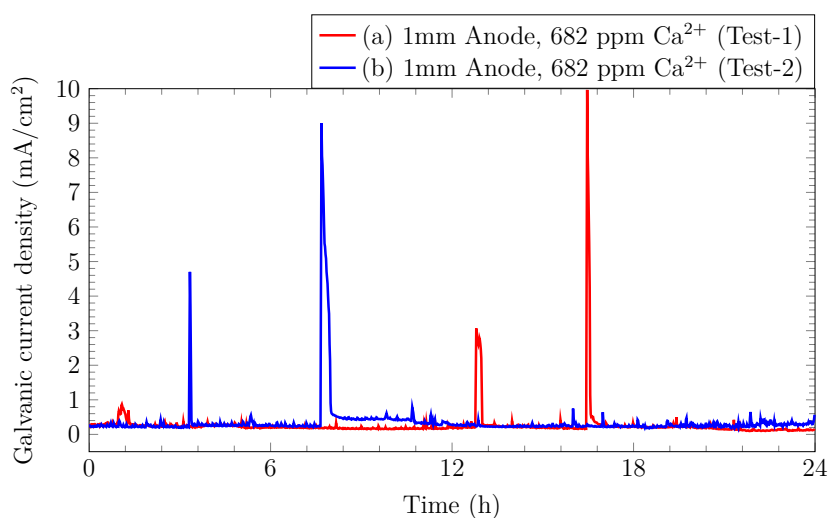


Figure 7.12: Repeated galvanic trend for freshly polished (a) 1mm anode (Test1) and (b) 1mm anode (Test-2) in 0.625mm pit for 24 h in 3.3 wt% NaCl, 682 ppm Ca^{2+} at 50 °C, pH 7.5, saturated CO_2

SEM analysis of anode surface after 24 h pit coupling revealed presence of mixed $\text{Ca}_x\text{Fe}_{(1-x)}\text{CO}_3$ deposited on the anode as shown in Figure 7.19. This implies that pit initiates and propagates beneath formed film. Presence of multiple pits on anode pins (Figure 7.17) also suggest that micro-pitting develops within pits and that

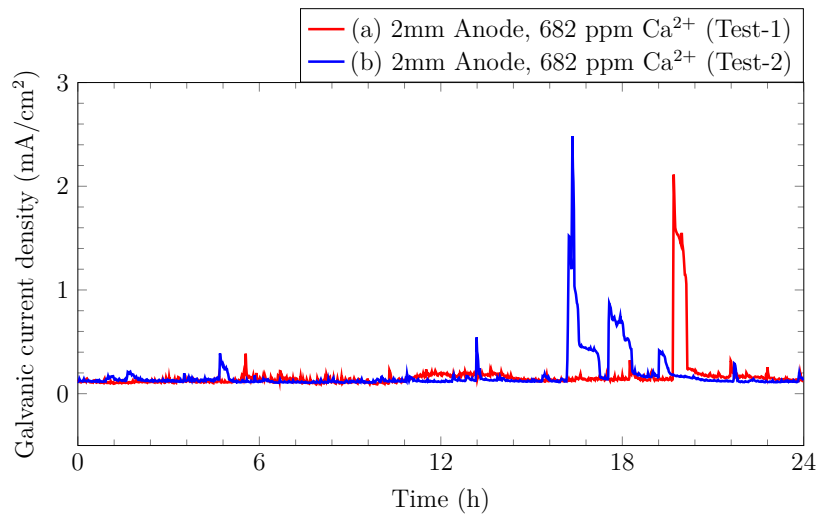


Figure 7.13: Repeated galvanic trend for freshly polished (a) 2mm anode (Test1) and (b) 2mm anode (Test-2) in 0.625mm pit for 24 h in 3.3 wt% NaCl, 682 ppm Ca^{2+} at 50 °C, pH 7.5, saturated CO_2

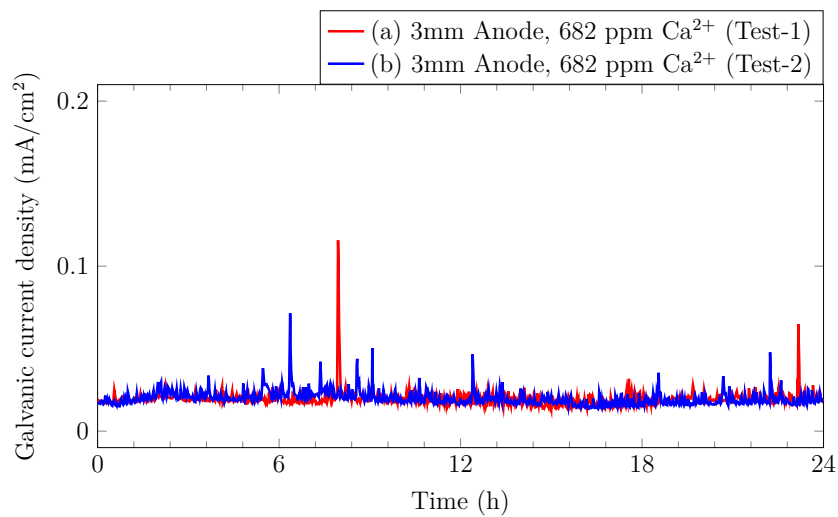


Figure 7.14: Repeated galvanic trend for freshly polished (a) 3mm anode (Test1) and (b) 3mm anode (Test-2) in 0.625mm pit for 24 h in 3.3 wt% NaCl, 682 ppm Ca^{2+} at 50 °C, pH 7.5, saturated CO_2

several anode/cathode spots spatially evolve on actively corroding pit sites. Presence of Ca^{2+} on anode could be responsible for the significant galvanic current and pitting recorded in artificial pit containing 682 ppm Ca^{2+} .

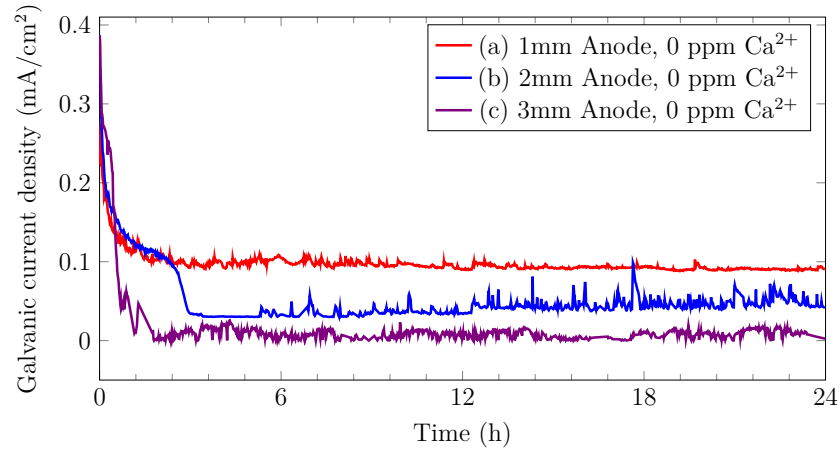


Figure 7.15: Galvanic trend for freshly polished (1) 1mm anode, (b) 2mm anode and (c) 3mm anode in passivated 4.9 cm² cathode, 0.625mm pit for 24 h in 3.5 wt% NaCl, 0 ppm Ca²⁺ at 50 °C, pH 7.5, saturated CO₂

7.2.3 Measured corrosion rate for anode and cathode electrodes

Approximate corrosion rate of uncoupled cathode and anode electrodes were obtained by briefly interrupting galvanic measurement for 1mm pit in order to take LPR/OCP measurement after about 1 h, 12 h and close to end of 24 h galvanic test. The mixed (galvanic) current density after 1 h, 12 h and 24 h in coupled pit was 1.3 mA/cm², 0.22 mA/cm² and 0.15 mA/cm² respectively. The galvanic current was obtained by multiplying the surface area of the anode electrode with the galvanic current density in order to derive corrosion rate for coupled anode and cathode. Corrosion rate for coupled anode and coupled cathode was calculated by factoring electrode surface area into equation 7.5 [258].

$$\text{Corrosion rate (mmpy)} = 3.27 \times 10^{-3} \frac{I \times E_w}{A\rho} \quad (7.5)$$

Where:

3.27×10^{-3} = constant for expression in mmpy, I = corrosion current in μA , (derived as galvanic current in Table 7.3), A = Area of electrode in cm², ρ = metal density in (g/cm³), 27.5 g/cm³ for Fe. E_w = equivalent weight (27.56g).

A summary of applied data is presented in Table 7.3 while Figure 7.18 illustrates the corrosion rates for uncoupled and coupled pit electrodes. Corrosion rate of electrodes generally reduce as exposure time increases. The corrosion rate of the coupled anode (Figure 7.18) was high at the start of the experiment but declined steadily with time. This was due to fast deposition of corrosion product on the pit anode as observed in Figure 7.19. EDX examination of pit anode shows presence of

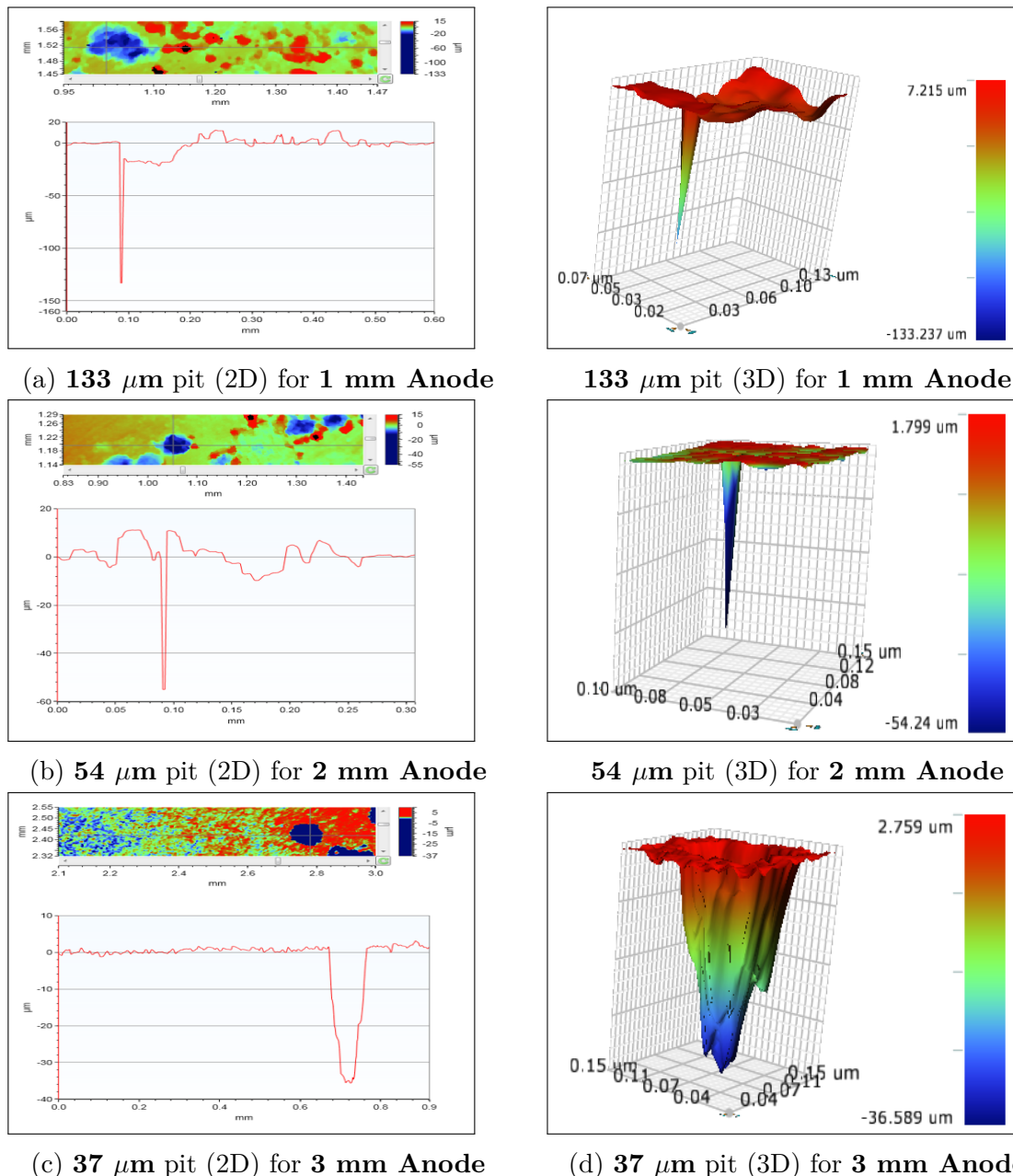


Figure 7.16: Morphology of maximum pit depth recorded on (a) 1 mm anode, (b) 2 mm anode and (c) 3 mm anode in artificial pit under saturated CO_2 , 3.3 wt.% NaCl , 682 ppm Ca^{2+} , pH 7.5, 50°C for 24 h.

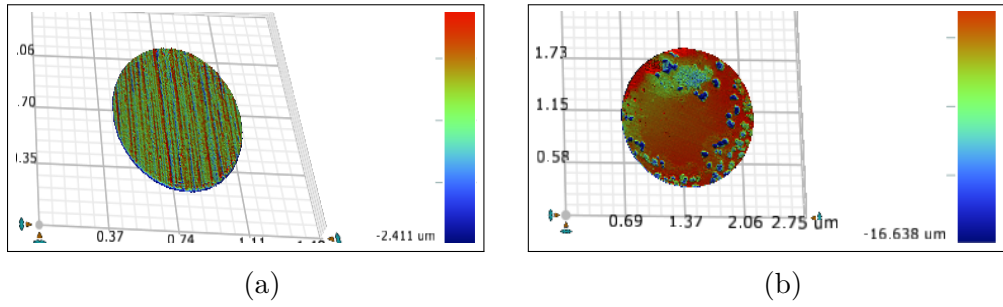


Figure 7.17: Profilometry of 1mm anode (a) freshly polished before coupling into artificial pit assembly (b) after corrosion in an artificial pit

mixed carbonate in the pit. Similar results were obtained on the anode electrode for tests conducted in Ca^{2+} - free solution where FeCO_3 was detected in the pit (Figure 7.20). It implies that similar product formed on steel surface also forms within corrosion pit. Pitting observed on anode electrode in Ca^{2+} - free coupling were of low magnitude. Bar chart depicting top-10 average pit for Ca^{2+} - free and 682 ppm Ca^{2+} solution is featured in Figure 7.21. Relatively lower corrosion rate was also reported for anode electrode in work by Han et al. [208] who investigated galvanic trend in CO_2 corrosion using the artificial pit. Higher corrosion rate observed on coupled anode electrode was due to the influence of Ca^{2+} on the mixed carbonate formed on the pit anode.

Table 7.3: Corrosion data obtained using 1mm anode pit coupling

Elapsed coupling time	1 h	12 h	24 h
Galvanic current density	1.30 mA/cm ²	0.22 mA/cm ²	0.15 mA/cm ²
Galvanic current	0.0100 mA	0.0017 mA	0.0012 mA
Uncoupled anode	1.200 mmpy	0.900 mmpy	0.200 mmpy
Uncoupled cathode	0.060 mmpy	0.060 mmpy	0.050 mmpy
Coupled anode	14.590 mmpy	2.480 mmpy	1.750 mmpy
Coupled cathode	0.023 mmpy	0.004 mmpy	0.003 mmpy

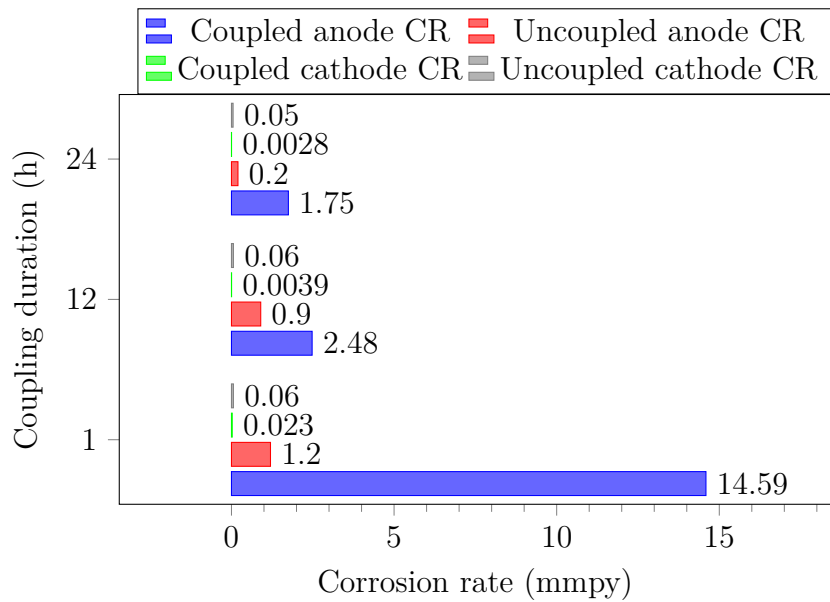


Figure 7.18: Chart depicting general corrosion rate (CR) for passivated cathode and freshly polished 1 mm anode electrode in coupled and uncoupled pit at experiment start, 12 h into test and towards test finishing under saturated CO_2 , 3.3 wt.% NaCl, 682 ppm Ca^{2+} , pH 7.5, 50 °C.

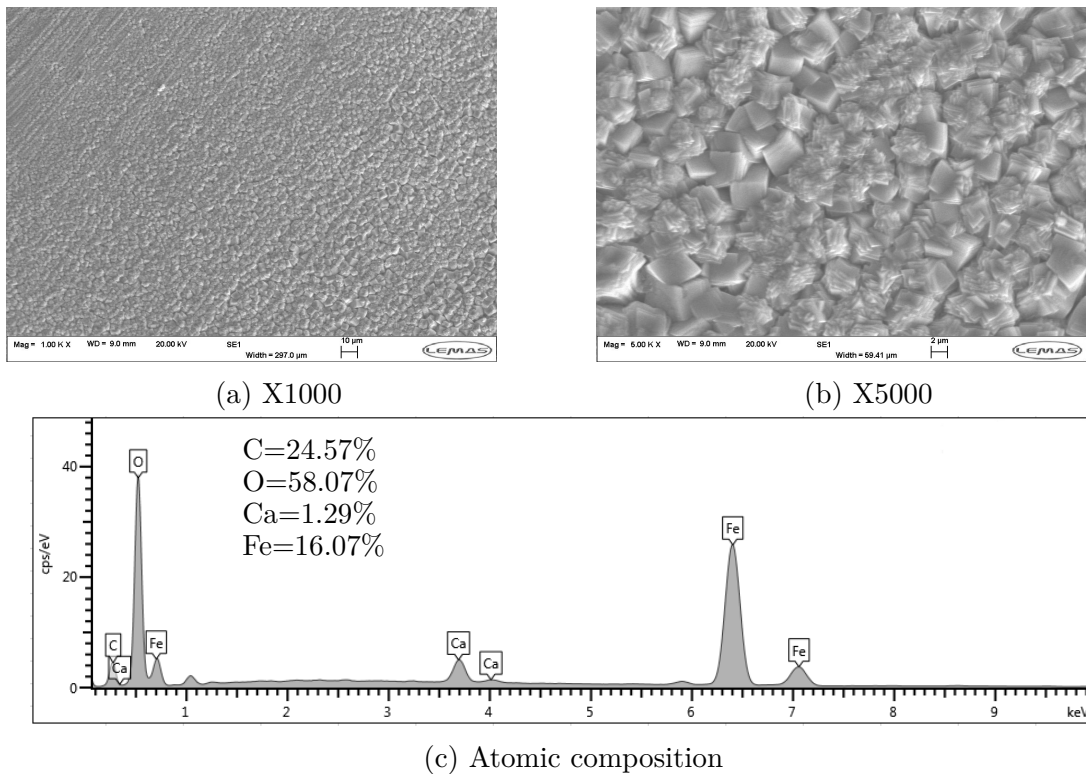


Figure 7.19: SEM results featuring (a) x1000 magnification (b) x5000 magnification and (c) atomic composition of mixed CaCO_3 and FeCO_3 formed on anode pin in 3.3 wt% NaCl, 682 ppm Ca^{2+} , pH 7.5, 50 °C for 24 h

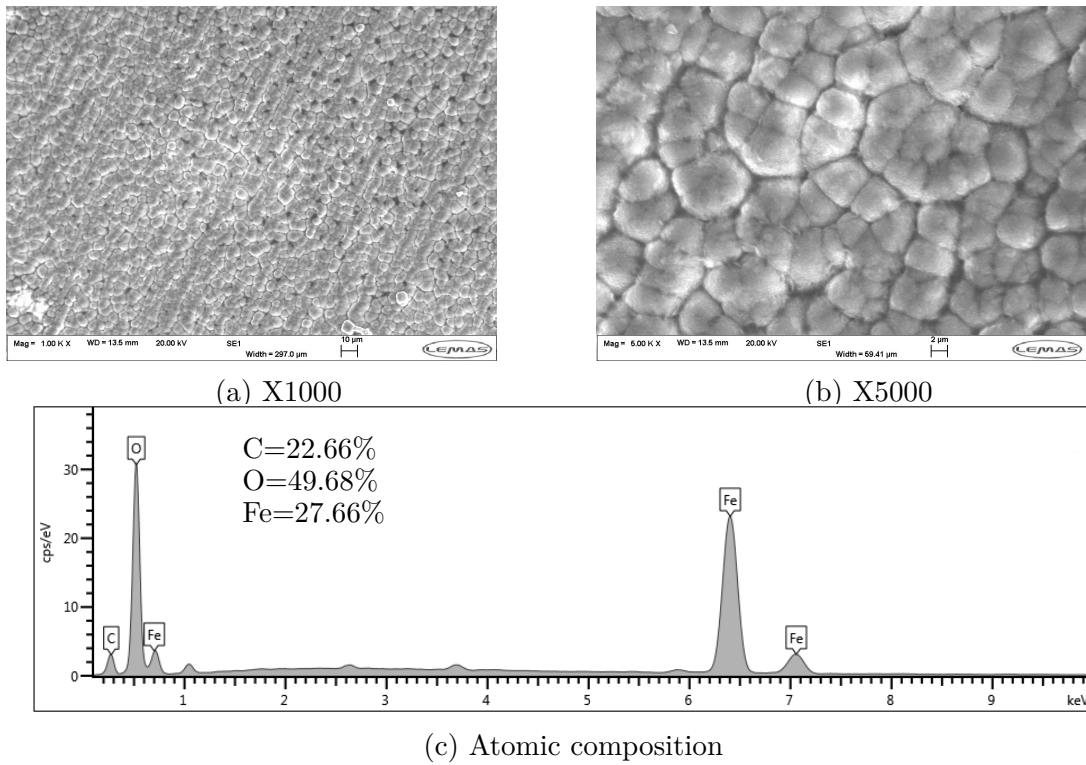


Figure 7.20: SEM results featuring (a) X1000 magnification (b) X5000 magnification and (c) atomic composition of FeCO_3 formed on anode pin in 3.5 wt% NaCl, 0 ppm Ca^{2+} , pH 7.5, 50 °C for 24 h

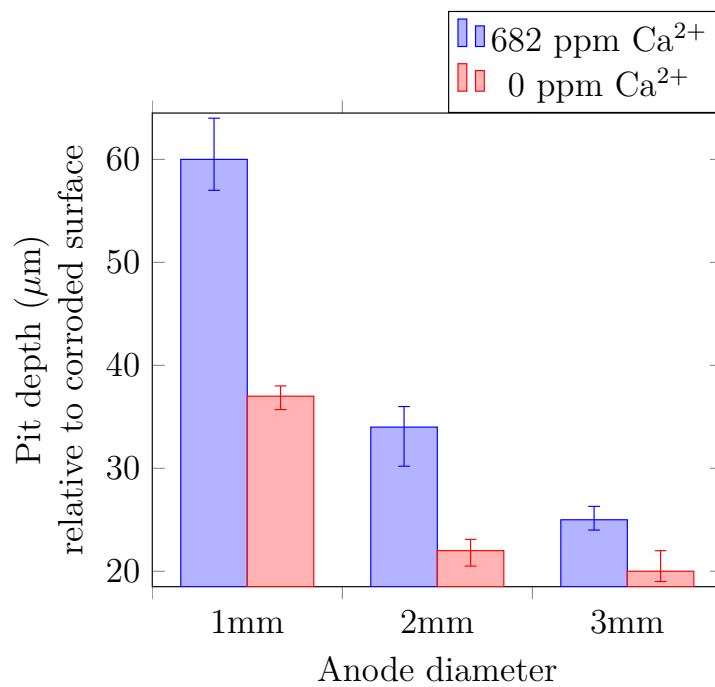


Figure 7.21: Bar chart depicting pitting trend (top-10 average) of pits formed on coupled anodes in saturated CO_2 , 80°C over a duration of 1 h in (a) 682 ppm Ca^{2+} , 3.3 wt% NaCl and (b) 0 ppm Ca^{2+} , 3.5 wt% NaCl

7.2.4 Derivation of charge associated with galvanic current in artificial pit

Figure 7.21 features a comparison of pitting recorded under a galvanic influence in the artificial pit. The corresponding charge was derived from the galvanic current density measured during 24 h coupling in a 682 ppm Ca^{2+} and Ca^{2+} -free solutions by integrating the product of measured current (I) with time (t) as presented in Equation 7.6. Electrochemical measurements were taken at intervals of 60 seconds covering 24h galvanic test duration.

$$Q = \int_0^{24h} I dt = \int_0^{24h} iA dt \quad (7.6)$$

Where Q is the total charge recorded after 24 h galvanic test measured at intervals of 60 seconds, 'i' is current density (A/m^2) and 'A' is test surface area (m^2). To relate the total charge derived to the pit anode size, charge density was calculated by dividing the total charge by the area of the anode electrode. Table 7.4 shows the charge density with respect to the anode electrodes in Ca^{2+} -free and 682 ppm Ca^{2+} solution. A plot depicting charge density in coupled artificial pit for 682 ppm Ca^{2+} and Ca^{2+} -free solutions is shown as Figure 8.15. Charge densities in 682 ppm Ca^{2+} solutions were generally higher than that observed Ca^{2+} -free solutions. The charge per unit area also drops as the pit anode size increased. From Figure 7.22 and Figure 7.21, it is safe to state that Ca^{2+} presence increase pitting in low carbon steel. It as well shows that higher pit depth recorded in 1mm pit was due to higher charge density on the anode electrode. This implies that a tiny compromised spot on the film formed on carbon steel would produce higher charge density with greater consequence than compromised spot of larger size.

Table 7.4: Charge recorded in artificial pit coupling in saturated CO₂, 3.3 wt.% NaCl, pH 7.5, 50 °C in 682ppm Ca²⁺ and Ca²⁺-free solutions.

Anode diameter	0ppm Ca ²⁺		682ppm Ca ²⁺	
	Total charge	Charge density	Total charge	Charge density
1mm	0.066375 C	8.45 C/cm ²	0.1806952 C	23.00 C/cm ²
2mm	0.1405023 C	4.47 C/cm ²	0.4553327 C	14.49 C/cm ²
3mm	0.0898531 C	0.13 C/cm ²	0.1188381 C	1.68 C/cm ²

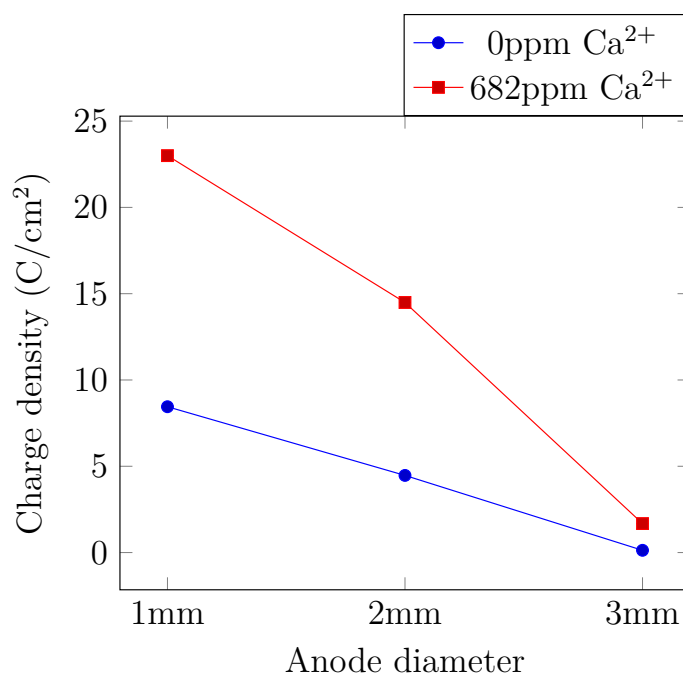


Figure 7.22: Plot depicting charge recorded for 1mm, 2mm and 3mm anode diameter in artificial pit coupling in saturated CO₂, 3.3 wt.% NaCl, pH 7.5, 50 °C in 682ppm Ca²⁺ and Ca²⁺-free solutions.

7.3 Conclusions

An investigation was conducted on the influence of Ca²⁺ on pitting corrosion in saturated CO₂ environment using an artificial pit. The following are the major findings revealed:

- a. Calcium presence increases the galvanic current between film covered and

compromised spots on low carbon steel.

- b. Galvanic current density declines as corrosion products forms inside the pit.
- c. Pseudo-passivation is delayed under $\text{Ca}_x\text{Fe}_{(1-x)}\text{CO}_3$ film condition compared to that observed in FeCO_3 film.
- d. Corrosion products that form on steel surface also grow within pits while micro-level stochastic pits emerge beneath the film on pit anodes.
- e. The extent of pit penetration under galvanic influence depends on the area of compromised spot on the film.

Chapter 8

Discussion

8.1 Introduction

Chapters 5, 6 and 7 presented findings on experimental work on low carbon steel pitting in saturated CO₂ environments. This discussion chapter draws on these results and provides insights into the advances made on the understanding of pitting corrosion under the following headings:

- Rationale for considering the top-10 pits as a measure of pitting severity
- Generating stress free stochastic pits.
- Calcium polymorphs and the pitting trend.
- Application of artificial pit to understand pitting in Ca²⁺ - rich solution.
- Pseudo-passivation and galvanic effects in calcium pitting.
- The effect of anode / cathode area ratio on carbon steel pitting in 682 ppm Ca²⁺ solution.

- The effect of chloride ion on carbon steel pitting in Ca^{2+} solution.
- The relationship between charge and carbon steel pitting in 682 ppm Ca^{2+} solution.
- Pitting and steel micro-structure.

8.2 Rationale for considering the top-10 pits as a measure of pitting severity

Several factors can be considered to determine the severity of pitting. This includes; pit mouth diameter, pit base diameter, pit depth (relative to the corroded surface), absolute pit depth, pit volume, amongst others [259, 260]. These factors contribute to weight loss, which adds to that recorded from general (uniform) corrosion. The catastrophic effect of pitting in pipes applied for oil and gas application often occur when pits grow until eventual rupture. The deepest pit is likely to perforate first and therefore becomes important in pitting investigations. Pit growth is often stochastic in nature, making it difficult to identify the deepest pit among other pits, particularly in pitting of similar depth profile. Pits with depth ranking among top-10 is a fair representation of the deepest pits in a stochastic pit representation. The average of top-10 pits was therefore considered in analysing the pitting trend for investigations conducted in this work.

8.3 Generating stress free stochastic pits

It is often required to generate pitting on steels so as to understand their growth or means of mitigating pit growth. The common method to induce pit growth in the laboratory is by the use of nano-indentation tools [261] as well as acid

etching [123]. Indentation however induces mechanical stress on the metal and pitting kinetics under such method does not reflect the true pitting experienced on steel. Acid etching on the other hand is difficult to reproduce and it could take a long time to generate desirable pitting profile. Krawczyk et al. [262] work on corrosion behaviour of stainless steel utilised polarisation effect in 10^{-2} - 3M HCl solution but no clear relationship was established on the pitting threshold. Potentiostatic polarisation technique described in Chapter 5 of this thesis offers a promising technique for generating stochastic stress-free pitting profile for laboratory investigations. Significant pitting was recorded under 150mV polarisation at 30°C, pH 3.8 where non-protective scale forms on steel surface. However, very low pitting was recorded under 150mV polarisation at 80°C, pH6.6 where protective FeCO_3 formed on steel surface.

8.3.1 Effect of pH on carbon steel pitting

The effect of pH on pitting trend was observed by conducting pit counts after 24 h potentiostatic polarization at 30°C. Low temperature was utilised to reduce the likelihood of forming protective FeCO_3 film on the sample. Pit depth was observed to decline as pH was increased under applied potential in Fe_3C growth condition as shown in Figure 8.1. This implies that increase in pH retards growth of pit at 30°C.

The polarisation curve of X65 carbon steel under conditions favouring Fe_3C scales and FeCO_3 films are shown in Figures 8.2 and 8.3 respectively. An active trend was observed under Fe_3C scale condition while distinct deviations were recorded in the polarisation curves in conditions favouring FeCO_3 films. These points termed **pseudo-active** and **trans-active** suggest that carbon steel could exhibit a passive trend under high pH conditions. A similar observation was reported by Kahyarian et al. [263] who investigated the effect of iron dissolution in CO_2 corrosion. Regions identified as **transition** and **pre-passivation** was identified in Kahyarian et al [263] work. The likely parameter influencing such a trend is the solution pH and not the

nature of the film formed on the steel surface since the FeCO_3 film was not formed in the work by Kahyarian et al. [263].

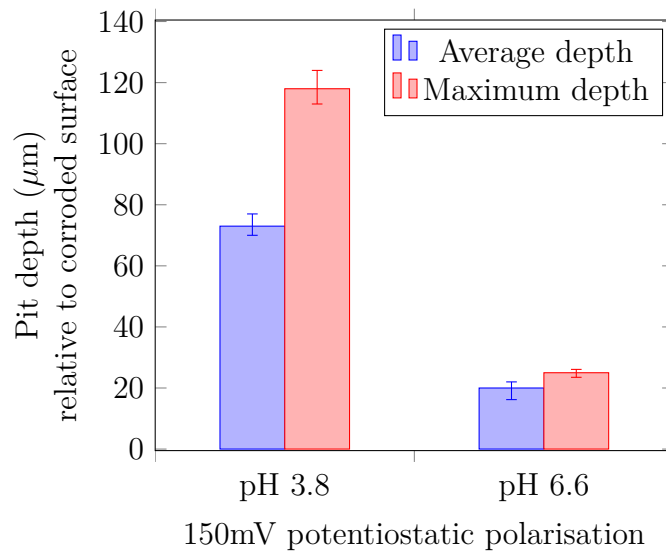


Figure 8.1: Pit depth profile of samples subjected to 150mV potentiostatic test at pH 3.8 and pH 6.6 for test conducted at 30°C, 3.5wt% NaCl, CO_2 condition for 24Hrs.

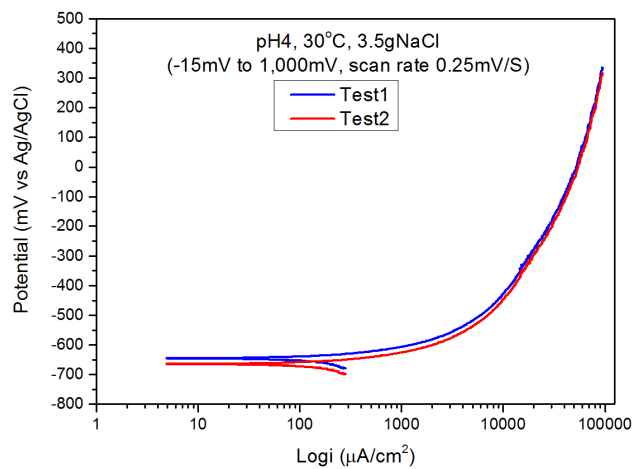


Figure 8.2: Polarisation curve of X65 carbon steel under film-free condition (pH 4, 30°C, 3.5wt% NaCl, -15mV to 1,000mV, scan rate 0.25mV/s, 250RPM).

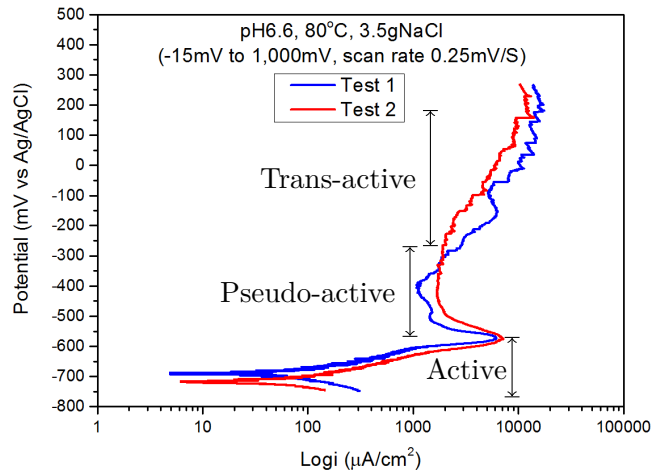


Figure 8.3: Polarisation curve of X65 carbon steel under protective film conditions (pH6.6, 80°C, 3.5%NaCl, -15mV to 1,000mV, scan rate 0.25mV/s, 250RPM).

8.4 Comparison of Ca^{2+} pitting under pH 3.8 and pH 6

Comparing Figure 6.2(a) (0ppm Ca^{2+} , pH 6) and Figure 6.4(b) (5,000ppm Ca^{2+} , pH 6), the starting corrosion rate in the Ca^{2+} -free solution was significantly lower than that in 5,000 ppm Ca^{2+} solution. While FeCO_3 films formed in Ca^{2+} -free solution, mixed $\text{Ca}_x\text{Fe}_{(1-x)}\text{CO}_3$ was detected in the Ca^{2+} -rich solution. This suggests higher corrosion rate for solutions where saturation tends towards mixed $\text{Ca}_x\text{Fe}_{(1-x)}\text{CO}_3$ formation than when FeCO_3 was favoured.

At pH 3.8, Figure 6.1(a) (0ppm Ca^{2+} , pH 3.8), the corrosion rate was lower compared to Figure 6.4(a) containing 5,000 ppm Ca^{2+} . As expected, a Fe_3C layer was detected at pH 3.8 in Ca^{2+} -free solution (Figure 6.1(b)), aragonite deposits were recorded after a 4-day test in 5,000 ppm Ca^{2+} solution. Higher corrosion rate in the Ca^{2+} solution suggests that Fe^{2+} dissolution progressed significantly as aragonite began to deposit on the steel surface.

Higher corrosion rate in Ca^{2+} solution solutions suggests that films form faster on the steel surface and as well cover the mouth of induced pits. The high corrosion rate in

Ca^{2+} being sustained throughout the test duration implies that Ca^{2+} promotes film porosity thereby allowing free interaction between the bulk and the steel surface. For pH 3.8 solutions, higher pitting was recorded in Ca^{2+} -rich solution compared to that in Ca^{2+} -free solutions (Figure 8.13). EDX analysis of products formed in the pits at pH 6 revealed higher Ca^{2+} concentration at the pit mouth but with near-zero Ca^{2+} presence inside pit as shown in Figure 6.22. For pH 3.8 solution, significant Ca^{2+} presence was recorded from the pit mouth all through the pit vertex as shown in Figures 8.6 to 8.8. This suggests that the needle-shaped aragonite (Figure 6.21(a)) fill up the entire pit cavity.

8.5 Calcium polymorphs and the pitting trend

Many investigations have been made on polymorphs of calcium such as calcite, aragonite and vaterite [147, 148, 149, 150, 151, 152, 153, 154]. Little is however known on how the different polymorphs influence pitting kinetics in low carbon steel. Chapter 6 of this thesis presented findings on how different calcium polymorphs influence pitting. A simplified chart featuring the pitting relationship under the experimental test conditions utilised in this work is shown in Figures 8.4(a) and 8.4(b). Figure 8.4(a) depicts the pitting trend relative to the corroded surface while the latter features the pit depth relative to the original sample surface. Comparison of both graphs show that metal thinning due to general corrosion is significant and important in assessing the overall pitting trend. Absolute pitting was observed to increase from initial $70\mu\text{m}$ depth at pH 3.8, where no form of film protectiveness is expected, to well above $250\mu\text{m}$ after 96 h (depicted in red (Figure 8.4(b))). At pH6 (depicted in black (Figure 8.4(b))), pitting increased slightly from initial $70\mu\text{m}$ depth to about $97\mu\text{m}$ after 96 h. This suggests that mixed carbonate formed at pH6 retards general and pitting corrosion compared to aragonite deposited at pH3.8. In Ca^{2+} free solution, absolute pitting after 96 h test at pH3.8 and pH6 were $140\mu\text{m}$ and $46\mu\text{m}$ respectively. Although pit growth was observed beneath FeCO_3 film in Ca^{2+}

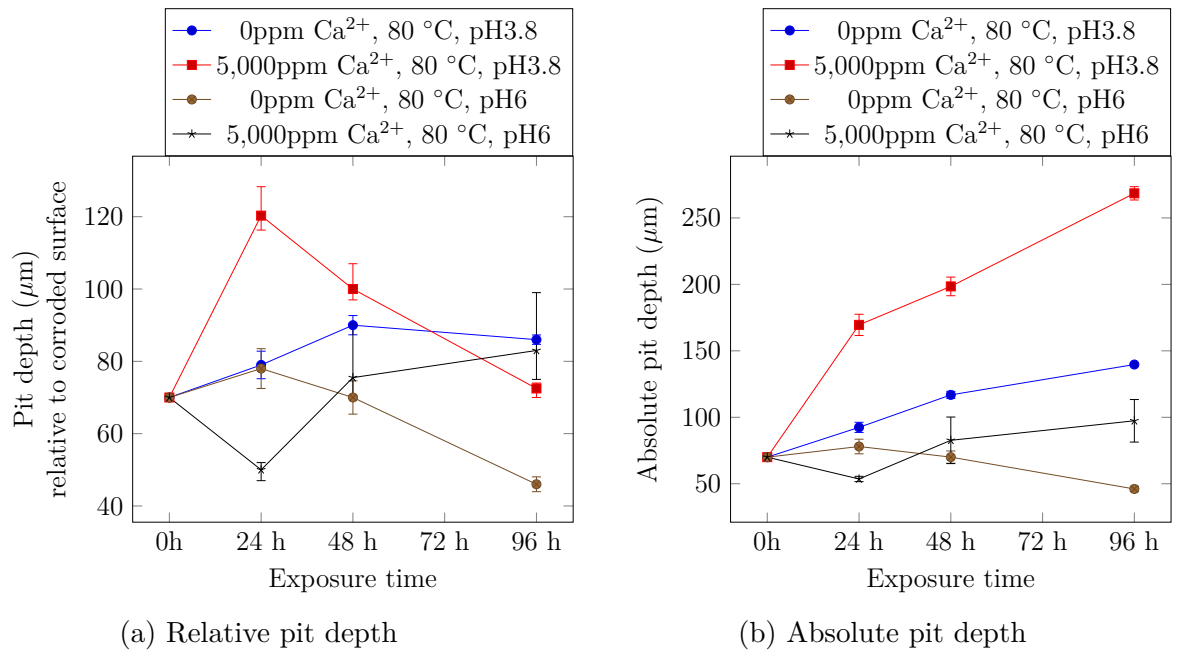


Figure 8.4: Plot showing (a) relative pit depth and (b) absolute pit depth recorded on X65 carbon steel corroded for 96 h

free system at pH 6, the relatively low pitting was due to the formation of protective FeCO_3 film that adheres to the steel surface. In summary, pitting trend displayed in (Figure 8.4(b)) confirms that calcium influence both general and pitting corrosion in low carbon steel. Pitting extent is however less under conditions favouring the formation of mixed $\text{Fe}_x\text{Ca}_{1-x}\text{CO}_3$.

The pitting trend was observed to differ in accordance with the nature of Ca^{2+} polymorph that forms on steel surface. Figure 8.5 shows maximum pit depth and top-10 average pits from initial $70\mu\text{m}$ depth in solution containing 5,000ppm Ca^{2+} . An amorphous layer forms on the steel surface during the first 24h of exposure under pH3.8 and pH6 conditions. However, the propagation rate reduced significantly after the first 24 h when aragonite begins to emerge for experiments conducted at pH3.8 (red & blue trend lines in Figure 8.5). This suggests that pitting rate declines upon the emergence of aragonite compared to that recorded under amorphous film conditions. However, the pitting trend at pH6 was almost linear throughout the experiment.

Calcite and aragonite will normally precipitate at the same rate if both evolve

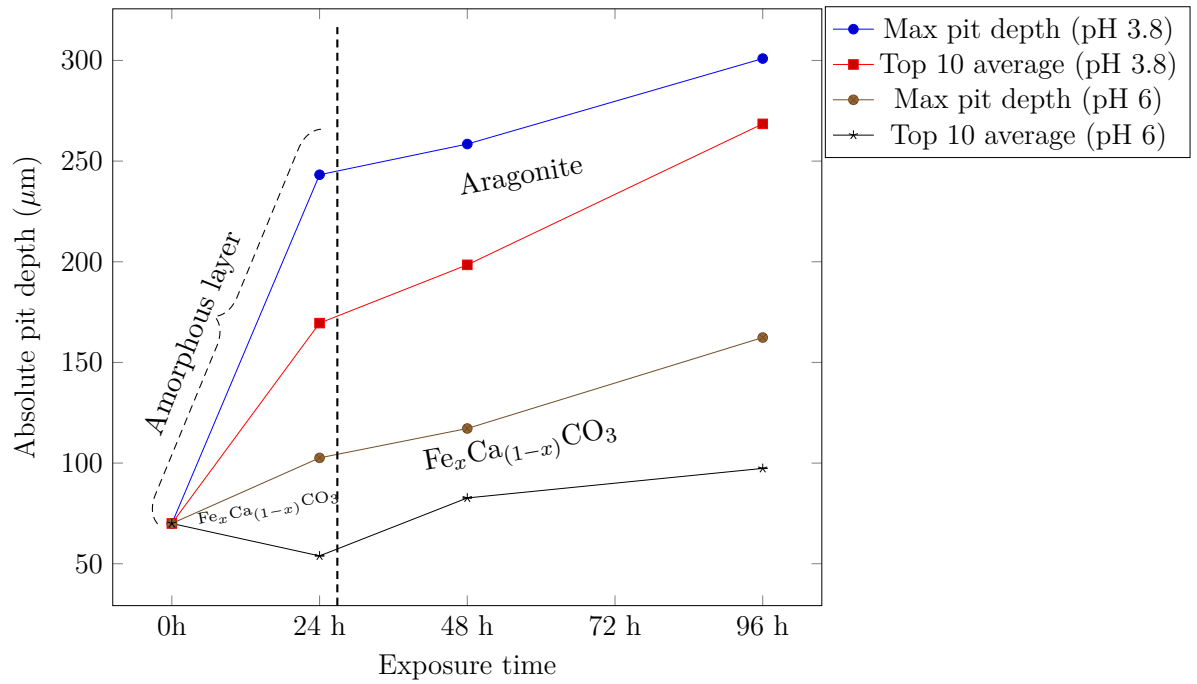


Figure 8.5: Plot showing maximum pit depth and top-10 average of pits from initial $70\mu\text{m}$ depth in solution containing $5,000\text{ppm Ca}^{2+}$, $2\text{ wt}\% \text{NaCl}$ at $80\text{ }^\circ\text{C}$ for 96 h

together [243]. Concentrations of $\text{Ca}^{2+}/\text{CO}_3^{2-}$ are important parameters that determine the nature of crystalline polymorph formed on steel surface [244]. As calcium complexes form in solution at low pH, amorphous calcium carbonate (ACC) being the least stable polymorph will precipitate first in accordance with the Ostwald's step rule [239]. ACC however rapidly transforms into calcite which is a more stable polymorph [245, 239]. The electrochemical environment influences the morphology and attributes of the formed product [246]. Relating Figure 6.6 with Figure 6.8 reveals that pit growth declines as amorphous CaCO_3 transforms to aragonite. A cross section view of aragonite shown in Figure 8.6 shows aragonite densely lined the pit mouth and occupied the pit cavity probably due to its needle-like structure. EDX mapping across the deposited aragonite featured in Figure 8.7 and line scan (Figure 8.8) revealed consistent Ca^{2+} presence from pit mouth to the pit base. Reduced pitting beneath aragonite polymorph could therefore be due to needle-like aragonite that fills the entire pit and thereby disrupts electrolyte interaction with the pit wall.

Taking pH effect into perspective, a bar chart depicting the top-ten average pits at

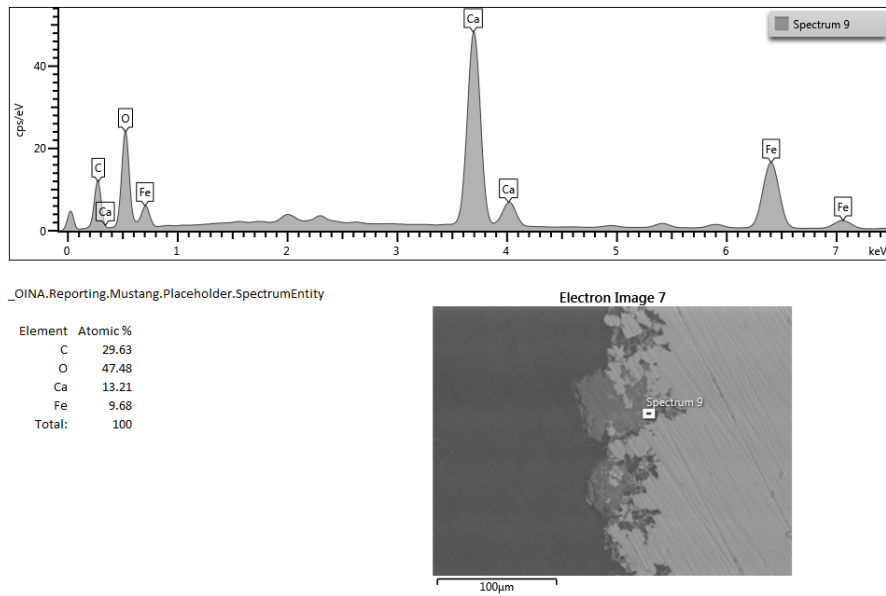


Figure 8.6: Cross section showing Ca^{2+} inside a pit on X65 carbon steel corroded at 2 wt% NaCl, 5,000 ppm Ca^{2+} , 80 °C for 96 h at pH 3.8

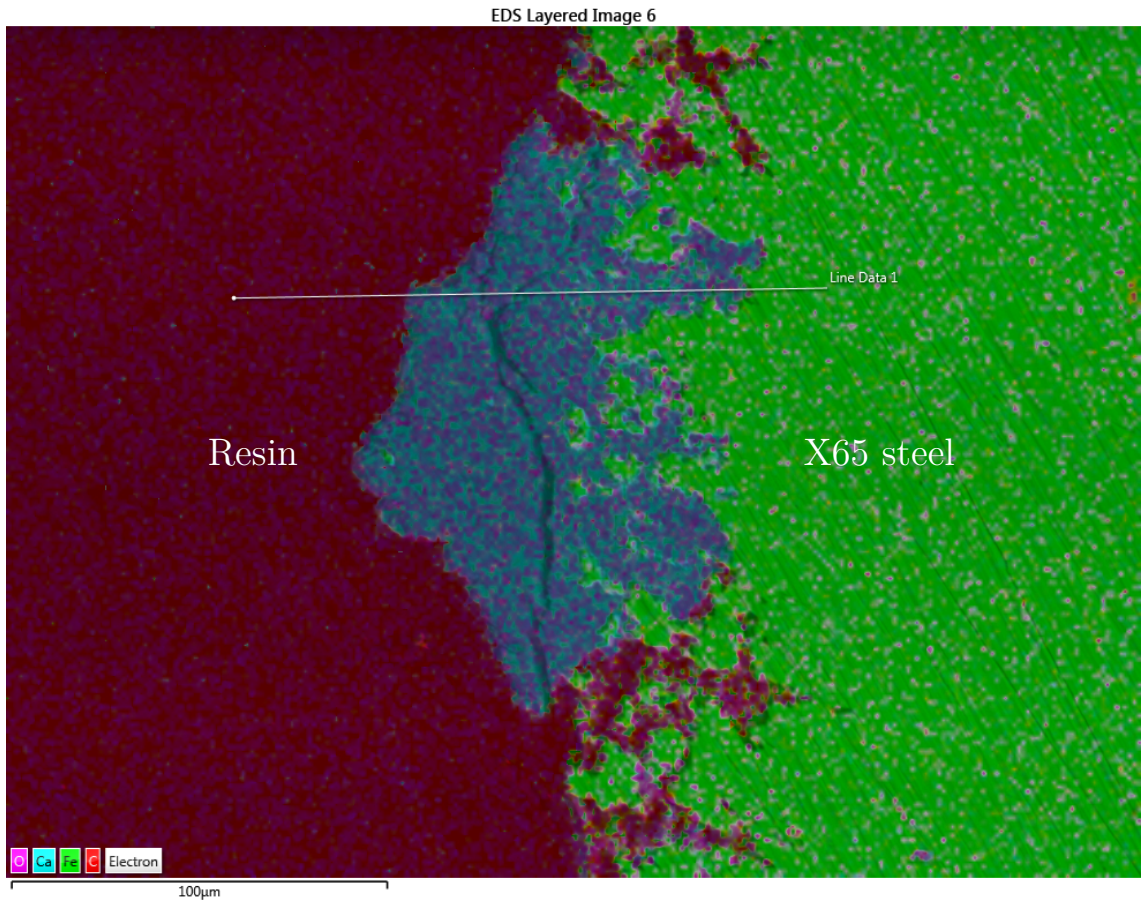


Figure 8.7: EDX mapping showing Ca^{2+} inside a pit on X65 carbon steel corroded at 2 wt% NaCl, 5,000 ppm Ca^{2+} , 80 °C for 96 h at pH 3.8

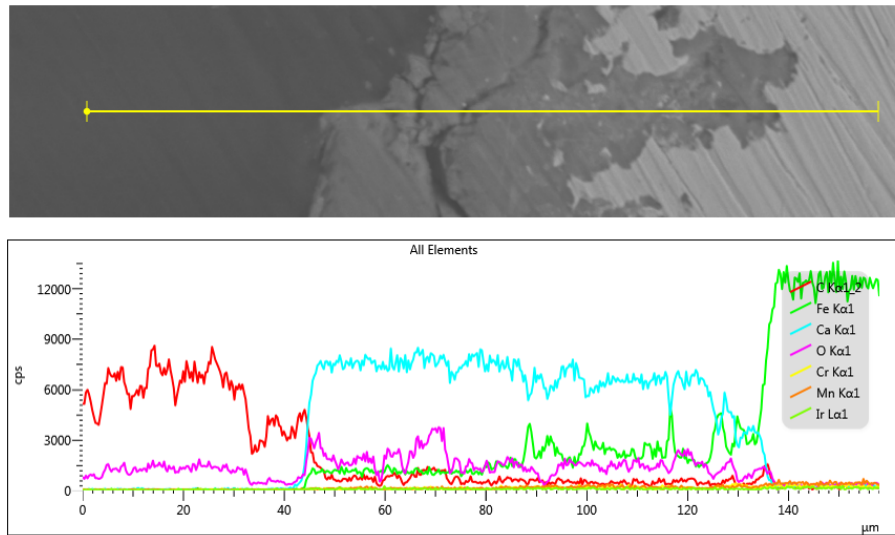
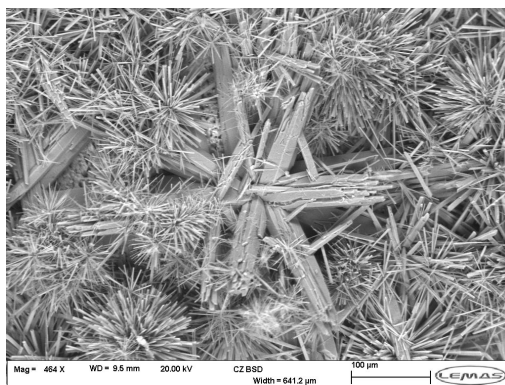


Figure 8.8: EDX line scan showing Ca^{2+} inside a pit on X65 carbon steel corroded at 2 wt% NaCl, 5,000 ppm Ca^{2+} , 80 °C for 96 h at pH 3.8

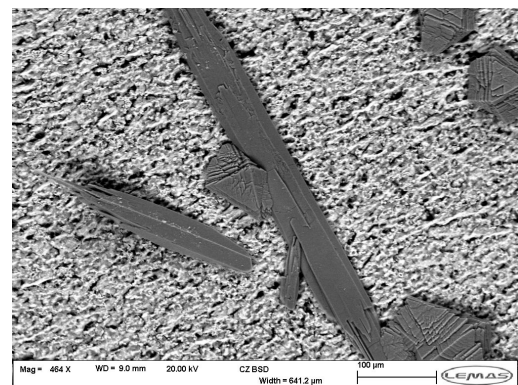
pH 6 in comparison with that at pH 3.8 is featured in Figure 6.5. EDX analysis show increasing atomic percentage of calcium on corrosion product as exposure time increased. This could infer that calcium preferentially displaced iron from the mixed corrosion product formed as exposure time increased. Connecting this observation to the progressive corrosion recorded (Figure 8.13) suggests that calcium influences corrosion process. Lower pitting was recorded at pH 6 compared to the growth at pH 3.8 probably due to the presence of mixed $\text{Fe}_x\text{Ca}_{(1-x)}\text{CO}_3$ that forms at pH 6 [247]. FeCO_3 and CaCO_3 coexist as a porous mixture due to similar hexagonal crystal structures in which contributory ratio is a function of ionic concentration, pH, temperature amongst others [160]. The slow calcite deposition observed at pH 6 was due to the inhibition of calcite growth as anodic dissolution progress. Fe^{2+} inhibits calcite deposition [236, 237] while the tendency of film formation at pH 6 consumes Fe^{2+} in solution. Hence, calcite crystals [248] began to deposit at pH 6 as Fe^{2+} concentration drops in the solution.

The growth of aragonite (Figure 8.9) after a 4 day test at pH 3.8 indicates that aragonite is preferentially formed at low pH. XRD patterns identified calcite-like peaks only at pH 6. A mixture of needle-like and rod-like aragonite [249] formed in 2 wt% NaCl, pH3.8 solution after 4 days exposure. However, patches of hexagonal

platelet vaterite with rod-like aragonites [249] emerged on an amorphous layer in 3.5 wt% NaCl solution. Growth of aragonite and vaterite polymorph from the amorphous layer implies the layer was rich in CaCO_3 as amorphous CaCO_3 layers often precede growth of crystalline polymorphs [238]. More aragonite coverage was observed in lower Cl^- concentration probably due to lower stability of vaterite [248]. The pit count on samples bearing corrosion products shown in Figure 8.9(a) and 8.9(b) were identical which suggests that aragonite and vaterite have a similar influence on pit propagation. The corrosion products formed at high pH were observed to be compact and thin unlike those formed at low pH. This was probably due to high bulk precipitation at high pH which diminishes the Fe^{2+} concentration that would have contributed to film formation on the sample surface. Top-view SEM images of products formed on corroded pit after 24 h exposure at pH 3.8 and pH 6 are shown at Figure 8.10. The thick films formed at low pH covers the pit mouth while thin films was observed to line pits at high pH. Cross section images of both conditions also revealed thin films and thick films at high pH and low pH respectively. Analysis of the pitting trend however show deeper pits at lower pH than at higher pH. This further strengthens the assertion that events beneath the Ca^{2+} rich films promote pit growth.



(a) Needle-like & rod-like aragonites



(b) Aragonites & vaterites on amorphous layer

Figure 8.9: Top-view SEM of film formed on pits in X65 carbon steel corroded in 5,000 ppm Ca^{2+} at 80 °C for 96 h in (a) 2 % NaCl, (b) 3.5 % NaCl,

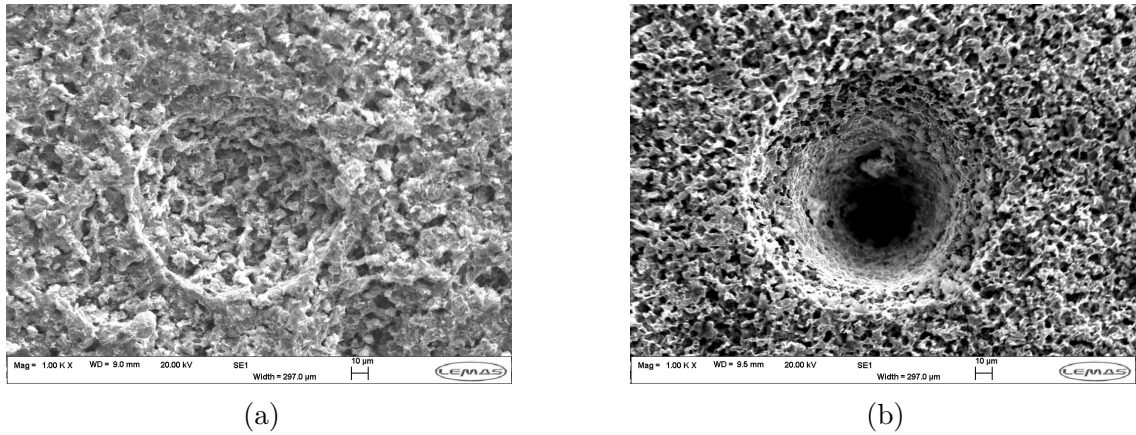


Figure 8.10: Top-view SEM of film formed on pits in X65 carbon steel corroded in 2 % NaCl, 5,000 ppm Ca^{2+} at 80 °C for 24 h in (a) pH 3.8 (b) pH 6.

8.6 The effect of chloride ion on carbon steel pitting in Ca^{2+} solution

Chapter 6 of this thesis presented results on X65 carbon steel pitting in 5,000 ppm Ca^{2+} solution. For solutions at 80 °C, pH 3.8, increase in Cl^- concentration from 2 wt.% NaCl to 3.5 wt.% NaCl recorded needle like aragonites and mixture of aragonite and vaterite crystals respectively on the steel surface (Figure 8.9). Pit growth under both film conditions were however similar for the 4-day investigations conducted. Jiang et al. [163] observation on pit initiation process in Ca^{2+} solutions reported that pit initiation could be delayed with increase in Cl^- concentration under stagnant condition while solution flow influences pitting in Ca^{2+} solutions. The fact that similar growth pattern was recorded in Ca^{2+} solution containing 2 wt. % NaCl and 3.5 wt. % NaCl suggests that Cl^- could influence pit initiation by promoting disruption of films, Cl^- has minimal effect on pit growth in Ca^{2+} -rich solutions.

8.7 Artificial pit concept in pitting investigation

Several artificial pit designs have been developed to investigate pitting corrosion [264, 181, 265, 266, 251, 208, 52]. A summary of the pros and cons of the artificial pits in literature as well as the latest design featured in the Table 8.1. Technicalities and conventions of the artificial pit is however yet to be thoroughly explained in literature. Han et al. [251] who investigated the electrochemical effect on localised corrosion in mild steel deferred the discussion on the electrochemical theory to a later date. Fernandez-Domene et al. [253] investigated the galvanic trend on X65 carbon steel where galvanic current was measured relative to the anode electrode. The galvanic current density of positive magnitude was therefore ascribed to the anode. Section 8.7 of this Chapter provides detailed discussion on the artificial pit concept. The artificial pit works based on potential difference created between a tiny film free (anode) in an insulated coupling to a passivated cathode of larger area as featured in Figure 8.11.

Table 8.1: Advantages and disadvantages of artificial pi model in use

Inventor	Advantage	Disadvantage
Newman [191].	Ease of deign	Pit profile is difficult to re-enact
Turnbull et al.[192].	Electrolyte condition at both electrodes can be controlled easily	Significant separation of anode from cathode
Palmer et al. [55].	Ease of design	Pit profile is difficult to re-enact
Han et al. [56].	Reasonable proximity of anode and cathode electrodes	Complex design
Amri et al. [52].	Improved proximity of anode and cathode electrodes	Pit depth can be adjusted by linear displacement of anode
Current approach.	Ability to reliably re-enact pit depth through thread pitch displacement.	Inability to examine pit wall kinetics

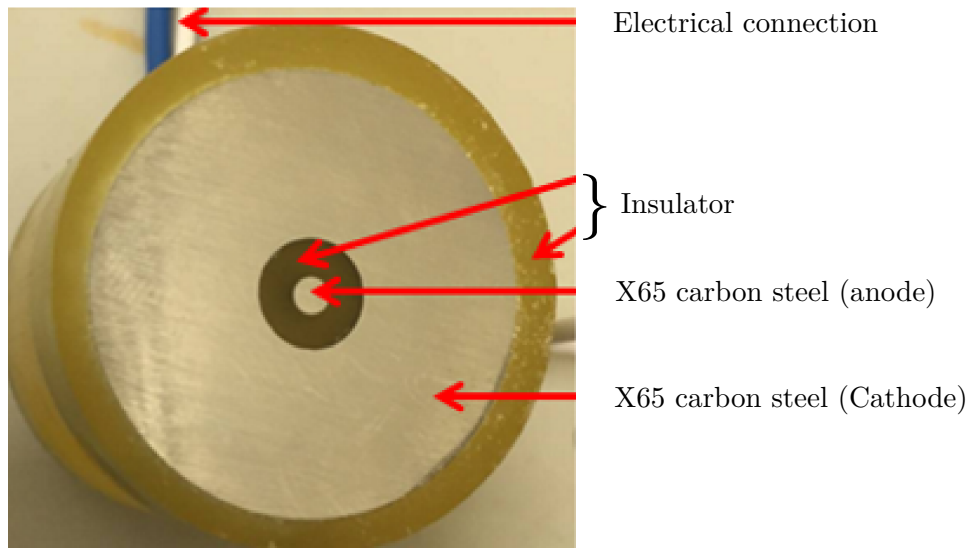


Figure 8.11: Artificial Pit in Flush Position

8.7.1 Suggested sign convention in Artificial pit

A suggested schematic representation for reactions that occur in an artificial pit is depicted at Figure 8.12.

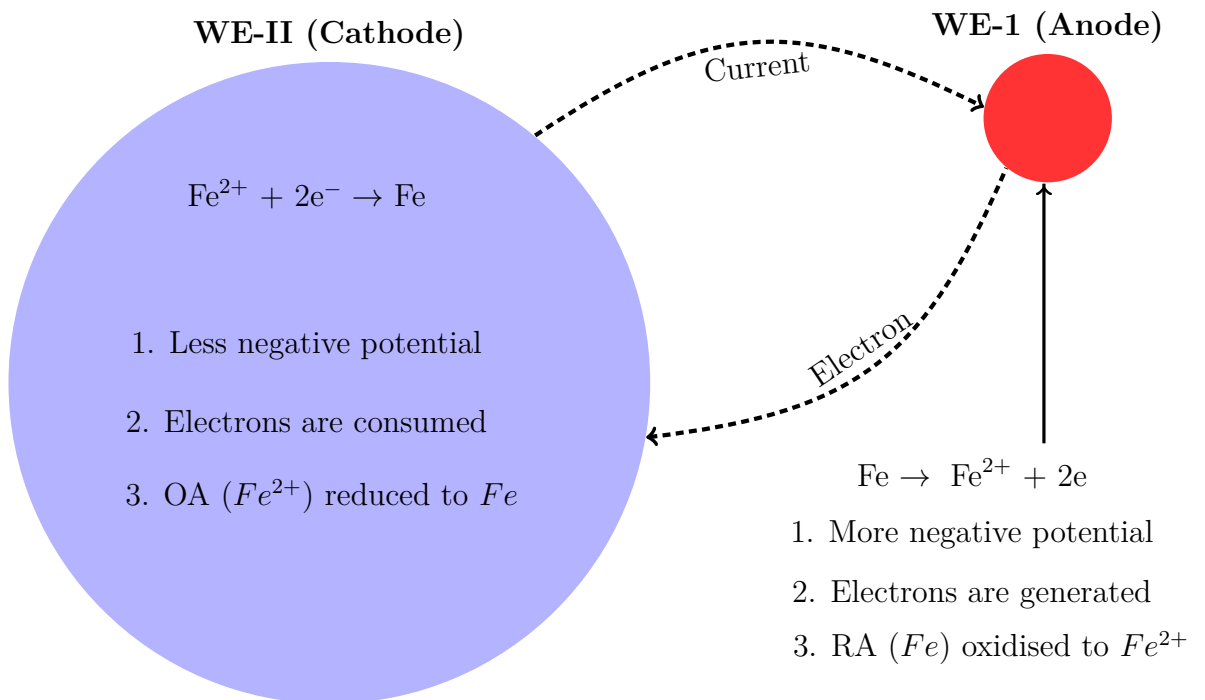


Figure 8.12: Schematic representation of the electrochemistry in an artificial Pit

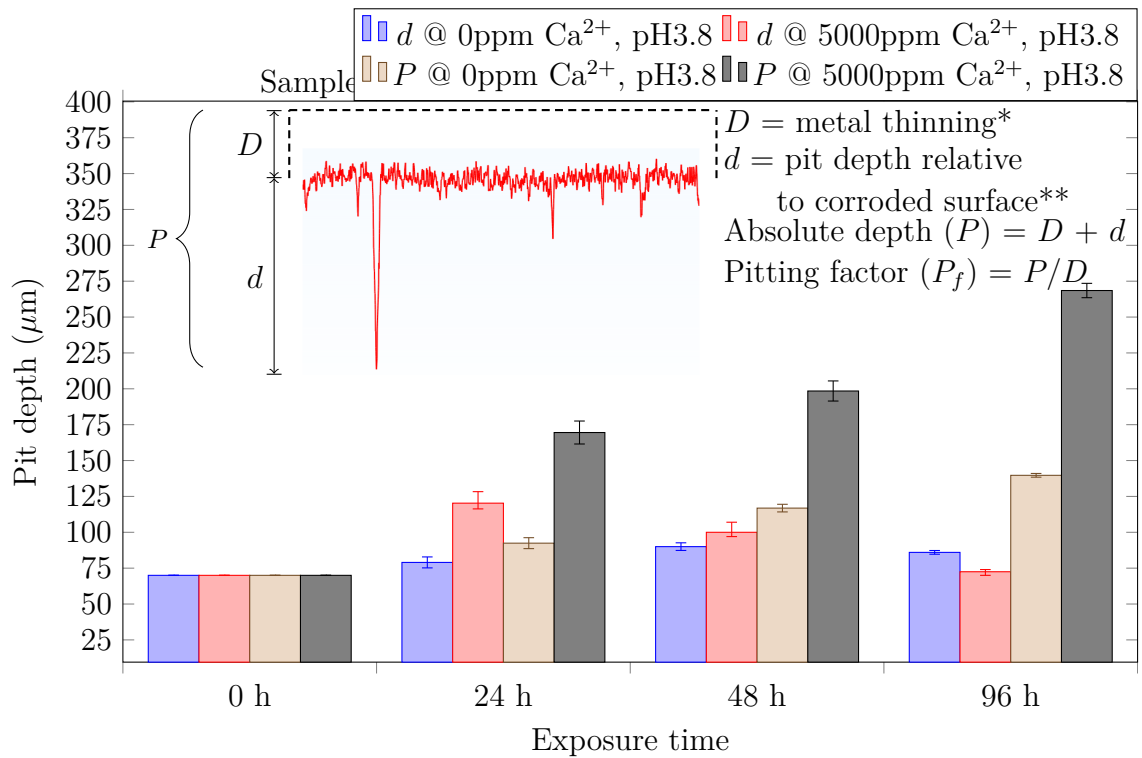
The schematics assumes that anodic reaction in the coupling occurs only on the film free surface (being the net anode electrode) while corresponding cathodic

reactions occur at the larger passivated surface. Hence, opposing reaction on the electrodes is ignored. The film free electrode (WE-1) has more negative potential while the film covered cathode (WE-2) has less negative potential. The galvanic mode of the measuring instrument does not interfere with the circuit but merely measure current resulting from flow of electrons between WE-1 and WE-2. The more negative electrode (WE-1) has higher reduction potential and therefore possess higher tendency of getting reduced than the less negative electrode (WE-2) which has lower reduction potential. A Redox system is therefore established in the coupling, where the Reducing agent (RA) and Oxidising agent (OA) are respectively at WE-1 and WE-2. The RA (Fe) is therefore oxidised to Fe^{2+} at the WE-1 while the OA (Fe^{2+}) is reduced to Fe at WE-2. Electrons generated at the WE-1 are consumed at the WE-2 while positive charge flows in opposite direction to electron flow.

8.8 Effect of calcium on carbon steel pitting

Many studies on low carbon steel and CRA corrosion provide insight on calcium effect on general corrosion. However, scenario that plays in general corrosion might be different for pitting. For instance, Wang et al. [267] work on 3-Cr steel reported reduction in corrosion rate with increase in Ca^{2+} concentration purportedly due to the influence of Cr, in which 2 distinct corrosion layer formed on the steel surface. It is important to take pitting into perspective and distinguish pitting from general corrosion as pitting poses the greatest challenge to steel applied in the petroleum industry. Tests conducted on API-X65 samples in calcium-free solutions recorded less pitting compared to that in 5,000 ppm calcium solutions (Figure 8.13).

Calcium forms part of the corrosion product deposited within and outside a corroded pit in calcium-rich solution. EDX analysis of pit wall (Figures 8.7 and 8.8) reveals calcium presence along pit walls and at the base of the pit. Pitting in 682 ppm Ca^{2+} was higher than that conducted in 0 ppm Ca^{2+} as shown in Figure 7.21. This



* Uniform corrosion calculated from LPR measurement during corrosion test

** Pit depth obtained from white light interferometry

Figure 8.13: Bar chart depicting trend in relative and absolute pitting from initial $70\mu\text{m}$ depth in saturated CO_2 , 2 wt% NaCl, 80°C over a duration of 4 days at pH 3.8

agrees with findings by Ding et al. [164] who assessed the influence of Ca^{2+} on X65 carbon steel corrosion in 512 mg/L Ca^{2+} solution. Similar trend was recorded in 5,000 ppm Ca^{2+} tests conducted in Chapter 6 of this thesis. Navabzadeh et al. [146] also studied how calcium influences FeCO_3 protectiveness and observed that corrosion rate increased with the addition of calcium. In a similar study, the work by Ding et al. [164] on the influence of Ca^{2+} on X65 carbon steel corrosion reported that corrosion rate could be enhanced when Ca^{2+} concentration is increased by 256 ppm to 512 ppm due to growth in crystal size and loose scale structure.

Pits increase in depth in the presence of calcium. This suggests that calcium adsorbs to the steel wall and the electro-chemistry within pits promote pit growth. Uniform presence of calcium up to the base of pits suggests that calcium is not consumed within pits but rather creates aggressive environment that promotes pit growth. Solution pH affects pitting kinetics in calcium solution. High pitting was recorded

in calcium-solution at pH 3.8, 80°C but pitting at pH 6 was quite low with no clearly defined trend. This implies that the mixed carbonate formed at pH 6 (Figure 6.15) offers a sort of protection compared to the calcium polymorphs that form at low pH (Figure 8.9). Pits grow significantly under amorphous calcium deposits but pitting became less beneath aragonite deposit as depicted in Figure 8.5. Pitting beneath aragonite and vaterite deposits were however similar for experiments conducted in this work.

8.9 Pseudo-passivation and galvanic effects in calcium pitting

Pseudo-passivation is a term used to describe an occurrence where measured potential increases significantly up to 200 mV and beyond. The event has not been adequately studied and was attributed to the formation of protective FeCO_3 films on the steel surface. This work recorded similar occurrence in solution containing mixed $\text{Ca}_x\text{Fe}_{1-x}\text{CO}_3$ film. Pseudo-passivation was however delayed under mixed $\text{Ca}_x\text{Fe}_{1-x}\text{CO}_3$ film compared to when FeCO_3 forms on steel surface. Repeated tests of electrochemical results for pseudo-passive trend under FeCO_3 and $\text{Ca}_x\text{Fe}_{1-x}\text{CO}_3$ film are shown in Figure 7.4 and Figure 7.5 respectively. Pit count conducted on samples that exhibited pseudo-passive trend in 682 ppm Ca^{2+} solution shows higher pitting after 4 days exposure compared to pitting recorded after 2 days exposure. This suggests that pitting increased despite the pseudo-passive layer formed. This casts doubt on the belief that pseudo-passivation relates to additional protection of protective film as reported in literature [51, 194]. For the artificial pit experiments conducted under mixed carbonate condition, galvanic current increased as anode/cathode area ratio increased. This tallies with similar experiments conducted under FeCO_3 film conditions. Profilometry of anode electrodes reveals pitting which increased as galvanic current increased. This suggests that galvanic

current influence pitting under mixed $Ca_xFe_{1-x}CO_3$ film conditions.

8.10 The effect of anode / cathode area ratio on carbon steel pitting in 682 ppm Ca^{2+} solution

Anode electrode represents the compromised spot on an actively corroding pit which could eventually heal or continue to grow as pitting progresses. Figure 8.14 shows the galvanic trend on 1mm, 2mm and 3mm anode in a coupled pit for 24 h. Similar trend was observed for 682 ppm Ca^{2+} solutions presented as Figures 7.12 to 7.14. The fluctuation in current density was attributed to localised events on the anode electrode (Figure 7.16). Fernandez-Domene et al. [253] work on galvanic corrosion on X65 carbon steel also linked current fluctuation to the localised events occurring on anode electrode. Figure 7.21 shows that pit depth decreases as anode diameter increases in both 682 ppm Ca^{2+} and Ca^{2+} -free solutions. Similar trend was also reported in related literature [252, 253]. It implies that pit depth occasioned by galvanic trend reduces as compromised film area increases in Ca^{2+} -rich solutions. Cathode to anode area ratio creates galvanic coupling for localised corrosion [44]. The OCP variation between the anode and relatively large cathode drives the localised attack [63, 103]. The 1mm electrode recorded the highest galvanic current density (Figure 7.12) as well as deepest pits (Figure 7.16). This suggests that galvanic current density influences pit growth in low carbon steel. Pit depths for smaller anodes are higher than that recorded on larger anode electrodes.

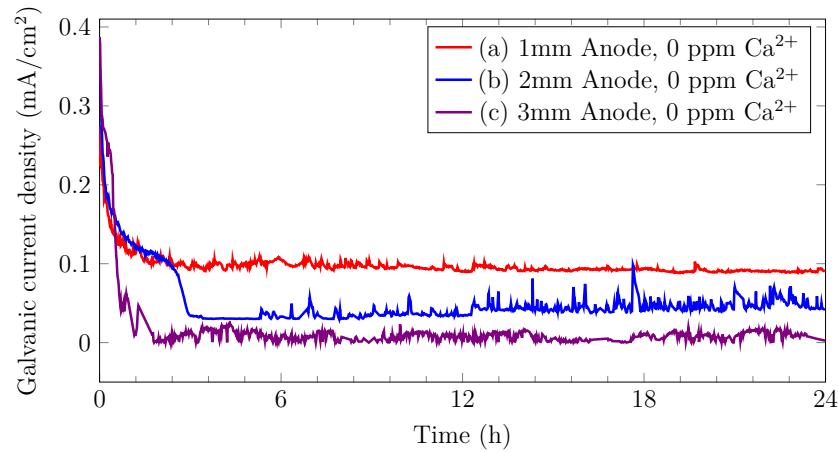


Figure 8.14: Galvanic trend for freshly polished (1) 1mm anode, (b) 2mm anode and (c) 3mm anode in passivated 4.9 cm² cathode, 0.625mm pit for 24 h in 3.5 wt% NaCl, 0 ppm Ca²⁺ at 50 °C, pH 7.5, saturated CO₂

8.11 The relationship between charge and carbon steel pitting in 682 ppm Ca²⁺ solution

Figure 8.14 shows the galvanic trend for coupled artificial pit in 0ppm Ca²⁺ solution while Figures 7.12 to 7.14 shows pitting trend in 682 ppm Ca²⁺ solution. A plot depicting charge density in coupled artificial pit for 682 ppm Ca²⁺ and Ca²⁺-free solutions is shown as Figure 8.15. Charge densities in 682 ppm Ca²⁺ solutions were generally higher than that observed Ca²⁺-free solutions. The charge per unit area also drops as the pit anode size increased. From Figure 8.15 and Figure 7.21, it is safe to state that Ca²⁺ presence increase pitting in low carbon steel. It as well shows that higher pit depth recorded in 1mm pit was due to higher charge density on the anode electrode. This implies that a tiny compromised spot on the film formed on carbon steel would produce higher charge density with greater consequence than compromised spot of larger size.

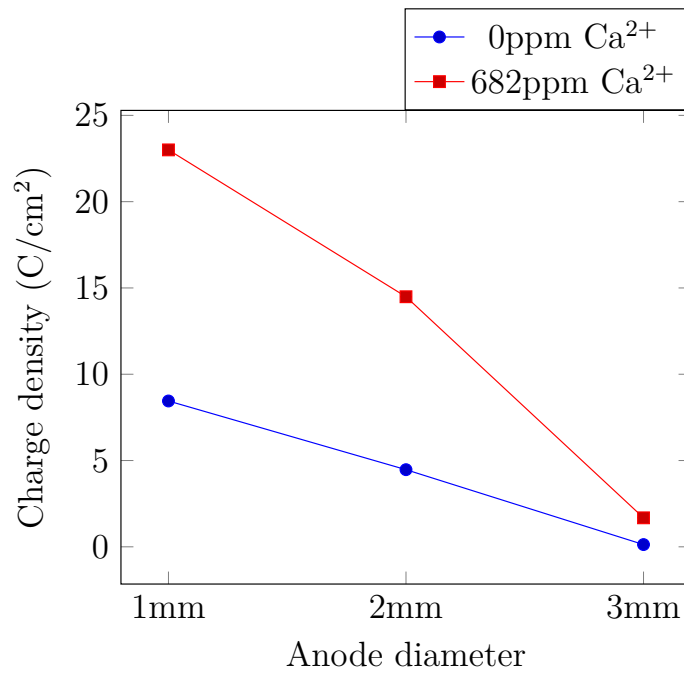


Figure 8.15: Charge recorded for 1mm, 2mm and 3mm anode diameter in artificial pit coupling in saturated CO₂, 3.3 wt.% NaCl, pH 7.5, 50 °C in 682ppm Ca²⁺ and Ca²⁺-free solutions.

8.12 Pitting and steel micro-structure

A number of factors such as electrolyte chemistry, pH, temperature, flow, steel impurities, mechanical stress amongst others can lead to pitting occurrence. The nature of corrosion products that form on steel surface can as well determine the extent of pitting on steel surface. Favourable conditions could cause carbon steel to passivate in sweet environment due to the presence of Fe₃O₄ beneath FeCO₃, an important aspect of localised corrosion [110]. The nature of corrosion product formed on steel determines the extent of corrosion performance of the metal. Lopez et al. [120] work on corrosion layers and carbon steel micro-structure reported that steel micro-structure influence corrosion properties of metals. The micrograph of low carbon steel features pearlite (dark spots) in ca 15vol% and ferrite (bright portions) in about 85 vol% (Figure 8.16). A look at Figure 8.7 shows pitting progressing in different directions making it difficult to accurately predict the likely axis of growth in the steel lattice structure. This suggests that the steel micro-structure influence

pitting kinetics in low carbon steel. It is safe to assume that pitting preferentially progress along ferrite-rich regions in the steel crystal. Pearlite region slow down pitting kinetics due to the presence of Fe_3C interlaced with Ferrite. Pit growth in the direction of pearlite region could be attributed to metastable pitting, where pitting kinetics is significantly hindered and pit could eventually heal. For pits that failed to survive the metastable phase, Ferrite component of the pearlite regions are consumed as part of anodic dissolution while Fe_3C left from the pearlite region becomes obvious afterwards.

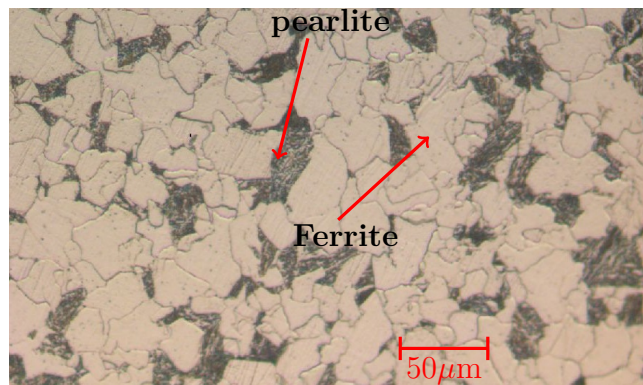


Figure 8.16: Micrograph of X65 carbon steel.

Chapter 9

Conclusions, research relevance and future work

9.1 Conclusions

A comprehensive investigation of pitting corrosion in API-X65 carbon steel has been conducted. Novel technique for generating stochastic stress-free pits that is suitable for pitting investigation has been proffered. Influence of calcium on general and pitting corrosion was examined. The effect of CaCO_3 polymorphs on pitting corrosion was also investigated. An improved artificial pit was designed and utilised to understand how galvanic trend and charge density influence pitting in low carbon steel. Robust post-experiment analysis was conducted to reveal information on formed products, corrosion type and the extent of corrosion for experiments conducted in CO_2 saturated solution. Highlight of major findings are provided under respective headings below:

9.1.1 Generating stress free stochastic pits

Although pitting corrosion in passive materials is generally well understood, the growth of surface pits in actively-corroding materials has received much less attention to date and remains poorly understood. One of the key challenges which exists is repeatedly and reliably generating surface pits in a practical time-frame in the absence of deformation and/or residual stress so that studies on pit propagation and healing can be performed. Another pertinent issue is how to evaluate pitting while addressing general corrosion in low carbon steel. In Chapter 5 of this thesis, potentiostatic polarisation was employed to induce corrosion pits (free from deformation or residual stress) on actively corroding X65 carbon steel. The influence of applied potential (50 mV, 100 mV and 150 mV vs open circuit potential) was investigated over 24 h in a CO₂-saturated, 3.5 wt.% NaCl solution at 30 °C and pH 3.8. Scanning electron microscopy (SEM) was utilised to examine pits, while surface profilometry was conducted to measure pit depth as a function of applied potential over the range considered. Analyses of light pitting (up to 120 μm) revealed that pit depth increased linearly with increase in applied potential. The work relates total pit volume (measured using white light interferometry) to dissipated charge or total mass loss (using the current response for potentiostatic polarisation in conjunction with Faraday's law). By controlling the potential of the surface (anodic) the extent of pitting and general corrosion could be controlled. This allowed pits to be evaluated for their ability to continue to propagate after the potentiostatic technique was employed. Linear growth from a depth of 70 μm at pH 3.8, 80 °C was demonstrated. The technique offers promise for the study of inhibition of pitting. The following were the conclusions reached from findings presented in Chapter 5 of this thesis:

- a. The application of anodic potential was shown to accelerate both general and pitting corrosion, but to different extents (depending upon applied potential) in relation to their contribution towards total material loss from the steel surface.
- b. Potentiostatic polarisation between 50 and 150mV at pH 3.8 and 30°C in a CO₂

environment was shown to generate reproducible pits, which were stress free.

- c. Average pit depth increased linearly with increase in applied potential in the range of 50 to 150mV, with 150mV producing the more repeatable and deepest pits averaging $70\mu m$.
- d. The pitting factors associated with polarised samples agreed with those obtained in literature in similar CO_2 environments, demonstrating that the polarisation effect produces the correct balance between the relative thickness losses associated with both general and pitting corrosion on the steel surface for pit propagation studies.
- e. Transfer of the polarised samples into test solutions at $80^\circ C$ for 48h showed that the developed pits continued to propagate, indicating the potential of this technique in performing pit propagation studies in reasonable time-frames.
- f. Potentiostatic polarisation is suitable for generating repeatable shallow pits in low carbon steel.
- g. Pitting in low carbon steel reduces as pH increases at low temperature.
- h. Pitting in low carbon steel increase with rise in temperature under film-free conditions.
- i. Pitting increase with increase in applied potential at conditions where $FeCO_3$ film is not favoured.
- j. Pitting propagation rate reduce as exposure time increase.
- k. Pitting in low carbon steel reduce significantly under protective film conditions.

9.1.2 Calcium polymorphs and pitting trend

Micro-pits could propagate during in-service life in facilities such as crude oil storage tanks in which calcium salts are present. Calcium is known to influence pit initiation

and propagation but explanation on pitting kinetics on low carbon steel remains debatable. More so, knowledge is lacking on how different CaCO_3 polymorphs influence pitting in low carbon steel. The effect of calcium on pitting in UNS K03014 (X65) carbon steel was investigated using potentiostatic induced pits in an environment typical of crude oil storage tanks and liquid aquifers. SEM, EDX and XRD investigations were performed to profile formed corrosion products followed by surface profilometry to determine the extent of pit growth. It was revealed that Ca^{2+} influence general and pitting corrosion while the kinetics of pit propagation depends on the nature of the calcium carbonate polymorph that forms on steel surface. Pit propagation was high when amorphous CaCO_3 deposit formed at pH 3.8 but pit growth retarded as aragonite started to grow on the steel surface. The conclusions reached from the findings in Chapter 6 of this thesis are as follows:

- a. Amorphous layer forms on X65 carbon steel during first 48 h in CO_2 saturated solution containing Ca^{2+} at low pH, 80 °C but transforms to aragonite polymorph after about 96h.
- b. Aragonite precipitates at low pH while calcite is identified with mixed $\text{Fe}_x\text{Ca}_{(1-x)}\text{CO}_3$ that forms at high pH.
- c. Increasing Cl^- concentration at low pH reduce aragonite precipitation and promotes vaterite growth. Aragonite and vaterite have similar influence on pit propagation kinetics.
- d. Pit propagation at 80 °C, low pH is significantly higher than propagation at high pH due to the formation of mixed but porous $\text{Fe}_x\text{Ca}_{(1-x)}\text{CO}_3$ that forms on the latter.
- e. Calcium generally increase pitting but propagation rate is less beneath aragonite film compared to amorphous CaCO_3 film.
- f. Calcite hexagonal structure are less compact than that of aragonite which is a possible explanation for the difference in pitting kinetics under both conditions.

- g. Pit growth under amorphous $Fe_xCa_{(1-x)}CO_3$ film remains unpredictable and likely to be influenced by molar constituent of cations in the mixture.
- h. Calcium preferentially displaces iron from mixed corrosion product formed as exposure time increase.
- i. Calcium influences both general and pitting corrosion in X65 carbon steel.
- j. A compact film lines the pit wall at high pH while thicker films form at low pH.

9.1.3 Calcium influence on galvanic current and pitting

Corrosion products that forms on carbon steel in sweet (CO_2) environments can protect the steel by retarding interactions between the substrate steel and a corrosive electrolyte. Such protective films could become damaged at local sites leading to OCP differences and the emergence of galvanic current with the consequence of pitting in certain environments. The large protected surface (with a higher positive potential) becomes a cathode while the tiny exposed surface (with lower positive potential) becomes the anode. Films formed in Ca^{2+} - rich environment often comprise mixed calcium and iron carbonates in the form, $Ca_xFe_{(1-x)}CO_3$. This work utilised an artificial pit to investigate pitting under $Ca_xFe_{(1-x)}CO_3$ film conditions. Mixed carbonate films were grown on cathode discs (25mm diameter) for 96 h at pH 7.5, 50 °C. Freshly polished anode pins were screwed onto the cathode disc and the galvanic currents were measured for 24 h. The anode/cathode area ratios were varied by using pins of 1mm, 2mm and 3mm diameter. SEM, XRD and EDX were employed to examine the electrode surfaces after the test while surface profilometry was conducted to obtain pit profiles on the anode pins. Galvanic current increased with the addition of 682 ppm Ca^{2+} to the solution while pseudo-passivation occurred under mixed calcium-iron carbonate films. The galvanic current was observed to drop as corrosion products formed on the anode electrode. Profilometry check revealed the emergence of stochastic pits on the anode electrode.

Pitting threshold was commensurate with magnitude of galvanic current density recorded. The following are the major findings revealed from Chapter 7 of this thesis:

- a. Calcium presence increases the galvanic current between film covered and compromised spots on low carbon steel.
- b. Galvanic current density declines as corrosion products forms inside the pit.
- c. Pseudo-passivation is delayed under $\text{Ca}_x\text{Fe}_{(1-x)}\text{CO}_3$ film condition compared to that observed in FeCO_3 film.
- d. Corrosion products that form on steel surface also grow within pits while micro-level stochastic pits emerge beneath the film on pit anodes.
- e. The extent of pit penetration under galvanic influence depends on the area of compromised spot on the film.

9.2 Relevance of research

- Potentiostatic polarisation approach presented in this thesis can be applied to array of metal types to generate repeatable stress-free stochastic pits for pitting investigation.
- Corrosion studies involving application of inhibitors will find the potentiostatic polarisation method useful. Inhibitors can be applied on polarisation induced pits to examine the growth or healing of such pits.
- The artificial pit design in this thesis is unique in that it offers ability to accurately control pit depth by simply rotating a nylon bolt which bears the pit anode. Pit displacement can be easily determined through the bolt pitch. The design can be utilised to determine events that progress within a corroding pit.

- Work done on the influence of calcium polymorph type on general and pitting corrosion has opened a new front of thought in the corrosion/scaling field. The wide ranging trend observed for general and pitting corrosion under formed aragonite, calcite and vaterite scales would be useful in determining the best conditions to mitigate corrosion effect. This is applicable in environment typical of crude oil storage tanks where calcium is often present.

9.3 Industrial application

- The methodology for generating reproducible stress-free pitting pattern provided in Chapter 5 can be applied to wide range of metals to study pitting or for other experimental investigations.
- Application of methodology presented th Chapter 5 of this thesis is ideal for use in selecting inhibitors that will be suitable for addressing pitting corrosion menace.
- Chapter 6 of this thesis provides useful information on parameters that corrosion engineers could consider in order to minimize pit growth in environment where mixed carbonate ($\text{Ca}_x\text{Fe}_{(1-x)}\text{CO}_3$) is expected to form on metals.
- The findings in this thesis can be applied to pitting corrosion models in order to accurately predict failure due to pitting occurrence.

9.4 Future Work

The research gaps outlined in Section 3.14 of this thesis have been addressed. Future work is required on the following aspects:

- **Calcium promotes pitting at low pH where FeCO_3 was not detected:** There is the need to thoroughly study how calcium influence pitting at high pH.
- **Calcium often coexist with other cations such as magnesium in brine solution:** Need to understand pit growth under Mg influence.
- **Metals used for oil and gas application are often received in different surface-finish conditions:** There is the need to understand how surface roughness influence pit propagation in low carbon steel.
- **API-X65 carbon steel and other metallic alloys are employed in oil and gas applications:** There is the need to investigate the influence of steel micro-structure on galvanic current and pitting in low carbon steel.
- **Proximity of anodic and cathodic surfaces is suggested to preferentially permit electron migration thereby completing corrosion circuit without complementing opposite reactions on both electrodes:** Need to understand the influence of proximity of artificial pit electrodes on the magnitude of galvanic coupling. There is also the need to understand how discrete anodic and cathodic sites relates to net anode and net cathode measurement and how Hydrogen evolution trend in artificial pit electrodes.
- **Does magnetite (Fe_3O_4) forms between the bare steel and mixed $\text{Ca}_x\text{Fe}_{(1-x)}\text{CO}_3$ layer as suggested in the case of the pseudo-passive film identified with FeCO_3 layer ?** Need to conduct FTR comparison on pseudo-passive layer formed under FeCO_3 and mixed $\text{Ca}_x\text{Fe}_{(1-x)}\text{CO}_3$ conditions.
- **Are anodic and cathodic sites spatially distributed on a corroding steel?** There is the need to understand the events occurring at discrete anodic and cathodic sites on a corroding steel.

Bibliography

- [1] G. Koch, J. Varney, N. Thompson, O. Moghissi, M. Gould, and J. Payer, “International measures of prevention, application, and economics of corrosion technologies study,” *NACE International IMPACT Report*, 2016.
- [2] NACE, “International measures of prevention, application and economics of corrosion technologies studies.” <https://www.nace.org/Publications/Cost-of-Corrosion-Study/>. Accessed: 8th March 2018.
- [3] G2M3 Laboratories, “Cost of Corrosion Annually in the US Over \$1.1 Trillion in 2016.” <http://www.g2mtlabs.com/corrosion/cost-of-corrosion/>. Accessed: 8th March 2018.
- [4] Relina.com, “Cost of Corrosion, Corrosion in the U.K.” <http://www.relinea.com/blog-layout/cost-of-corrosion>. Accessed: 10th February 2018.
- [5] M. Deyab and S. A. El-Rehim, “Inhibitory effect of tungstate, molybdate and nitrite ions on the carbon steel pitting corrosion in alkaline formation water containing Cl^- ion,” *Electrochimica Acta*, vol. 53, no. 4, pp. 1754–1760, 2007.
- [6] A. Valor, F. Caleyó, D. Rivas, and J. Hallen, “Stochastic approach to pitting-corrosion-extreme modelling in low-carbon steel,” *Corrosion Science*, vol. 52, no. 3, pp. 910–915, 2010.
- [7] R. Vera, F. Vinciguerra, and M. Bagnara, “Comparative study of the behavior of API 5L-X65 Grade Steel and ASTM A53-B grade steel against corrosion in seawater,” *Int. J. Electrochem. Sci*, vol. 10, pp. 6187–6198, 2015.

- [8] S. N. Nafday OA, “Iron carbonate scale formation and CO_2 corrosion in the presence of acetic acid,” *Corrosion/2005; Houston, TX; USA*, vol. 2005, p. pp. 27, 2005.
- [9] F. Farelas, M. Galicia, B. Brown, S. Nešić, and H. Castaneda, “Evolution of dissolution processes at the interface of carbon steel corroding in a CO_2 environment studied by eis,” *Corrosion Science*, vol. 52, no. 2, pp. 509–517, 2010.
- [10] M. Kermani and A. Morshed, “Carbon dioxide corrosion in oil and gas production-a compendium,” *Corrosion*, vol. 59, no. 8, pp. 659–683, 2003.
- [11] J. Amri, E. Gulbrandsen, and R. P. Nogueira, “The effect of acetic acid on the pit propagation in CO_2 corrosion of carbon steel,” *Electrochemistry Communications*, vol. 10, no. 2, pp. 200–203, 2008.
- [12] W. Liang, P. Xiaolu, and G. Kewei, “Corrosion mechanism discussion of X65 steel in nacl solution saturated with supercritical CO_2 ,” *Acta Metall Sin*, vol. 51, no. 6, pp. 701–712, 2015.
- [13] T. Li, Y. Yang, K. Gao, and M. Lu, “Mechanism of protective film formation during CO_2 corrosion of X65 pipeline steel,” *Journal of University of Science and Technology Beijing, Mineral, Metallurgy, Material*, vol. 15, no. 6, pp. 702–706, 2008.
- [14] X. Jiang, S. Nešić, B. Kinsella, B. Brown, and D. Young, “Electrochemical investigation of the role of chloride on localized carbon dioxide corrosion behavior of mild steel,” *Corrosion*, vol. 69, no. 1, pp. 15–24, 2012.
- [15] V. Ruzic, M. Veidt, and S. Nestic, “Protective iron carbonate films-part 1: Mechanical removal in single-phase aqueous flow,” *Corrosion*, vol. 62, no. 5, pp. 419–432, 2006.
- [16] B. Sherar, P. Keech, and D. Shoesmith, “Carbon steel corrosion under anaerobicaerobic cycling conditions in near-neutral ph saline solutionspart

- 1: Long term corrosion behaviour,” *Corrosion Science*, vol. 53, no. 11, pp. 3636–3642, 2011.
- [17] Industry, Business News and Energy, “Californian oil pipeline corroded.” <https://www.upi.com/Energy-News/2015/06/04/PHMSA-California-oil-pipeline-corroded/2221433415086/>. Accessed: 23rd April 2018.
- [18] S. Oyadongha, “Underwater gas leak reported in Bayelsa.” <https://www.vanguardngr.com/2016/02/underwater-gas-leak-reported-in-bayelsa/>. Accessed: 8th March 2018.
- [19] S. Netic, J. Postlethwaite, and S. Olsen, “An electrochemical model for prediction of corrosion of mild steel in aqueous carbon dioxide solutions,” *Corrosion*, vol. 52, no. 4, pp. 280–294, 1996.
- [20] G. A. Zhang and Y. F. Cheng, “On the fundamentals of electrochemical corrosion of x65 steel in CO_2 -containing formation water in the presence of acetic acid in petroleum production,” *Corrosion Science*, vol. 51, no. 1, pp. 87–94, 2009.
- [21] W. Liang, P. Xiaolu, and G. Kewei, “Corrosion mechanism discussion of X65 steel in nacl solution saturated with supercritical CO_2 ,” *Acta Metall Sin*, vol. 51, no. 6, pp. 701–712, 2015.
- [22] Y. Sun and S. Netic, “A parametric study and modeling on localized CO_2 corrosion in horizontal wet gas flow,” *CORROSION/2004, paper*, no. 380, 2004.
- [23] M. Henriquez, N. Pebere, N. Ochoa, and A. Vilorio, “Electrochemical investigation of the corrosion behavior of API 5L-X65 carbon steel in carbon dioxide medium,” *Corrosion*, vol. 69, no. 12, pp. 1171–1179, 2013.

- [24] A. Dugstad, “Fundamental aspects of CO_2 metal loss corrosion-part 1: mechanism,” in *CORROSION 2006*, NACE International, 2006.
- [25] A. Dugstad, H. Hemmer, and M. Seiersten, “Effect of steel microstructure on corrosion rate and protective iron carbonate film formation,” *Corrosion*, vol. 57, no. 4, pp. 369–378, 2001.
- [26] V. Ruzic, M. Veidt, and S. Nestic, “Protective iron carbonate films-part 3: Simultaneous chemo-mechanical removal in single-phase aqueous flow,” *Corrosion*, vol. 63, no. 8, pp. 758–769, 2007.
- [27] X. Jiang, Y. Zheng, D. Qu, and W. Ke, “Effect of calcium ions on pitting corrosion and inhibition performance in CO_2 corrosion of N80 steel,” *Corrosion science*, vol. 48, no. 10, pp. 3091–3108, 2006.
- [28] Y. Tan, “Understanding the effects of electrode inhomogeneity and electrochemical heterogeneity on pitting corrosion initiation on bare electrode surfaces,” *Corrosion Science*, vol. 53, no. 5, pp. 1845–1864, 2011.
- [29] “Images of pitting corrosion.” <https://www.google.co.uk/search?q=pitting+corrosion+images&rlz/>. Accessed: 14th January 2018.
- [30] F. Nasirpouri, A. Mostafaei, L. Fathyunes, and R. Jafari, “Assessment of localized corrosion in carbon steel tube-grade AISI 1045 used in output oilgas separator vessel of desalination unit in oil refinery industry,” *Engineering Failure Analysis*, vol. 40, pp. 75–88, 2014.
- [31] D. Han, R. Jiang, and Y. Cheng, “Mechanism of electrochemical corrosion of carbon steel under deoxygenated water drop and sand deposit,” *Electrochimica Acta*, vol. 114, pp. 403–408, 2013.
- [32] E. Morikawa, O. Kizilkaya, and R. S. Perkins, “Infrared characterization of localized corrosion products,” *Infrared Physics & Technology*, vol. 51, no. 5, pp. 407–409, 2008.

- [33] R. Melchers, “Pitting corrosion of mild steel in marine immersion environment-part 1: Maximum pit depth,” *Corrosion*, vol. 60, no. 9, pp. 824–836, 2004.
- [34] R. Melchers, “Pitting corrosion of mild steel in marine immersion environment-part 2: Variability of maximum pit depth,” *Corrosion*, vol. 60, no. 10, pp. 937–944, 2004.
- [35] H. Liu, C. Fu, T. Gu, G. Zhang, Y. Lv, H. Wang, and H. Liu, “Corrosion behavior of carbon steel in the presence of sulfate reducing bacteria and iron oxidizing bacteria cultured in oilfield produced water,” *Corrosion Science*, vol. 100, pp. 484–495, 2015.
- [36] D. Kuang and Y. F. Cheng, “Understand the ac induced pitting corrosion on pipelines in both high ph and neutral ph carbonate/bicarbonate solutions,” *Corrosion Science*, vol. 85, pp. 304–310, 2014.
- [37] M. Kermani and D. Harr, “The impact of corrosion on oil and gas industry,” in *Giornata di studio IGF S. Donato Milanese 1996*, 2008.
- [38] R. Newman, “Pitting corrosion of metals,” *The Electrochemical Society interface*, vol. 19, no. 1, pp. 33–38, 2010.
- [39] F. Ropital, “Corrosion and degradation of metallic materials,” *Understanding of the Phenomena and Applications in Petroleum and Process Industries, IFP, Publications, Editions Technip, Paris*, 2010.
- [40] M. N, D. S, and T. N, “Corrosion Monitoring with Bruker 3D Optical Microscopes - Fast, Accurate Metrology for Cost Savings in the Refining Industry,” tech. rep., Bruker Nano Surfaces Division, 2014.
- [41] M. Nuhi, T. Abu Seer, A. M. Al Tamimi, M. Modarres, and A. Seibi, “Reliability analysis for degradation effects of pitting corrosion in carbon steel pipes,” *Procedia Engineering*, vol. 10, pp. 1930–1935, 2011.

- [42] G. T. Burstein, “Revealing corrosion pits,” *Nature*, vol. 350, no. 6315, pp. 188–189, 1991. 10.1038/350188a0.
- [43] Y. Hua, R. Barker, and A. Neville, “Effect of temperature on the critical water content for general and localised corrosion of X65 carbon steel in the transport of supercritical CO_2 ,” *International Journal of Greenhouse Gas Control*, vol. 31, pp. 48–60, 2014.
- [44] G. Zhang and Y. Cheng, “Localized corrosion of carbon steel in a CO_2 -saturated oilfield formation water,” *Electrochimica Acta*, vol. 56, no. 3, pp. 1676–1685, 2011.
- [45] G. S. Frankel and N. Sridhar, “Understanding localized corrosion,” *Materials Today*, vol. 11, no. 10, pp. 38–44, 2008.
- [46] Y. Hua, R. Barker, and A. Neville, “Understanding the influence of SO_2 and O_2 on the corrosion of carbon steel in water-saturated supercritical CO_2 ,” *Corrosion*, vol. 71, no. 5, pp. 667–683, 2014.
- [47] P. Marcus, V. Maurice, and H.-H. Strehblow, “Localized corrosion (pitting): A model of passivity breakdown including the role of the oxide layer nanostructure,” *Corrosion Science*, vol. 50, no. 9, pp. 2698–2704, 2008.
- [48] Y. Hua, R. Barker, and A. Neville, “Comparison of corrosion behaviour for X65 carbon steel in supercritical CO_2 saturated/unsaturated supercritical CO_2 ,” *The Journal of Supercritical Fluids*, vol. 97, pp. 224–237, 2015.
- [49] S. Netic, “Key issues related to modelling of internal corrosion of oil and gas pipelines a review,” *Corrosion Science*, vol. 49, no. 12, pp. 4308–4338, 2007.
- [50] S. Netic, “Effects of multiphase flow on internal CO_2 corrosion of mild steel pipelines,” *Energy and Fuels*, vol. 26, no. 7, pp. 4098–4111, 2012.
- [51] W. Li, B. Brown, D. Young, and S. Netic, “Investigation of pseudo-passivation of mild steel in CO_2 corrosion,” *Corrosion*, vol. 70, no. 3, pp. 294–302, 2014.

- [52] J. Amri, E. Gulbrandsen, and R. Nogueira, “Pit growth and stifling on carbon steel in CO_2 -containing media in the presence of HAc,” *Electrochimica Acta*, vol. 54, no. 28, pp. 7338–7344, 2009.
- [53] Z. Xia, K. Chou, and Z. Szklarska-Smialowska, “Pitting corrosion of carbon steel in CO_2 -containing nacl brine,” *Corrosion*, vol. 45, no. 8, pp. 636–642, 1989.
- [54] Y. Zhang, X. Pang, S. Qu, X. Li, and K. Gao, “Discussion of the CO_2 corrosion mechanism between low partial pressure and supercritical condition,” *Corrosion Science*, vol. 59, pp. 186–197, 2012.
- [55] J. W. Palmer, J. Marsh, and R. C. Newman, “Evaluation of inhibitor performance for protection against localized corrosion,” in *CORROSION 2002*, NACE International.
- [56] J. Han, Y. Yang, B. Brown, and S. Netic, “Electrochemical investigation of localized CO_2 corrosion on mild steel,” *CORROSION/2007, paper*, vol. 7323, 2007.
- [57] J. Han, B. N. Brown, and S. Netic, “Investigation of the galvanic mechanism for localized carbon dioxide corrosion propagation using the artificial pit technique,” *Corrosion*, vol. 66, no. 9, pp. 095003–095003–12, 2010.
- [58] S. Nešić, “Key issues related to modelling of internal corrosion of oil and gas pipelines—a review,” *Corrosion science*, vol. 49, no. 12, pp. 4308–4338, 2007.
- [59] S. Papavinasam, A. Doiron, and R. W. Revie, “Model to predict internal pitting corrosion of oil and gas pipelines,” *Corrosion*, vol. 66, no. 3, pp. 035006–035006–11, 2010.
- [60] K. Videm and A. Koren, “Corrosion, passivity, and pitting of carbon steel in aqueous solutions of bicarbonate, carbondioxide and chloridel,” *Corrosion*, vol. 49, no. 9, pp. 746–754, 1993.

- [61] S. Nestic, N. Thevenot, J. L. Crolet, D. Drazic, *et al.*, “Electrochemical properties of iron dissolution in the presence of CO_2 basics revisited,” in *CORROSION 96*, NACE International, 1996.
- [62] G. Schmitt and M. Horstemeier, “Fundamental aspects of CO_2 metal loss corrosion-part ii: Influence of different parameters on CO_2 corrosion mechanisms,” in *CORROSION 2006*, NACE International.
- [63] J. Han, S. Nestic, and B. N. Brown, “Galvanic model for localized CO_2 corrosion,” *ICC/2008, paper*, no. 2687, 2008.
- [64] M. Shayegani, A. Afshar, M. Ghorbani, and M. Rahmaniyan, “Mild steel carbon dioxide corrosion modelling in aqueous solutions,” *Corrosion Engineering, Science and Technology*, vol. 43, no. 4, pp. 290–296, 2008.
- [65] G. Burstein, C. Liu, R. Souto, and S. Vines, “Origins of pitting corrosion,” *Corrosion Engineering, Science and Technology*, vol. 39, no. 1, pp. 25–30, 2004.
- [66] A. Kina and J. Ponciano, “Inhibition of carbon steel CO_2 corrosion in high salinity solutions,” *Int. J. Electrochem. Sci*, vol. 8, pp. 12600–12612, 2013.
- [67] M. Nie, J. Wharton, A. Cranny, N. Harris, R. Wood, and K. Stokes, “Characterisation of crevice and pit solution chemistries using capillary electrophoresis with contactless conductivity detector,” *Materials*, vol. 6, no. 10, p. 4345, 2013.
- [68] K. Addis, M. Singer, and S. Nestic, “A corrosion model for oil and gas mild steel production tubing,” *Corrosion*, vol. 70, no. 12, pp. 1175–1176, 2014.
- [69] D. Shoesmith, “Kinetics of aqueous corrosion,” *ASM Handbook.*, vol. 13, pp. 29–36, 1987.

- [70] T. Tanupabrungrsun, D. Young, B. Brown, Neesic, *et al.*, “Construction and verification of pourbaix diagrams for CO_2 corrosion of mild steel valid up to 250°C,” in *CORROSION 2012*, NACE International, 2012.
- [71] M. Di Benedetti, G. Loreto, F. Matta, and A. Nanni, “Acoustic emission monitoring of reinforced concrete under accelerated corrosion,” *Journal of Materials in Civil Engineering*, vol. 25, no. 8, pp. 1022–1029, 2012.
- [72] Z. Ahmad, *Chapter 3 - Corrosion Kinetics*, pp. 57–119. Oxford: Butterworth-Heinemann, 2006.
- [73] A. Ejaz, Z. Lu, J. Chen, Q. Xiao, X. Ru, G. Han, and T. Shoji, “The effects of hydrogen on anodic dissolution and passivation of iron in alkaline solutions,” *Corrosion Science*, vol. 101, pp. 165–181, 2015.
- [74] W. S. Tait, *An introduction to electrochemical corrosion testing for practicing engineers and scientists*. Clair, Racine, Wis., 1994.
- [75] N. Sato, “Basics of corrosion chemistry,” *Green corrosion chemistry and engineering: Opportunities and challenges*, pp. 1–32, 2011.
- [76] P. Roberge, “Lecture 6: The Theory for Aqueous Corrosion (IV), Corrosion Doctors.” http://www.corrosionclinic.com/corrosion_online_lectures/me303106.htm. Accessed: 20th January 2018.
- [77] K. J. Vetter, *Electrochemical kinetics: theoretical aspects*. Elsevier, 2013.
- [78] O. Y. Ababio, “New school chemistry for senior secondary schools,” 2005.
- [79] G. Instruments, “Getting started with electrochemical corrosion measurement,” 2011.
- [80] M. Curioni, A. C. Balaskas, and G. E. Thompson, “An alternative to the use of a zero resistance ammeter for electrochemical noise measurement: Theoretical analysis, experimental validation and evaluation of electrode asymmetry,” *Corrosion Science*, vol. 77, pp. 281–291, 2013.

- [81] N. G. Thompson and J. H. Payer, *DC electrochemical test methods*. NACE international, 1998.
- [82] E. Barsoukov and J. R. Macdonald, *Impedance spectroscopy: theory, experiment, and applications*. John Wiley & Sons, 2005.
- [83] E. E. Stansbury and R. A. Buchanan, *Fundamentals of electrochemical corrosion*. ASM international, 2000.
- [84] K. Mondal, “Mod-01 Lec-04 thermodynamics of corrosion,” *Environmental Degradation of Materials*.
- [85] Z. Ahmad, *Chapter 2 - Basic Concepts in Corrosion*, pp. 9–56. Oxford: Butterworth-Heinemann, 2006.
- [86] R. H. Petrucci, W. S. Harwood, G. F. Herring, and J. D. Madura, *General chemistry: principles and modern applications*. Pearson Education International, 2007.
- [87] T. L. Brown and H. E. LeMay, *Qualitative inorganic analysis: to accompany Chemistry, the central science*. Prentice Hall, 1985.
- [88] Modified from University of Cambridge, “Energy diagram for corrosion reactions in Fe.” https://www.doitpoms.ac.uk/tlplib/aqueous_corrosion/energy.php. Accessed: 10th February 2018.
- [89] J. O. Bockris and A. K. Reddy, *Modern electrochemistry: an introduction to an interdisciplinary area*. Springer Science & Business Media, 2012.
- [90] L. R. Hilbert, “Monitoring corrosion rates and localised corrosion in low conductivity water,” *Corrosion Science*, vol. 48, no. 12, pp. 3907–3923, 2006.
- [91] J. R. Scully, “Polarisation resistance method for determination of instantaneous corrosion rates,” *Corrosion*, vol. 56, no. 2, pp. 199–218, 2000.

- [92] ASTM, “G46-94,” *Standard Guide for Examination and Evaluation of Pitting Corrosion*, ASTM International, West Conshohocken, PA, 2005.
- [93] M. Arenas and R. Reddy, “Corrosion of steel in ionic liquids,” *Journal of Mining and Metallurgy, Section B: Metallurgy*, vol. 39, no. 1-2, pp. 81–91, 2003.
- [94] F. F. Eliyan and A. Alfantazi, “Mechanisms of corrosion and electrochemical significance of metallurgy and environment with corrosion of iron and steel in bicarbonate and carbonate solutions—a review,” *Corrosion*, vol. 70, no. 9, pp. 880–898, 2014.
- [95] L. Oblonsky and T. Devine, “Corrosion of carbon steels in CO_2 saturated brine a surface enhanced raman spectroscopic study,” *Journal of the Electrochemical Society*, vol. 144, no. 4, pp. 1252–1260, 1997.
- [96] M. A. Islam and Z. Farhat, “Characterization of the corrosion layer on pipeline steel in sweet environment,” *Journal of Materials Engineering and Performance*, vol. 24, no. 8, pp. 3142–3158, 2015.
- [97] C. Bian, Z. M. Wang, X. Han, C. Chen, and J. Zhang, “Electrochemical response of mild steel in ferrous ion enriched and CO_2 saturated solutions,” *Corrosion Science*, vol. 96, pp. 42–51, 2015.
- [98] W. Sun, S. Netic, and S. Papavinasam, “Kinetics of corrosion layer formation. Part 2-Iron sulfide and mixed iron sulfide/carbonate layers in carbon dioxide/hydrogen sulfide corrosion,” *Corrosion*, vol. 64, no. 7, pp. 586–599, 2008.
- [99] J. L. Crolet, N. Thevenot, A. Dugstad, *et al.*, “Role of free acetic acid on the CO_2 corrosion of steels,” in *CORROSION 99*, NACE International, 1999.
- [100] Y. Hua, R. Barker, T. Charpentier, M. Ward, and A. Neville, “Relating iron carbonate morphology to corrosion characteristics for water-saturated

- supercritical CO_2 systems,” *The Journal of Supercritical Fluids*, vol. 98, pp. 183–193, 2015.
- [101] M. Nordsveen, S. Nešić, R. Nyborg, and A. Stangeland, “A mechanistic model for carbon dioxide corrosion of mild steel in the presence of protective iron carbonate films part 1: Theory and verification,” *Corrosion*, vol. 59, no. 5, pp. 443–456, 2003.
- [102] L. Moiseeva and Y. I. Kuznetsov, “Inhibition of carbon-dioxide corrosion of equipment of the petroleum and gas industry,” *Chemical and petroleum engineering*, vol. 33, no. 1, pp. 81–87, 1997.
- [103] J. Han, Y. Yang, S. Nesic, and B. N. Brown, “Roles of passivation and galvanic effects in localized CO_2 corrosion of mild steel,” *CORROSION/2008, paper*, no. 08332, 2008.
- [104] D. W. Hoepfner, “Pitting corrosion: Morphology and characterization,” *framework*, vol. 25, p. 26, 1985.
- [105] B. Lin, R. Hu, C. Ye, Y. Li, and C. Lin, “A study on the initiation of pitting corrosion in carbon steel in chloride-containing media using scanning electrochemical probes,” *Electrochimica Acta*, vol. 55, no. 22, pp. 6542–6545, 2010.
- [106] N. Cui, H. Ma, J. Luo, and S. Chiovelli, “Use of scanning reference electrode technique for characterizing pitting and general corrosion of carbon steel in neutral media,” *Electrochemistry communications*, vol. 3, no. 12, pp. 716–721, 2001.
- [107] P. Pistorius and G. Burstein, “Metastable pitting corrosion of stainless steel and the transition to stability,” *Philosophical Transactions of the Royal Society of London A: Mathematical, Physical and Engineering Sciences*, vol. 341, no. 1662, pp. 531–559, 1992.

- [108] J. H. Espina-Hernández, F. Caleyó, V. Venegas, and J. M. Hallen, “Pitting corrosion in low carbon steel influenced by remanent magnetization,” *Corrosion Science*, vol. 53, no. 10, 2011.
- [109] H. S. Isaacs, “The localized breakdown and repair of passive surfaces during pitting,” *Corrosion Science*, vol. 29, no. 2, pp. 313–323, 1989.
- [110] J. Han, D. Young, and S. Nescic, “Characterization of the passive film on mild steel in CO_2 environments,” in *Proceedings of the 17th International Corrosion Congress*, 2008.
- [111] L. Caceres, T. Vargas, and L. Herrera, “Influence of pitting and iron oxide formation during corrosion of carbon steel in unbuffered nacl solutions,” *Corrosion Science*, vol. 51, no. 5, pp. 971–978, 2009.
- [112] J. Han and J. W. Carey, “Localized CO_2 corrosion propagation at moderate $FeCO_3$ supersaturation initiated by mechanical removal of corrosion scale,” *Journal of Applied Electrochemistry*, vol. 41, no. 11, pp. 1367–1371, 2011.
- [113] G. Zhang, N. Yu, L. Yang, and X. Guo, “Galvanic corrosion behavior of deposit-covered and uncovered carbon steel,” *Corrosion Science*, vol. 86, pp. 202–212, 2014.
- [114] X. Gao, B. Brown, and S. Nescic, “Effect of chloride on localized corrosion initiation of carbon steel in a CO_2 aqueous environment,” in *CORROSION 2014*, NACE International.
- [115] G. Frankel, “Pitting corrosion of metals a review of the critical factors,” *Journal of the Electrochemical Society*, vol. 145, no. 6, pp. 2186–2198, 1998.
- [116] H. Strehblow, “Breakdown of passivity and localized corrosion: Theoretical concepts and fundamental experimental results,” *Materials and Corrosion*, vol. 35, no. 10, pp. 437–448, 1984.

- [117] V. Ruzic, M. Veidt, and S. Nestic, "Protective iron carbonate films-part 2: Chemical removal by dissolution in single-phase aqueous flow," *Corrosion*, vol. 62, no. 7, pp. 598–611, 2006.
- [118] J. L. Crolet, N. Thevenot, and S. Nestic, "Role of conductive corrosion products in the protectiveness of corrosion layers," *Corrosion*, vol. 54, no. 3, pp. 194–203, 1998.
- [119] Y. Cheng and J. Luo, "Electronic structure and pitting susceptibility of passive film on carbon steel," *Electrochimica Acta*, vol. 44, no. 17, pp. 2947–2957, 1999.
- [120] D. Lopez, W. d. Schreiner, S. De Sánchez, and S. Simison, "The influence of carbon steel microstructure on corrosion layers: an XPS and SEM characterization," *Applied surface science*, vol. 207, no. 1-4, pp. 69–85, 2003.
- [121] L. Li, M. Mahmoodian, C.-Q. Li, and D. Robert, "Effect of corrosion and hydrogen embrittlement on microstructure and mechanical properties of mild steel," *Construction and Building Materials*, vol. 170, pp. 78–90, 2018.
- [122] J. Wei, J. Dong, Y. Zhou, X. He, C. Wang, and W. Ke, "Influence of the secondary phase on micro galvanic corrosion of low carbon bainitic steel in nacl solution," *Materials Characterization*, vol. 139, pp. 401–410, 2018.
- [123] B. Fang, R. Eadie, W. Chen, and M. Elboujdaini, "Passivation/immersion method to grow pits in pipeline steel and a study of pit nucleation and growth resulting from the method," *Corrosion Engineering, Science and Technology*, vol. 44, no. 1, pp. 32–42, 2009.
- [124] X. Lou and P. M. Singh, "Role of water, acetic acid and chloride on corrosion and pitting behaviour of carbon steel in fuel-grade ethanol," *Corrosion Science*, vol. 52, no. 7, pp. 2303–2315, 2010.
- [125] M. Palynchuk, "Pit gauges: History and development," *Western Instrument*.

- [126] B. Yang, “Real-time localized corrosion monitoring in industrial cooling water systems,” *Corrosion*, vol. 56, no. 7, pp. 743–756, 2000.
- [127] F. O. Pessu, *Investigation of pitting corrosion of carbon steel in sweet and sour oilfield corrosion conditions: a parametric study*. PhD thesis, 2015.
- [128] M. G. Fontana, *Corrosion engineering*. Tata McGraw-Hill Education, 2005.
- [129] G. H. Koch, M. P. Brongers, N. G. Thompson, Y. P. Virmani, and J. H. Payer, “Corrosion cost and preventive strategies in the united states,” tech. rep., 2002.
- [130] R. Pierre, *Handbook of corrosion engineering*. McGraw-Hill Professional, 1999.
- [131] W. C. Lyons and G. J. Plisga, *Standard handbook of petroleum and natural gas engineering*. Gulf Professional Publishing, 2011.
- [132] F. Blateyron, *New foundations for modern surface texture analysis ISO 25178 & ISO/TS 16610*. Digital surf Special Standards Edition, 2011.
- [133] W. C. Lyons and G. J. Plisga, “Images of corrosion pits.” <https://www.slideshare.net/mustafahasan33633/pitting-corrosion-and-crevice-corrosion>. Accessed: 8th March 2018.
- [134] I. M. Gadala and A. Alfantazi, “Bicarbonate, temperature, and pH influences on the passivation of API-X100 pipeline steel in simulated groundwater solutions,” in *2014 10th International Pipeline Conference*, pp. V002T06A072–V002T06A072, American Society of Mechanical Engineers.
- [135] R. M. Fernández-Domene, R. Leiva-García, R. Akid, and J. Andrews, “Galvanic corrosion following local breakdown of a scale formed on X-65 in CO₂ saturated solutions,” in *CORROSION 2015*, NACE International.

- [136] G. K. Lawrence Onyeji, Sikiru Mohammed, “Electrochemical response of micro-alloyed steel under potentiostatic polarization in CO_2 saturated brine,” *Corrosion Science*, 2018.
- [137] S. Nešić and K.-L. Lee, “A mechanistic model for carbon dioxide corrosion of mild steel in the presence of protective iron carbonate films-part 3: Film growth model,” *Corrosion*, vol. 59, no. 7, pp. 616–628, 2003.
- [138] W. Sun and S. Nescic, “Kinetics of corrosion layer formation: Part 1-iron carbonate layers in carbon dioxide corrosion,” *Corrosion*, vol. 64, no. 4, pp. 334–346, 2008.
- [139] T. Berntsen, M. Seiersten, and T. Hemmingsen, “Effect of $feco_3$ supersaturation and carbide exposure on the CO_2 corrosion rate of carbon steel,” *Corrosion*, vol. 69, no. 6, pp. 601–613, 2013.
- [140] J. Heuer and J. Stubbins, “An xps characterization of $FeCO_3$ films from CO_2 corrosion,” *Corrosion Science*, vol. 41, no. 7, pp. 1231–1243, 1999.
- [141] S. Guo, L. Xu, L. Zhang, W. Chang, and M. Lu, “Corrosion of alloy steels containing 2% chromium in CO_2 environments,” *Corrosion Science*, vol. 63, pp. 246–258, 2012.
- [142] F. Pessu, R. Barker, and A. Neville, “The influence of pH on localized corrosion behavior of X65 (UNS K03014) carbon steel in CO_2 -saturated brines,” in *CORROSION 2015*, NACE International.
- [143] L. Wei, X. Pang, C. Liu, and K. Gao, “Formation mechanism and protective property of corrosion product scale on X70 steel under supercritical CO_2 ,”
- [144] J. Han, D. Young, H. Colijn, A. Tripathi, and S. Nescic, “Chemistry and structure of the passive film on mild steel in CO_2 corrosion environments,” *Industrial & Engineering Chemistry Research*, vol. 48, no. 13, pp. 6296–6302, 2009.

- [145] G. J.L. and B. M.R, “Gas europa 10,” vol. 2, p. p.68, 1984.
- [146] S. Navabzadeh Esmaeely, Y.-S. Choi, D. Young, and S. Nešić, “Effect of calcium on the formation and protectiveness of iron carbonate layer in CO₂ corrosion,” *Corrosion*, vol. 69, no. 9, pp. 912–920, 2013.
- [147] J. Kawano, N. Shimobayashi, A. Miyake, and M. Kitamura, “Precipitation diagram of calcium carbonate polymorphs: its construction and significance,” *Journal of Physics: Condensed Matter*, vol. 21, no. 42, p. 425102, 2009.
- [148] J. Chen and L. Xiang, “Controllable synthesis of calcium carbonate polymorphs at different temperatures,” *Powder Technology*, vol. 189, no. 1, pp. 64–69, 2009.
- [149] N. H. de Leeuw and S. C. Parker, “Surface structure and morphology of calcium carbonate polymorphs calcite, aragonite, and vaterite: an atomistic approach,” *The Journal of Physical Chemistry B*, vol. 102, no. 16, pp. 2914–2922, 1998.
- [150] Y.-B. Hu, M. Wolthers, D. A. Wolf-Gladrow, and G. Nehrke, “Effect of pH and phosphate on calcium carbonate polymorphs precipitated at near-freezing temperature,” *Crystal Growth & Design*, vol. 15, no. 4, pp. 1596–1601, 2015.
- [151] C. A. Weiss, K. Torres-Cancel, R. D. Moser, P. G. Allison, E. R. Gore, M. Q. Chandler, and P. Malone, “Influence of temperature on calcium carbonate polymorph formed from ammonium carbonate and calcium acetate,” *J Nanotech Smart Mater*, vol. 1, pp. 1–6, 2014.
- [152] D. L. Bryce, E. B. Bultz, and D. Aebi, “Calcium-43 chemical shift tensors as probes of calcium binding environments. insight into the structure of the vaterite CaCO₃ polymorph by ⁴³Ca solid-state nmr spectroscopy,” *Journal of the American Chemical Society*, vol. 130, no. 29, pp. 9282–9292, 2008.
- [153] L. M. Tavares, E. M. da Costa, J. J. de Oliveira Andrade, R. Hubler, and B. Huet, “Effect of calcium carbonate on low carbon steel corrosion behavior

- in saline CO_2 high pressure environments,” *Applied Surface Science*, vol. 359, pp. 143–152, 2015.
- [154] J. Sun, L. Wang, and D. Zhao, “Polymorph and morphology of $CaCO_3$ in relation to precipitation conditions in a bubbling system,” *Chinese Journal of Chemical Engineering*, pp. –, 2017.
- [155] J. Shuai, K. Han, and X. Xu, “Risk-based inspection for large-scale crude oil tanks,” *Journal of Loss Prevention in the Process Industries*, vol. 25, no. 1, pp. 166–175, 2012.
- [156] Z. J. Yang, D. S. Chen, L. Chen, Y. Z. Liu, R. An, and G. Wang, “Finite element analysis and research on corrosion defect of tank floor,” in *Applied Mechanics and Materials*, vol. 853, pp. 514–518, Trans Tech Publ, 2017.
- [157] Q. Cheng, B. Tao, L. Song, W. Zhang, X. Liu, W. Li, B. Hou, and Q. Liu, “Corrosion behaviour of Q235B carbon steel in sediment water from crude oil,” *Corrosion Science*, vol. 111, pp. 61 – 71, 2016.
- [158] A. M. Trevelin, R. E. Marotto, E. V. de Castro, G. P. Brandão, R. J. Cassella, and M. T. W. Carneiro, “Extraction induced by emulsion breaking for determination of Ba, Ca, Mg and Na in crude oil by inductively coupled plasma optical emission spectrometry,” *Microchemical Journal*, vol. 124, pp. 338 – 343, 2016.
- [159] R. B. Rebak, T. E. Perez, *et al.*, “Effect of carbon dioxide and hydrogen sulfide on the localized corrosion of carbon steels and corrosion resistant alloys,” in *CORROSION 2017*, NACE International, 2017.
- [160] A. M. Nejad and M. S. Karimi, “Investigation of the influence of scaling on corrosion behavior of tubing in oil wells,” *International Journal of scientific & Technology*, vol. 6, no. 05, pp. 64 – 75, 2017.

- [161] A. Sander, B. Berghult, A. Broo, E. Johansson, and T. Hedberg, “Iron corrosion in drinking water distribution systems: the effect of pH, calcium and hydrogen carbonate,” *Corrosion Science*, vol. 38, no. 3, pp. 443 – 455, 1996.
- [162] L. M. Tavares, E. M. da Costa, J. J. de Oliveira Andrade, R. Hubler, and B. Huet, “Effect of calcium carbonate on low carbon steel corrosion behavior in saline CO_2 high pressure environments,” *Applied Surface Science*, vol. 359, pp. 143 – 152, 2015.
- [163] X. Jiang, Y. Zheng, D. Qu, and W. Ke, “Effect of calcium ions on pitting corrosion and inhibition performance in CO_2 corrosion of N80 steel,” *Corrosion science*, vol. 48, no. 10, pp. 3091–3108, 2006.
- [164] C. Ding, K. wei Gao, and C. feng Chen, “Effect of Ca^{2+} on CO_2 corrosion properties of X65 pipeline steel,” *International Journal of Minerals, Metallurgy and Materials*, vol. 16, no. 6, pp. 661 – 666, 2009.
- [165] A. Turnbull, D. Coleman, A. J. Griffiths, P. E. Francis, and L. Orkney, “Effectiveness of corrosion inhibitors in retarding the rate of propagation of localized corrosion,” *Corrosion*, vol. 59, no. 3, pp. 250–257, 2003.
- [166] J. Mora-Mendoza and S. Turgoose, “ Fe_3C influence on the corrosion rate of mild steel in aqueous CO_2 systems under turbulent flow conditions,” *Corrosion Science*, vol. 44, no. 6, pp. 1223–1246, 2002.
- [167] M. Ergun and A. Y. Turan, “Pitting potential and protection potential of carbon steel for chloride ion and the effectiveness of different inhibiting anions,” *Corrosion science*, vol. 32, no. 10, pp. 1137–1142, 1991.
- [168] W. Tian, S. Li, N. Du, S. Chen, and Q. Wu, “Effects of applied potential on stable pitting of 304 stainless steel,” *Corrosion Science*, vol. 93, pp. 242–255, 2015.
- [169] M. Pagitsas, A. Diamantopoulou, and D. Sazou, “General and pitting corrosion deduced from current oscillations in the passive–active transition

- state of the Fe/H_2SO_4 electrochemical system,” *Electrochimica acta*, vol. 47, no. 26, pp. 4163–4179, 2002.
- [170] M. Pagitsas, A. Diamantopoulou, and D. Sazou, “A point defect model for the general and pitting corrosion on iron–oxide electrolyte interface deduced from current oscillations,” *Chaos, Solitons & Fractals*, vol. 17, no. 2, pp. 263–275, 2003.
- [171] G. Schmitt and S. Feinen, “Effect of anions and cations on the pit initiation in CO_2 corrosion of iron and steel,” in *CORROSION 2000*, NACE International.
- [172] Q. Liu, L. Mao, and S. Zhou, “Effects of chloride content on CO_2 corrosion of carbon steel in simulated oil and gas well environments,” *Corrosion Science*, vol. 84, pp. 165–171, 2014.
- [173] E. Gulbrandsen and K. Bilkova, “Solution chemistry effects on corrosion of carbon steels in presence of CO_2 and acetic acid,” *CORROSION/2006, paper*, no. 06364, 2006.
- [174] C. Brossia and G. Cragolino, “Effect of environmental variables on localized corrosion of carbon steel,” *Corrosion*, vol. 56, no. 5, pp. 505–514, 2000.
- [175] M. Alvarez and J. Galvele, “The mechanism of pitting of high purity iron in NaCl solutions,” *Corrosion Science*, vol. 24, no. 1, pp. 27–48, 1984.
- [176] Y. Hua, R. Barker, and A. Neville, “Effect of temperature on the critical water content for general and localised corrosion of X65 carbon steel in the transport of supercritical CO_2 ,” *International Journal of Greenhouse Gas Control*, vol. 31, pp. 48–60, 2014.
- [177] G. Zhang and Y. Cheng, “Localized corrosion of carbon steel in a CO_2 -saturated oilfield formation water,” *Electrochimica Acta*, vol. 56, no. 3, pp. 1676–1685, 2011.

- [178] S. Nestic, “Key issues related to modelling of internal corrosion of oil and gas pipelines—a review,” *Corrosion Science*, vol. 49, no. 12, pp. 4308–4338, 2007.
- [179] S. Papavinasam, A. Doiron, and R. W. Revie, “Model to predict internal pitting corrosion of oil and gas pipelines,” *Corrosion*, vol. 66, no. 3, pp. 035006–035006, 2010.
- [180] X. Jiang, S. Nešić, B. Kinsella, B. Brown, and D. Young, “Electrochemical investigation of the role of Cl^- on localized carbon dioxide corrosion behavior of mild steel,” *Corrosion*, vol. 69, no. 1, pp. 15–24, 2012.
- [181] A. Turnbull, D. Coleman, and A. Griffiths, “Assessment of test methods for evaluating effectiveness of corrosion inhibitors in retarding propagation of localised corrosion,” *British Corrosion Journal*, vol. 36, no. 3, pp. 210–214, 2001.
- [182] P. Zhang and Z. Liu, “Physical-mechanical and electrochemical corrosion behaviors of additively manufactured Cr-Ni-based stainless steel formed by laser cladding,” *Materials & Design*, vol. 100, pp. 254–262, 2016.
- [183] J. Zhang, D.-H. Yang, and X.-B. Ou, “Microstructures and properties of aluminum film and its effect on corrosion resistance of AZ31B substrate,” *Transactions of Nonferrous Metals Society of China*, vol. 18, pp. s312–s317, 2008.
- [184] B. Fang, R. Eadie, W. Chen, and M. Elboujdaini, “Passivation/immersion method to grow pits in pipeline steel and a study of pit nucleation and growth resulting from the method,” *Corrosion Engineering, Science and Technology*, vol. 44, no. 1, pp. 32–42, 2009.
- [185] R. Miresmaeili, A. Abdollah-Zadeh, *et al.*, “The mutual effects of hydrogen and microstructure on hardness and impact energy of sma welds in X65 steel,” *Materials Science and Engineering: A*, vol. 679, pp. 87–94, 2017.

- [186] I. M. Robertson, P. Sofronis, A. Nagao, M. Martin, S. Wang, D. Gross, and K. Nygren, “Hydrogen embrittlement understood,” *Metallurgical and Materials Transactions B*, vol. 46, no. 3, pp. 1085–1103, 2015.
- [187] M. Dadfarnia, A. Nagao, S. Wang, M. L. Martin, B. P. Somerday, and P. Sofronis, “Recent advances on hydrogen embrittlement of structural materials,” *International Journal of Fracture*, vol. 196, no. 1-2, pp. 223–243, 2015.
- [188] R. P. Gangloff, “Probabilistic fracture mechanics simulation of stress corrosion cracking using accelerated laboratory testing and multi-scale modeling,” *Corrosion*, vol. 72, no. 7, pp. 862–880, 2016.
- [189] W. Tian, S. Li, N. Du, S. Chen, and Q. Wu, “Effects of applied potential on stable pitting of 304 stainless steel,” *Corrosion Science*, vol. 93, pp. 242–255, 2015.
- [190] C. Gabrielli, S. Joiret, M. Keddam, N. Portail, P. Rousseau, and V. Vivier, “Single pit on iron generated by SECM: An electrochemical impedance spectroscopy investigation,” *Electrochimica Acta*, vol. 53, no. 25, pp. 7539–7548, 2008.
- [191] R. Newman, “The dissolution and passivation kinetics of stainless alloys containing molybdenum. dissolution kinetics in artificial pits,” *Corrosion Science*, vol. 25, no. 5, pp. 341–350, 1985.
- [192] S. Zhou and A. Turnbull, “Development of pre-pitting procedure for turbine disc steel,” *British Corrosion Journal*, vol. 35, no. 2, pp. 120–124, 2000.
- [193] A. Turnbull, D. Coleman, and A. Griffiths, “Assessment of test methods for evaluating effectiveness of corrosion inhibitors in retarding propagation of localised corrosion,” *British Corrosion Journal*, vol. 36, no. 3, pp. 210–214, 2001.

- [194] J. Han, Y. Yang, S. Nesic, B. N. Brown, *et al.*, “Roles of passivation and galvanic effects in localized CO_2 corrosion of mild steel,” *CORROSION/2008*, paper, no. 08332, 2008.
- [195] A. Dugstad, M. Seiersten, R. Nyborg, *et al.*, “Flow assurance of ph stabilized wet gas pipelines,” in *CORROSION 2003*, NACE International, 2003.
- [196] A. Ikhvani, H. Nurlaila, F. Ferdinand, R. Fachria, A. Hasan, M. Yani, I. Setyawati, *et al.*, “Preliminary study: optimization of ph and salinity for biosurfactant production from pseudomonas aeruginosa in diesel fuel and crude oil medium,” in *IOP Conference Series: Earth and Environmental Science*, vol. 58, p. 012056, IOP Publishing, 2017.
- [197] J. W. Johnson, J. J. Nitao, and K. G. Knauss, “Reactive transport modelling of CO_2 storage in saline aquifers to elucidate fundamental processes, trapping mechanisms and sequestration partitioning,” *Geological Society, London, Special Publications*, vol. 233, no. 1, pp. 107–128, 2004.
- [198] S. Dara, M. Lindstrom, J. English, A. Bonakdarpour, B. Wetton, and D. P. Wilkinson, “Conversion of saline water and dissolved carbon dioxide into value-added chemicals by electrodialysis,” *Journal of CO2 Utilization*, vol. 19, pp. 177–184, 2017.
- [199] S. Dupraz, M. Parmentier, B. Ménez, and F. Guyot, “Experimental and numerical modeling of bacterially induced pH increase and calcite precipitation in saline aquifers,” *Chemical Geology*, vol. 265, no. 1, pp. 44–53, 2009.
- [200] W. Li, B. Brown, D. Young, and S. Nešić, “Investigation of pseudo-passivation of mild steel in CO_2 corrosion,” *Corrosion*, vol. 70, no. 3, pp. 294–302, 2013.
- [201] J. Han, D. Young, H. Colijn, A. Tripathi, and S. Nešić, “Chemistry and structure of the passive film on mild steel in CO_2 corrosion environments,” *Industrial & Engineering Chemistry Research*, vol. 48, no. 13, pp. 6296–6302, 2009.

- [202] M. Singer, “29 - top-of-the-line corrosion,” in *Trends in Oil and Gas Corrosion Research and Technologies* (A. El-Sherik, ed.), Woodhead Publishing Series in Energy, pp. 689 – 706, Boston: Woodhead Publishing, 2017.
- [203] F. Pessu, R. Barker, and A. Neville, “The influence of pH on localized corrosion behavior of X65 carbon steel in CO_2 -saturated brines,” *Corrosion*, vol. 71, no. 12, pp. 1452–1466, 2015.
- [204] Y. Cheng and J. Luo, “Metastable pitting of carbon steel under potentiostatic control,” *Journal of the Electrochemical Society*, vol. 146, no. 3, pp. 970–976, 1999.
- [205] ASTM, *G1 - Standard practice for preparing, cleaning, and evaluating corrosion test specimens*. ASTM International, 2011.
- [206] S. A. Mohammed, Y. Hua, R. Barker, and A. Neville, “Investigating pitting in X65 carbon steel using potentiostatic polarisation,” *Applied Surface Science*, vol. 423, pp. 25 – 32, 2017.
- [207] W. C. Lyons and G. J. Plisga, *Standard handbook of petroleum and natural gas engineering*. Gulf Professional Publishing, 2011.
- [208] J. Han, B. Brown, and S. Nešić, “Investigation of the galvanic mechanism for localized carbon dioxide corrosion propagation using the artificial pit technique,” *Corrosion*, vol. 66, no. 9, pp. 095003–095003, 2010.
- [209] P. de Groot, *Coherence scanning interferometry*, pp. 187–208. Springer, 2011.
- [210] “Geometrical product specifications (gps) and surface texture: Areal.”
- [211] R. Leach, L. Brown, X. Jiang, R. Blunt, M. Conroy, and D. Mauger, “Guide to the measurement of smooth surface topography using coherence scanning interferometry,” *Measurement good practice guide*, no. 108, 2008.
- [212] A. Olszak, “Lateral scanning white-light interferometer,” *Applied optics*, vol. 39, no. 22, pp. 3906–3913, 2000.

- [213] V. P. Metrology, “Roughness & texture analysis,”
- [214] ASTM, “G46-94,” *Standard Guide for Examination and Evaluation of Pitting Corrosion*, ASTM International, West Conshohocken, PA, 2005.
- [215] N. P. Library, “Guide for the measurement of smooth surface topography using coherence scanning interferometry,” *A NATIONAL MEASUREMENT GOOD PRACTICE GUIDE*, vol. Number 108.
- [216] Y. Yuan, Y. Ji, and S. P. Shah, “Comparison of two accelerated corrosion techniques for concrete structures,” *ACI Structural Journal*, vol. 104, no. 3, p. 344, 2007.
- [217] M. Geng, F. Feng, P. Sebastian, A. Matchett, and D. Northwood, “Charge transfer and mass transfer reactions in the metal hydride electrode,” *International journal of hydrogen energy*, vol. 26, no. 2, pp. 165–169, 2001.
- [218] H. J. Flitt and D. P. Schweinsberg, “Evaluation of corrosion rate from polarisation curves not exhibiting a tafel region,” *Corrosion Science*, vol. 47, no. 12, pp. 3034–3052, 2005.
- [219] A. Fu and Y. Cheng, “Electrochemical polarization behavior of X70 steel in thin carbonate/bicarbonate solution layers trapped under a disbanded coating and its implication on pipeline scc,” *Corrosion Science*, vol. 52, no. 7, pp. 2511–2518, 2010.
- [220] G. Glass, C. Page, N. Short, and J.-Z. Zhang, “The analysis of potentiostatic transients applied to the corrosion of steel in concrete,” *Corrosion Science*, vol. 39, no. 9, pp. 1657–1663, 1997.
- [221] “Validation of corrosion rates measured by the tafel extrapolation method,” *Corrosion Science*, vol. 47, no. 12, pp. 3202 – 3215, 2005.
- [222] K. Uddin, L. Somerville, A. Barai, M. Lain, T. Ashwin, P. Jennings, and J. Marco, “The impact of high-frequency-high-current perturbations on film

- formation at the negative electrode-electrolyte interface,” *Electrochimica Acta*, vol. 233, pp. 1–12, 2017.
- [223] “Evaluation of corrosion rate from polarisation curves not exhibiting a Tafel region,” *Corrosion Science*, vol. 47, no. 12, pp. 3034 – 3052, 2005.
- [224] W. S. Tait, *An introduction to electrochemical corrosion testing for practicing engineers and scientists*. PairODocs Publications, 1994.
- [225] Z. Ahmad, “Chapter 3 - corrosion kinetics,” in *Principles of Corrosion Engineering and Corrosion Control* (Z. Ahmad, ed.), pp. 57 – 119, Oxford: Butterworth-Heinemann, 2006.
- [226] F. Pessu, R. Barker, and A. Neville, “Understanding pitting corrosion behavior of x65 carbon steel in CO_2 -saturated environments: The temperature effect,” *Corrosion*, vol. 72, no. 1, pp. 78–94, 2015.
- [227] M. Kermani and A. Morshed, “Carbon dioxide corrosion in oil and gas productiona compendium,” *Corrosion*, vol. 59, no. 8, pp. 659–683, 2003.
- [228] Y.-G. Huang, X.-L. Lin, X.-H. Zhang, Q.-C. Pan, Z.-X. Yan, H.-Q. Wang, J.-J. Chen, and Q.-Y. Li, “ Fe_3C carbon nanocapsules/expanded graphite as anode materials for lithium ion batteries,” *Electrochimica Acta*, vol. 178, pp. 468–475, 2015.
- [229] J. Liu, B. Yu, Q. Zhang, L. Hou, Q. Huang, C. Song, S. Wang, Y. Wu, Y. He, and J. Zou, “Synthesis and magnetic properties of Fe_3C core shell nanoparticles,” *Nanotechnology*, vol. 26, no. 8, p. 085601, 2015.
- [230] A. K. Gangopadhyay, R. Jensen, R. Carter, D. Uy, A. O’Neill, S. Simko, H. Gao, R. Stockwell, C. Phillips, and M. Graham, “Development of zero phosphorus engine oils,” *Lubrication Science*, vol. 20, no. 2, pp. 163–180, 2008.

- [231] M. Hanesch, “Raman spectroscopy of iron oxides and (oxy) hydroxides at low laser power and possible applications in environmental magnetic studies,” *Geophysical Journal International*, vol. 177, no. 3, pp. 941–948, 2009.
- [232] M. Prakash, S. Shekhar, A. Moon, and K. Mondal, “Effect of machining configuration on the corrosion of mild steel,” *Journal of Materials Processing Technology*, vol. 219, pp. 70 – 83, 2015.
- [233] S. Navabzadeh, D. Young, B. Brown, and S. Nestic, “Effect of incorporation of calcium into iron carbonate protective layers in CO_2 corrosion of mild steel,” *CORROSION*, vol. 73, no. 3, pp. 238–246, 2017.
- [234] M. Ni and B. D. Ratner, “Differentiating calcium carbonate polymorphs by surface analysis techniquesan XPS and TOF-SIMS study,” *Surface and Interface Analysis*, vol. 40, no. 10, pp. 1356–1361, 2008.
- [235] B. Xu and K. M. Poduska, “Linking crystal structure with temperature-sensitive vibrational modes in calcium carbonate minerals,” *Physical Chemistry Chemical Physics*, vol. 16, no. 33, pp. 17634–17639, 2014.
- [236] R. E. Herzog, Q. Shi, J. N. Patil, and J. L. Katz, “Magnetic water treatment: the effect of iron on calcium carbonate nucleation and growth,” *Langmuir*, vol. 5, no. 3, pp. 861–867, 1989.
- [237] H. A. Alsaiani, S. Yean, M. B. Tomson, A. T. Kan, *et al.*, “Iron calcium carbonate: Precipitation interaction,” in *SPE International Oilfield Scale Conference*, Society of Petroleum Engineers, 2008.
- [238] E. M. Pouget, P. H. Bomans, A. Dey, P. M. Frederik, G. de With, and N. A. Sommerdijk, “The development of morphology and structure in hexagonal vaterite,” *Journal of the American Chemical Society*, vol. 132, no. 33, pp. 11560–11565, 2010.
- [239] P. Bots, L. G. Benning, J.-D. Rodriguez-Blanco, T. Roncal-Herrero, and S. Shaw, “Mechanistic insights into the crystallization of amorphous calcium

- carbonate (acc),” *Crystal Growth & Design*, vol. 12, no. 7, pp. 3806–3814, 2012.
- [240] S. M. Antao and I. Hassan, “The orthorhombic structure of $CaCO_3$, $SrCO_3$, $PbCO_3$ and $BaCO_3$: linear structural trends,” *The Canadian Mineralogist*, vol. 47, no. 5, pp. 1245–1255, 2009.
- [241] B. Jones, “Review of calcium carbonate polymorph precipitation in spring systems,” *Sedimentary Geology*, vol. 353, pp. 64 – 75, 2017.
- [242] B. Jones, “Review of aragonite and calcite crystal morphogenesis in thermal spring systems,” *Sedimentary Geology*, vol. 354, pp. 9 – 23, 2017.
- [243] M. AlKhatib and A. Eisenhauer, “Calcium and strontium isotope fractionation during precipitation from aqueous solutions as a function of temperature and reaction rate; ii. aragonite,” *Geochimica et Cosmochimica Acta*, vol. 209, pp. 320 – 342, 2017.
- [244] C. Blue, A. Giuffre, S. Mergelsberg, N. Han, J. De Yoreo, and P. Dove, “Chemical and physical controls on the transformation of amorphous calcium carbonate into crystalline $CaCO_3$ polymorphs,” *Geochimica et Cosmochimica Acta*, vol. 196, pp. 179–196, 2017.
- [245] J. D. Rodriguez-Blanco, S. Shaw, and L. G. Benning, “The kinetics and mechanisms of amorphous calcium carbonate (acc) crystallization to calcite, via vaterite.,” *Nanoscale*, vol. 3, no. 1, pp. 265–271, 2011.
- [246] D. J. Tobler, J. D. Rodriguez-Blanco, K. Dideriksen, N. Bovet, K. K. Sand, and S. L. Stipp, “Citrate effects on amorphous calcium carbonate (acc) structure, stability, and crystallization,” *Advanced Functional Materials*, vol. 25, no. 20, pp. 3081–3090, 2015.
- [247] H. A. Alsaiani, N. Zhang, S. Work, A. T. Kan, M. B. Tomson, *et al.*, “A new correlation to predict the stoichiometry of mixed scale: Iron-calcium

- carbonate,” in *SPE International Conference on Oilfield Scale*, Society of Petroleum Engineers, 2012.
- [248] A. Boughriet, L. Gengembre, J. Laureyns, P. Recourt, H. Langelin, and A. Nacer, “Generation of Uranyl/Carbonate/Hydroxide coatings at the vaterite surface,” *Physical Chemistry Chemical Physics*, vol. 2, no. 5, pp. 1059–1068, 2000.
- [249] B. Njegić Džakula, J. Kontrec, M. Ukrainczyk, S. Sviben, and D. Kralj, “Polymorphic composition and morphology of calcium carbonate as a function of ultrasonic irradiation,” *Crystal Research and Technology*, vol. 49, no. 4, pp. 244–256, 2014.
- [250] E. Langerak, M. M. H. Beekmans, J. J. Beun, H. V. M. Hamelers, G. Lettinga, *et al.*, “Influence of phosphate and iron on the extent of calcium carbonate precipitation during anaerobic digestion,” *Journal of Chemical Technology and Biotechnology*, vol. 74, no. 11, pp. 1030–1036, 1999.
- [251] J. Han, Y. Yang, B. Brown, and S. Nesic, “Electrochemical investigation of localized CO_2 corrosion on mild steel,” *Corrosion/2007*, paper, no. 07323, 2007.
- [252] J. Han, S. Nešić, and B. N. Brown, “Galvanic model for localized CO_2 corrosion,” *ICC/2008*, paper, no. 2687, 2008.
- [253] R. M. Fernández-Domene, J. Andrews, R. Leiva-García, and R. Akid, “Galvanic corrosion following local breakdown of a scale formed on X-65 in CO_2 saturated solutions,” in *CORROSION 2015*, NACE International, 2015.
- [254] S. Sisira, D. Alexander, K. Thomas, G. Vimal, K. P. Mani, P. Biju, N. Unnikrishnan, and C. Joseph, “Microstructural characterization and optical properties of green emitting hexagonal and monoclinic $CePO_4 : Tb^{3+}$ nanocrystals,” *Materials Research Express*, vol. 4, no. 2, p. 025010, 2017.

- [255] J. Singh, C. Singh, D. Kaur, S. B. Narang, R. Jotania, and R. Joshi, “Investigation on structural and microwave absorption property of Co^{2+} and Y^{3+} substituted M-type Ba-Sr hexagonal ferrites prepared by a ceramic method,” *Journal of Alloys and Compounds*, vol. 695, pp. 792–798, 2017.
- [256] S. N. Esmaeely, D. Young, B. Brown, and S. Nešić, “Effect of incorporation of calcium into iron carbonate protective layers in CO_2 corrosion of mild steel,” *Corrosion*, vol. 73, no. 3, pp. 238–246, 2016.
- [257] P. M. Davidson, G. H. Symmes, B. A. Cohen, R. J. Reeder, and D. H. Lindsley, “Synthesis of the new compound $CaFe(CO_3)_2$ and experimental constraints on the $(Ca,Fe)CO_3$ join,” *Geochimica et Cosmochimica Acta*, vol. 57, no. 23-24, pp. 5105–5109, 1993.
- [258] Y. Wang, J. Wang, and X. Zhang, “The electrochemical corrosion properties of pani/coal composites on magnesium alloys,” *Int. J. Electrochem. Sci*, vol. 12, pp. 4044–4055, 2017.
- [259] E. Schmidl, R. Pippig, R. Morgenstern, T. Lampke, and I. Scharf, “Nondestructive analysis of pitting corrosion characteristics on EN AW-2024-T3 using 3D optical pattern profilometry,” *Corrosion Engineering, Science and Technology*, pp. 1–5, 2018.
- [260] L. Wei, X. Pang, and K. Gao, “Effect of flow rate on localized corrosion of X70 steel in supercritical CO_2 environments,” *Corrosion Science*, vol. 136, pp. 339–351, 2018.
- [261] D. Yavas, P. Mishra, A. Alshehri, P. Shrotriya, K. R. Hebert, and A. F. Bastawros, “Nanoindentation study of corrosion-induced grain boundary degradation in a pipeline steel,” *Electrochemistry Communications*, vol. 88, pp. 88–92, 2018.

- [262] B. Krawczyk, P. Cook, J. Hobbs, and D. L. Engelberg, “Corrosion Behavior of Cold Rolled Type 316L Stainless Steel in HCl-Containing Environments,” *Corrosion*, vol. 73, no. 11, pp. 1346–1358, 2017.
- [263] A. Kahyarian, B. Brown, and S. Nestic, “Electrochemistry of CO_2 corrosion of mild steel: Effect of CO_2 on iron dissolution reaction,” *Corrosion Science*, vol. 129, pp. 146–151, 2017.
- [264] R. Newman, “The dissolution and passivation kinetics of stainless alloys containing molybdenum. dissolution kinetics in artificial pits,” *Corrosion Science*, vol. 25, no. 5, pp. 341–350, 1985.
- [265] A. Turnbull, D. Coleman, A. Griffiths, P. Francis, and L. Orkney, “Effectiveness of corrosion inhibitors in retarding the rate of propagation of localized corrosion,” *Corrosion*, vol. 59, no. 3, pp. 250–257, 2003.
- [266] J. W. Palmer, J. Marsh, R. C. Newman, *et al.*, “Evaluation of inhibitor performance for protection against localized corrosion,” in *CORROSION 2002*, NACE International, 2002.
- [267] B. Wang, L. Xu, G. Liu, and M. Lu, “Corrosion behavior and mechanism of 3cr steel in CO_2 environment with various Ca^{2+} concentration,” *Corrosion Science*, vol. 136, pp. 210 – 220, 2018.

Appendix A

Pit count technique

The in-built automated capability of the NPFlex was explored to perform optimised circular scan of corroded samples. A 10mm scan diameter was set for NPFlex analysis leaving out only 1mm edge that was covered in resin during the corrosion test. The measurement was programmed to commence from the centre of the sample and scanned outwards in anti-clockwise direction covering minute area ($1118.1\mu\text{m} \times 838.6\mu\text{m}$) that extends over the entire area of the sample in 172 measurements with 25% area overlap as shown in Figure A.1. Analysis technique is provided below.

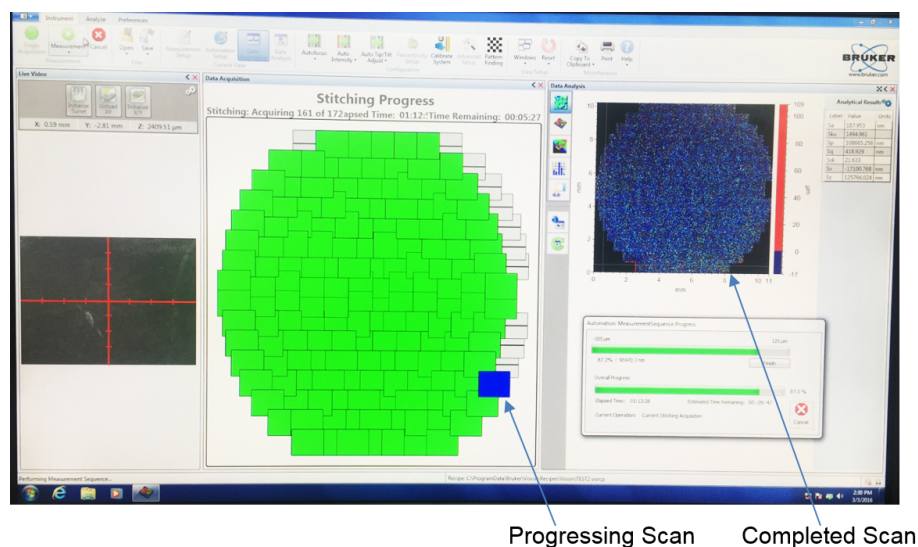
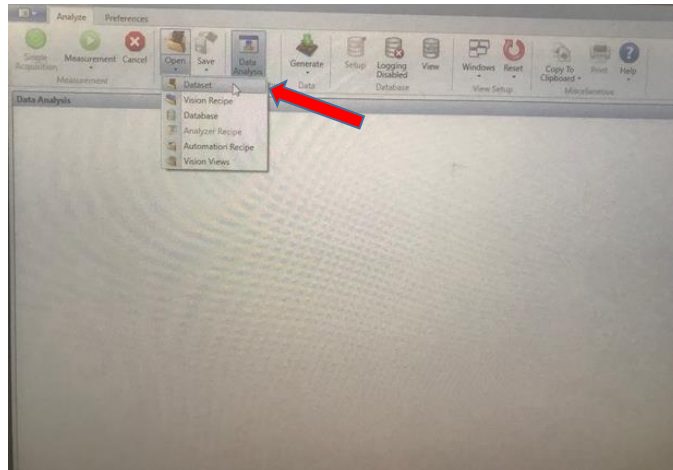


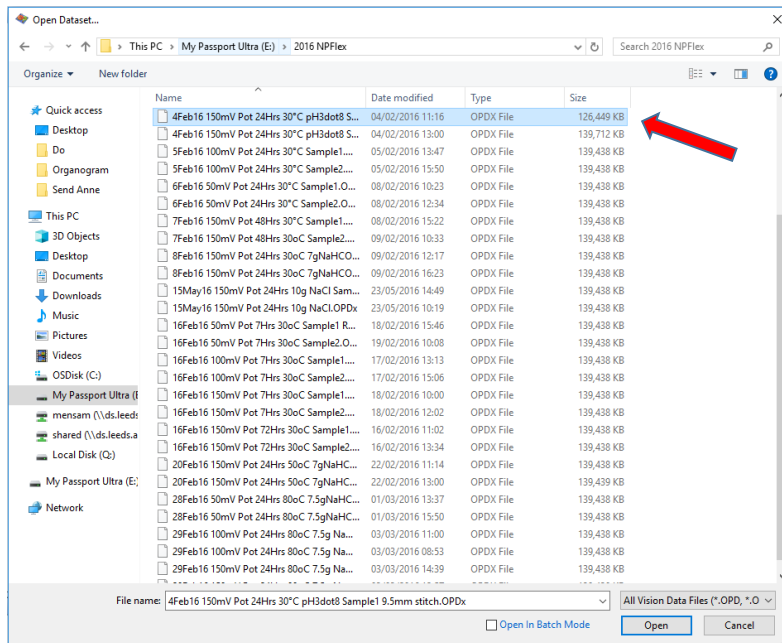
Figure A.1: Interface showing data collection process

1. Open **Vision64** Software.

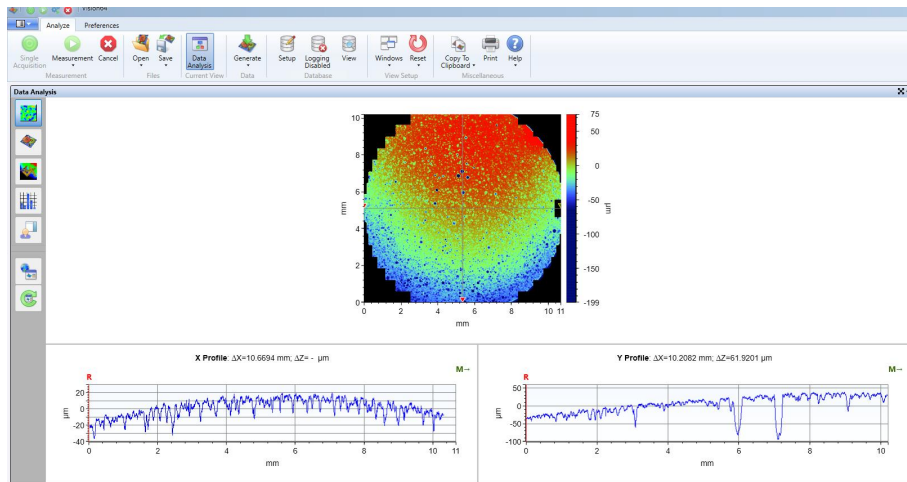
2. Select **Dataset**.



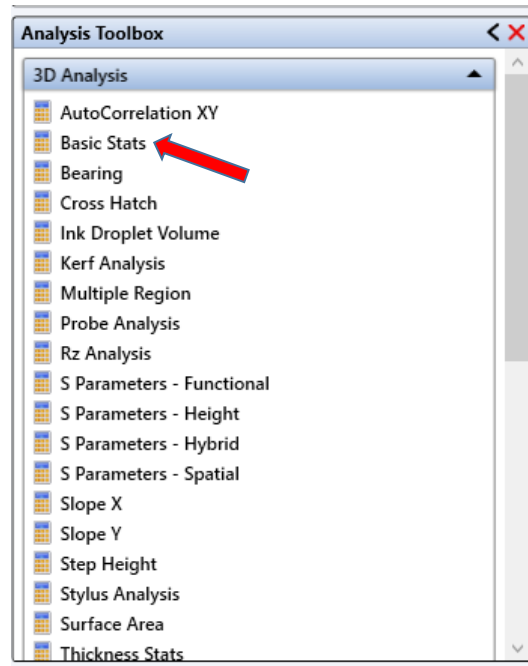
3. Locate dataset.



4. Check that appropriate data loads up.



5. Select **Basic Stats** from the Analysis Toolbox.



6. Check that **Percentage Data Points** measures up to 80%.

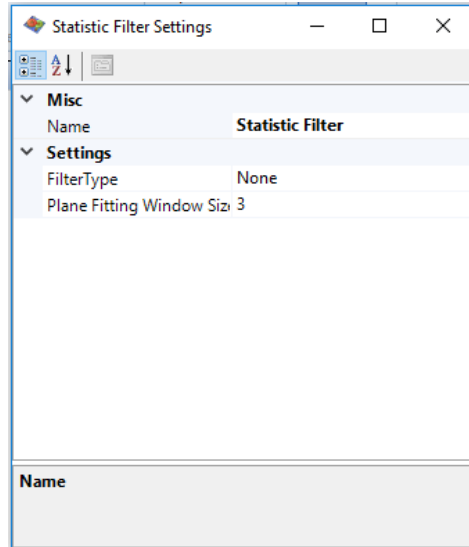
Analytical Results 		
Label	Value	Units
Average	-1.64	μm
Data Points	30478157.824	
Percent Data Points	85.39	%
Ra	19.414	μm
Rp	74.793	μm
Rq	23.796	μm
Rt	274.172	μm
Rv	-199.379	μm



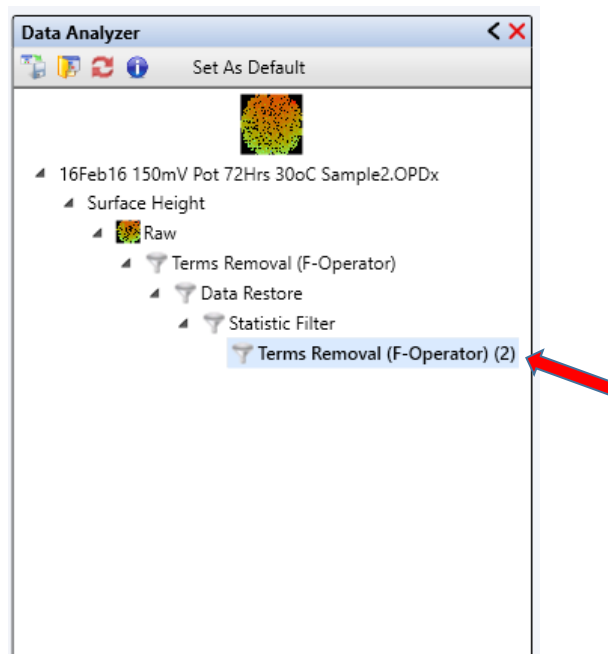
7. Select **Statistics Filter** from the 3D Filter pane.

3D Filter 
 Data Fill
 Data Flattening
 Data Modification
 Data Restore
 Fourier Filter
 Gaussian Regression Filter
 Mask Data
 Microform
 Remove Modal Tilt
 Statistic Filter 
 Terms Removal (F-Operator)
 Threshold
 Trim Pixels

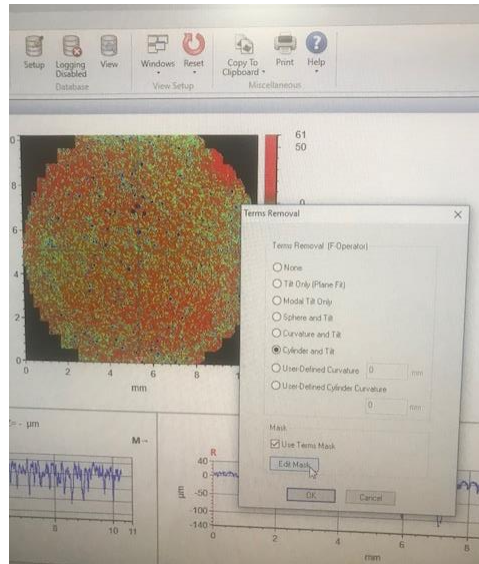
8. Apply statistics filter (use the default setting).



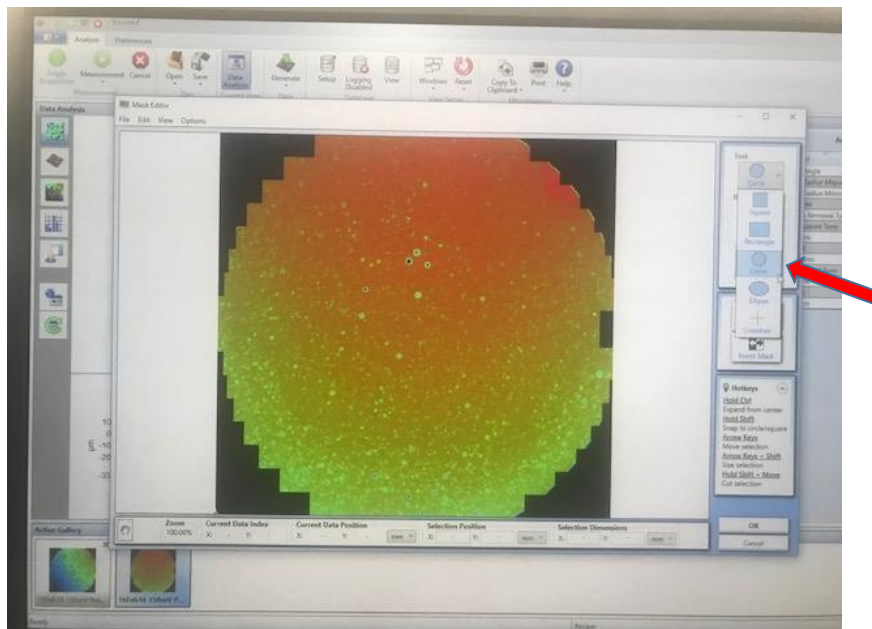
9. Select **Terms Removal (F-Operator)** from 3D Filter pane.



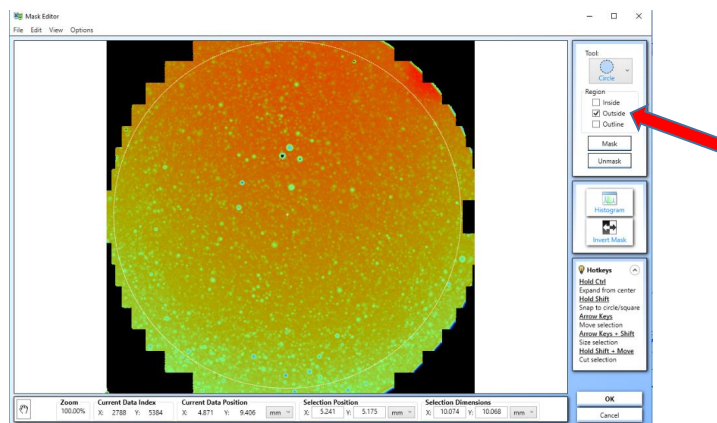
10. Select suitable **F-Operator** parameter (Cylinder and Tilt).



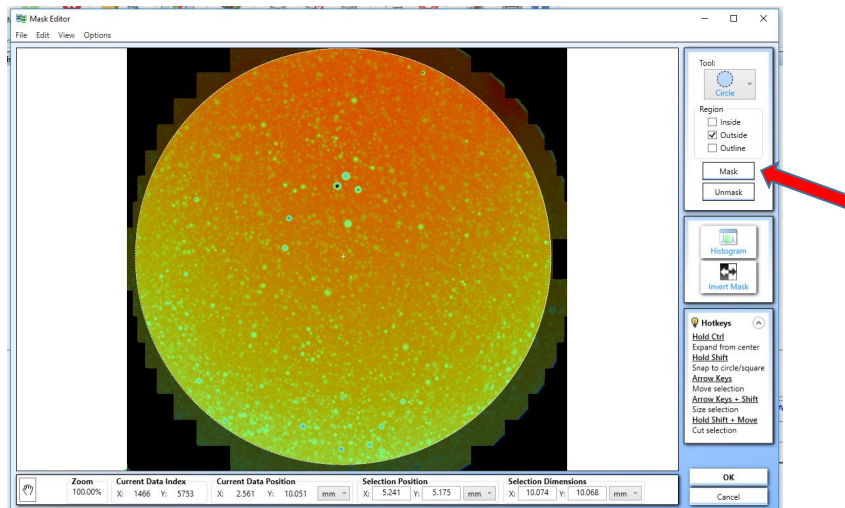
11. Select **Circle** tool from the pane which pops up.



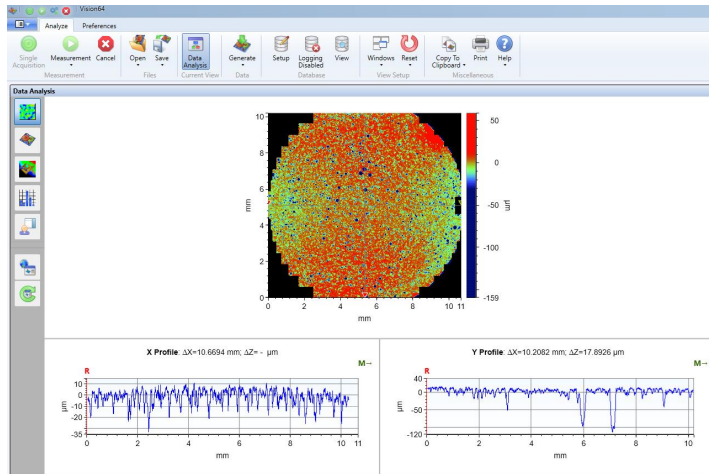
12. Select **outside** region option from the pane.
Click the left mouse and hover round the scanned data to create a circular pattern on the featured data.



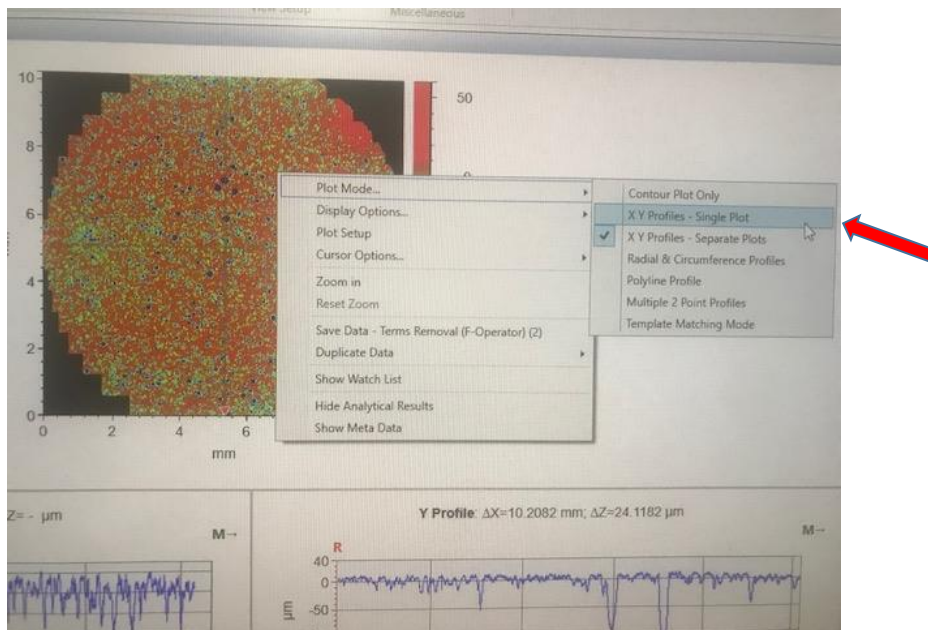
13. Select **Mask** to exclude edges of sample (which was hitherto immersed in resin).



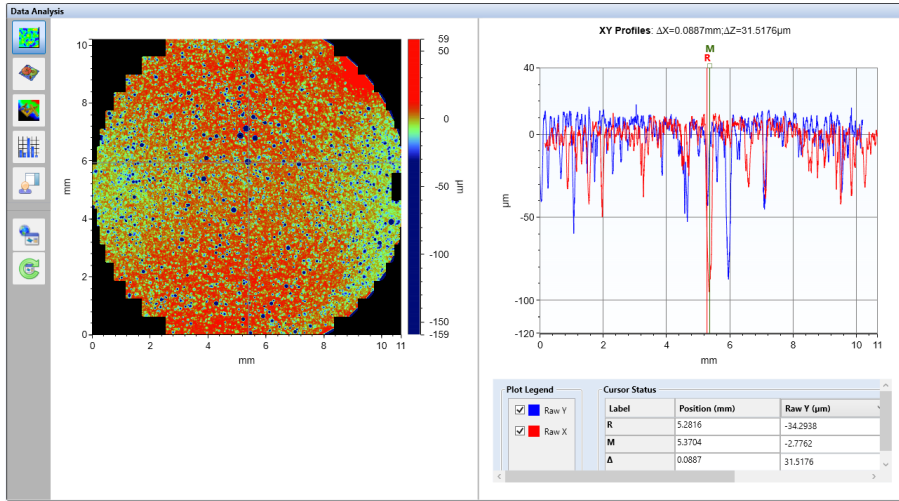
14. Check that tilt is removed from X and Y profile data.



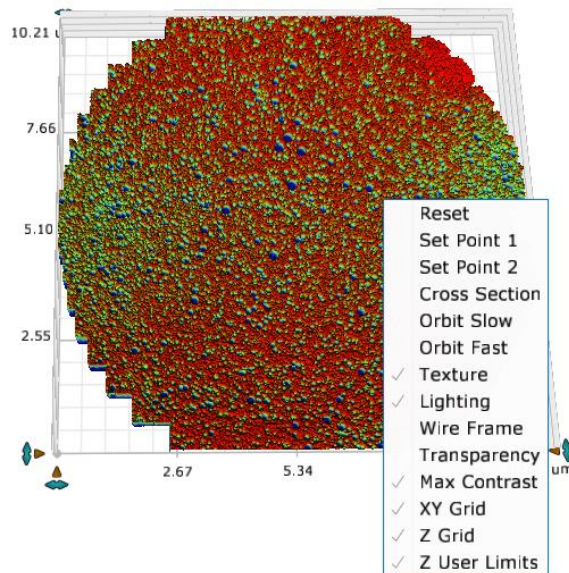
15. Right-click the data image, select plot mode and click **XY profile – Single Plot**. This combines the X and Y data for a better view.



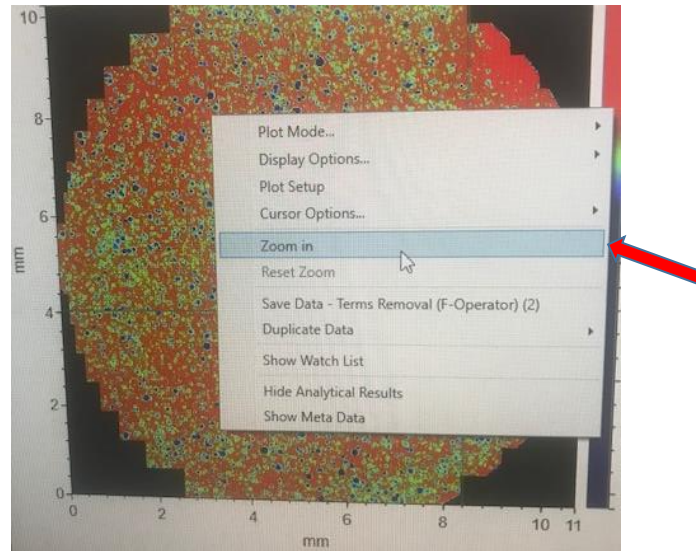
16. Check that XY profile and cursor status is displayed.



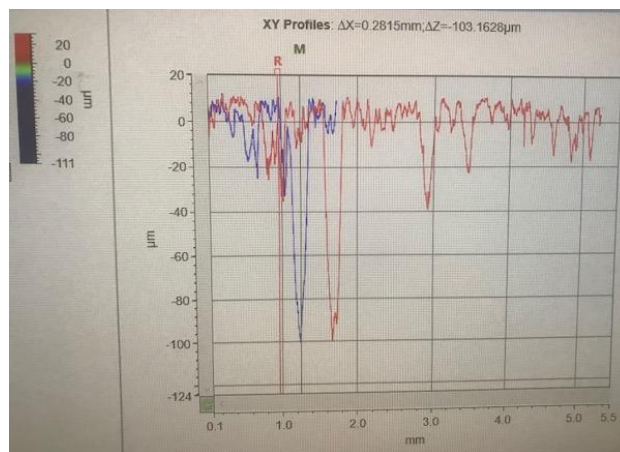
17. Right click the data image to select desirable view effects.



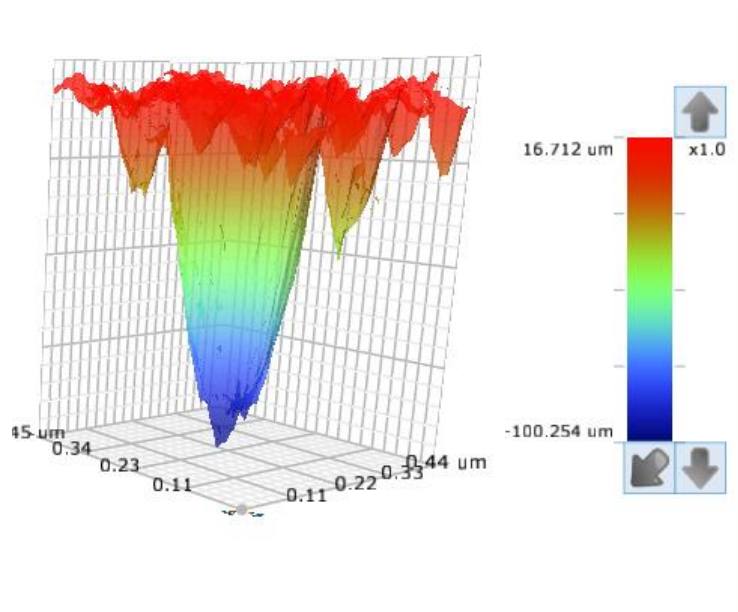
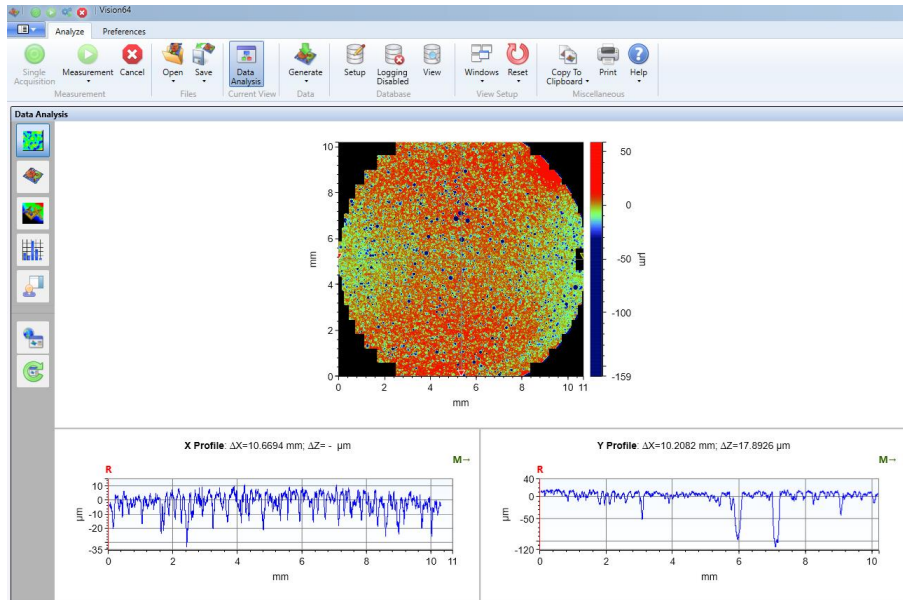
18. Right-click on data and select **zoom in** function to reveal more details on data.



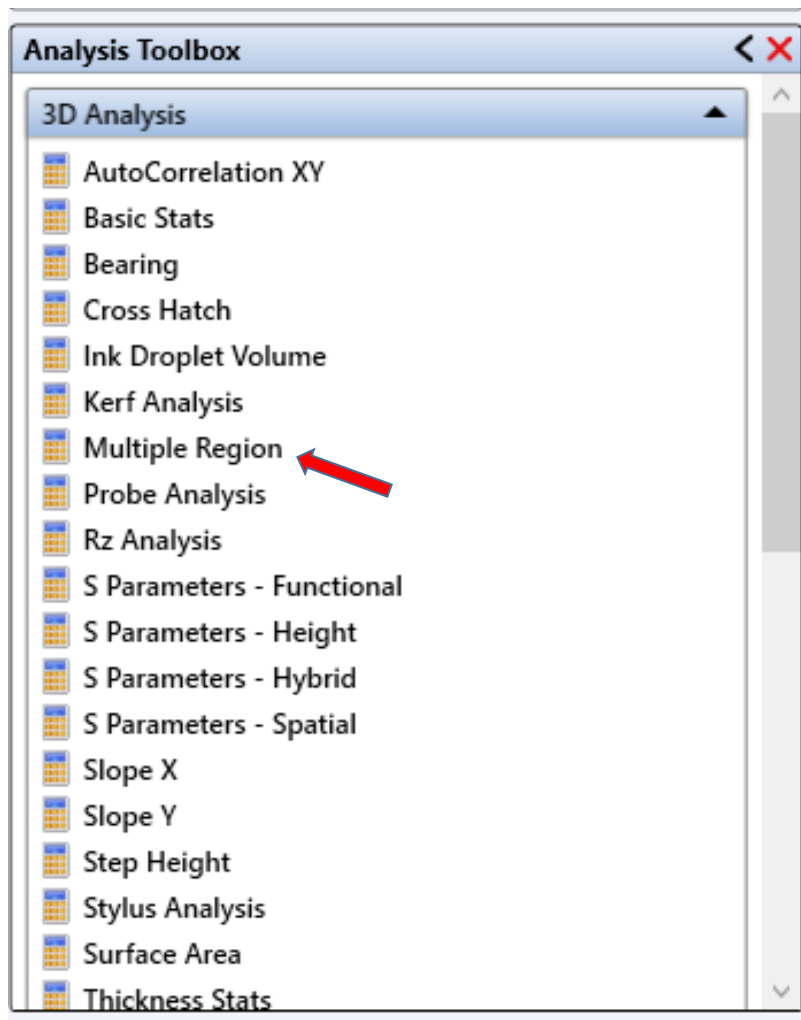
19. Take 2D measurements by using the XY profile guide.



20. To take 3D measurements, select 3D option from the **Data Analysis** pane.



21. It is important to obtain discrete pit information in order to conduct pitting analysis. The Multiple Region analysis tools come handy here. It provides discrete pit information such as roughness, depth, diameter, volume, amongst other. To conduct the multiple region analysis, select **Multiple Region** from the Analysis Toolbox.



22. Select **By threshold(s)**, **Minimum Region Size** and input suitable parameters based on depth of pit screening required. Select the **Exclude Edge Regions** box and click **OK**.

The image shows a software dialog box titled "Multiple Region Analysis" with a close button (X) in the top right corner. The dialog is divided into several sections:

- Region Finding Routine:** Contains four radio button options: "By Separation", "By Height", "By Levels", and "By Threshold(s)". The "By Threshold(s)" option is selected. To its right is a text input field containing "10" and a dropdown menu set to "nm".
- Region Finding Options:** Contains several settings:
 - "Minimum Region Size": A text input field with "10" and a dropdown menu set to "pix".
 - "Number of Levels": A dropdown menu set to "2".
 - "Region Level": A dropdown menu set to "Valleys".
 - "Background Level": A dropdown menu set to "2".
 - "Exclude Edge Regions": A checked checkbox.
 - "Regions have greater area than background": An unchecked checkbox.
 - "Use Intensity": An unchecked checkbox.
 - "Use Periodic Array": An unchecked checkbox.
 - "Trim Regions": A button located below the checkboxes.
- Buttons:** On the right side, there are three buttons: "OK" (highlighted with a blue border), "Cancel", and "Statistics".
- Zero Level:** A section with three radio button options: "Automatic" (selected), "Manual", and "Background".
- Term Removal:** A section with four radio button options: "None" (selected), "Mean", "Tilt", and "Curvature and Tilt".

23. Tick required parameters in the pane that pops up. On the output section, tick **Log** and select location where **csv** output is to be saved.

Multiple Region Statistics

Individual Parameters Displayed

<input checked="" type="checkbox"/> Mean	<input checked="" type="checkbox"/> Rq	<input type="checkbox"/> X Sag	<input checked="" type="checkbox"/> XY Diameter
<input type="checkbox"/> Data Points	<input checked="" type="checkbox"/> Rsk	<input type="checkbox"/> Y Sag	<input checked="" type="checkbox"/> Full Diameter
<input type="checkbox"/> Ra	<input type="checkbox"/> Rku	<input type="checkbox"/> Line Width	<input checked="" type="checkbox"/> Full X Diameter
<input checked="" type="checkbox"/> Rt	<input checked="" type="checkbox"/> Area	<input type="checkbox"/> Line Width Std Dev	<input checked="" type="checkbox"/> Full Y Diameter
<input type="checkbox"/> Rt%	<input checked="" type="checkbox"/> Volume	<input type="checkbox"/> Max X Slope	<input type="checkbox"/> A Diameter
<input type="checkbox"/> Rp	<input type="checkbox"/> Tilt Magnitude	<input type="checkbox"/> Max Y Slope	<input type="checkbox"/> Y Center
<input type="checkbox"/> Rp%	<input type="checkbox"/> Tilt Angle	<input type="checkbox"/> Diameter	<input type="checkbox"/> X Center
<input checked="" type="checkbox"/> Rv	<input type="checkbox"/> X Tilt	<input type="checkbox"/> X Diameter	
<input checked="" type="checkbox"/> Rv%	<input type="checkbox"/> Y Tilt	<input type="checkbox"/> Y Diameter	

Relative Parameters Displayed

<input checked="" type="checkbox"/> X Tilt	<input checked="" type="checkbox"/> Y Tilt	<input checked="" type="checkbox"/> Mean	<input type="checkbox"/> Incline
<input type="checkbox"/> Tilt Magnitude	<input type="checkbox"/> Tilt Angle	<input type="checkbox"/> Pitch	

Output File

Log Include Time Stamp Include Header Include Summary

File: ...

Line Width
Orientation
 Vertical
 Horizontal

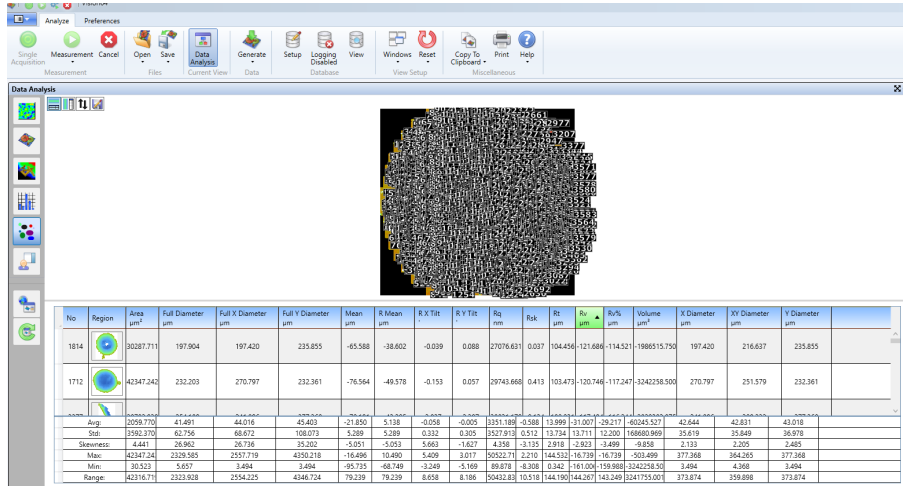
R% Percent
4.00 %

Full Diameter
Restore Size
4

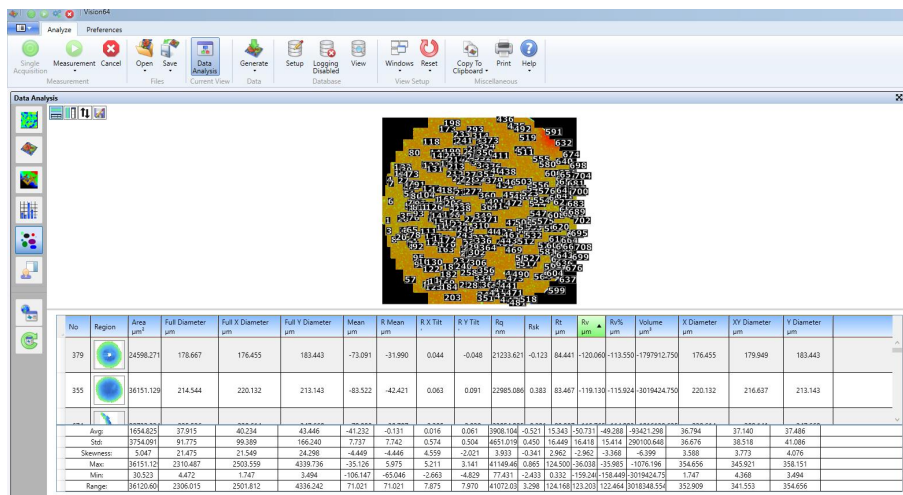
Pitch
Nominal
1.00 um

OK Cancel

24. Numbers are assigned to discrete data position.



25. Screening threshold in the Multiple Region analysis pane can be increased to identify pits of higher depths.

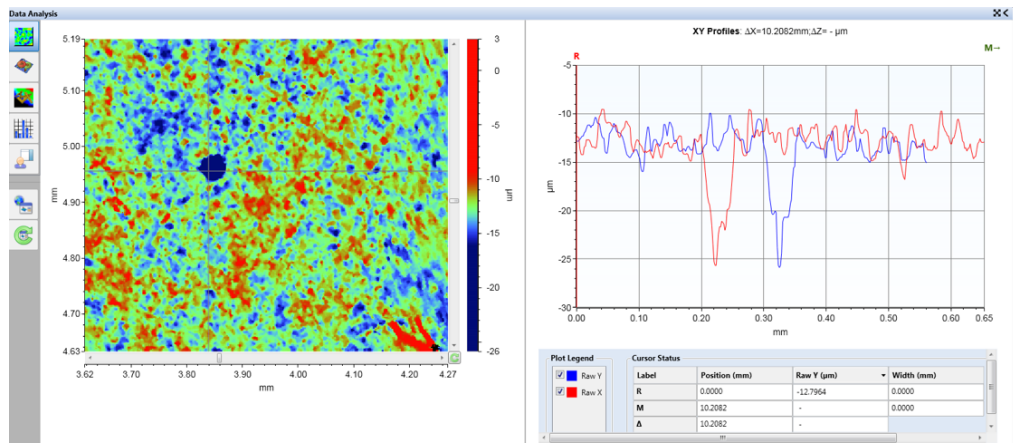


26. The csv output can be analysed further to rank pits based on depth, volume, pit-mouth diameter, etc.

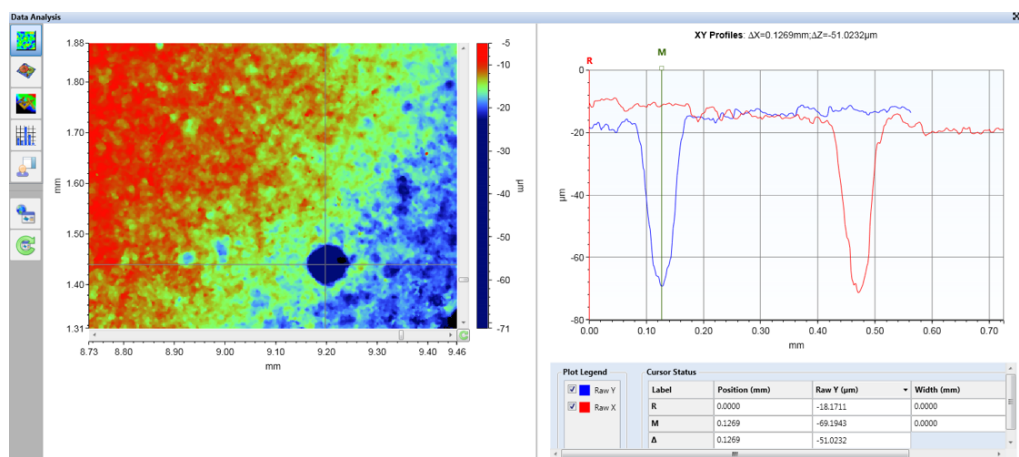
Region No	Rt (µm)	Rv (µm)	Rq (nm)	Rsk (°)	Mean (µm)	X Diameter	Y Diameter	Area (µm²)	Volume (µm³)	µXY Diamet	Rv% (µm)	Full X Dian	Full Y Dian	Full Diame	R Mean (µ)	R X Tilt (°)	R Y Tilt (°)
5401	151.765	-160.655	50868.19	0.082	-90.67	307.485	310.979	30806.6	-2793227	309.232	-158.606	307.485	310.979	244.761	-79.848	5.492	-5.124
6201	149.954	-159.207	46593.65	-0.268	-79.128	138.019	260.314	19800.1	-1566739	199.167	-157.734	138.019	260.314	167.72	-68.306	5.674	-2.777
6160	125.96	-135.789	22341.52	-2.94	-25.342	454.24	522.376	96720.45	-2451045	488.308	-112.093	2650.314	3719.524	2228.47	-14.52	0.381	0.407
6185	120.831	-130.758	38372.69	-0.368	-56.193	186.937	358.151	33562.8	-1885995	272.544	-128.056	186.937	358.151	216.301	-45.371	2.189	1.175
3220	114.469	-123.873	31283.52	-0.009	-60.139	207.902	262.061	35342.27	-2125437	234.982	-116.106	207.902	262.061	213.545	-49.317	0.26	0.439
3033	113.452	-122.898	33545.46	0.374	-73.454	279.532	237.602	46104.59	-3386549	258.567	-119.236	279.532	237.602	242.285	-62.632	-0.078	0.194
6013	110.07	-120.07	33953.59	0.078	-67.191	249.832	384.357	31841.32	-2139458	317.094	-118.596	249.832	384.357	259.17	-56.369	4.213	2.493
2929	106.364	-115.75	36378.83	-0.094	-60.475	272.544	297.003	46687.57	-2823415	284.773	-113.818	272.544	297.003	255.419	-49.653	-0.072	-0.095
2054	106.429	-115.471	27857.76	-1.007	-39.957	370.38	284.773	50457.13	-2016097	327.577	-108.887	370.38	284.773	253.464	-29.135	0.309	0.223
5745	104.205	-114.254	29495.35	0.145	-63.07	317.968	384.357	30327.39	-1912748	351.162	-110.959	317.968	384.357	280.492	-52.248	3.607	2.993
3192	102.025	-111.532	20602.84	-1.239	-32.575	379.115	274.291	41211.8	-1342468	326.703	-91.214	379.115	274.291	229.069	-21.753	-0.026	0.281
3423	101.838	-111.356	24886.33	-0.776	-40.449	186.937	153.743	20050.39	-811012	170.34	-100.589	186.937	153.743	159.778	-29.627	0.472	-0.183
2219	100.179	-109.344	38678.09	-0.001	-60.493	283.026	171.213	2742.11	-1678194	227.12	-108.793	283.026	171.213	190.295	-49.671	-0.282	0.374
2620	96.015	-105.027	16892.06	-1.431	-29.292	202.661	171.213	22016.05	-644893	186.937	-80.698	202.661	171.213	167.427	-18.47	-0.064	-0.095
3048	95.373	-104.636	27944.16	-0.193	-47.865	276.038	317.968	53628.45	-2566918	297.003	-96.823	276.038	317.968	261.308	-37.043	0.328	-0.233
2179	91.775	-101.061	23476.15	-0.796	-37.96	150.249	167.719	17962.63	-681866	158.984	-91.323	150.249	167.719	151.231	-27.138	0.064	0.085
2913	91.148	-100.674	19338.79	-1.097	-33.801	190.431	213.143	26740.97	-903859	201.787	-88.141	190.431	213.143	184.52	-22.979	0.358	0.229
5341	87.826	-97.913	24004.76	0.051	-53.35	386.104	358.151	29594.84	-1578894	372.127	-96.554	386.104	358.151	300.083	-42.528	3.067	3.099
3018	88.502	-97.174	16773.28	-1.732	-27.267	195.672	214.89	28215.22	-769335	205.281	-81.428	195.672	214.89	189.538	-16.445	-0.043	-0.125
4191	84.664	-94.614	27899.1	-0.251	-49.243	134.525	136.272	13057.63	-643003	135.398	-93.924	134.525	136.272	133.122	-38.422	0.433	-0.461
5783	85.178	-94.426	13859.53	-2.022	-22.138	587.017	656.9	161746.1	-3580813	621.959	-69.096	587.017	656.9	453.808	-11.317	0.21	0.054
3158	84.451	-94.157	22794.13	-0.604	-39.156	195.672	246.338	31856.58	-1247383	221.005	-86.095	195.672	246.338	201.398	-28.334	0.166	-0.197
2326	83.981	-93.28	20029.15	-0.728	-36.598	148.501	151.996	17254.5	-631482	150.249	-82.825	148.501	151.996	148.22	-25.776	0.143	0.178
2676	81.412	-90.917	15486.57	-1.606	-25.392	255.073	207.902	28331.2	-719399	231.488	-74.122	255.073	207.902	189.927	-14.571	0.135	-0.082
2450	81.369	-90.684	19978.33	-0.805	-34.743	239.349	164.225	24744.78	-859715	201.787	-81.467	239.349	164.225	177.499	-23.921	-0.081	0.244
4569	80.844	-90.024	14658.29	-1.429	-24.851	251.579	263.808	34051.16	-846194	257.694	-67.96	251.579	263.808	208.219	-14.029	0.429	0.256
5682	77.383	-86.793	6532.886	-0.917	-17.852	291.762	426.286	46925.65	-837697	359.024	-34.293	291.762	426.286	244.433	-7.03	0.064	0.055
5859	77.314	-86.678	12425.95	-2.462	-19.599	849.079	976.615	329972.1	-6467095	912.847	-65.102	849.079	976.615	648.177	-8.777	0.225	0.047
3001	77.965	-86.469	23152.79	-0.133	-43.81	138.019	143.26	15343.78	-672208	140.64	-83.347	138.019	143.26	139.772	-32.988	0.076	0.232
3988	76.41	-86.374	18457.25	-1.054	-31.611	118.801	117.054	10820.31	-342039	117.926	-78.978	118.801	117.054	117.375	-20.789	0.182	0.229
4913	75.586	-85.085	18221.24	-0.721	-31.901	153.743	172.96	19085.87	-608050	163.352	-74.061	153.743	172.96	155.887	-21.079	0.029	0.216
3761	75.595	-84.627	14007.13	-1.268	-26.568	124.042	171.213	16131.27	-428582	147.628	-68.865	124.042	171.213	143.314	-15.747	0.181	-0.009
2952	73.693	-83.163	13938.12	-1.007	-27.837	248.085	225.373	29884.81	-831903	236.729	-66.57	248.085	225.373	195.065	-17.015	0.271	0.039
3117	73.846	-82.918	11094.08	-1.487	-22.582	255.073	358.151	41187.38	-930086	306.612	-56.802	255.073	358.151	229.001	-11.76	-0.055	0.261
4128	73.251	-82.662	18408.51	-0.616	-33.002	197.42	297.003	35290.39	-1164659	247.211	-73.496	197.42	297.003	211.974	-22.18	0.3	0.247
1768	73.105	-81.973	15209.42	-0.914	-28.186	284.773	293.509	41510.92	-1170036	289.141	-68.184	284.773	293.509	229.899	-17.364	0.326	0.137
2040	72.392	-81.789	18793.89	-0.639	-35.101	139.766	134.525	11958.81	-419770	137.145	-77.453	139.766	134.525	123.395	-24.279	-0.187	0.025
1970	72.394	-81.744	17425.74	-1.004	-31.008	117.054	138.019	11986.28	-371674	127.537	-76.039	117.054	138.019	123.537	-20.186	0.077	0.293
615	72.977	-81.739	20742.37	-0.562	-36.805	167.719	146.754	17910.74	-659207	157.237	-80.264	167.719	146.754	151.012	-25.983	0.368	0.047
3573	72.95	-81.613	18213.15	-0.668	-32.74	209.649	220.132	24943.18	-816642	214.89	-73.966	209.649	220.132	178.21	-21.918	0.005	-0.211
3637	72.111	-81.556	14065.48	-1.069	-28.518	146.754	155.49	17333.86	-494320	151.122	-68.702	146.754	155.49	148.56	-17.696	0.184	0.015
6123	71.254	-80.902	20742.55	-0.538	-35.341	160.731	139.766	16439.55	-580990	150.249	-75.851	160.731	139.766	144.677	-24.519	-0.346	0.27
2802	71.77	-80.779	14726.84	-0.502	-31.812	239.349	253.326	40122.14	-1276381	246.338	-66.333	239.349	253.326	226.02	-20.991	0.107	-0.023

Appendix B

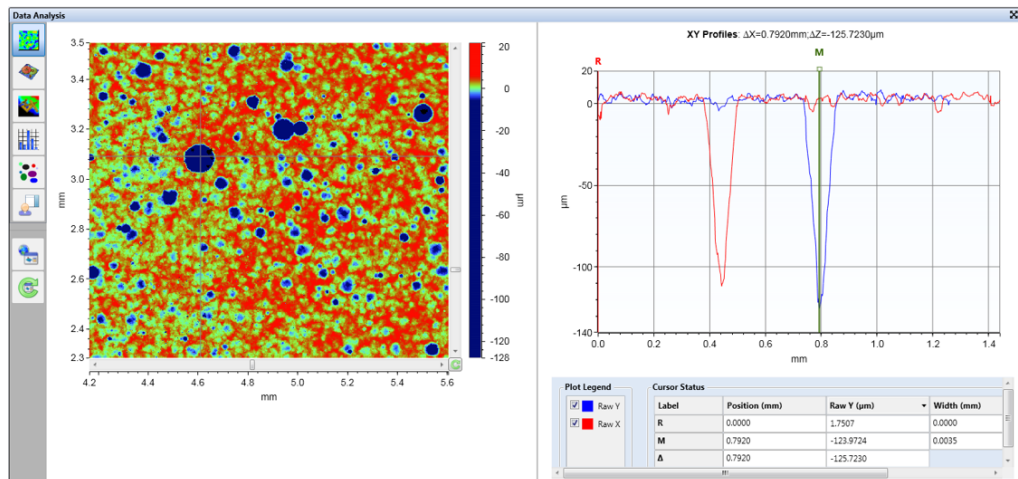
2D profilometry of corroded pit



(a) 50mV vs (Ag/AgCl) potentiostatic for 24 h



(b) 100mV vs (Ag/AgCl) potentiostatic for 24 h

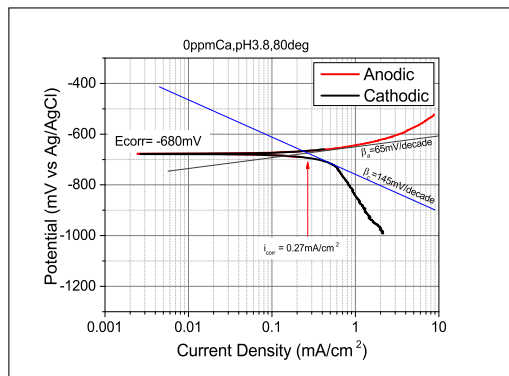


(c) 150mV vs (Ag/AgCl) potentiostatic for 24 h

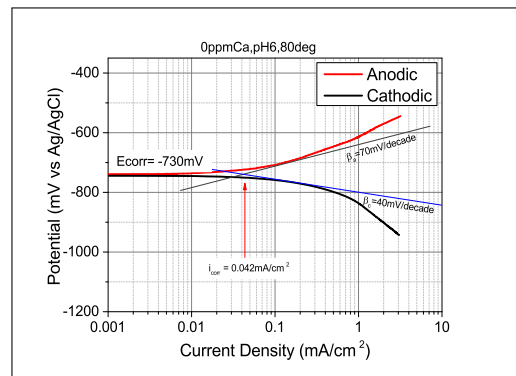
Figure B.1: NPFlex images of corrosion pits formed on X65 carbon steel under (a) 50mV, (b) 100mV and (c) 150mV potentiostatics in 3.5% NaCl solution, unbuffered, 30°C, P_{CO_2} of 1bar for 24 Hrs.

Appendix C

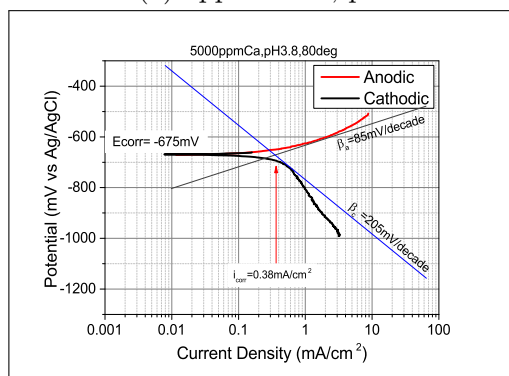
Tafel plot for Calcium tests



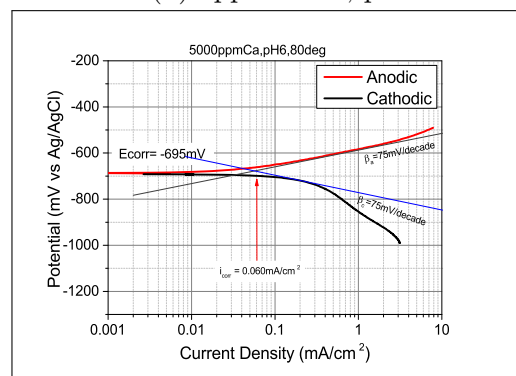
(a) 0ppm Ca²⁺, pH3.8



(b) 0ppm Ca²⁺, pH6



(c) 5000ppm Ca²⁺, pH3.8

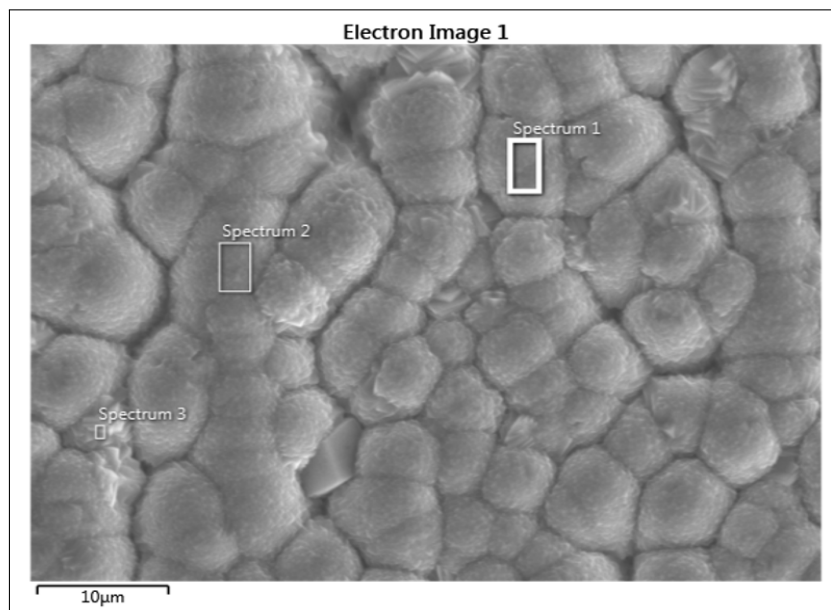


(d) 5000ppm Ca²⁺, pH6

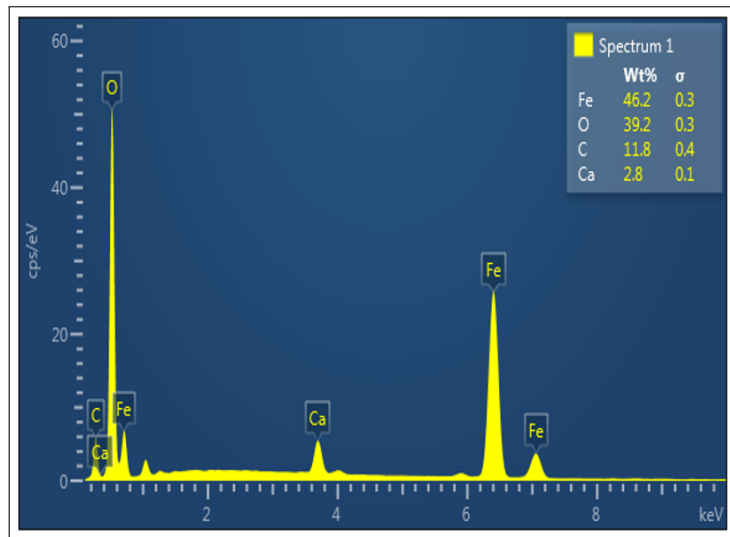
Figure C.1: Tafel plots featuring β_a , β_c and I_{corr} derivatives from anodic and cathodic linear extrapolations at OCP for experiments conducted in saturated CO₂, 2 wt.% NaCl, 80 °C containing (a) 0ppm Ca²⁺, pH3.8 (b) 0ppm Ca²⁺, pH6 (c) 5,000ppm Ca²⁺, pH 3.8 (d) 5,000ppm Ca²⁺, pH 6

Appendix D

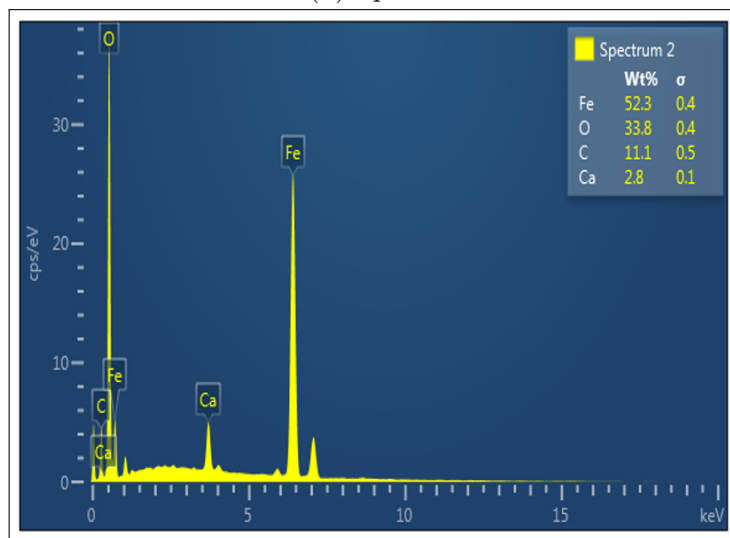
EDX spectrum of corrosion
product detected inside pit in 682
ppm Ca^{2+} solution



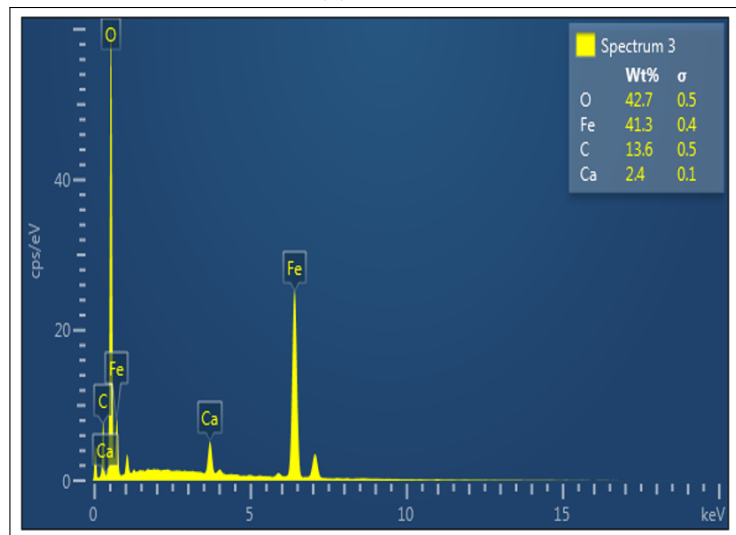
(a) Electron image



(b) Spectrum 1



(c) Spectrum 2



(d) Spectrum 3